

©Copyright 2009
Brian L. Polagye

Hydrodynamic Effects of Kinetic Power Extraction by In-Stream Tidal Turbines

Brian L. Polagye

A dissertation

submitted in partial fulfillment of the
requirements for the degree of

Doctor of Philosophy

University of Washington

2009

Program Authorized to Offer Degree:

Department of Mechanical Engineering

University of Washington
Graduate School

This is to certify that I have examined this copy of a doctoral dissertation by

Brian L. Polagye

and have found that it is complete and satisfactory in all respects, and that any and all revisions
required by the final examining committee have been made.

Chair of the Supervisory Committee:

Philip C. Malte

Reading Committee:

Philip C. Malte

Mitsuhiro Kawase

James J. Riley

Date _____

In presenting this dissertation in partial fulfillment of the requirements for the doctoral degree at the University of Washington, I agree that the Library shall make its copies freely available for inspection. I further agree that extensive copying of the dissertation is allowable only for scholarly purposes, consistent with "fair use" as prescribed in the U.S. Copyright Law. Requests for copying or reproduction of this dissertation may be referred to ProQuest Information and Learning, 300 North Zeeb Road, Ann Arbor, MI 48106-1346, 1-800-521-0600, to whom the author has granted "the right to reproduce and sell (a) copies of the manuscript in microform and/or (b) printed copies of the manuscript made from microform."

Signature _____

Date _____

University of Washington

Abstract

Hydrodynamic Effects of Kinetic Power Extraction by In-Stream Tidal Turbines

Brian L. Polagye

Chair of the Supervisory Committee:
Professor Philip C. Malte
Department of Mechanical Engineering

The hydrodynamic effects of extracting kinetic power from tidal streams presents unique challenges to the development of in-stream tidal power. In-stream tidal turbines superficially resemble wind turbines and extract kinetic power from the ebb and flood of strong tidal currents. Extraction increases the resistance to flow, leading to changes in tidal range, transport, mixing, and the kinetic resource itself. These far-field changes have environmental, social, and economic implications that must be understood to develop the in-stream resource. This dissertation describes the development of a one-dimensional numerical channel model and its application to the study of these effects. The model is applied to determine the roles played by site geometry, network topology, tidal regime, and device dynamics. A comparison is also made between theoretical and modeled predictions for the maximum amount of power which could be extracted from a tidal energy site. The model is extended to a simulation of kinetic power extraction from Puget Sound, Washington. In general, extracting tidal energy will have a number of far-field effects, in proportion to the level of power extraction. At the theoretical limit, these effects can be very significant (e.g., 50% reduction in transport), but are predicted to be immeasurably small for pilot-scale projects. Depending on the specifics of the site, far-field effects may either augment or reduce the existing tidal regime. Changes to the tide, in particular, have significant spatial variability. Since tidal streams are generally subcritical, effects are felt throughout the estuary, not just at the site of extraction.

The one dimensional numerical modeling is supported by a robust theory for predicting the performance characteristics of in-stream devices. The far-field effects of tidal power depend on the total power dissipated by turbines, rather than the power extracted. When the low-speed wake downstream of a turbine mixes with the free-stream, power is lost, such that the total power dissipated by the turbine is significantly greater than the power extracted.

This dissertation concludes with a framework for three-dimensional numerical modeling of near-field extraction effects.

TABLE OF CONTENTS

	Page
LIST OF FIGURES	iv
LIST OF TABLES	ix
GLOSSARY	xi
1. Introduction.....	1
1.1. Basis for Tidal Energy	2
1.2. Properties of Tidal Energy Sites	5
1.3. In-stream Device Overview	6
1.4. Available Resource	8
1.5. Dissertation Structure and Objectives.....	10
2. Theoretical Performance of In-stream Turbines	12
2.1. Review of Theoretical Performance of Wind Turbines	13
2.2. Theoretical Performance of In-stream Turbines	15
2.3. Summary	32
3. Literature Review of Far-field Extraction Effects	34
3.1. Analytical Theory	34
3.2. Numerical Models.....	39
4. 1D Model for Far-field Extraction Effects.....	41
4.1. Development of 1D Channel Model	41
4.2. Extraction from a Single Constriction	53
4.3. Summary	77

5.	Application of 1D Channel Model: Tidal Energy Extraction from Channel Networks.....	79
5.1.	Multiply-Connected Networks.....	83
5.2.	Branching Networks	87
5.3.	Serial Constriction Networks.....	91
5.4.	Hybrid Networks.....	94
5.5.	Potential for Extrapolation.....	96
5.6.	Conclusions.....	100
6.	Application of 1D Channel Model: Tidal Energy Extraction from Puget Sound	104
6.1.	Tidal Energy in Puget Sound	104
6.2.	Grid Generation	106
6.3.	Model Calibration.....	108
6.4.	Extraction Effects in Puget Sound	116
6.5.	Comparison to Qualitative Predictions	126
6.6.	Effects of Possible Development on Puget Sound.....	127
7.	3D Models for Far-field and Near-field Extraction Effects.....	129
7.1.	Approaches for Numerical Modeling of Kinetic Power Extraction.....	130
7.2.	3D Oceanographic Models.....	135
7.3.	Implementation of Parameterized Turbines.....	137
7.4.	Summary.....	149
8.	Conclusions and Future Work	151
8.1.	Long-term Potential for Tidal Energy.....	151
8.2.	Future Work.....	152
	References.....	155

Appendix 1: Boundary Conditions for 1D Models.....	164
Appendix 2: Method of Characteristics	168
Appendix 3: Implementation Details for 1D Channel Model.....	171
Appendix 4: Derivation of Dissipation Factor.....	175
Appendix 5: Baseline Tidal Regimes for Prototype Channel Networks.....	177
Appendix 6: Alternative Calculation for Maximum Dissipation.....	182
Appendix 7: Segment Properties for Puget Sound Model	184

LIST OF FIGURES

Figure Number	Page
Figure 1.1 – Average electrical generation by renewable type in the United States (2002-2007)...	1
Figure 1.2 – Elevation time series for four tidal regimes.....	4
Figure 1.3 – Representative turbine power curve	8
Figure 2.1– Schematic of actuator disc theory applied to wind turbines	13
Figure 2.2 – Black box power loss in a confined channel with a free surface.....	15
Figure 2.3 – Schematic of actuator disc theory applied to hydrokinetic turbines.....	18
Figure 2.4 – Measures of turbine performance at various blockage ratios and Froude numbers for a turbine at the theoretical maximum efficiency.....	24
Figure 2.5 – Performance metric comparison for extraction coefficient and ratio of power extraction to power dissipation	25
Figure 2.6 – Contours of maximum theoretical blockage ratio as a function of streamtube velocity ratio (α) and Fr for hydrokinetic turbines.....	26
Figure 2.7 – Extraction coefficient and ratio of extraction to dissipation as a function of blockage ratio and streamtube velocity ratio for three Froude numbers	28
Figure 2.8 – Extraction coefficient and ratio of extraction to dissipation as a function of blockage ratio and axial induction factor for three Froude numbers.....	29
Figure 2.9 – Drag coefficients for isolated turbines.....	31
Figure 3.1 – Dynamic system consisting of two infinite bays connected by a narrow channel.....	34
Figure 3.2 – Dynamic system consisting of a finite bay connected to the open ocean by a narrow channel.....	35
Figure 4.1 – Schematic of constricted channel with rows of turbines	47
Figure 4.2 – Response of steady-state flow to kinetic power extraction	50
Figure 4.3 – Schematic for a single constriction network.....	53

Figure 4.4 – Spatial variation of changes to the tide with extraction in a single-constriction network	55
Figure 4.5 – Changes to the tide with extraction in a single-constriction network.....	55
Figure 4.6 – Restorative forcing across constricted channel.....	57
Figure 4.7 – Spatial variation of changes to currents with extraction in a single-constriction network	58
Figure 4.8 – Changes to currents with extraction in a single-constriction network.....	58
Figure 4.9 – Spatial variation of changes to transport with extraction in a single-constriction network	59
Figure 4.10 – Changes to transport with extraction in a single-constriction network	59
Figure 4.11 – Changes to total dissipated power and power input to system with extraction in a single-constriction network.....	60
Figure 4.12 – Changes to kinetic power density with extraction in a single-constriction network	60
Figure 4.13 – Velocity response relative to turbine dissipation for single constriction networks .	62
Figure 4.14 – Non-dimensional change in currents in single constriction networks	63
Figure 4.15 – Non-dimensional change in kinetic power density in single constriction networks.	63
Figure 4.16 – Non-dimensional change in tidal amplitude in single constriction networks	64
Figure 4.17 – Occurrence distribution of speeds for different tidal regimes	68
Figure 4.18 – Power density time series for four tidal regimes	69
Figure 4.19 – Tide constituent response to 300MW turbine dissipation in a single constriction network for four tidal regimes	71
Figure 4.20 – Current constituent response to 300MW turbine dissipation in a single constriction network for four tidal regimes	72
Figure 4.21 – Non-dimensional response to turbine dissipation in a single constriction network for four tidal regimes	73

Figure 4.22 – Time series with power dissipation including turbine dynamics.....	75
Figure 4.23 – Non-dimensional response to extraction up to $P/P_{\max} = 0.6$ including turbine dynamics	76
Figure 4.24 – Non-dimensional response to extraction including turbine dynamics.....	77
Figure 5.1 – Coastline for southeast region of Alaska.....	79
Figure 5.2 – Coastline for Penobscot Bay, coast of Maine.....	80
Figure 5.3 – Schematics of prototype channel networks	81
Figure 5.4 – Single constriction network response to 300MW turbine dissipation	82
Figure 5.5 – Multiply-connected network response to 300MW turbine dissipation.....	84
Figure 5.6 – Effect of redirection in multiply-connected networks	86
Figure 5.7 – Non-dimensional response to dissipation for multiply-connected networks.....	87
Figure 5.8 – Branching network response to 300MW turbine dissipation	89
Figure 5.9 – Effect of redirection in branching networks	90
Figure 5.10 – Non-dimensional response to dissipation for branching networks.....	91
Figure 5.11 – Serial constriction network response to 300MW turbine dissipation	92
Figure 5.12 – Non-dimensional response to dissipation for serial constriction networks	94
Figure 5.13 – Schematic of a hybrid branching-serial network	95
Figure 5.14 – Hybrid network response to 300MW turbine dissipation.....	96
Figure 5.15 – Segments of prototype channel networks with equivalent responses to extraction.	97
Figure 5.16 – Relative changes to kinetic power density with non-dimensional turbine dissipation (all networks).....	98
Figure 5.17 – Errors associated with extrapolation of P_{\max} from response at $P < P_{\max}$ for the hybrid network	100

Figure 5.18 – Correlation of change in tidal elevation seaward of constriction with variation from theory	102
Figure 6.1 – Puget Sound coastline with major features labeled.	105
Figure 6.2 – Puget Sound channel network superimposed on Puget Sound coastline.....	107
Figure 6.3 – Version of Puget Sound channel network resolving features of flow in South Sound and around Bainbridge Island.	108
Figure 6.4 – Comparison of modeled to observed tidal amplitude	110
Figure 6.5 – Tidal amplitude calibration by constituent	111
Figure 6.6 – Comparison of modeled to observed tidal phase lag	113
Figure 6.7 – Tidal phase lag calibration by constituent	114
Figure 6.8 – Power dissipation in regions of Puget Sound	115
Figure 6.9 – Relative change to tides in Puget Sound due to power extraction in Admiralty Inlet.	119
Figure 6.10 – Relative changes in Puget Sound due to power extraction in Admiralty Inlet.....	120
Figure 6.11 – Relative change to tides in Puget Sound due to power extraction in Tacoma Narrows.....	122
Figure 6.12 – Relative changes in Puget Sound due to power extraction in Tacoma Narrows.. .	123
Figure 6.13 – Relative change to tidal transport in Puget Sound as a function of power dissipated by turbines in Tacoma Narrows and Admiralty Inlet	125
Figure 7.1 – Voronoi diagram of unstructured grid.	137
Figure 7.2 – Vertical structure of horizontal velocity in the prototype domain without power extraction.	139
Figure 7.3 – Sample cross-sections of the prototype grid for turbine parameterization in SUNTANS	140
Figure 7.4 – Flow quantities on a non-dimensional x - z cross-section passing through a parameterized turbine ($D = 10\text{m}$, $\beta = 0.3$)	141

Figure 7.5 – Non-dimensional velocity deficit at four downstream positions.....	142
Figure 7.6 – Free surface and depth-averaged velocity change across the parameterized turbine.	143
Figure 7.7 – Non-dimensional velocity deficit at $x/D = 20$, comparing the effect of vertical shear.	144
Figure 7.8 – Comparison of vertical eddy diffusivity (ν_t) between a case with vertical shear and without.....	145
Figure 7.9 – Non-dimensional velocity deficit at $x/D = 60$ for three different vertical resolutions	146
Figure 7.10 – Free surface and depth-averaged velocity change across the parameterized turbine with different pressure treatments.....	147
Figure 7.11 – Non-dimensional velocity deficit at four positions far downstream of parameterized turbine.	148

LIST OF TABLES

Table Number	Page
Table 1.1 – Representative tidal constituents.....	3
Table 2.1– Comparison of analytical and numerical performance for an isolated turbine	23
Table 2.2 – Geometric properties and drag on existing and future tidal energy devices.	32
Table 4.1 – Baseline properties for single constriction network channel segments.	54
Table 4.2 – Single constriction network geometries and tidal forcings.....	61
Table 4.3 – Comparison between theoretical and model predictions for the maximum possible turbine dissipation in a single constriction network.....	66
Table 4.4 – Comparison between theoretical and model predictions for maximum turbine dissipation under four tidal regimes (single constriction network).....	74
Table 5.1 – Baseline properties for multiply-connected network channel segments.....	83
Table 5.2 – Multiply-connected network geometries	86
Table 5.3 – Baseline properties for branching network channel segments.....	87
Table 5.4 – Comparison between theoretical and model predictions for maximum possible turbine dissipation (branching network)	90
Table 5.5 – Baseline properties for serial constriction network channel segments	91
Table 5.6 – Comparison between theoretical and model predictions for maximum possible turbine dissipation (serial constriction network).....	93
Table 5.7 – Baseline properties for hybrid network channel segments	95
Table 5.8 – Polynomial fit coefficients for non-dimensional response curves (transport basis). ..	99
Table 5.9 – Polynomial fit coefficients for non-dimensional response curves (kinetic power basis).	99
Table 6.1 – Volumes of major basins in Puget Sound.....	107

Table 6.2 – External tide boundary values.....	111
Table 6.3 – Comparison of modeled transport amplitudes to amplitude modeled by Lavelle et al.	115
Table 6.4 – Baseline tidal regime in Puget Sound	118
Table 6.5 – Far-field effects of proposed Admiralty Inlet pilot project on regions of Puget Sound	127
Table 6.6 – Far-field effects of possible Admiralty Inlet commercial project on regions of Puget Sound.	128
Table 7.1 – Comparison of 3D oceanographic models	135
Table 7.2 – Comparison between theoretical and model data calculations for dissipation coefficient	149

GLOSSARY

Definitions

Array – a group of turbines, generally consisting of several transects.

Actuator disc – a parameterization of a horizontal axis turbine in which the forces acting on the blades are spread over the rotor swept area.

Blockage ratio – the non-dimensional ratio of the turbine swept area to the channel cross-sectional area.

Channel – a segment of constant rectangular cross-section.

Current – the motion of water.

Device – a generic in-stream tidal turbine.

Dissipated power – power dissipated in a tidal stream by turbines. This will generally be greater than extracted power because of unavoidable losses associated with the mixing of the turbine wake with the free stream.

Diurnal – once daily.

Ebb tide – the movement of water out of an estuary into the open ocean.

Extracted power – power extracted from a tidal stream by turbines.

Flood tide – the movement of water into an estuary from the open ocean.

Frictional dissipation – power naturally dissipated by friction between moving water and solid surfaces (e.g., seabed).

Froude number – the non-dimensional ratio of inertial to gravitational forces in a fluid flow.

Kinetic power density – the kinetic power in a fluid flow per square meter of cross-sectional area.

Maximum dissipation – the theoretical maximum average power which may be dissipated by turbines at a particular location in a channel network.

Network – one or more channel segments connected by junctions and joined to the open ocean.

Reynolds number – the non-dimensional ratio of inertial to viscous forces in a fluid flow.

Semidiurnal – twice daily.

Sill – a relatively shallow shelf connecting deeper bodies of water.

Theoretically extractable resource – the maximum amount of power which can be extracted from a tidal stream at a particular site. Related to P_{\max} by the ratio of extracted to dissipated power for a particular array configuration.

Tidal constituent – a harmonic function with defined amplitude, frequency and phase lag which describes an aspect of the lunar or solar forces acting on the Earth's oceans.

Tides – the rise and fall of water.

Transect – a row of turbines arranged perpendicular to the direction of flow.

Transport – the volume (or volume flow rate) of water moving across a defined cross-sectional area.

Turbine – a generic in-stream tidal turbine.

Notation

a – axial induction factor. A non-dimensional parameterization of the change in velocity from upstream of a turbine to the rotor plane in actuator disc theory.

A – cross sectional area (m^2).

α – a measure of device performance. The non-dimensional ratio of the velocity upstream of a turbine to the velocity in fully expanded wake downstream of the turbine. $\alpha = 1/3$ corresponds to a turbine operating at theoretical maximum extraction.

b – channel width (m).

β – drag factor in SUNTANS parameterization.

ε – blockage ratio.

Fr – Froude number.

g – acceleration due to gravity (9.81 m/s).

h – instantaneous water depth (m).

H – time-averaged water depth (m).

η_d –dissipation coefficient. The proportion of upstream kinetic power which is dissipated by the turbine, including power extracted and power lost in the mixing of the wake with the free-stream.

η_e –extraction coefficient. The proportion of upstream kinetic power which is extracted by the turbine.

K – kinetic power density (kW/m^2).

K_1 – Diurnal declinational. The strongest diurnal tidal constituent at most sites.

L – channel length.

M_2 – Semidiurnal lunar tidal constituent. The strongest semidiurnal tidal constituent at most sites.

n – the Manning roughness coefficient ($\text{m/s}^{1/3}$).

ρ – fluid density. Nominally 1024 kg/m^3 for sea water.

P – Power dissipated by in-stream turbines.

P_{\max} – The theoretical maximum average power which may be dissipated by turbines at a particular location in a channel network (MW).

P/P_{\max} – Turbine dissipation non-dimensionalized by the maximum possible dissipation.

Q – volume flow rate or transport (m^3/s).

R_h – hydraulic radius (m).

S_f – friction slope. A non-dimensional measure of the rate of frictional dissipation in a channel, as described relative to the energy grade line.

ζ – water surface elevation relative to mean sea level (m).

ACKNOWLEDGEMENTS

The author would like to express his sincere appreciation to a number of individuals, without whom this dissertation would not have been possible:

- Philip Malte for his support and encouragement during this study of tidal energy. Thank you for teaching me to look at research with a critical eye and write in a way that others may understand. Without your initiative to teach a class on this subject, none of this would have happened.
- Roger Bedard of the Electric Power Research Institute for his tireless work in securing fellowship funding for this research and introducing me to the more practical aspects of tidal energy.
- Mitsuhiro Kawase for his patience in teaching oceanography to an engineer.
- James Riley for helping to kick the tires on the numerical model.
- Alberto Aliseda for listening to theories when I was worried I might be on the wrong track.
- Dale Durran for encouraging me to take a closer look at boundary conditions.
- Stephen Burges for going above and beyond what is expected of a GSR and taking the time not only to understand my research in detail, but also to help me see the big picture.
- Craig Collar and Snohomish Public Utility District for their financial support of this research.
- My parents and my extended family for being supportive during my pursuit of a doctoral degree.
- Many friends who have been subjected to theoretical discussions of tidal energy on the way up and down mountains in the Cascades.

DEDICATION

To Michelle. Thank you for Everything.

1. Introduction

Discussions of energy policy encompass a diversity of concerns including climate change, a general desire to live more sustainably, and long-term energy security. This is a complex problem and a cohesive policy requires decreased energy use through lifestyle changes, improved energy efficiency, and tapping sustainable forms of energy. In-stream tidal energy, like all renewable energy, fits into the final category.

For the United States in 2007, renewable energy accounted for just over 8% of all electricity generated [1]. As shown in Figure 1.1, most of this is produced by conventional hydroelectric plants [1], though for policy reasons this is not always classified as renewable generation.

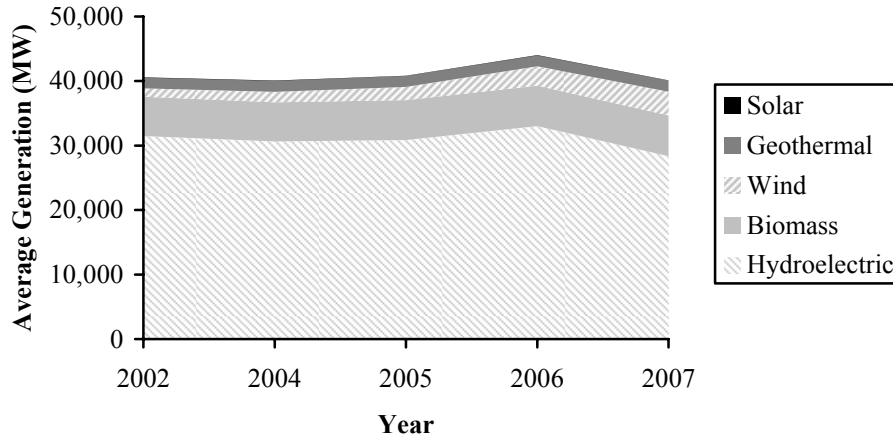


Figure 1.1 – Average electrical generation by renewable type in the United States (2002-2007)

A commonly cited impetus for investment in renewable energy is the reduction in oil consumption or the need for alternatives to high oil prices. This is something of a red herring; petroleum liquids accounted for only 1% of US electrical generation in 2007 [1] and replacing these with renewable energy would have a negligible effect on both consumption and prices. Nevertheless, a key barrier to the electrification of the transportation sector is the need for new generation to support fleets of electric vehicles. In this way, renewable energy could, in fact, help to reduce our dependence on oil without requiring the construction of a new generation of thermal power plants.

Marine energy is a relatively new form of renewable energy and includes power generation from tidal currents, ocean currents, and waves. In-stream tidal energy extracts kinetic energy from the

motion of moving water. In principle, this is similar to wind energy and it is not a coincidence that many in-stream tidal devices resemble wind turbines. It is also possible to harness the energy in the tides using a barrage. This is a fundamentally different technology, analogous to conventional hydroelectric power. In a barrage scheme, a dam is constructed across the mouth of an estuary. At high tide, the gates in the dam close, maintaining the water level in the estuary as the water level drops in the open ocean. This creates a potential head which is exploited at low tide by conventional turbines. If the gates are closed as the ocean level rises and then opened again near high tide, power may be generated on both stages of the tide. The generating capacity of a barrage can be very large, but its operation fundamentally alters the tidal regime of an estuary and requires a large capital investment. For example, the proposed Severn Barrage in the UK would, on average, generate 2 GW of electricity at a cost of £23bn [2]. By comparison, in-stream tidal energy utilizes a modular approach with a lower unit cost structure and potentially smaller environmental footprint.

1.1. Basis for Tidal Energy

An excellent description of the tide generating force is given by Boone [3] and only a brief summary is presented here. At a basic level, the gravitational pull of the sun and the moon on the Earth's oceans produces a twice daily rise and fall in water depth. As the depth of the open ocean rises, water floods into estuaries and then, as the depth falls, ebbs back out. The relative declination between celestial bodies also sets up a once daily variation, such that successive high and low tides are not of the same strength. In addition to this daily variation, there is a fortnightly variation dependent upon the relative alignment of the sun and the moon with the Earth. When their gravitational fields act in opposition, the amplitude of the tides and currents is weakest, and when they act in concert tides and currents are strongest. This cycle has a 14.8 day period, with weak tides referred to as 'neap tides' and strong tides as 'spring tides'. Finally, the relative separation between the earth, sun, and moon gives rise to a seasonal variation with the strongest annual tides occurring around the solstice and weakest around the equinox. Therefore, the tides are a variable resource.

Since the motion of the earth, moon, and sun are well characterized, and tidal energy is derived from these gravitational interactions, it is possible to predict the tides far in advance. This is in contrast to wind energy, which derives from uneven heating of the earth's surface and is, therefore, as "predictable" as the weather. The tides exactly repeat on an 18.6 year cycle (the tidal

epoch). Since these motions are periodic, tides or currents may be represented as a superposition of harmonic functions, or constituents. The mathematical representation of this is given by (1.1), where $h(t)$ is the time varying depth of water (the tide), H is the mean sea level, h_i is the amplitude of the i^{th} constituent, ω_i is the frequency, and ϕ_i is the relative phase.

$$h(t) = H + \sum_i h_i \cos(\omega_i t + \phi_i) \quad (1.1)$$

Table 1.1 shows the periods of the tidal constituents used to force models in this dissertation and their description [4]. For example, the M2 tide, with a period of 12.42 hours, is the primary tide force generated by the moon.

Table 1.1 – Representative tidal constituents

Constituent	Period (h)	Name
M2	12.42	Principal semidiurnal lunar
S2	23.93	Principal semidiurnal solar
N2	12.0	Lunar elliptic semidiurnal
K1	25.82	Diurnal declinational
O1	12.66	Lunar diurnal
P1	24.07	Solar diurnal

Depending on the relative strength of the semidiurnal (twice daily) and diurnal (once daily) constituents, a tidal energy site may be classified into one of four regimes by its form factor, or Formhazl (F), which is the ratio of the amplitudes of the diurnal (K1+O1) to the semidiurnal (M2+S2) constituents. The four classifications are described as follows, with a representative time series shown for each in Figure 1.2.

- Semidiurnal – two high and low waters each day of approximately the same height. ($0 < F < 0.25$).
- Mixed, mainly semidiurnal – two high and low waters each day, but with significant inequality in height and timing. ($0.25 < F < 1.5$).
- Mixed, mainly diurnal – either one high and low water each day or two high and low waters with significant inequality in the height and timing. ($1.25 < F < 3.0$).
- Diurnal – one high and low water each day of approximately the same height. ($F > 3.0$).

Most potential in-stream tidal energy sites have a semi-diurnal or mixed, mainly diurnal regime [5].

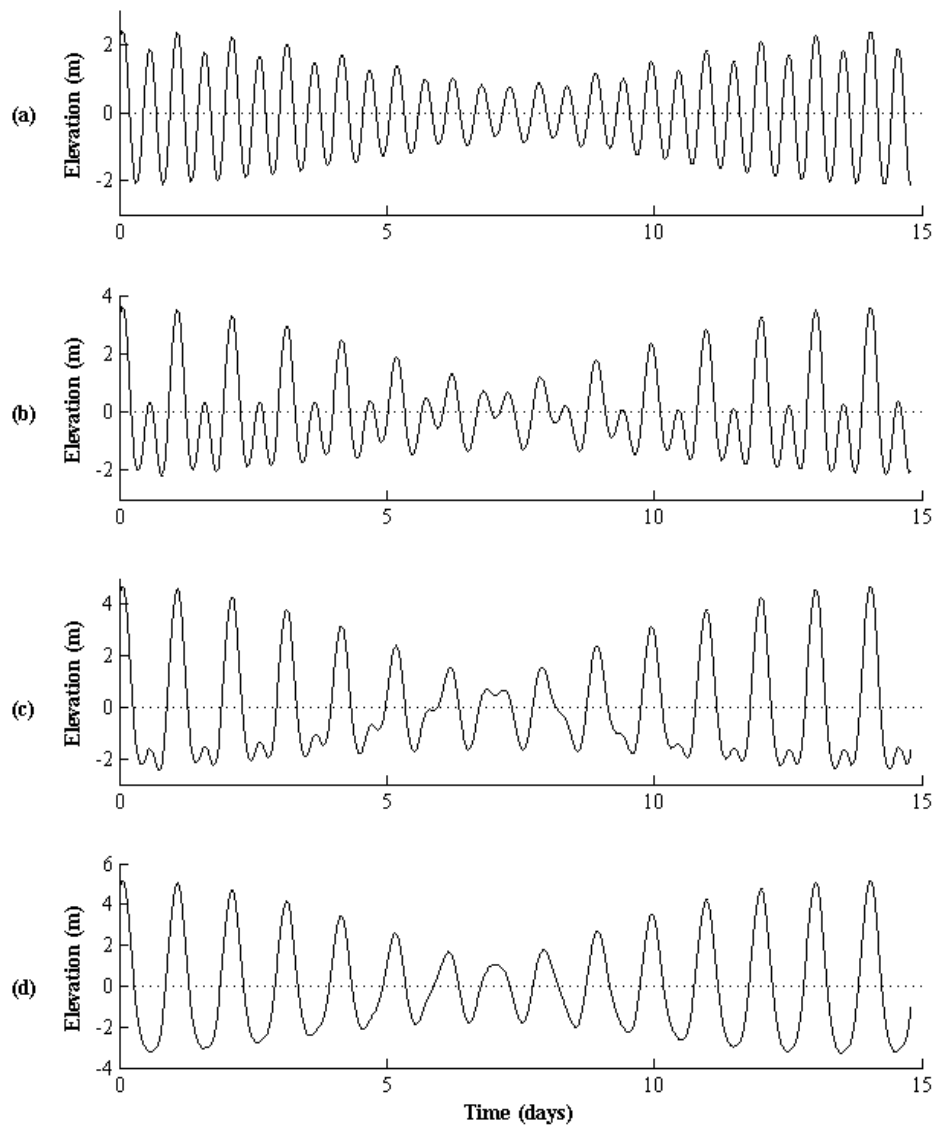


Figure 1.2 – Elevation time series for four tidal regimes. (a) semidiurnal ($F=0.1$), (b) mixed, mainly semidiurnal ($F=0.9$), (c) mixed, mainly diurnal ($F=2.3$), (d) diurnal ($F=4.7$).

While tidal currents ebb and flood around the world, in-stream tidal energy requires extreme currents to generate cost-effective power. In oceanographic terms, currents of 1 m/s are exceptionally strong, but currents at the most promising in-stream sites may regularly exceed 4 m/s. There are two mechanisms which can give rise to such currents and both are the result of a phase difference in the tide across narrow channels.

The first is when a narrow channel connects two large bodies of water in which the tides are out of phase. The phase difference generates a driving head across the constriction. In this case, the water flowing through the channel is negligible in comparison to the volume of water in the adjacent bodies. Deception Pass, connecting Skagit Bay to the Strait of Juan de Fuca, is an example of this type of site in Washington.

The second is when a narrow channel connects one part of an embayment to another. In this case, frictional power dissipation across the channel gives rise to a phase difference, which generates a driving head. Coming full circle, the driving head leads to strong currents, which are the mechanism for frictional power dissipation. However, in this case, the water elevation landward of the channel is dependent on the volume of water passing through the channel. Admiralty Inlet, separating Puget Sound from the Strait of Juan de Fuca, and Tacoma Narrows, separating the South Sound from the Main Basin, are examples of this type of site in Washington.

Both cases require narrow, constricted channels connecting large bodies of water. By their nature, such constrictions are relatively small-scale topographic features. Therefore, strong tidal currents tend to be very localized, which is in contrast to wind or wave energy, where the resource is relatively uniform over a large area.

1.2. Properties of Tidal Energy Sites

Desirable tidal energy sites have a number of key characteristics, though the strength of the currents is only necessary requirement.

A common measure of the intensity of the in-stream resource is kinetic power density (K , W/m^2) which is given by (1.2), where ρ is the density of seawater (nominally 1024 kg/m^3) and u is the time-varying speed (m/s).

$$K(t) = \frac{1}{2} \rho u^3 \quad (1.2)$$

For the purposes of feasibility assessment, this quantity is often reported as an annual average. The minimum economic threshold for site development is around 1 kW/m^2 and for outstanding sites the kinetic power density may exceed 5 kW/m^2 [6]. While power density is a common measure of resource intensity, it is also important to account for large scale turbulence, which could place considerable stress on the device and support structure. In addition, currents are ideally bi-directional (180° degree difference between ebb and flood) with a blunt vertical profile.

A water depth of 30-40 m is optimal for device deployment, but depths up to 80m can be accommodated by existing foundation technology [7]. A level bedrock seabed is preferred, but it is possible to install turbines on other substrates (e.g., cobbles, consolidated sediments) or on minor slopes.

The power generated by turbines must be interconnected with the electrical grid. Transmission lines (115 kV) near a load center may accept up to 100 MW of power from an in-stream facility, but distribution lines (15 kV) are able to accept less than 10 MW [7].

Ideally, in-stream sites have few existing uses or are large enough to accommodate existing uses and tidal energy. Commercial shipping, fishing, and diving are all examples of existing uses which might conflict with tidal energy.

The environmental characteristics of a site are of tremendous interest to the public and regulatory agencies, but often difficult to quantify. In particular the noise or flow alterations related to turbine operation may trigger avoidance or aggregation behavior in fish and marine mammals. Since there are only a handful of device demonstrations presently operating around the world, these near-field effects have not yet been studied in detail. As will be discussed in detail in this dissertation, tidal power extraction may also lead to changes in the far-field; that is, alter the estuary-wide tidal regime. These changes may have broad implications for the physical environment (e.g., sediment transport, dissolved oxygen) and biological processes. A complete inventory of potential environmental concerns may be found in Cada [8].

1.3. In-stream Device Overview

Only a brief overview of in-stream devices is given here. A descriptive database of tidal energy devices and projects is maintained by the United States Department of Energy [9]. While there are a number of device variants, the leading designs have a horizontal axis; that is, the axis of rotation is along the same principal axis as the fluid flow. Like wind turbines, the motion of water over the blades generates a lifting force that acts to rotate the blades. An electrical generator converts this rotation to electricity, which is transmitted to the shore via a power cable. The axial force on the rotor is resisted by a support structure either embedded in the seabed (pile foundation) or held in place by its mass (gravity foundation). The support structure also serves to elevate the rotor out of the slowest region of the boundary layer. The designs of the blades and drivetrain (gearbox, generator) borrow heavily from the wind industry, and foundation technology is adapted from offshore oil and gas structures.

In contrast to wind turbines, which may be over 100 m in diameter, the largest proposed tidal turbines are no more than 20 m across. This reflects both the more limited depth of tidal channels and the larger stresses due to the relatively higher density of seawater (1024 kg/m^3) compared to air (1.2 kg/m^3). Most designs for utility-scale turbines call for a peak electrical output on the order of 1-2 MW per device. Smaller devices, which are more suitable for remote, distributed generation, are also being developed.

In order to prevent blade damage due to cavitation, the tip speed of the turbine rotor is generally restricted to 10-12 m/s. For utility-scale turbines, this limits the rate of blade rotation to around 10 RPM. In contrast, the propellers on large ships rotate at about 100 RPM. Batten et al. [10] have studied blade cavitation to better understand incipient conditions. This research could allow for higher, more efficient, tip speed ratios, but could also increase the hazard posed to fish and marine mammals.

The power curve for a hypothetical in-stream turbine is shown in Figure 1.3, with a constant efficiency of 50%, cut-in speed of 1 m/s, and rated speed of 2.5 m/s. Three operating states are possible.

- I. Below cut-in speed: The water speed is insufficient to rotate the blades and the turbine generates no power. Typical cut-in speeds are between 1 and 2 knots (0.5-1 m/s).

$$P_{\text{extracted}} = 0 \quad (1.3)$$

- II. Between cut-in and rated speed: The turbine extracts power in proportion to the kinetic power incident over its swept area (A). The constant of proportionality is the extraction efficiency (η_e). For variable pitch turbines this is roughly constant over a range of velocities;

$$P_{\text{extracted}} = \frac{1}{2} \eta_e \rho A u^3. \quad (1.4)$$

- III. Above rated speed: Constant power is extracted from the flow by changing blade pitch with current speed;

$$P_{\text{extracted}} = P_{\text{rated}}. \quad (1.5)$$

The extracted power is related to the generated power by the balance of system efficiency, which includes the efficiency of the gearbox, generator, and power transmission back to shore.

Wind turbines have a fourth operating regime defined by a cut-out speed, above which the turbine blades are feathered to avoid damage during periods of extremely high winds. Since tidal currents are largely predictable, there is no tidal analogue to extreme weather. The possible exception to this is a tsunami event, which is not generally considered in the design of a tidal turbine.

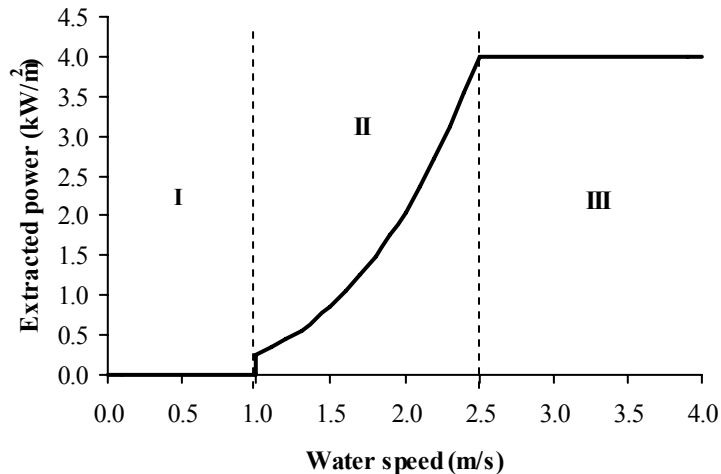


Figure 1.3 – Representative turbine power curve. Region I is below the cut-in speed and the turbine extracts no power. In Region II, power is extracted in proportion to the kinetic power incident on the rotor swept area. Region III is above the rated speed and power extraction is constant.

Device utilization is quantified by the capacity factor, defined as the ratio of average power extracted to power extracted at rated speed. Feasibility studies indicate that the lowest cost of energy for in-stream tidal turbines would be achieved with capacity factors between 30 and 40% [6] depending on the particulars of the tidal regime. Therefore, the selection of the rated speed is an economic decision.

1.4. Available Resource

While the similarities between tidal and wind energy are obvious and striking, there are also important differences. Even the largest wind turbines extend no more than a few hundred meters into the air, while the characteristic length scale for the atmosphere is measured in kilometers. For most tidal energy sites, the characteristic length scales of the device and resource are comparable (e.g., 20 m rotor in 40 m water) and the extracted power may constitute an appreciable fraction of the total power in the system. As will be discussed in this dissertation, kinetic power extraction from tidal streams has the effect of increasing the frictional resistance to flow. Since tidal streams are generally subcritical, the effect of increasing friction is felt estuary-wide. While small increases in friction due to extraction may be indistinguishable from natural friction, large-scale

extraction may measurably alter both tides and currents. This has environmental, social, and economic implications.

In addition to environmental impacts, far-field extraction effects complicate resource assessment. Near-term development goals for tidal energy are focused on resolving engineering and environmental issues associated with operating small arrays of turbines. However, the long-term potential for the technology is determined, among other factors, by the available resource. Since the extraction reduces currents, the kinetic resource will be reduced by extraction in a site-specific manner. As a result, it is not generally possible to determine the recoverable resource from measurements or models of the natural tidal regime.

The goal of resource assessment is to determine the practically recoverable resource at a particular site. This may be constrained by a number of factors:

- (1) Theoretically recoverable resource – the point at which adding more turbines to the flow extracts less power.
- (2) Available space – tidal energy sites are highly localized; thus, if turbines are too tightly packed, the wake of one device may degrade the performance of another.
- (3) Existing uses – those uses incompatible with tidal energy may restrict turbines to a particular location within a site or prohibit any development.
- (4) Interconnection – the ability of the electrical grid to accept power generated by turbines.
- (5) Near-field environmental effects – the operation of turbines may degrade critical habitat for listed or endangered species.
- (6) Far-field environmental effects – the operation of turbines may alter the tidal regime, with broad implications.

Since the theoretically recoverable resource depends on the change in kinetic power density with extraction, a determination of the theoretically recoverable resource necessarily requires an understanding of far-field effects.

The type of resource assessment described above has only been carried out for a handful of tidal energy sites around the world, and never as part of a coordinated study. For example, a site characterization report by Hagerman [11] quantified the resource intensity, available space, existing uses, and interconnection potential for the Minas Passage, Nova Scotia. However, the author lacked the tools to rigorously assess the far-field environmental effects. This was done at a

later date by Karsten et al. [12]. In addition to the Minas Passage, far-field environmental effects have been assessed for the Johnstone Strait, British Columbia [13], Massett Sound, British Columbia [14], Portland Bill, UK [15] and Puget Sound, Washington [16] (topic of Chapter 6). These constitute only a small fraction of potential tidal energy sites worldwide.

A number of other *ad hoc* studies have been carried out with the goal of resource assessment [17, 18], but would be more accurately described as site inventories. These studies categorize sites in terms of their measurable physical properties, and then apply engineering rules to determine the theoretically recoverable resource. The standard method has been to determine the average kinetic power on a cross-sectional slice and then assume that some fraction of that power (e.g., 15%) could be extracted without significant environmental impact. As demonstrated by Garrett and Cummins [19, 20], this has no physical basis and gives an incorrect estimate for the theoretically recoverable resource. Further, if there are multiple sites in the same region, the regional resource is often presented as the sum of the resources at each site. This neglects the mutual influence of one site on another due to system-wide far-field effects. Site inventories are an essential first step in directing developers to locations of interest, but only part of a rigorous resource assessment.

1.5. Dissertation Structure and Objectives

This dissertation investigates the hydrodynamic effects of in-stream energy extraction, principally the far-field effects. In doing so, it compares analytical estimates for the theoretically recovered resource to those obtained from a computationally efficient, one-dimensional channel model. Chapter 2 applies streamtube theory to the development of a robust theoretical framework for predicting the performance of an in-stream turbine. Chapter 3 summarizes the available literature on analytical and numerical approaches for investigating far-field effects. Chapter 4 details the development of a one-dimensional channel model for tidal energy extraction and its application to a simple channel network. Chapter 5 discusses the application of the model to investigate the extraction effects in prototypical channel networks. The study of simple models may allow for qualitative predictions of extraction effects in more complex networks. In Chapter 6, the model is used to study the effects of in-stream development in Puget Sound, Washington. This concludes the efforts related to barotropic far-field effects. Chapter 7 explores the possibilities for incorporating models for arrays of turbines into three-dimensional oceanographic codes to

investigate both near-field and far-field effects. In Chapter 8, general conclusions are presented and suggestions are made for future work.

2. Theoretical Performance of In-stream Turbines

As discussed in Chapter 1, most device concepts for tidal in-stream energy extraction resemble wind turbines. A consequence of power extraction by these devices will be increased resistance to flow in tidal channels. This will be discussed in more detail in subsequent chapters. For resource assessments, the quantity of interest is the amount of electricity which could be generated from a tidal energy site. This is related to the extracted power by the balance of system efficiency (i.e. gearbox and generator). However, the power extracted by an array of devices depends on the flow velocity, which depends on the perturbation to the natural flow regime by the array. This perturbation is not a function of the power extracted, but rather the total power dissipated in the operation of turbines. Dissipated power includes power extracted by the devices, power lost due to wake rotation, power lost due to the mixing of the low speed wake with the high speed channel flow, and power lost due to drag on support structures. Therefore, in order to determine the extraction potential for a site, it is first necessary to quantify the maximum possible dissipation and the fraction of dissipation attributable to extraction.

The relation between extraction and dissipation has been explored for wind turbines by Corten [21] using classical actuator disc theory. It has been extended by Garrett and Cummins [22] to hydrokinetic turbines operating at the theoretical maximum efficiency in a confined channel. However, their derivation employs a number of simplifying assumptions that are only appropriate under restricted conditions.

This chapter lays out the theoretical basis for wind turbine performance, summarizes previous work by Garrett and Cummins, and then presents a theoretical basis for determining device performance under a less restrictive set of simplifying assumptions. Results are discussed for a range of Froude numbers, blockage ratios (ratio of turbine swept area to channel swept area), and device efficiencies. The physical limits of this theory are also presented. While the theory is discussed in the context of a single turbine, the analysis applies equally to the case of several turbines on a particular cross-sectional transect [22]. This discussion applies not just to the theoretical performance of in-stream tidal turbines, but all water turbines operating in channels (e.g., rivers or irrigation canals).

2.1. Review of Theoretical Performance of Wind Turbines

Actuator disc theory describes energy extraction by a rotor in the context of a one-dimensional streamtube (Figure 2.1) and provides the theoretical underpinning for the classical Lanchester-Betz efficiency [23].

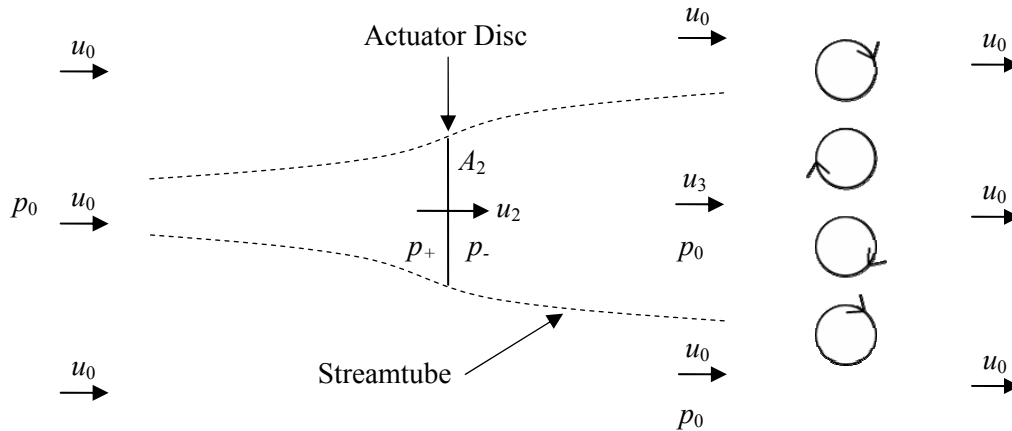


Figure 2.1– Schematic of actuator disc theory applied to wind turbines

The actuator disc approximates a real turbine by uniformly distributing the forces acting on the individual blades over the rotor swept area (A_2). As the flow approaches the actuator disc and the streamtube expands, the velocity in the streamtube decreases from the free-stream value (u_0). Energy conservation requires that as the velocity decreases, the static pressure must increase from the free-stream value (p_0) to a higher value (p_+). Across the rotor, the pressure decreases discontinuously to a value below that of the free-stream (p_-). Beyond the actuator disc, the streamtube continues to expand, and the velocity decreases until the static pressure has returned to the free-stream value. This expansion region extends approximately one diameter beyond the rotor [24]. Theory requires that the flow passing through the actuator disc be separable from the free-stream by a well-defined streamtube [23]. While the shear between the free-stream and wake is significant, the expansion region is of limited length and minimal mixing occurs.

The axial force (F) acting over the rotor swept area (A_2) is proportional to the pressure drop

$$F = A_2(p_+ - p_-). \quad (2.1)$$

In combination with Bernoulli's principle, conservation of mass and momentum require that the streamtube velocity at the turbine rotor (u_2) be

$$u_2 = \frac{u_0 + u_3}{2}. \quad (2.2)$$

u_2 may also be related to the upstream velocity (u_0) by an axial induction factor (a),

$$u_2 = (1 - a)u_0. \quad (2.3)$$

The power extracted ($P_{\text{extracted}}$) is related to the free-stream conditions by the extraction coefficient (η_e) as

$$P_{\text{extracted}} = \frac{1}{2} \rho A_2 u_0^3 \eta_e = \frac{1}{2} \rho A_2 u_0^3 4a(1 - a)^2. \quad (2.4)$$

For a wind turbine, $a = 1/3$ is optimal and yields $\eta_e = 16/27$, the classical Lanchester-Betz efficiency. Also, at the theoretical maximum efficiency, the wake velocity (u_3) is 1/3 of the free-stream velocity (u_0). Experiments and observations indicate that one-dimensional momentum theory describes the behavior of real wind turbines up to axial induction factors of 0.4-0.5 [23,25]. Beyond this point, the wind turbine operates in a turbulent wake state [23] in which significant mixing occurs between the wake and the free-stream in the expansion region.

As shown by Corten [21], when the free-stream mixes with the wake, significant energy is lost to turbulence. This constitutes an energy loss in excess of the loss due to extraction by the rotor. For a turbine operating at the theoretical maximum efficiency, losses due to wake mixing constitute 1/3 of the total energy dissipated by the turbine (extraction and wake losses). Corten [21] further observed that for rotors operating below the theoretical maximum, wake losses constitute a smaller portion of the total dissipation. This is consistent with reduced shear between the wake and free-stream. Corten's analysis is suitable for wind turbines and requires that the pressure at the end of the expansion region is atmospheric pressure, and that the velocity in the free-stream adjacent to the wake is unchanged from the upstream value. These assumptions are valid for wind turbines operating in the atmospheric boundary layer, but are not necessarily valid for hydrokinetic turbines operating in water channels.

2.2. Theoretical Performance of In-stream Turbines

For turbines operating in a water channel, the dynamics of extraction are as described above when the area swept by the turbine is very small in comparison to the channel cross-section. However, as the swept area increases, the confinement of the free surface and channel walls becomes dynamically significant and the velocity adjacent to the streamtube increases. Therefore, the shear between the wake and adjacent free-stream may be higher for a water turbine than for a wind turbine, leading to increased mixing losses.

Garrett and Cummins [22] have previously extended Corten's analysis [21] to a water channel and closed the governing equations with the assumptions that the cross-sectional area of the channel remains approximately constant throughout the domain and the velocity downstream of the mixing region is approximately equal to the upstream velocity. However, as demonstrated by Bryden and Couch [26] and Polagye et al. [27], energy extraction may significantly decrease the downstream water depth and increase velocity. Further, Garrett and Cummins' derivation assumes that the pressure far downstream of the turbine is reduced from the value far upstream of the turbine. If one assumes that the pressure is hydrostatic at these locations, then the depth of the water must be different and the assumption of constant velocity violates conservation of mass. Therefore, it is clear that these assumptions are not justified under all conditions. The question then becomes whether they are still acceptably accurate under a restrictive set of conditions.

Before proceeding to a solution to this problem under a different set of assumptions, a few properties of the expected solution should be investigated. Consider the example shown in Figure 2.2, in which it is assumed that there is a power loss occurring in a rectangular channel of constant width (b). Upstream of the loss, the velocity is u_1 and the depth is h_1 (Figure 2.2). Downstream, the velocity is u_2 (not the same as u_2 in Figure 2.1) and depth is h_2 , which vary from upstream values due to the power loss.

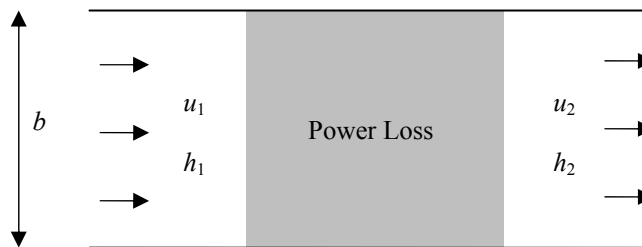


Figure 2.2 – Black box power loss in a confined channel with a free surface (top view)

Further, assume that:

- (1) The loss occurs over only a portion of the channel cross-section as parameterized by a blockage ratio (ε) for a porous medium,

$$\varepsilon = \frac{A^*}{h_1 b}, \quad (2.5)$$

where A^* is the area of the blockage causing the power loss.

- (2) The relation between the upstream and downstream velocity is parameterized by

$$\beta = \frac{u_2}{u_1}. \quad (2.6)$$

- (3) The power loss (P_{loss}) is parameterized by a loss coefficient (η^*), given by

$$P_{loss} = \rho u_1 A^* \left(\frac{1}{2} u_1^2 \right) \eta^*. \quad (2.7)$$

Further, the upstream flow conditions may be non-dimensionalized in terms of the Froude number

$$Fr = \frac{u}{\sqrt{gh}}, \quad (2.8)$$

where g is the acceleration due to gravity (9.81 m/s^2).

The energy balance across the loss is given by

$$\rho u_1 h_1 b \left(\frac{1}{2} u_1^2 + gh_1 \right) = \rho u_2 h_2 b \left(\frac{1}{2} u_2^2 + gh_2 \right) + P_{loss}. \quad (2.9)$$

The substitution of (2.5)-(2.8) into (2.9) allows the loss coefficient (η^*) to be expressed (with some algebraic rearrangement) as

$$\eta^* = \frac{1}{\varepsilon} \left(1 - \beta^2 - \frac{2}{Fr_1^2} \left(\frac{1}{\beta} - 1 \right) \right) = \eta^*(\varepsilon, \beta, Fr_1). \quad (2.10)$$

Therefore, the loss coefficient is a function of the blockage ratio (ε), parameterized velocity (β), and upstream Froude number (Fr_1). Therefore, for the in-stream turbines, the coefficients

describing extraction and dissipation should also depend on the blockage ratio, a parameterized velocity difference, and the upstream Froude number.

2.2.1. Approach

This study approaches the problem using a similar framework to Garrett and Cummins [22]. As shown in Figure 2.3, extraction is modeled as an actuator disc in the water channel. The following assumptions are common between the two approaches:

- (1) Over the control volume, frictional losses due to the channel walls are negligible in comparison with losses due to operation of the turbine.
- (2) Losses due to drag on the device support structure are assumed negligible. The validity of this assumption is discussed in section 2.2.6.
- (3) By the nature of the one-dimensional approximation, losses due to wake rotation are ignored.
- (4) Over the control volume, the channel bottom slope is negligible.

However, neither channel cross-sectional area nor downstream velocity is prescribed. Rather, assumptions are made to relate pressure, depth, and cross-sectional area at three locations:

- (5) Upstream of the turbine (cross-section I), at the end of the expansion region (cross-section II), and at the end of the mixing region (cross-section III) the pressure is hydrostatic.
- (6) Far upstream (cross-section I) and far downstream of the turbine (cross-section III), the depth is uniform in the across-channel direction.
- (7) At the end of the wake expansion region (cross-section II), there is, by definition, no across-channel pressure gradient. In conjunction with the first assumption, this requires that the depth is uniform in the across-channel direction.

These assumptions do not preclude cross-channel depth variations or non-hydrostatic pressure distributions on other cross-sections. For example, it is plausible that the pressure field will be non-hydrostatic and the depth will vary on a cross-section containing the turbine streamtube.

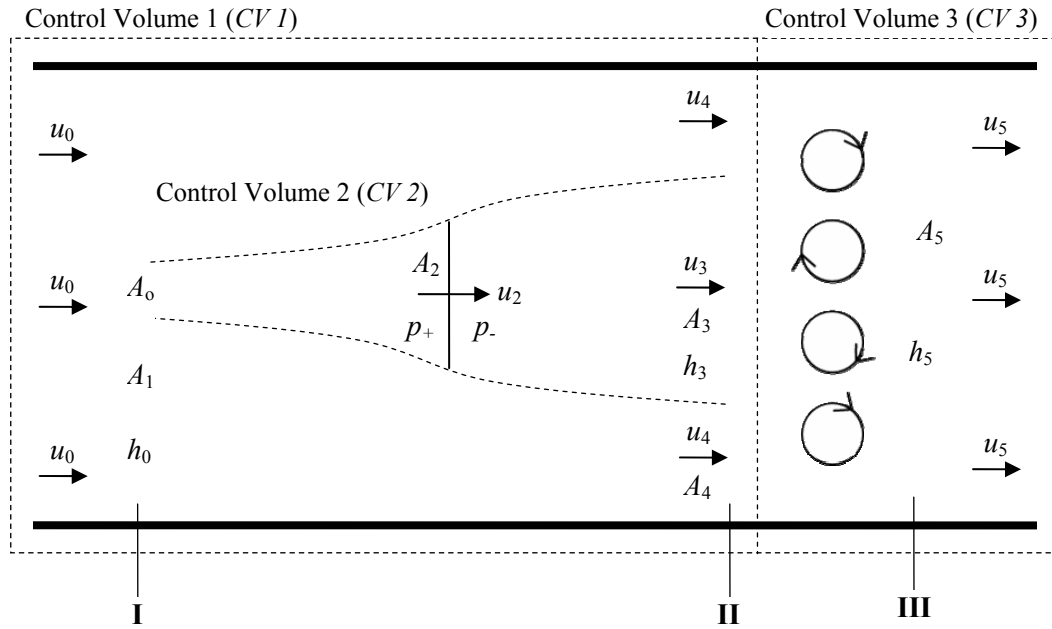


Figure 2.3 – Schematic of actuator disc theory applied to hydrokinetic turbines (top view)

The governing equations are discussed in the context of three control volumes. The first consists of the entire region from upstream of the turbine to the end of the expansion region (*CV 1*). The second is the turbine stream tube (*CV 2*). The third encompasses the wake mixing region (*CV 3*).

The blockage ratio (ε) is defined as the ratio of the turbine swept area to the channel cross-sectional area upstream of the turbine,

$$\varepsilon = \frac{A_2}{A_0 + A_1}. \quad (2.11)$$

The velocity at the actuator disc is u_2 and the pressures immediately upstream and downstream of the rotor are p_+ and p_- respectively. The change in velocity along the streamtube is parameterized in terms of the ratio of velocity at the location upstream of the turbine to the end of wake expansion;

$$u_3 = \alpha u_0. \quad (2.12)$$

The decision to relate u_3 to u_0 via the streamtube velocity ratio (α), rather than relating u_2 to u_0 via an induction factor (a), assists in the numerical solution to the governing equations. The results may still be interpreted in terms of the axial induction factor by computing an implied induction

factor via (2.3). However, the velocity at the rotor disc is described by (2.2) only when the blockage ratio is very small and the dynamics are equivalent to those of a wind turbine.

At the boundaries of the control volumes, the cross-sectional areas are related to water depth (h) and the channel width (b) by

$$A_0 + A_1 = h_0 b, \quad (2.13)$$

$$A_3 + A_4 = h_3 b, \quad (2.14)$$

$$A_5 = h_5 b. \quad (2.15)$$

Conservation of mass for *CV 1* is expressed as

$$(A_0 + A_1)u_0 = A_3u_3 + A_4u_4. \quad (2.16)$$

Similarly, conservation of mass for *CV 2* yields

$$A_0u_0 = A_2u_2 = A_3u_3. \quad (2.17)$$

With the assumption of hydrostatic pressure, conservation of momentum for *CV 1* may be expressed as

$$F = \rho u_0^2 (A_0 + A_1) + \rho g \frac{h_0^2}{2} b - \rho u_3^2 A_3 - \rho u_4^2 A_4 - \rho g \frac{h_3^2}{2} b. \quad (2.18)$$

Applying the energy equation to streamlines upstream and downstream of the turbine along with the assumption of hydrostatic pressure at cross-sections I and II yields

$$\frac{1}{2} u_0^2 + gh_0 = \frac{1}{2} u_2^2 + \frac{p_+}{\rho}, \quad (2.19)$$

$$\frac{1}{2} u_2^2 + \frac{p_-}{\rho} = \frac{1}{2} u_3^2 + gh_3. \quad (2.20)$$

As per (2.1), the axial force on the turbine is product of the time swept area and the pressure difference across the turbine;

$$F = \rho A_2 \left(\frac{1}{2} (u_0^2 - u_3^2) + g(h_0 - h_3) \right). \quad (2.21)$$

The energy balance for the annular region outside the stream tube (*CV 1* – *CV 2*) is

$$\frac{1}{2}(u_0^2 - u_4^2) + g(h_0 - h_3) = 0. \quad (2.22)$$

For the mixing region (*CV 3*), conservation of mass requires that

$$A_3u_3 + A_4u_4 = A_5u_5. \quad (2.23)$$

Since no external forces act on the flow in this region, conservation of momentum yields

$$\rho u_3^2 A_3 + \rho u_4^2 A_4 + \rho g \frac{h_3^2}{2} b - \rho u_5^2 A_5 - \rho g \frac{h_5^2}{2} b = 0. \quad (2.24)$$

The energetics of the mixing region are analogous to a hydraulic jump, where momentum is conserved, but energy is lost.

In order to proceed with a solution, it is first useful to reduce the number of equations through substitution and rearrangement. This is done separately for the region which extends from upstream of the turbine to the end of the wake expansion (*CV 1*) and for the mixing region (*CV 3*), which results in two sets of coupled algebraic equations.

Equating (2.18) and (2.21) and substituting (2.11), (2.13), (2.14) and (2.17) yields

$$\varepsilon \left(\frac{1}{2}(u_0^2 - u_3^2) + g(h_0 - h_3) \right) = u_0^2 - \varepsilon u_3 u_2 - u_4^2 \frac{A_4}{h_0 b} + g \frac{h_0}{2} - g \frac{h_3}{2} \left(\frac{h_3}{h_0} \right). \quad (2.25)$$

Substituting (2.11), (2.13), and (2.17) into (2.16), conservation of mass for *CV 1* is expressed as

$$A_4 u_4 = (u_0 - \varepsilon u_2) h_0 b. \quad (2.26)$$

Substituting (2.12), (2.22) and (2.26) into (2.25) and grouping terms containing ε yields

$$\varepsilon \left(\frac{1}{2}(u_4^2 - \alpha^2 u_0^2) + u_2(\alpha u_0 - u_4) \right) = u_0(u_0 - u_4) + g \frac{h_0}{2} \left(1 - \left(\frac{h_3}{h_0} \right)^2 \right). \quad (2.27)$$

A second equation may be obtained by rearranging (2.14) and substituting (2.13) and (2.16), so that h_3 is expressed as

$$h_3 = \frac{1}{b} \left(A_3 + \frac{h_0 b u_0 - A_3 u_3}{u_4} \right) = \frac{1}{b} \left(A_3 \left(1 - \frac{u_3}{u_4} \right) + h_0 b \frac{u_0}{u_4} \right). \quad (2.28)$$

Substituting (2.11) and (2.13) into (2.17) allows the area of the expanded wake (A_3) to be expressed as

$$A_3 = \frac{u_2}{u_3} \varepsilon h_0 b. \quad (2.29)$$

Finally, substituting (2.12) and (2.29) into (2.28) yields a compact expression for h_3 ;

$$h_3 = h_0 \left(\frac{\varepsilon u_2}{\alpha u_0} \left(1 - \frac{\alpha u_0}{u_4} \right) + \frac{u_0}{u_4} \right). \quad (2.30)$$

(2.22), (2.27), and (2.30) constitute a system of three equations and three unknowns (u_2 , u_4 , and h_3) and may be solved numerically. In summary:

$$(1) \frac{1}{2}(u_0^2 - u_4^2) + g(h_0 - h_3) = 0 \quad (2.22)$$

$$(2) \varepsilon \left(\frac{1}{2}(u_4^2 - \alpha^2 u_0^2) + u_2(\alpha u_0 - u_4) \right) = u_0(u_0 - u_4) + g \frac{h_0}{2} \left(1 - \left(\frac{h_3}{h_0} \right)^2 \right) \quad (2.27)$$

$$(3) h_3 = h_0 \left(\frac{\varepsilon u_2}{\alpha u_0} \left(1 - \frac{\alpha u_0}{u_4} \right) + \frac{u_0}{u_4} \right). \quad (2.30)$$

Thus, all quantities up to the end of the wake expansion region may be computed.

Likewise, algebraic rearrangement of (2.23) and (2.24) along with the area relations (2.14) and (2.15) yield

$$h_3 u_3 + \frac{A_4}{b}(u_4 - u_3) = h_5 u_5, \text{ and} \quad (2.31)$$

$$0 = u_3^2 h_3 + \frac{A_4}{b}(u_4^2 - u_3^2) - u_5^2 h_5 + \frac{g}{2}(h_3^2 - h_5^2). \quad (2.32)$$

(2.31) and (2.32) constitute a system of two equations and two unknowns (u_5 , h_5) and may also be solved numerically to define all quantities in the mixing region.

Once these two systems of equations are solved, metrics relevant to the extraction and dissipation of kinetic power may be calculated. Applying energy conservation to the streamtube,

$$P_{\text{extracted}} = \rho u_2 A_2 \left(\frac{1}{2} (u_0^2 - u_3^2) + g(h_0 - h_3) \right). \quad (2.33)$$

The power extracted by the turbine may also be expressed in terms of an extraction coefficient given by

$$P_{\text{extracted}} = \frac{1}{2} \rho u_0^3 A_2 \eta_e. \quad (2.34)$$

Substituting (2.22) into (2.33) and equating the extracted power in (2.33) and (2.34), one may obtain an expression for the extraction coefficient (η_e)

$$\eta_e = \frac{u_2 (u_4^2 - \alpha^2 u_0^2)}{u_0^3}. \quad (2.35)$$

Likewise, applying conservation of energy to the entire system gives the total dissipated power (extraction and wake losses) as

$$P_{\text{dissipated}} = \rho u_0 (A_0 + A_1) \left(\frac{1}{2} (u_0^2 - u_5^2) + g(h_0 - h_5) \right). \quad (2.36)$$

Dissipated power may also be expressed in terms of a dissipation coefficient (η_d) and free-stream conditions

$$P_{\text{dissipated}} = \frac{1}{2} \rho u_0^3 A_2 \eta_d. \quad (2.37)$$

Equating these expressions and substituting for Fr yields

$$\eta_d = \frac{1}{\varepsilon} \left(1 - \left(\frac{u_5}{u_0} \right)^2 + \frac{2}{Fr_0^2} \left(1 - \frac{u_0}{u_5} \right) \right), \quad (2.38)$$

which is very similar to the relation derived previously for a “black box” approach to power dissipation (2.10).

Examination of (2.35) and (2.38) indicate that the dissipation and extraction coefficients should be independent of the channel width, but will depend on the streamtube velocity ratio (α), blockage ratio (ε), and free-stream conditions (u_0 , h_0). For the dissipation coefficient, the influence of upstream conditions is reduced to a Froude number dependence. This is also demonstrated for the extraction coefficient in Section 2.2.2. These results are in contrast to [22],

where, because of the assumptions made, performance coefficients depend only on α and ε . With the definitions chosen for the performance coefficients (η_e, η_d), the ratio of power extracted to total power dissipated may be expressed simply as the ratio of the extraction and dissipation coefficients or, more explicitly, as

$$\frac{P_{extracted}}{P_{dissipated}} = \frac{\eta_e}{\eta_d} = \frac{u_2}{u_0} \left(\frac{\varepsilon(u_4^2 - \alpha^2 u_0^2)}{(u_0^2 - u_5^2) + 2g(h_0 - h_5)} \right). \quad (2.39)$$

Per Garrett and Cummins [22] and Corten [21], the equivalent expression when Fr and ε are small is

$$\frac{P_{extracted}}{P_{dissipated}} = \frac{u_2}{u_0}. \quad (2.40)$$

By comparison, (2.39) includes an additional factor related to the blockage ratio and free-stream conditions.

2.2.2. Comparison to Previous Results

While the governing equations are not linearly independent for $\varepsilon = 0$, it is possible to solve the system for small ε . Under this condition, the calculated coefficients of extraction and dissipation at small Fr approach the analytical results given in Corten [21] and Garrett and Cummins [22], as shown in Table 2.1.

Table 2.1– Comparison of analytical and numerical performance for an isolated turbine ($\varepsilon = 10^{-4}$, $\alpha = 1/3$, $Fr = 0.01$)

	Extraction Coefficient (η_e)	$\frac{P_{extracted}}{P_{dissipated}}$
Analytical results ($\varepsilon = 0$)	16/27 (0.5927)	2/3 (0.667)
Numerical results ($\varepsilon = 10^{-4}$)	0.5927	0.667

Figure 2.4 shows that the changes to these measures of performance are dependent on the Froude number, rather than particular values of upstream depth or velocity. As discussed previously, this result is consistent with the underlying physics of the problem. As ε increases, the extraction coefficient (efficiency) increases for a given α due to the confining effects of the water channel. It is, therefore, possible for a turbine to extract far more energy than is predicted by the classical Lanchester-Betz limit. Second, for a turbine operating at the maximum theoretical efficiency, as ε increases wake losses rise from 1/3 of the total dissipation to more than 1/2. Therefore, while increasing ε should theoretically improve the performance of an individual turbine or row of

turbines, it will also significantly increase the wake losses associated with operation. This trade-off is discussed in more detail for a range of α in Section 2.2.4.

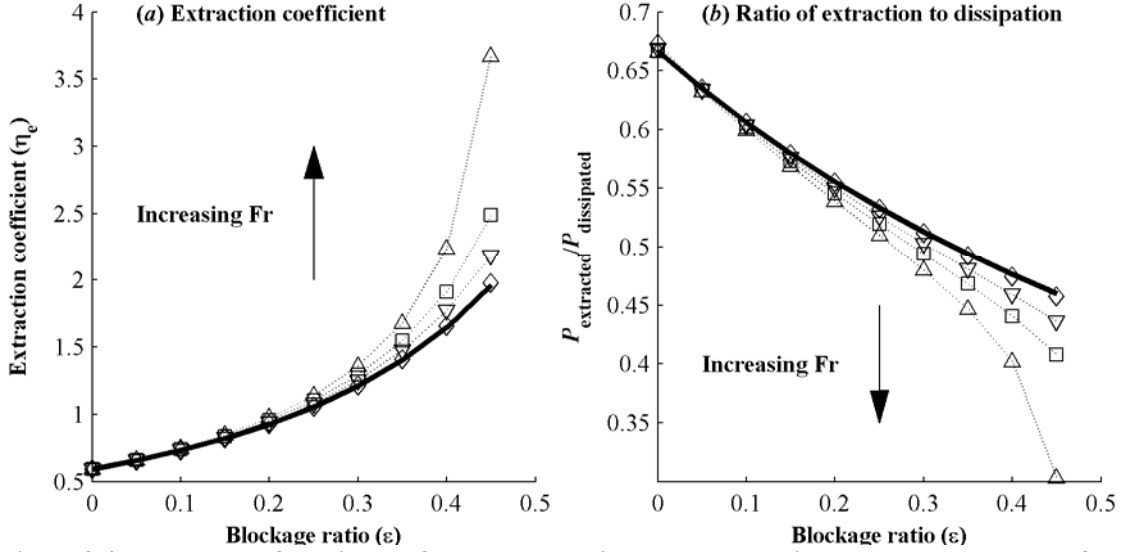


Figure 2.4 – Measures of turbine performance at various blockage ratios and Froude numbers for a turbine at the theoretical maximum efficiency ($\alpha = 1/3$). \diamond $Fr \approx 0.05$ ($u_0 = 1\text{m/s}$, $h_0 = 40\text{m}$), ∇ $Fr \approx 0.15$ ($u_0 = 3\text{m/s}$, $h_0 = 40\text{m}$), \square $Fr \approx 0.2$ ($u_0 = 2\text{m/s}$, $h_0 = 10\text{m}$), \triangle $Fr \approx 0.25$ ($u_0 = 5\text{m/s}$, $h_0 = 40\text{m}$), Solid line: analytical results from [22].

The solid line in Figure 2.4 corresponds to the analytical results derived in [22] for a hydrokinetic turbine operating at the theoretical maximum efficiency ($\alpha = 1/3$);

$$\eta_e = \frac{16}{27}(1 - \epsilon)^{-2}, \quad (2.41)$$

$$\frac{P_{\text{extracted}}}{P_{\text{dissipated}}} = \frac{2}{3(1 + \epsilon)}. \quad (2.42)$$

For small Fr or ϵ , results agree quite well with those obtained under simplifying assumptions in [22]. Figure 2.5 compares these two sets of results over a wider range of Fr and ϵ . The comparison is made up to the physical limit of the theory (discussed further in the following section). When the potential energy in the system greatly exceeds the kinetic energy (small Fr) or extraction does not greatly reduce total energy (small ϵ), the results obtained under simplifying assumptions are within 1% of the complete solution. For these conditions the change in water depth due to extraction is relatively minor in comparison with the total depth. For higher ϵ or Fr , the simplifying assumptions made by Garrett and Cummins are no longer valid and underpredict the extraction coefficient and overpredict the ratio of extraction to dissipation.

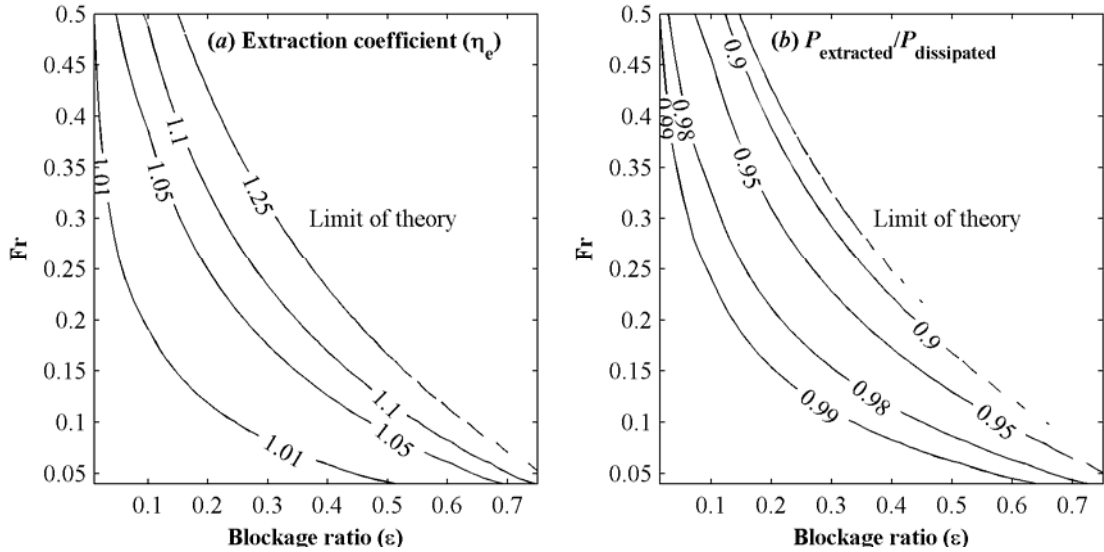


Figure 2.5 – Performance metric comparison: (a) extraction coefficient, (b) ratio of power extraction to power dissipation. Contours show ratio of present results to Garrett and Cummins results [22] for a turbine operating at theoretical maximum ($\alpha = 1/3$).

The results derived in [22] indicate that $\alpha = 1/3$ corresponds to the theoretical maximum efficiency. The present results confirm that this is approximately correct (e.g., $\alpha_{\text{optimal}} = 1/3 \pm 0.02$).

Finally, the free surface profile is as qualitatively described in [22]. The water depth decreases from cross-section I to II in Figure 2.3 and then increases by a smaller amount from cross-section II to III. That is to say, $h_3 < h_5 < h_0$.

2.2.3. Physical Limits of Theory

For the results given in Garrett and Cummins [22], the blockage ratio is allowed to approach unity. However, as noted previously, the present theory is only applicable to a more restricted range of Fr and ε . Numerically, it may still be possible to solve the system of equations as $\varepsilon \rightarrow 1$, but the results are not physically meaningful. For small Fr , as $\varepsilon \rightarrow 1$ the cross-sectional area of the annular region surrounding the wake must be less than zero to satisfy conservation of mass, momentum, and energy. This is clearly non-physical. For larger Fr , the fluid velocity in the annular region increases until the local Fr is critical. Since there is no mechanism for the flow to go through a supercritical transition, results obtained beyond this point are also non-physical. Figure 2.6 shows the maximum physically allowable blockage ratio as a function of parameterized streamtube velocity (α) and Fr . This is consistent with the physics of channel flows, since as Fr increases less power dissipation is required to push the flow to the critical point. For ε outside the range shown in Figure 2.6, this theory is probably not applicable to

predictions for device performance. In general, with increasing ε , the shear between the wake and free-stream grows, calling into the question the assumption of a clearly defined streamtube separating the two regions.

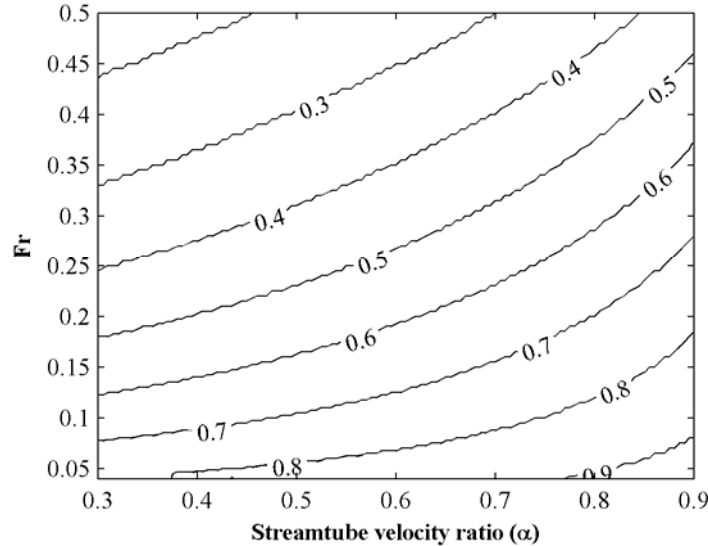


Figure 2.6 – Contours of maximum theoretical blockage ratio (ε) as a function of streamtube velocity ratio (α) and Fr for hydrokinetic turbines.

2.2.4. General Results

Practical devices cannot operate at the theoretical maximum efficiency. As shown in Figure 2.7, when $\alpha \neq 1/3$ the extraction coefficient decreases. Because of blockage effects, it is possible for devices with modest free-stream efficiencies ($\varepsilon = 0$) to exceed the classical Lanchester-Betz limit by a significant margin. This is, however, a somewhat spurious comparison since that limit does not apply to confined flows.

While $\alpha = 1/3$ corresponds to a maxima for the extraction coefficient, that operating state also leads to the highest relative wake losses for a given Fr and ε . As pointed out in Garrett and Cummins [22], minimized wake losses correspond to $\alpha = 1$, but in this state no power is extracted and it is not of practical interest. However, as $\alpha \rightarrow 1$, the extraction coefficient decreases more slowly than the relative wake loss. For example, when blockage effects are negligible, $\alpha = 5/8$ corresponds to an efficiency of 50% and 81% of total dissipation is attributable to extraction. At the maximum theoretical blockage, only 56% of dissipation is attributable to extraction ($\varepsilon \approx 0.74$, for $Fr = 0.15$). In contrast, for a device operating at the theoretical maximum efficiency, 66% of the total dissipation is attributable to extraction for an isolated device, declining to $\sim 33\%$ for the maximum theoretical blockage. Thus, the *maximum* wake loss for an efficient, practical device is

comparable to the *minimum* wake loss for a device operating at the theoretical optimum. The lower wake losses for non-ideal turbines are consistent with reduced shear between the wake and free-stream. Since far-field environmental effects depend on total dissipation (rather than extraction), this trade-off calls into question what constitutes an optimal array design. Arrays could either be optimized to maximize power production for individual devices or be optimized to extract the maximum possible power for a given allowable far-field impact.

The discussion to this point implicitly assumes that a particular device may be, to the first order, parameterized by the streamtube velocity ratio (α). That is to say, α remains constant with increasing blockage ratio (ε). However, it is equally possible to reconsider these results under the assumption that for a particular device, the axial induction factor (a) remains constant with increasing blockage ratio. These results are shown in Figure 2.8, with the axial induction factor (a) given by (2.3). In this case, the ratio of extraction to dissipation is nearly constant with Fr and ε (Figure 2.8*b,d,f*),

$$\frac{P_{\text{extracted}}}{P_{\text{dissipated}}} \approx f(a) = 1 - a = \frac{u_2}{u_0} \quad \text{for } \varepsilon < 0.8(\varepsilon_{\text{max}}). \quad (2.43)$$

Interestingly, this is identical to the ratio of extraction to dissipation given by (2.40) when blockage effects are negligible.

The induction factor (a) and streamtube velocity ratio (α) are directly related by (2.2) and (2.3) for wind turbines and are, therefore, specific to a device. However, for hydrokinetic turbines, if blockage effects are significant, the velocity at the turbine (u_2) is actually closer to the wake velocity (u_3) than the upstream velocity (u_0) and (2.3) is not valid. That is to say, there is not a general relation between a and α for hydrokinetic turbines. Since both the axial induction factor (a) and streamtube velocity ratio (α) are one-dimensional parameterizations, the theory does not indicate if either should remain constant for a particular device over all ε and Fr . Without this information, the theory cannot be applied to predict the performance of real devices for various blockage ratios and upstream conditions. On one hand, a constant streamtube velocity ratio (α) describes the optimal device efficiency for all ε and Fr , which suggests that a particular device should have a constant α . On the other, the ratio of extraction to dissipation is nearly constant with the induction factor (a), which suggests that a particular device should have a constant a . Experimental data or a higher order theoretical approach is required to resolve this ambiguity.

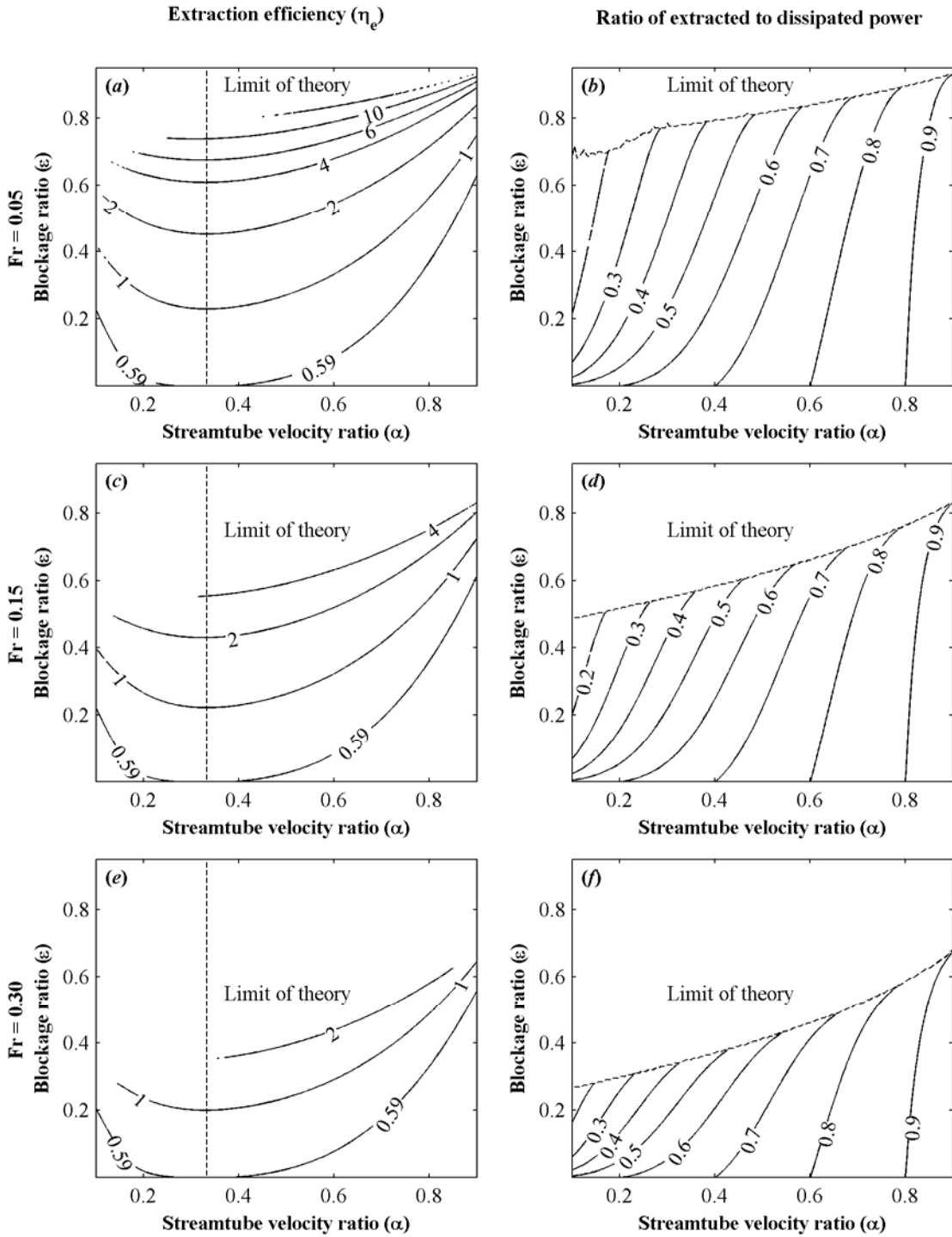


Figure 2.7 – Extraction coefficient (η_e) (a,c,e) and ratio of extraction to dissipation (b,d,f) as a function of blockage ratio (ϵ) and streamtube velocity ratio (α) for $Fr = 0.05$ (a,b), 0.15 (c,d), and 0.30 (e,f). The dashed vertical line corresponds to the maximum extraction efficiency ($\alpha = 1/3$) for a particular Fr and ϵ .

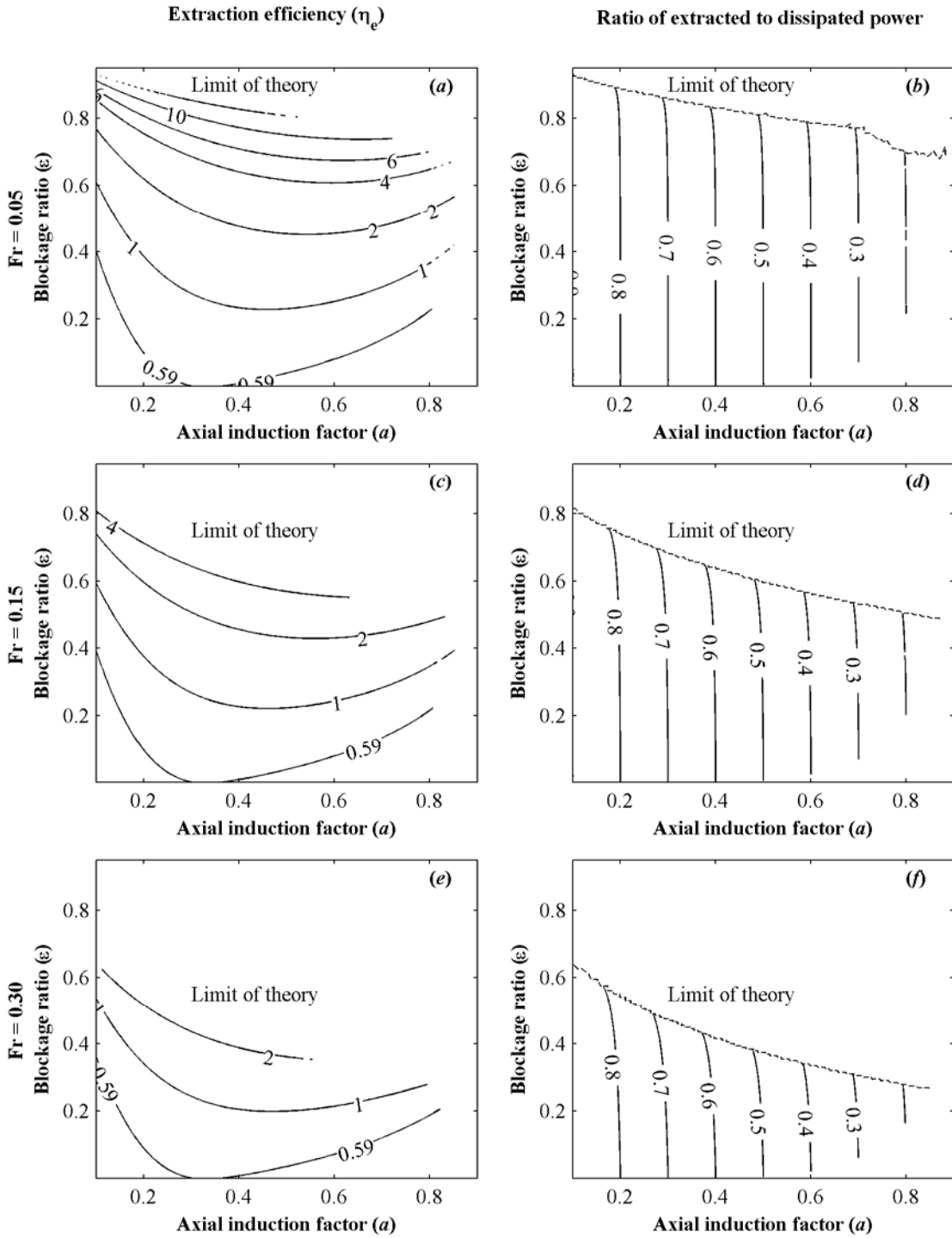


Figure 2.8 – Extraction coefficient (η_e) (a,c,e) and ratio of extraction to dissipation (b,d,f) as a function of blockage ratio (ϵ) and axial induction factor (a) for $Fr = 0.05$ (a,b), 0.15 (c,d), and 0.30 (e,f).

2.2.5. Simplified Solution after Garrett and Cummins

While Garrett and Cummins only present analytical solutions for a turbine operating at the theoretical maximum efficiency, the simplified form of the governing equations may be solved numerically for any α . The solution involves only a coupled pair of algebraic equations for u_2 and u_4 given by [22],

$$\alpha u_0(u_4 - u_0) = \varepsilon u_2(u_4 - \alpha u_0), \quad (2.44)$$

$$u_2(u_4 + u_0(2\alpha - 1)) = \alpha u_0(u_4 + \alpha u_0). \quad (2.45)$$

Once these have been solved, the ratio of extracted power to total dissipated power is given by u_2/u_0 and the extraction coefficient may be inferred from the equation derived for extracted power [22],

$$P_{extract} = \frac{1}{2} A_2 \left[\frac{u_3(u_4 + u_3)(u_4^2 - u_3^2)}{u_4 + 2u_3 - u_0} \right] = \frac{1}{2} \rho A_2 u_0^3 \eta_e. \quad (2.46)$$

Since these results are independent of Fr , this solution is preferable when the simplifications underlying its derivation are justifiable, as is the case for flows of moderate Fr and arrays of moderate ε .

2.2.6. Support Structure Drag

In the previous discussions, it has been assumed that drag on the device support structure is negligible in comparison to drag on the turbine rotor. If vertical shear is neglected, then the fraction of the total drag (D) attributable to the turbine (f_t) is given by

$$f_t = \frac{D_t}{D_t + D_s} = \frac{1/2 \rho u^2 (AC)_t}{1/2 \rho u^2 (AC)_t + 1/2 \rho u^2 (AC)_s} = \frac{(AC)_t}{(AC)_t + (AC)_s}, \quad (2.47)$$

where subscript t refers to the turbine, subscript s refers to the support structure, A is a frontal area of either the turbine or support structure, and C is the drag coefficient associated with the frontal area.

From theory, the axial force on the turbine rotor is given by (2.21) or, in terms of a drag coefficient (C_t) by

$$F = 1/2 \rho u_0^2 A_2 C_t. \quad (2.48)$$

Equating these two expressions for axial force and substituting (2.12) and (2.22), the drag coefficient for the turbine is given by

$$C_t = \left(\frac{u_4}{u_0} \right)^2 - \alpha^2. \quad (2.49)$$

f_t may be evaluated for a few sample devices with pile foundations. The Marine Current Turbine SeaGen demonstration in Strangford Loch, UK uses a cylindrical pile foundation. In fully turbulent flow, the drag coefficient for a smooth cylindrical pile is ≈ 0.4 [28]. If bio-fouling were to increase the pile roughness, the drag coefficient could approach 1.0 [29]. The Verdant Power KHPS demonstration in New York, USA, uses a foundation with a streamlined cross-section in order to minimize shadowing of the down-water turbine. A streamlined cross-section may reduce the drag coefficient to $O(10^{-2})$ [30].

In Figure 2.9, the theoretical drag coefficient is plotted as a function of the streamtube velocity ratio (α) for an isolated turbine. The drag coefficients implied by the reported efficiencies of the SeaGen and KHPS turbines are noted, as well as the drag coefficient for a future, more efficient, device.

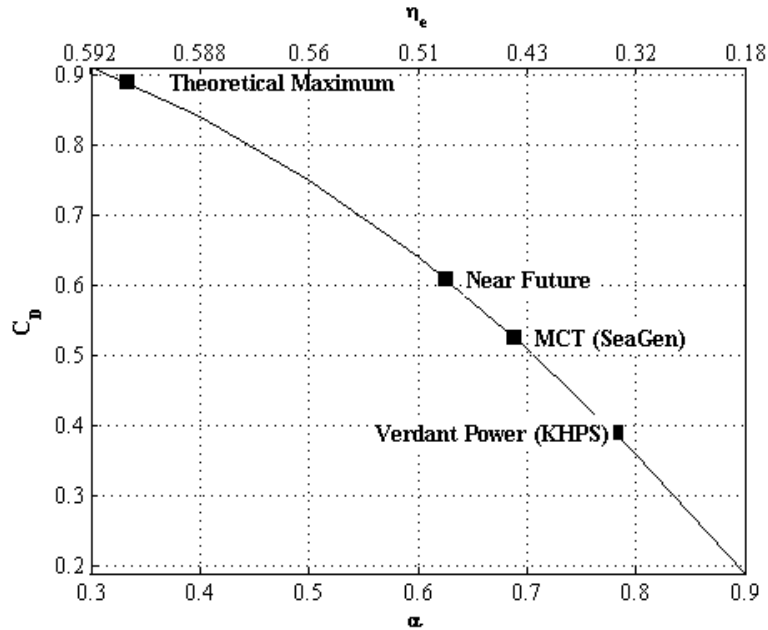


Figure 2.9 – Drag coefficients for isolated turbines ($\varepsilon=0$) as per (2.39).

The geometric properties for the two existing foundations are listed in Table 2.2, along with the estimated fraction of total drag attributable to the turbine (f_t). For SeaGen, these estimates

indicate that only 75% of the total drag is attributable to the turbine, falling to only 50% if the pile is badly fouled by marine growth. For the KHPS turbine, as a result of the streamlined support structure, nearly all of the drag is attributable to the turbine. This suggests that it is possible to engineer support structures to limit the associated drag. As such, it is instructive to consider a few scenarios around future enhancements to the SeaGen design. The existing pile foundation is designed to withstand the loads on rotors up to 18 m in diameter [31]. The pile length would also be reduced for a fully submerged device (SeaGen is surface piercing). With these modifications and increased rotor efficiency, 90% of the drag would be attributable to the turbine if the support structure still consists of a cylindrical pile. Further, f_t rises to nearly 100% for ovoid or streamlined pile supports. Therefore, while the assumption of negligible support structure drag may not be appropriate for all first-generation devices, it is justifiable for future arrays. Supports with non-cylindrical cross-section have a higher fabrication cost, but this may be offset by lower stresses on the foundation and diminished environmental impact. While these calculations quantify drag only for pile supports, the assumption of negligible support structure drag should extend to gravity foundations incorporating tubular members with ovoid cross-sections.

Table 2.2 – Geometric properties and drag on existing and future tidal energy devices.

	Pile			Device					
	L^1 (m)	D^4 (m)	C_s	η_e	α^5	C_t	N^6	D^7 (m)	f_t
Existing									
Verdant Power KHPS ²	5 ²	0.61	0.04	0.35	0.78	0.39	1	5	0.98
MCT SeaGen ³	40 ³	3.5	0.4	0.45	0.69	0.53	2	14	0.74
MCT SeaGen (fouled)	40	3.5	1.0	0.45	0.69	0.53	2	14	0.54
Future									
Cylindrical Pile	20	3.5	0.4	0.5	0.63	0.61	2	18	0.92
Oval Pile	20	3.5	0.15	0.5	0.63	0.61	2	18	0.97
Streamlined Pile	20	3.5	0.04	0.5	0.63	0.61	2	18	0.99

¹Pile length

²Assuming deployment in 10m water

³Assuming deployment in 40m water

⁴Pile frontal width

⁵Given by theory for η_e

⁶Number of rotors per pile

⁷Rotor diameter (each rotor)

2.3. Summary

The performance of a device in a water channel depends on the streamtube velocity ratio (α), blockage ratio (ε), and upstream Froude number (Fr). Results indicate that the assumptions used by Garrett and Cummins are only strictly valid when the blockage ratio or Froude number is small, but may be accurate to within a few percent over a wider range. For a very low blockage ratio, the performance coefficients for a theoretical water turbine are identical to those of a theoretical wind turbine, but as ε increases it is possible to exceed the Lanchester-Betz limit by a

substantial margin. The application of this framework is bounded by a maximum physical blockage ratio (ε), which is a function of Fr and the non-dimensional change in velocity along the turbine streamtube. In general, losses due to wake mixing are significant and should be accounted for in resource assessments.

3. Literature Review of Far-field Extraction Effects

The analysis and prediction of far-field extraction effects for tidal streams is a new and active area of research. As such, the literature is sparse, but expanding. For wind energy, the nearest technology analogue, far-field effects have not been historically investigated. Recent work is motivated by concerns that large wind farms could alter local and/or regional weather patterns [32, 33].

The literature on far-field effects for tidal energy may be divided into generalized analytical theories, principally derived from Garrett and Cummins [20], and numerical models, which are usually site specific. There have only been a few devices deployed in the open ocean and none of these have been of sufficient scale to produce measurable far-field effects. While there is a growing body of experimental data related to blade design and device performance, to date there has been no experimental work on far-field effects.

3.1. Analytical Theory

Analytical theories relate changes in transport (flow rate) to the increased frictional losses associated with kinetic power extraction. These were first proposed by Garrett and Cummins [19,20] for a dynamic system consisting of two bays of infinite surface area connected by a narrow channel, as shown in Figure 3.1. Variations in tidal amplitude and phase between the two bays result in a driving head across the channel. Modeling of kinetic power extraction in the Johnstone Strait by Sutherland et al. [13] agrees well with this theory.

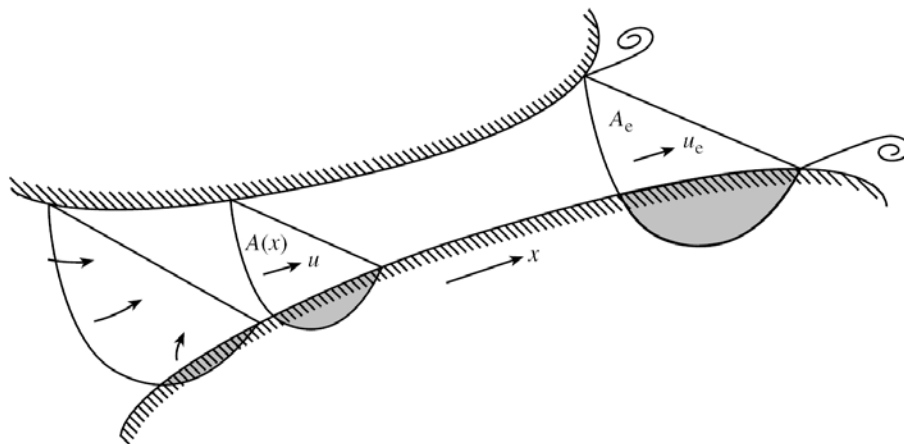


Figure 3.1 – Dynamic system consisting of two infinite bays connected by a narrow channel. Reproduced from Garrett and Cummins [20].

Blanchfield et al. [14,34] adapt the above theory to a dynamic system consisting of a finite bay connected to the open ocean by a narrow channel, as shown in Figure 3.2. The driving head for currents is generated by the phase lag across the narrow channel.

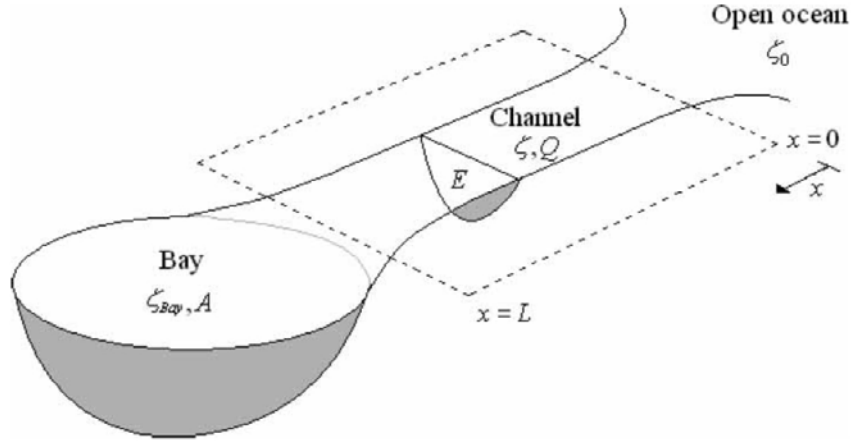


Figure 3.2 – Dynamic system consisting of a finite bay connected to the open ocean by a narrow channel. Reproduced from Blanchfield et al. [34].

The theory proposed by Blanchfield et al. closely corresponds to the channel networks discussed in this dissertation and is re-derived here. The flow in the constriction is governed by the one-dimensional Navier-Stokes equation

$$\frac{\partial u}{\partial t} + u \frac{\partial u}{\partial x} = -\frac{1}{\rho} \frac{\partial p}{\partial x} - F, \quad (3.1)$$

where u is velocity, p is pressure and F is a momentum sink associated with friction. This equation is integrated over the length of the channel. It is assumed that the tidal wavelength is much longer than the channel, such that the flow rate in the channel is a function only of time, not spatial position. When integrated along the channel, the first term in (3.1) is given by

$$\int_0^L \frac{\partial u}{\partial t} dx = \int_0^L \frac{1}{E} \frac{dQ}{dt} dx = \frac{dQ}{dt} \int_0^L \frac{1}{E} dx = c \frac{dQ}{dt}, \quad (3.2)$$

where Q is the flow rate and E is the cross-sectional area of the channel, which assumed to be effectively constant in time because the tidal elevation is a small fraction of the total water depth. Assuming that the velocity seaward of the channel inlet is nearly quiescent, the integrated form of the advective term is given by

$$\int_0^L u \frac{\partial u}{\partial x} dx = \int_0^L \partial \left(\frac{u^2}{2} \right) = \frac{u^2}{2} \Big|_0^L = \frac{1}{2} u_e |u_e| = \frac{1}{2E^2} Q|Q|, \quad (3.3)$$

where u_e is the exit velocity. This term represents an exit loss which always acts in the opposite direction of the flow. Assuming the pressure in the channel is hydrostatic, the integrated form of the pressure term is

$$\int_0^L g \frac{\partial \zeta}{\partial x} dx = -g(\zeta - \zeta_b), \quad (3.4)$$

where ζ is the time-varying tidal elevation adjacent to the channel and ζ_b is the time-varying tidal elevation of the basin. This term represents the driving head across the channel. Finally, the momentum sink consists of frictional losses in the channel and losses associated with turbine drag;

$$\int_0^L F dx = \int_0^L F_{turbine} dx + \int_0^L F_{friction} dx. \quad (3.5)$$

Both are parameterized as quadratic frictional losses;

$$\int_0^L F dx = \lambda_1 Q|Q| + \lambda_2 Q|Q|, \quad (3.6)$$

where λ_1 describes the turbine loss and λ_2 describes the frictional loss.

Substituting these terms back into the original equation (3.1) yields

$$c \frac{dQ}{dt} + \lambda_1 Q|Q| + \lambda_2 Q|Q| + \frac{1}{2E^2} Q|Q| = g(\zeta - \zeta_b) \quad (3.7)$$

This may be further reduced by combining the exit losses and frictional losses into a single parameter (λ_0) representing the natural losses in the channel;

$$c \frac{dQ}{dt} + (\lambda_1 + \lambda_0) Q|Q| = g(\zeta - \zeta_b) \quad (3.8)$$

This equation represents a balance between the forces driving flow through the channel (elevation difference between the ocean and the basin) and the forces opposing that flow (power dissipation due to friction). Blanchfield et al. use a non-dimensional form of (3.8),

$$\frac{dQ^*}{dt^*} = \zeta^* - \zeta_{bay}^* - (\lambda_1^* - \lambda_0^*)Q^*|Q^*|, \quad (3.9)$$

which makes use of the following non-dimensional variables:

$$Q^* = \frac{c\omega}{g\zeta_0}, \quad (3.10)$$

$$t^* = \omega t, \quad (3.11)$$

$$\zeta^* = \frac{\zeta}{\zeta_0}, \quad (3.12)$$

$$\zeta_b^* = \frac{\zeta_b}{\zeta_0}. \quad (3.13)$$

In the above equations, ζ_0 is the amplitude of the tidal forcing seaward of the channel. This forcing is assumed not to change with power extraction by turbines and is prescribed by

$$\zeta(t) = \zeta_0 \cos(\omega t). \quad (3.14)$$

λ_0^* is a non-dimensional representation of the natural power dissipation in the channel and λ_1^* is a non-dimensional representation of additional power dissipation due to turbines.

For the basin, if the surface area (A) is assumed to be independent of tidal elevation and the basin is co-tidal (ζ_b has no spatial variation), then continuity requires

$$\frac{d\zeta_b}{dt} = \frac{Q}{A}. \quad (3.15)$$

The corresponding non-dimensional form is

$$\frac{d\zeta_b^*}{dt^*} = \beta Q^*, \quad (3.16)$$

where β is a term describing the geometry of the bay in relation to the tidal forcing;

$$\beta = \frac{g}{cQ\omega^2}. \quad (3.17)$$

Non-dimensional mass conservation for the bay is given as

$$\frac{d\zeta_{bay}^*}{dt^*} = \beta Q^*, \quad (3.18)$$

Blanchfield et al. show that for this dynamic system, the maximum possible average power dissipation by turbines (P_{\max}) is given as

$$P_{\max} = \gamma \rho g \zeta_0 Q_0, \quad (3.19)$$

where Q_0 is the peak volume flow rate through the constriction without any power dissipation due to in-stream turbines. $\rho g \zeta_0 Q_0$ is the work done by the tide to drive flow through the channel. γ is a function of λ_0^* and β . This is convenient for resource assessment because, once γ has been specified, P_{\max} and the relative change in Q as a function of P may be determined from the natural conditions which may obviate the need for detailed modeling. This theory has been further extended by Karsten et al. [12], who propose a simplified approach for determining λ_0^* , β , and γ based on the observed phase lag and amplitude ratio across the constricted channel.

The analytical theory has several limitations. The theoretical system response is only accurate when flow cannot be diverted into other parts of the system, as shown by Sutherland et al. [13]. This situation could occur when a flow bifurcates around an island and kinetic power is extracted from only one branch. Second, results cannot be readily generalized to tidal regimes with multiple constituents. Third, the theory describes extraction solely in terms of increased drag, which does not provide any information about the size of an array associated with a particular level of power extraction. Finally, as discussed in Chapters 4 and 5, the assumption of constant tidal amplitude outside the channel does not hold when an entry region of appreciable length connects the channel to the open ocean. In spite of these limitations, the theory does provide the only mechanism for verification of model results.

As presented in the literature, (3.4) gives the maximum possible *extractable* power for a tidal channel, based on the implicit assumption that the additional dissipation associated with turbines is attributable only to power extraction. As shown in Chapter 2, this is not the case and the theory actually describes the maximum possible *dissipated* power, which includes both extraction and wake losses. The concept of a tidal fence [20,22], through which all flow passes without generating a wake, is not realistic.

3.2. Numerical Models

A number studies address far-field extraction effects using numerical models.

Bryden et al. model far-field effects using 1D, steady-state flow as a prototype for the more complicated time-dependent problem [26,35,36]. This is the first work demonstrating far-field effects as a consequence of kinetic power extraction from tidal streams. Couch and Bryden also apply 2D [37] and 3D [38] models for preliminary investigations of far-field effects in higher dimensions. Though the 2D and 3D models solve the unsteady form of the governing equations, the boundary conditions are time-invariant and the results correspond to steady-state solutions. For the 1D and 2D models, turbines are represented as localized discontinuities in bottom friction. The 3D model represents turbines as elevated drag acting over part of the water column.

Sutherland et al. [13] model the effects of far-field extraction on transport and tides in Johnstone Strait, British Columbia. Turbines are modeled as increased bottom drag in constricted channels for the purpose of determining the theoretically recoverable resource. The study employs a 2D model (TIDE2D) previously calibrated by Foreman et al. [39]. The model domain encompasses the entirety of the Strait of Juan de Fuca-Strait of Georgia system and extends westward into the Pacific Ocean. Model results agree well with the theory proposed by Garrett and Cummins [20] for channels in which power extraction cannot divert the flow into parallel channels. When flow redirection is possible, the theory overpredicts the theoretically recoverable resource by up to a factor of two.

Bluden and Bahaj [15,40] model changes in the horizontal velocity field for an array of turbines deployed in the vicinity of Portland Bill, in the southern UK. The study employs a 2D model (TÉLÉMAC-2D) over a relatively small domain. The model is calibrated against one station of observational data and it is unclear how faithfully the velocity field around Portland Bill is represented. Turbines are parameterized as elevated bottom drag over a 2 km² region. The parameterization is dimensionally consistent, but does not appear to be physically accurate. Extraction of kinetic power is shown to locally alter the strength and direction of currents by respectively 5-10% and 15°. An estimate of the rated power of the array is given (90 MW), but it is not clear how this is derived.

Karsten et al. [12] implement turbines in an existing, calibrated 2D (FVCOM) model of the Bay of Fundy as elevated bottom drag in the Minas Passage. Results of the numerical simulation agree well with an analytical theory extended from Blanchfield et al. [34]. Extraction is shown to

decrease the tidal range inside the Minas Basin, produce little change in the rest of the Bay of Fundy, and increase the tidal range for the Gulf of Maine. Extraction also reduces volume flow rates through the Minas Passage. The study investigates both the theoretically recoverable resource and effects of extraction at smaller scales.

As for analytical approaches, all modeling to date does not differentiate between extraction and dissipation. A similar criticism is the inability to relate the modeled drag to the size of an in-stream turbine installation.

4. 1D Model for Far-field Extraction Effects

This chapter details the development and application of a model for studying far-field extraction effects in channel networks. The basic requirements are that the model represent, with acceptable accuracy, the time-varying flows in a variety of networks and include kinetic power extraction by turbines. The method used to model kinetic power extraction should include the effects of rated and cut-in speeds. It should also be able give some indication of the scale of development (e.g., number of rows and lateral density of devices), not just how much power is being removed or how much drag has been added to the network. This would provide some initial guidance on the relative importance of device spacing.

This chapter follows the structure of Polagye et al. [27], but contains significant new information, including a more rigorous investigation of far-field effects in four tidal regimes and a comparison with the analytical theory proposed in Blanchfield et al. [34].

4.1. Development of 1D Channel Model

A one-dimensional (1D) model has been selected for investigation of far-field effects, in which flow variations in the vertical and across-channel directions are neglected. The product is a model applicable to the broad study of far-field effects, with an emphasis on the basic physics. While this approach cannot be used to investigate changes to the two-dimensional velocity field, such as is done by Blunden and Bahaj [15], it has the advantages of simplicity and very low computational cost. The code developed has the flexibility to study a broad range of network geometries, tidal regimes, and device dynamics. A model channel network consists of one or more segments connected by junctions. For the simulations described in this dissertation, one end of the domain is open to the ocean.

In this section, the model's functional modules are described in sequence: the numerical solution to the governing equations in each channel segment, the specification of the open boundary and initial conditions, the treatment of junctions between segments, and finally the inclusion of turbines. Additional details of the programmatic implementation are given in Appendix 3.

4.1.1. Governing Equations and Numerical Solution

One-dimensional channel flow is governed by the shallow water equations. These are a pair of coupled partial differential equations which require that:

- (1) The entire water column moves with the particle velocity of the wave.
- (2) The pressure distribution is hydrostatic.

(3) Transient friction losses may be modeled using steady-state relations.

(4) Coriolis forces may be neglected.

In addition, the formulation given below is valid only for cases in which the channel cross-sectional area is rectangular and constant and the channel has no bottom slope. With these restrictions, the conservation form of the shallow water equations is given by [41],

$$\frac{\partial h}{\partial t} + \frac{1}{b} \frac{\partial Q}{\partial x} = 0, \quad (4.1)$$

$$\frac{\partial Q}{\partial t} + \frac{\partial}{\partial x} \left(\frac{Q^2}{bh} + \frac{1}{2} g b h^2 \right) = -g h b S_f. \quad (4.2)$$

Here, h is the depth of the water, b is the width of the channel, g is the acceleration due to gravity, x is the spatial coordinate and t is the temporal coordinate. The channel velocity is related to the volume flow rate (Q) by

$$u = \frac{Q}{hb}. \quad (4.3)$$

S_f is the friction slope, which is given by Manning's equation [42] as

$$S_f = u|u| \frac{n^2}{R_h^{4/3}}, \quad (4.4)$$

where R_h is the hydraulic radius and n is the Manning constant ($s/m^{1/3}$). Therefore, a quadratic representation of friction is used, as per Garrett and Cummins [20].

A variety of numerical algorithms is applicable to the solution of the shallow water equations. Here, an explicit finite-difference approximation using the predictor-corrector MacCormack algorithm (second order in time and space) [41] is used. If the shallow water equations are written in compact notation,

$$\frac{\partial \bar{G}}{\partial t} + \frac{\partial \bar{F}}{\partial x} = -\bar{S}, \quad (4.5)$$

then the predictor step is determined by values at time level n as

$$\bar{G}_j^{(1)} = \bar{G}_j^n - \frac{\Delta t}{\Delta x} \left((1-\theta)\bar{F}_{j+1}^n - (1-2\theta)\bar{F}_j^n - \theta\bar{F}_{j-1}^n \right) - \Delta t \bar{S}_j^n, \quad (4.6)$$

and the corrector step is given by

$$\bar{G}_j^{(2)} = \bar{G}_j^n - \frac{\Delta t}{\Delta x} \left(\theta \bar{F}_{j+1}^{(1)} + (1 - 2\theta) \bar{F}_j^{(1)} - (\theta - 1) \bar{F}_{j-1}^{(1)} \right) - \Delta t \bar{S}_j^{(1)}. \quad (4.7)$$

Values for time step $n+1$ are the average of the predictor and corrector steps,

$$\bar{G}_j^{n+1} = \frac{1}{2} \left(\bar{G}_j^{(1)} + \bar{G}_j^{(2)} \right). \quad (4.8)$$

In (4.5) - (4.8), superscripts denote the time index and subscripts denote the grid index.

Superscripts in parentheses are intermediate time steps. Here, θ is a parameter controlling the direction of differencing. Its value alternates between zero and one on each full time step, so as not to bias the direction of the predictor or corrector.

The equations are solved on an unstaggered, uniform grid. For the cases discussed in this dissertation, Δx varies between 50 and 100m. This allows large arrays of turbines to be modeled in channels of reasonably realistic length. In order to satisfy the Courant stability condition for explicit algorithms, Δt must be chosen such that

$$\frac{|u| + c}{\Delta x / \Delta t} \leq 1, \quad (4.9)$$

where c is the celerity of the gravity wave, $(gh)^{1/2}$. Stability is satisfied so long as a wave of characteristic speed $u+c$ cannot move more than one grid cell (Δx) in a single time step (Δt). A time step of 1.5-2s meets this criterion and (4.9) is verified in the model after each time step.

4.1.2. Initial Conditions and Boundary Conditions

Since tidal streams are almost always subcritical, a well-posed solution to (4.1) and (4.2) requires the specification of one boundary condition at each end of the domain and initial conditions for both Q and h . The simplest possible channel model domain has one end open to the ocean and a solid, or closed, boundary at the landward end.

The specification of initial conditions is relatively unimportant since the influence of initial conditions becomes negligible as the model is “spun-up” over several tidal cycles. For the small domains studied in Chapters 4 and 5, three days are sufficient for spin-up. In the larger domain established to study extraction effects on Puget Sound (Chapter 6), five days are allotted for spin-up. The only restriction on the initial conditions is that they are not so poorly chosen as to

generate numerical instability during spin-up. Quiescent, high water is an exact solution corresponding to a standing wave, and allows for a stable spin-up.

At a solid boundary, zero normal velocity accurately reflects the physics of the problem. In contrast, the open boundary with the ocean is a purely numerical construct which must satisfy three criteria:

- (1) *Radiative*: Allow waves propagating from the interior of the domain to pass through the open boundary without reflection, as they do in the natural environment.
- (2) *Active*: Allow external waves (such as the tides) to propagate into the domain.
- (3) *Stable*: Maintain the mean sea level over long simulation times.

An implementation of a Flather-type boundary condition as proposed by Blayo and Debreu [43] satisfies these criteria and is used in this model. The Flather boundary condition holds the characteristic speed of an outgoing wave constant across the numerical boundary. Discontinuous changes in the characteristic speed result in numerical reflection at open boundaries. While it is common to force the open boundary with a specified free surface, this is a clamped boundary which will perfectly (and spuriously) reflect outward propagating waves [44]. A further discussion of open boundary conditions is given in Appendix 1. The method proposed by Blayo and Debreu applies the Flather radiation condition to incoming waves (4.10) and extrapolation of characteristic speed to outgoing waves (4.11). Implicit in the formulation is the assumption that the shallow water phase speed is constant across the numerical boundary.

$$u_0^{n+1} + \left(\sqrt{\frac{g}{h_o^{n+1}}} \right) \zeta_0^{n+1} = u_{ext}^{n+1} + \left(\sqrt{\frac{g}{h_0^{n+1}}} \right) \zeta_{ext}^{n+1} \quad (4.10)$$

$$u_0^{n+1} - \left(\sqrt{\frac{g}{h_o^{n+1}}} \right) \zeta_0^{n+1} = 2 \left(u_1^{n+1} - \left(\sqrt{\frac{g}{h_1^{n+1}}} \right) \zeta_1^{n+1} \right) - \left(u_2^{n+1} - \left(\sqrt{\frac{g}{h_2^{n+1}}} \right) \zeta_2^{n+1} \right) \quad (4.11)$$

In (4.10) and (4.11), the *ext* subscript denotes flow conditions external to the numerical domain and numeric subscripts denote the first, second, and third model grid points from the open boundary, respectively. These two equations are solved simultaneously for velocity and depth on the numerical boundary, subject to the time-varying external field and the values of the interior solution. For simplicity, the external current (u_{ext}) is chosen to be zero and the external tide (ζ_{ext}) is prescribed as

$$\zeta_{\text{ext}}(t) = \zeta_{0,\text{ext}} \cos(\omega t + \zeta_{\phi,\text{ext}}), \quad (4.12)$$

where ω is the frequency of the forcing tide.

While the boundary condition proposed by Blayo and Debreu has a number of excellent properties, it also distorts the amplitude and phase of the “external” tide across the open boundary. This is to be expected, since if it did not, the boundary would be clamped. Because the “external” region is an abstraction, the external forcing may be specified to achieve any amplitude and phase desired along the model boundary. Unlike clamped boundary conditions, the chosen approach allows tides and currents at the boundary to evolve in response to changes in the interior of the model as constrained by the external field. In particular, the amplitude and phase of the tides and currents along the boundary are free to respond to kinetic power extraction by in-stream turbines. This approach is consistent with recent work showing that variations in power dissipation along the continental shelf can alter the tidal regime in the open ocean [45].

4.1.3. Channel Junctions

At junctions between channel segments, the width, depth, elevation, and surface roughness are allowed to change discontinuously. Further, the junctions may be:

- (1) *serial* - joining one channel to another.
- (2) *divergent* - one channel bifurcates into two.
- (3) *convergent* - two channels merge into one.

These three junction types form the building blocks for any networked system of channels. At serial junctions, there are four unknowns, namely the depth and velocity of the upstream and downstream channels. These may be determined by simultaneously solving conservation of mass, conservation of energy, and the positive and negative characteristic equations on the left and right hand side of the junction, respectively [46]. For a divergent channel, behavior at the junction is governed by six equations. These are conservation of mass for the diverging branches (assuming constant density)

$$(uhb)_1 = (uhb)_2 + (uhb)_3, \quad (4.13)$$

conservation of energy between each branch (2,3) and the main channel (1)

$$\frac{u_1^2}{2g} + h_1 + z_1 = \frac{u_2^2}{2g} + h_2 + z_2, \quad (4.14)$$

$$\frac{u_1^2}{2g} + h_1 + z_1 = \frac{u_3^2}{2g} + h_3 + z_3, \quad (4.15)$$

the positive characteristic equation for the main channel

$$u_1 + 2(gh_1)^{1/2} = C_p, \quad (4.16)$$

and the negative characteristic equations for the branching channels

$$u_2 - 2(gh_2)^{1/2} = C_{n2}, \quad (4.17)$$

$$u_3 - 2(gh_3)^{1/2} = C_{n3}. \quad (4.18)$$

C_p and C_n are the positive and negative characteristic constants, respectively, determined by second-order interpolation, as described by Lai [49]. The calculation of the characteristic constants is described in more detail in Appendix 2. Equations (4.13) through (4.18) are solved simultaneously by the Newton-Raphson method [46]. This is a more general form of the method proposed by Dronkers [47] and comparable to the method used by Aral et al. [48]. For a convergent junction, the solution method is similar, with the characteristic equations reversed. For serial junctions, the energy conservation equation is modified to include loss coefficients related to expansion and contraction losses between segments of significantly different cross-section (e.g., inlet to constriction);

$$\frac{u_1^2}{2g}(1 - k_1) + h_1 + z_1 = \frac{u_2^2}{2g}(1 - k_2) + h_2 + z_2. \quad (4.19)$$

For this model, a loss coefficient of 0.2 is applied for sudden contractions (as for flow entering a constricted channel) and a loss coefficient of 1.0 is used for sudden expansions.

4.1.4. Turbine Model

For 1D modeling, it may be assumed that the diameter of each turbine is very small in comparison to the characteristic depth of the channel. Therefore, three-dimensional flow features, such as the wake of each turbine, are of a length scale much smaller than is resolved by the numerical grid. Further, turbines are assumed to be evenly distributed across the channel in rows perpendicular to the direction of the flow. Under these assumptions, energy dissipation by turbines is approximated as a flow discontinuity and modeled using a compatibility condition identical to a serial channel junction. This approach is similar to shock fitting, with the additional

simplification that the location of the discontinuity is known *a priori*. Since the bottom elevation of the channel does not change across the turbine transect, (4.19) may be simplified to

$$\frac{u_1^2}{2g}(1-k_1)+h_1=\frac{u_2^2}{2g}(1-k_2)+h_2, \quad (4.20)$$

with subscript 1 denoting the position just seaward of the row of turbines and subscript 2 the position landward.

Using the notation from Chapter 2, the dissipation factor (k) for a row of turbines is given by the product of its dissipation coefficient (η_d) and blockage ratio (ε),

$$k=\eta_d\varepsilon. \quad (4.21)$$

As discussed in Chapter 2, the total power dissipated by the operation of a turbine is the sum of the power extracted and the power lost in the mixing of the wake with the free stream. On flood tides, $k_1=k$ and $k_2=0$, and vice versa on ebb. The number of rows of turbines may be varied to achieve different levels of energy extraction. Rows of turbines are assumed to be evenly spaced in the along-channel direction. An example of a channel with four rows of turbines is shown in Figure 4.1.

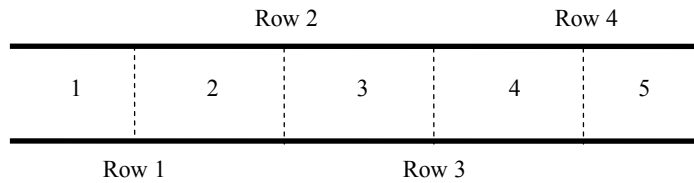


Figure 4.1 – Schematic of constricted channel with rows of turbines (top view). The four rows of turbines (dashed lines) subdivide the original channel into five segments.

The particular values of ε and η_d for each row are unimportant in quantifying environmental effects since, as will be shown, the system response to dissipation is a continuous function of the dissipation factor (k). However, as discussed in Chapter 2, these values do determine the ratio of extracted to dissipated power. Dissipated power will always be greater than extracted power as a consequence of unavoidable, non-negligible losses when the wake mixes with the free stream. All far-field effects of power extraction are quantified in terms of total dissipation. However, since dissipation and extraction are related by a constant of proportionality, the terms are used interchangeably in qualitative discussion.

In Chapters 4 and 5, each row of turbines is assumed to have a blockage ratio of 1/3 and operates at the theoretical maximum efficiency (streamtube velocity ratio of 1/3). Since the Froude number is generally below 0.15 for realistic tidal channels, (2.40) and (2.41) are reasonably accurate and imply a dissipation coefficient (η_d) of 8/3. In Chapter 6, which describes the application of the 1D model to Puget Sound, Washington, a practical, rather than theoretical, device efficiency is used.

It is also possible to investigate the dynamic effects of the rated and cut-in speed of a turbine, as described in Section 1.3, by expanding (4.20) to the three regimes of turbine operation:

$$u < u_{\text{cut-in}}: k = 0, \quad (4.22)$$

$$u_{\text{cut-in}} \leq u \leq u_{\text{rated}}: k = \varepsilon \eta_d, \quad (4.23)$$

$$u > u_{\text{rated}}: k = \varepsilon \eta_d \left(\frac{u_{\text{rated}}}{u} \right)^3. \quad (4.24)$$

This approach requires two basic assumptions. First, drag on the device support structure is negligible, such that below the cut-in speed, no power is dissipated by the device or support structure. Second, above rated speed, power is shed by pitching the blades to a non-optimal angle of attack, which reduces the extraction coefficient. The derivations of (4.20) and (4.24) are given in Appendix 4.

An alternative to this approach is to model turbines as an additional momentum sink in the governing equations. As suggested by Couch and Bryden for steady-state models [38], the discretized form of this term would be

$$S_{\text{turbine}} = \frac{1}{2} hb \frac{k^*}{\Delta x} u |u|, \quad (4.25)$$

where k^* is a factor describing the dissipation by the turbine. However, since the momentum sink associated with power extraction is much greater than the sink associated with natural friction, the inclusion of this term introduces large dispersive errors in the numerical solution around the extraction discontinuity. Energetically, these dispersive errors are on the same order as the kinetic energy extracted and are independent of the solution algorithm. This appears to be an intrinsic limitation of explicit solutions to the shallow water equations when there is a spatial discontinuity in the momentum sink. This approach has not been used to model extraction effects and the above discussion is included as a point of interest.

Before discussing the time-dependent problem of kinetic power extraction from tidal streams, it is instructive to consider the response of a steady-state system, since the two solutions share some general features. The steady-state problem consists of a single rectangular channel of constant width and depth. For tidal channels, the width is much greater than the depth. The water level at each end of the channel is maintained at a constant, but different elevation, such that a driving head is established and flow develops along the channel. This situation is physically analogous to two infinite reservoirs at different elevations connected by a narrow channel.

A representative case is shown in Figure 4.2 for a channel 5 km long, 1 km wide, and 50 m deep. The driving head is 0.5 m. In the natural state, the water depth decreases uniformly along the length of the channel as power in the flow is dissipated by friction with the seabed and walls. Conservation of mass requires that this decrease in depth (a) be matched by a proportional increase in velocity (c). Power extraction by turbines also leads to a decrease in depth, though in a discontinuous manner over the plane of dissipation. As an increasing fraction of the driving head is dissipated by power generation, less is available to drive the flow, as indicated by the reductions in channel flow rate shown in plot (b). While the velocity does increase discontinuously across each row of turbines (d), this is subordinate to the channel-wide reduction in velocity relative to the natural state. As a result of decreasing kinetic power (proportional to the cube of velocity), each additional row of turbines dissipates less power (P) from the flow, as labeled on plot (b). The same general flow structure and response are seen in the time-dependent problem.

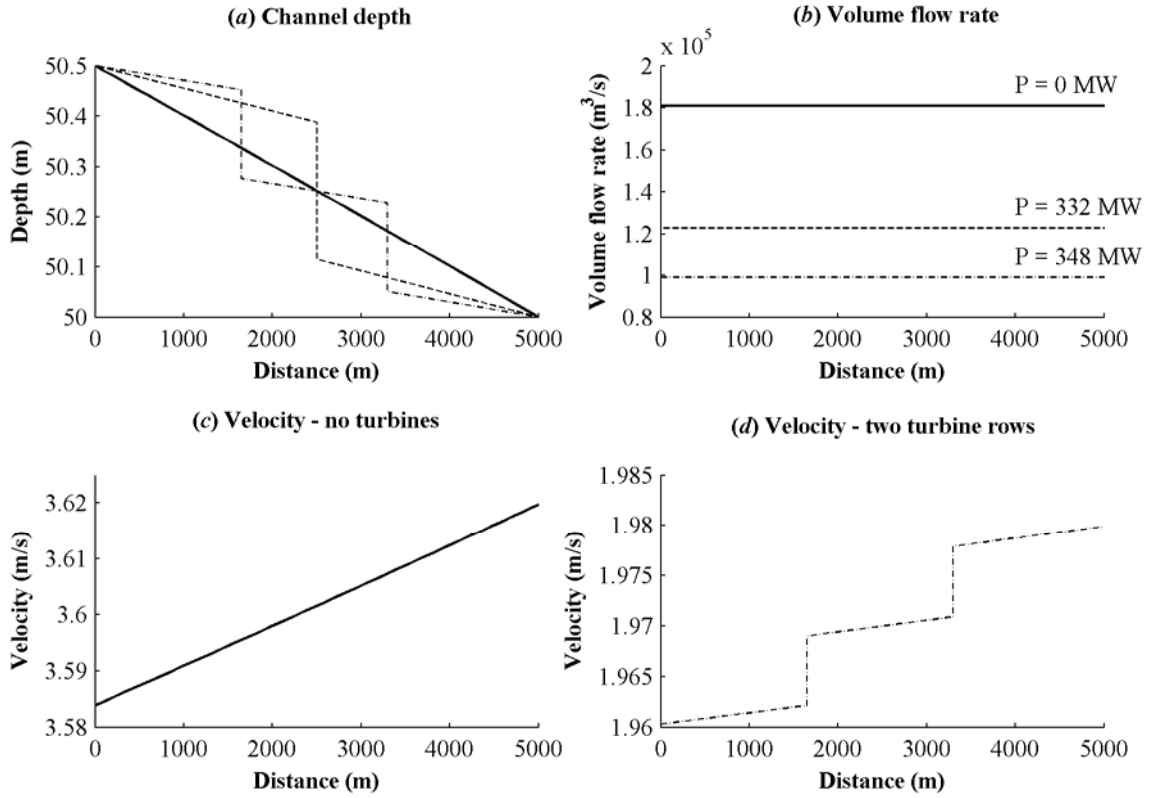


Figure 4.2 – Response of steady-state flow to kinetic power extraction. Natural state (no turbines): solid black, 1 turbine transect: dashed grey, 2 turbine transects: dot-dash black.

4.1.5. Quantifying Effects

At each time step, the kinetic power dissipated by in-stream turbines (P) is the difference in kinetic and potential power across the plane of dissipation;

$$P = \left| (\rho u h b)_1 \left(\frac{1}{2} u^2 + g \zeta \right)_1 - (\rho u h b)_2 \left(\frac{1}{2} u^2 + g \zeta \right)_2 \right|. \quad (4.26)$$

Here the subscripts 1 and 2 denote flow quantities seaward and landward of the dissipation discontinuity, respectively, and ζ is the elevation (m) relative to mean sea level. The total dissipation is the sum of dissipation for all turbine rows. Changes to the tidal regime are quantified as a function of the time-averaged power dissipated. If the M2 tide is dominant, then averaging is over an integer number of M2 periods (12.42 hours). When the four tidal constituents giving rise to the neap-spring cycle are used to force the model (M2, S2, K1, O1), then averaging is over an integer number of neap-spring periods (14.8 days). For longer-term

simulations, such as the one discussed in Chapter 6, the averaging period is the full simulation time, excluding model spin-up.

The changes to the tidal regime are quantified in terms of tides (water elevation), currents (water velocity), transport (volume flow rate), total power dissipated, and kinetic power density. These all are far-field extraction effects, as opposed to near-field changes in the immediate vicinity of a turbine [8]. As discussed previously, the effect of extraction on a steady-state flow is to reduce the magnitude of a flow quantity (e.g., velocity). When power is extracted from a time-varying flow, both the magnitude and phase of depth and velocity are altered relative to natural conditions.

The effect on tides (ζ), currents (u), and transport (Q) are determined by a least squares fit of the model output to harmonic constituents using the program *t_tide* [50]. Note that the term transport is used synonymously with flow rate, as is the convention in the oceanographic literature. The use of this term does not imply advection or diffusion of a scalar quantity, as is the convention in the engineering literature. Changes are quantified for each tidal constituent, fit to the forms

$$\zeta(t) = \sum_i \zeta_{0,i} \cos(\omega_i t + \zeta_{\phi,i}), \quad (4.27)$$

$$u(t) = \sum_i u_{0,i} \cos(\omega_i t + u_{\phi,i}), \quad (4.28)$$

$$Q(t) = \sum_i Q_{0,i} \cos(\omega_i t + Q_{\phi,i}). \quad (4.29)$$

In the above equations, ω_i is the frequency of the i^{th} constituent. Comparisons are made only for constituents being forced at the model boundary. While the model does generate overtides (e.g., M4) and compound tides (e.g., MK3), these are an order of magnitude weaker than the forced constituents and the effects of extraction on overtides and compound tides are not quantified. For longer duration simulations, changes to transport are also quantified in terms of cumulative transport,

$$Q_i = \sum_T |Q(t)| \Delta t, \quad (4.30)$$

or mean absolute transport (\bar{Q}),

$$\bar{Q} = \frac{\sum_T |Q(t)| \Delta t}{T}, \quad (4.31)$$

both of which include the contributions of all constituents, regardless of relative strength. The summation in (4.30) or average in (4.31) over period (T) is the same as the averaging period discussed above for extraction of kinetic power by turbines.

Changes to each of these quantities have environmental implications. An increase or decrease in the tidal range will affect shoreline processes. Changes to velocity could alter sedimentation patterns by either increasing scour (velocity increase) or deposition (velocity decrease). Changes to transport will affect an estuary's ability to flush pollutants.

For a given model cross-section, the instantaneous energy flux (power) across that section is given by [51]

$$D = \rho u h b \left(\frac{1}{2} u^2 + g \zeta \right). \quad (4.32)$$

Because power is dissipated by frictional losses and extraction by turbines, more power passes in over a cross-sectional area on flood than on ebb. Therefore, the time-average of this quantity is non-zero and describes the average power dissipated landward of that cross-section. This is a measure of total power dissipation and includes both power dissipated by natural mechanisms and power dissipated by turbines. In this model, bottom friction serves as a proxy for all natural losses (internal waves, eddies, etc.). Therefore, changes to total power dissipation may relate to mixing processes, with implications for dissolved oxygen and basic biological productivity.

The instantaneous kinetic power density (K) is given by

$$K = \frac{1}{2} \rho u^3. \quad (4.33)$$

Power density is proportional to the power extracted by a turbine and is one of the major drivers of project economics [7]. As such, increases or decreases in kinetic power density may, respectively, improve project economics or limit the scope of development.

In some cases, to simplify the presentation of results, conventions have been adopted in this dissertation so that only a single value is reported for changes in the flow for each channel segment. Changes to the amplitude and phase of tides, currents, and transport are reported at the

midpoint of the segment. For constricted channels, since it is possible for a turbine transect to be at the midpoint, the midpoint change is approximated as the average of the changes at the beginning and end of the segment. Changes to kinetic power density also follow this convention. Changes to the total power dissipated, which include both frictional dissipation and turbine dissipation, are reported for the entire segment. Contraction and expansion losses are grouped with the constricted channel.

4.2. Extraction from a Single Constriction

A basic, time-varying network suitable for kinetic power extraction consists of a basin connected to the open ocean by a narrow channel. In the channel, currents are sufficient to support power extraction by in-stream turbines. This is comparable to the type of network studied by Blanchfield et al. [34]. A schematic of the single constriction network is shown in Figure 4.3.

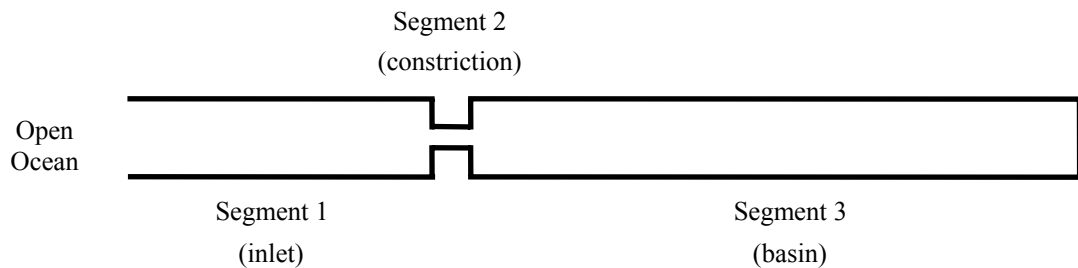


Figure 4.3 – Schematic for a single constriction network (top view).

The network is forced at the open boundary by a single constituent (M2). Turbines operate in a linear manner with neither a cut-in nor a rated speed. The geometric properties for the three channel segments are listed in Table 4.1 and the baseline tidal regime is quantified in Appendix 5. Network properties are selected such that the kinetic power density in the constricted channel is in line with potential tidal energy sites for the United States and Canada [6]. Perturbations about the base case with respect to geometry and forcing are discussed in Section 4.2.2 and compared with analytical solutions in Section 4.2.3. The influence of the tidal regime is considered in Section 4.2.4 and the effect of nonlinear device dynamics (cut-in and rated speed) is described in Section 4.2.5.

Table 4.1 – Baseline properties for single constriction network channel segments.

Segment	1	2	3
Length (L) (km)	40	5	80
Width (b) (km)	10	2	10
Depth (H) (m)	50	50	50
Manning roughness (n) ($\text{s/m}^{1/3}$)	0.035	0.035	0.035
Forcing amplitude ($\zeta_{0,\text{external}}$) (m)	2.4		
Dissipated power (MW)	115	508	46
Kinetic power density (kW/m^2)	0.04	3.0	0.003

4.2.1. Effects of Extraction

A brief word is warranted about the presentation of results. Extraction effects are often shown in this section with mixed axes; the abscissa is the dimensional turbine dissipation and the ordinate is the non-dimensional relative change to a fluidic quantity. While somewhat non-standard, this facilitates interpretation of results. The average power generated and average power dissipated by turbines are related by the ratio of extraction to dissipation. Average power generation, in megawatts, is an easily recognized quantity and array dissipation may, therefore, be compared with the scale of other generating options (i.e. thermal power plant). Conversely, the significance of far-field environmental impacts are more easily recognized in relative terms by those outside the oceanographic community. For example, a 10% reduction in tidal range is easier to contextualize than a 10cm reduction in tidal range. In comparing results between networks of the same type (but with different segment geometries), relative changes are discussed as a function of non-dimensional dissipation by turbines (P/P_{max}). The approach described here is appropriate for idealized analysis. However, it is important to remember that for real in-stream projects, the dimensional, rather than relative, changes to the environment will determine the ecosystem impacts.

Extraction effects are quantified in terms of the tide, currents, transport, total power dissipated, and kinetic power density.

There is considerable spatial variability in the relative changes to the tide, as shown in Figure 4.4. With respect to amplitude (a), there is almost no change in the inlet (segment 1), a pronounced reduction across the constricted channel (segment 2), and a nearly uniform reduction across the basin (segment 3). The change in phase (b) shows the opposite behavior, with a decreased phase lag in the inlet and increased phase lag in the basin. The phase lag across the entire system has, therefore, increased, which is consistent with additional dissipation due to turbines and the

relation between phase change and total power dissipated [52]. The relative change to both amplitude and phase varies with the magnitude of power extraction. However, there is also a decreasing marginal change for each additional row of turbines. That is to say, in Figure 4.4 the effect of four transects is less than twice the effect of two transects or, conversely, four transects do not dissipate twice the power of two transects. As shown in Figure 4.5, as extraction increases, a point of maximum dissipation (P_{max}) is achieved. Beyond this point, additional turbines dissipate less total power, which establishes a theoretical upper limit for this case. In Figure 4.5, each symbol denotes a finite, increasing number of turbine rows. Therefore, it is clear that the response to extraction is a continuous function of the power dissipated by turbines and does not depend on the particular values of η_d and ε .

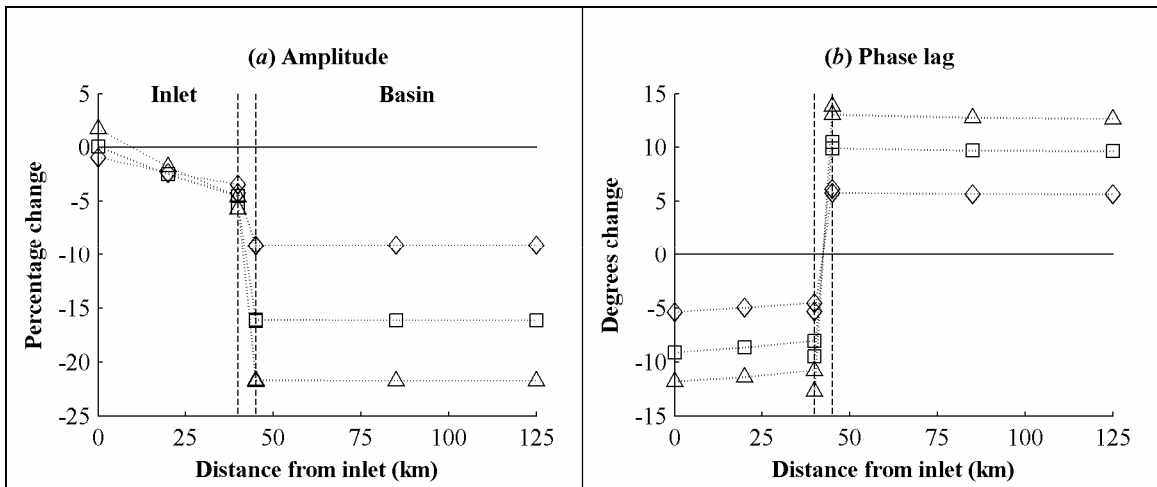


Figure 4.4 – Spatial variation of changes to the tide with extraction in a single-constriction network. \diamond 2 rows, 390MW dissipated, \square 4 rows, 620MW dissipated, \triangle 6 rows, 750 MW dissipated.

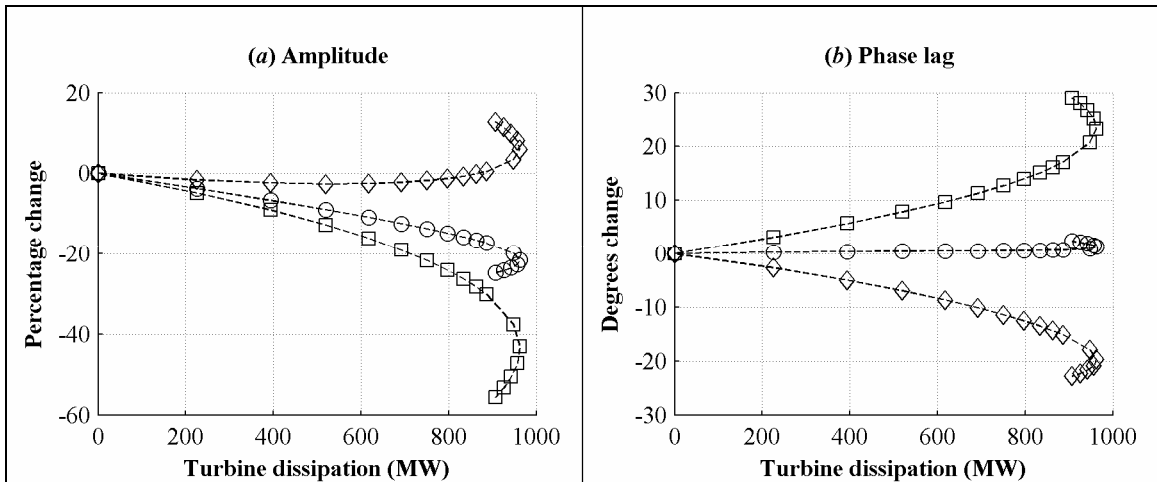


Figure 4.5 – Changes to the tide with extraction in a single-constriction network. Symbols denote a finite number of turbine rows: \diamond segment 1, \circ segment 2, \square segment 3.

The change in relative phase lag and amplitude between segment 1 and segment 3 is of particular relevance to the system response. Figure 4.6 shows the time-series for elevation and velocity across the constricted channel. Plots (*a,b*) reflect the results shown in Figure 4.5; seaward of the constriction, extraction decreases the phase lag with little change in amplitude while, landward of the constriction, extraction increases the phase lag and decreases the amplitude. The tidal phase lag in a segment is proportional to the power dissipated (frictional losses and extraction by turbines). Because the velocity decreases throughout the channel network as a result of extraction (discussed further on in this section), frictional dissipation decreases in all segments. In the segment with extraction, however, the total dissipation increases. Therefore, seaward of the turbines, the phase lag decreases and landward of the turbines, the phase lag increases. As with velocity, transport also decreases throughout the channel network as a result of extraction. As a result, less water enters the terminal basin over a tidal cycle, and the tidal amplitude is reduced. These relative changes in amplitude and phase alter the driving head (difference in depth) across the constricted channel increases (*c*). For flow through constricted channels, the dynamics are quasi-steady, meaning that the instantaneous flow rate is largely a function of the instantaneous driving head. The increase in driving head with higher levels of extraction partially restores the flow rate, but does not completely offset the increased resistance to flow caused by the turbines. As shown in plot (*d*), the phase shift in the driving head is reflected by a comparable phase shift in velocity.

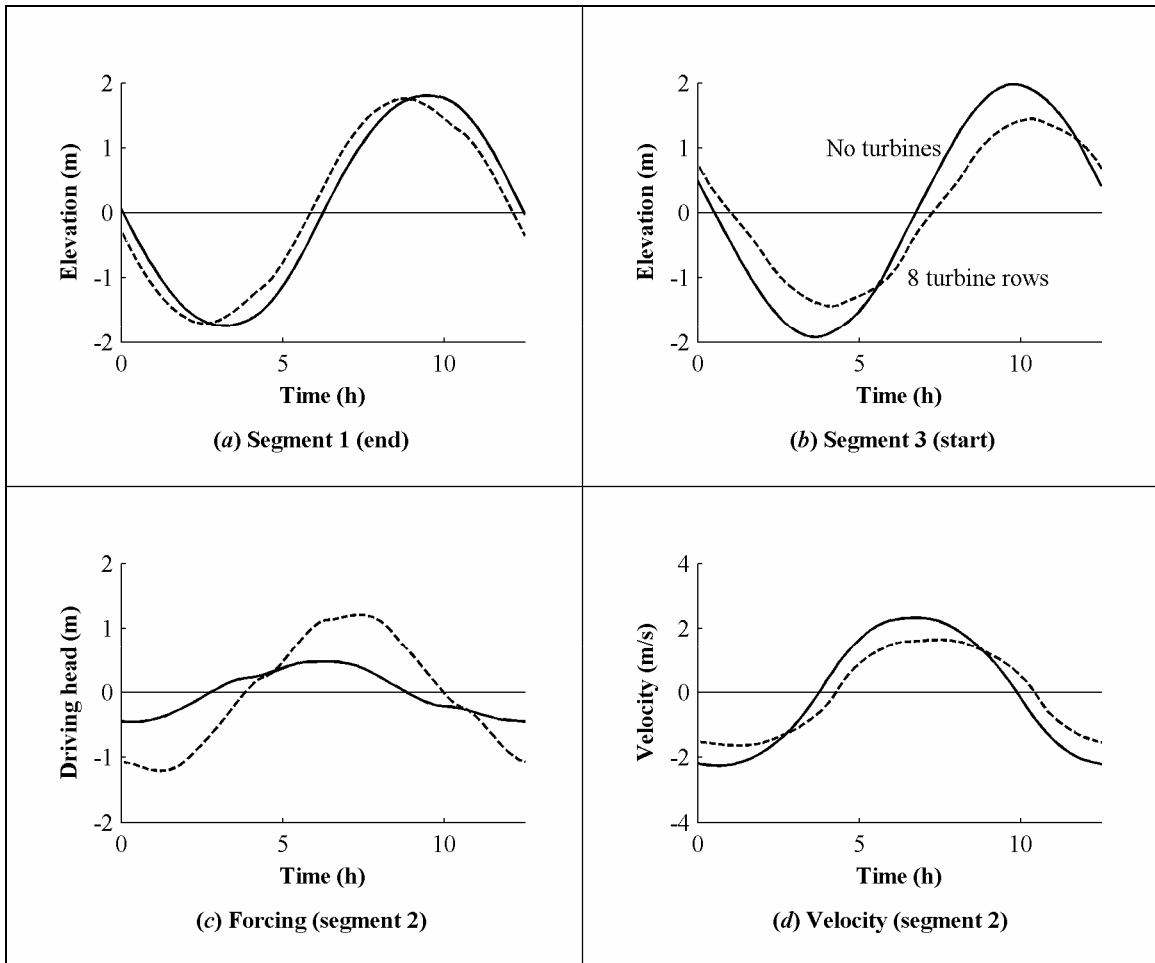


Figure 4.6 – Restorative forcing across constricted channel. Solid line: no turbine dissipation, Dashed line: 8 rows of turbines (830 MW dissipation).

The response of the currents to extraction is much more spatially uniform, as shown in Figure 4.7 and Figure 4.8. Phase lags increase with extraction, with the greatest change seaward of the terminal basin (segment 3). The relative changes to current amplitude and tidal amplitude in the terminal basins are nearly equivalent.

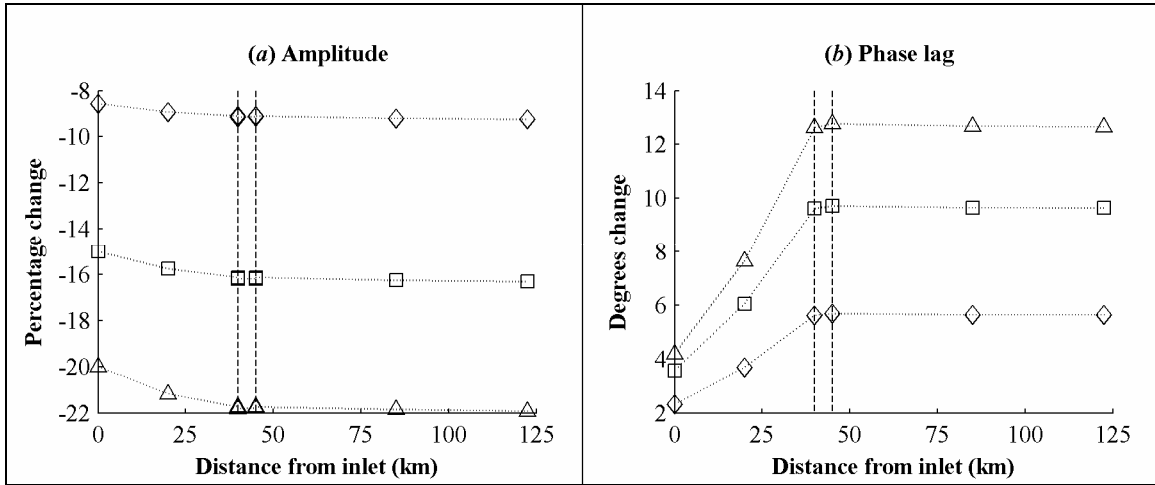


Figure 4.7 – Spatial variation of changes to currents with extraction in a single-constriction network. \diamond 2 rows, 390MW dissipated, \square 4 rows, 620MW dissipated, \triangle 6 rows, 750 MW dissipated.

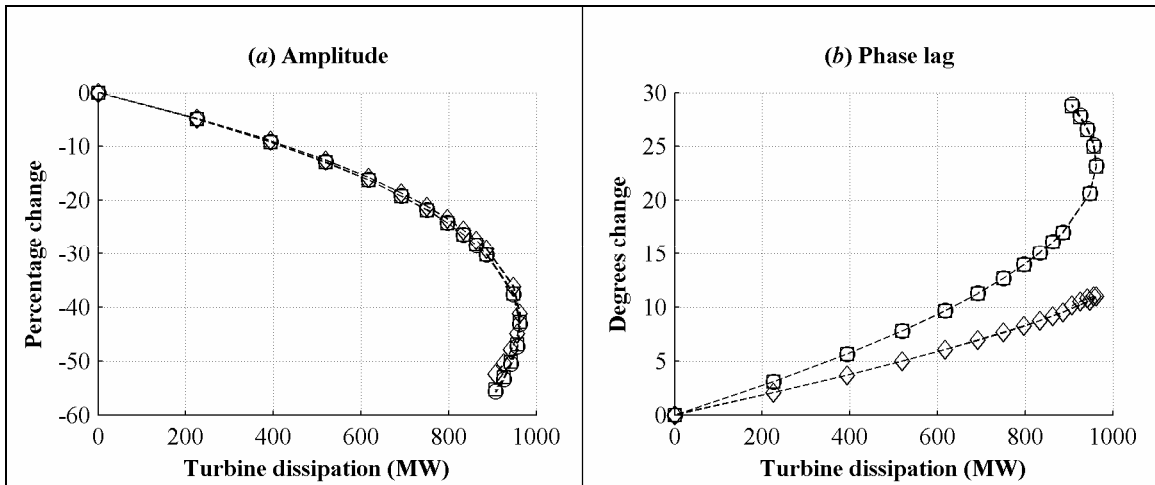


Figure 4.8 – Changes to currents with extraction in a single-constriction network. Symbols denote a finite number of turbine rows: \diamond segment 1, \circ segment 2, \square segment 3.

As shown below in Figure 4.9 and Figure 4.10, the response to transport is nearly identical to changes in current. This is as expected since, assuming that the tides and currents are approximately sinusoidal,

$$Q(t) \propto h(t)u(t) = (H + \zeta_0 \cos(\omega t + \zeta_\phi))(u_0 \cos(\omega t + u_\phi)). \quad (4.34)$$

If, as for the network described in Table 4.1, the mean water depth (H) is much greater than the tidal amplitude (ζ_0), then

$$Q(t) \propto u_0 \cos(\omega t + u_\phi), \quad (4.35)$$

and relative changes in transport and current will be identical. This approximation is accurate for all the channel networks discussed in Chapters 4 and 5. Therefore, changes to transport are not generally quantified, but it should be understood that relative changes in transport and current are approximately equal. The maximum turbine dissipation (P_{max}) corresponds to approximately a 40% reduction in transport, which is in agreement with results described in Sutherland et al. [13].

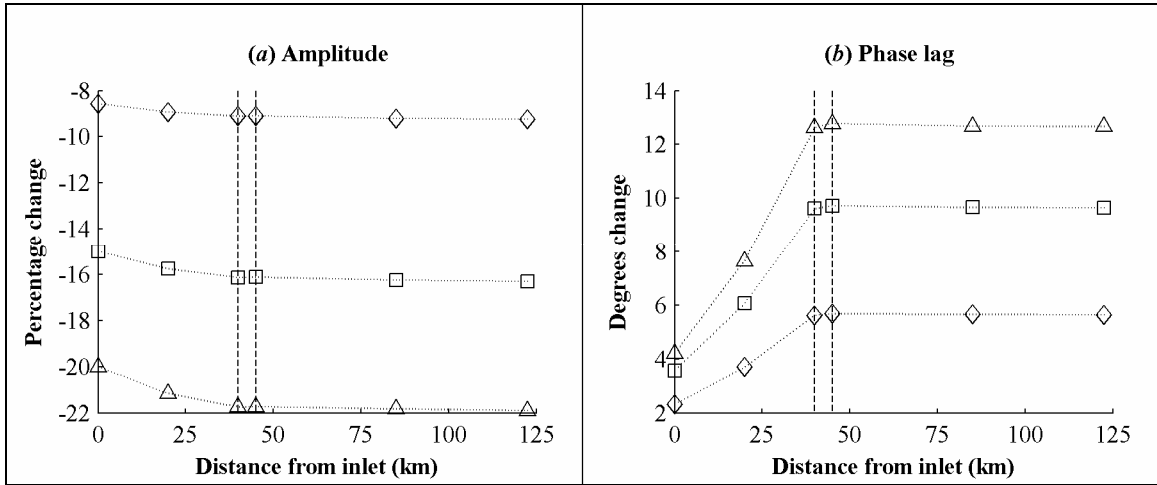


Figure 4.9 – Spatial variation of changes to transport with extraction in a single-constriction network. \diamond 2 rows, 390MW dissipated, \square 4 rows, 620MW dissipated, \triangle 6 rows, 750 MW dissipated.

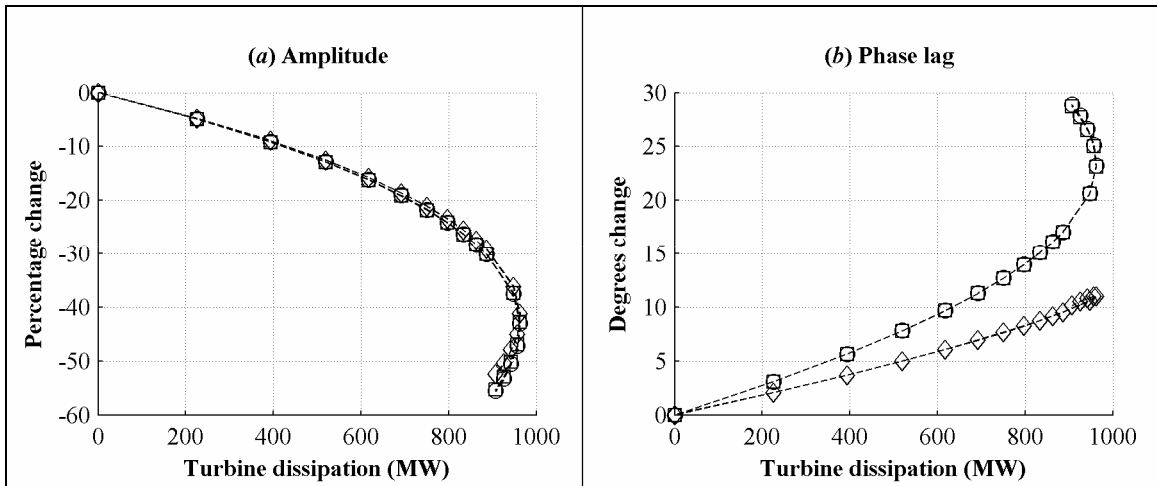


Figure 4.10 – Changes to transport with extraction in a single-constriction network. Symbols denote a finite number of turbine rows: \diamond segment 1, \circ segment 2, \square segment 3.

Figure 4.11a shows the changes to total dissipation (dissipation by turbines and dissipation due to friction with the channel walls). Frictional power dissipation varies with velocity. Since power extraction by turbines reduces velocity throughout the system, frictional dissipation decreases. Total dissipation increases in the constricted channel (segment 2) because the power dissipated by turbines is greater than the reduction in frictional dissipation for that segment. Note that the

increase in total dissipation in segment 2 is always less than the power dissipated by turbines. Further, the energy flux balance for the entire system shows that the dissipation by turbines is offset by both reduced dissipation elsewhere in the system, as well as an increased power flux at the head of the system (Figure 4.11*b*). This suggests that kinetic power extraction within an estuary will also remove energy from adjacent coastal processes.

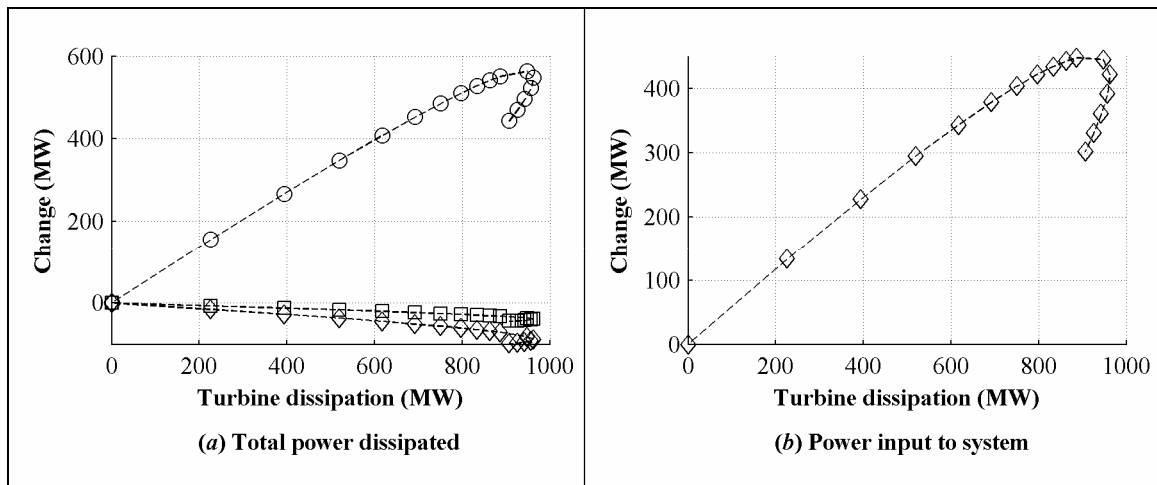


Figure 4.11 – Changes to total dissipated power and power input to system with extraction in a single-constriction network. Symbols denote a finite number of turbine rows: \diamond segment 1, \circ segment 2, \square segment 3.

Figure 4.12 shows the reduction in kinetic power density with extraction. Since this quantity varies with the cube of velocity, this is the largest relative change and is an amplified version of the effect on currents.

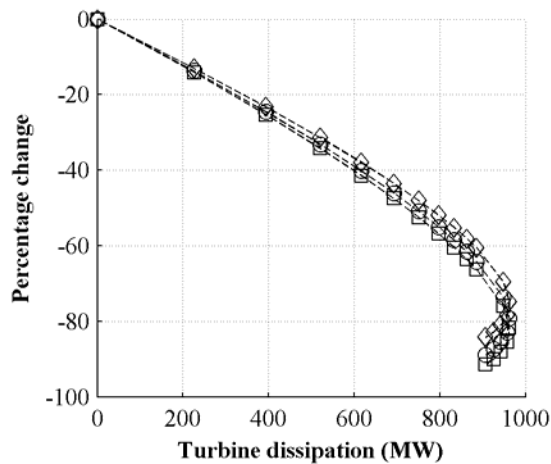


Figure 4.12 – Changes to kinetic power density with extraction in a single-constriction network. Symbols denote a finite number of turbine rows: \diamond segment 1, \circ segment 2, \square segment 3.

4.2.2. Influence of Network Geometry and Tidal Forcing

The preceding discussion applies only to the geometry and tidal forcing described in Table 4.1. A number of variations on this are described in Table 4.2, with each case consisting of a variation in one parameter from the base case. For case S2, ' $L_3 = 60\text{km}$ ' means that the length of segment 3 has been decreased to 60km from the base value of 80km. The response to kinetic power extraction for these variations is shown in Figure 4.13, as quantified by the relative change in peak velocity in the terminal basin (segment 3). The results clearly indicate that geometry and tidal forcing play an important role in determining the system response. The data also indicate that there is no correlation between power density in the constricted channel and the maximum dissipation (P_{\max}). That is to say, the theoretically recoverable resource does not depend on the resource intensity.

Table 4.2 – Single constriction network geometries and tidal forcings

Case	Variation	Symbol (Figure 4.13)	Power Density ¹ (kW/m ²)	P_{\max} (MW)
S1	Base case	◆	3.0	960
S2	$L_3 = 60\text{km}$	□	1.6	830
S3	$L_3 = 100\text{km}$	■	4.3	1000
S4	$b_2 = 1.5\text{km}$	△	5.9	910
S5	$b_2 = 2.5\text{ km}$	▲	1.7	990
S6	$H_{123} = 30\text{m}$	◁	5.2	680
S7	$H_{123} = 70\text{m}$	◀	1.4	1100
S8	$\zeta_{0,\text{external}} = 2.8\text{m}$	▶	5.6	1300
S9	$\zeta_{0,\text{external}} = 2.0\text{m}$	▷	1.8	680
S10	$L_1 = 80\text{km}$	o	2.7	930

¹Natural power density in segment 2 (constriction)

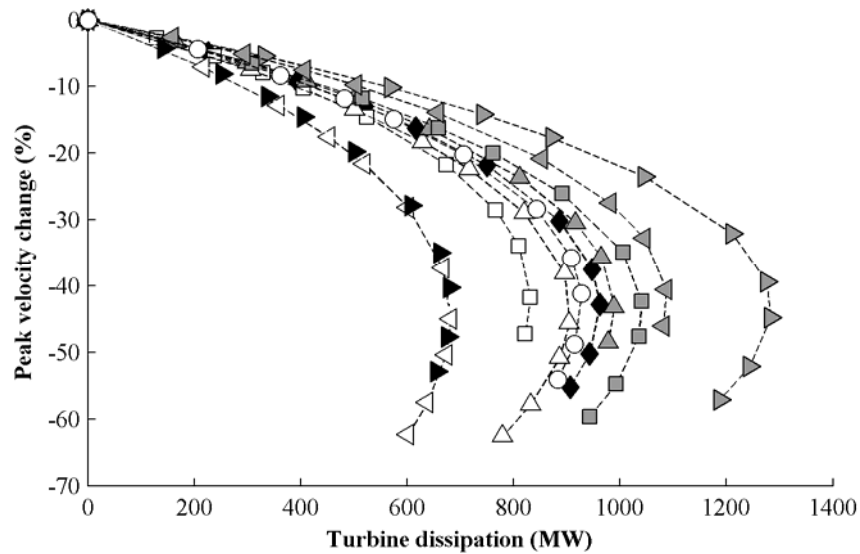


Figure 4.13 – Velocity response relative to turbine dissipation for single constriction networks. Each symbol denotes a particular geometry or external forcing in Table 4.2.

The site-specific nature of the response to extraction complicates standardized resource assessment. For the purposes of a regional or national assessment, it would be desirable to determine the level of extraction corresponding to a particular level of far-field impact (e.g., a 10% reduction in transport). This is attempted in some early studies of the tidal resource (e.g., [6]), but relies upon the assumption that extracting a fixed percentage of the natural kinetic power on a transect will cause the same relative far-field changes at different sites. This is demonstrably incorrect [53].

As suggested by Garrett and Cummins [20], extraction effects in single constriction networks are actually equivalent when compared to the fraction of P_{\max} dissipated (P/P_{\max}). This equivalence is shown in Figure 4.14 for changes in current amplitude.

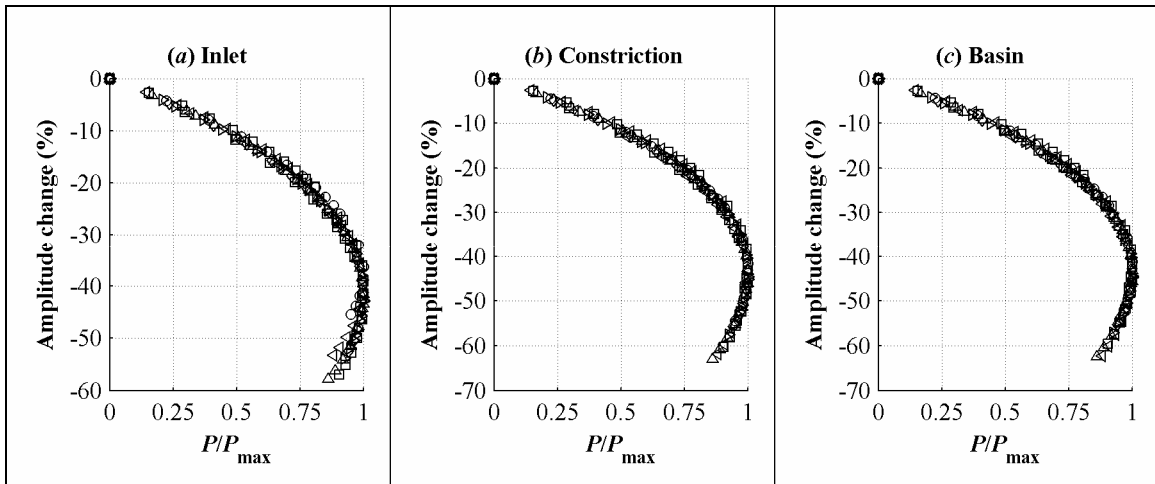


Figure 4.14 – Non-dimensional change in currents in single constriction networks. All series in Table 4.2 are displayed.

Since kinetic power density is a function of velocity, its relative change is similarly equivalent between different segment geometries, as shown in Figure 4.15. Note that the non-dimensionalized response varies slightly between the three segments.

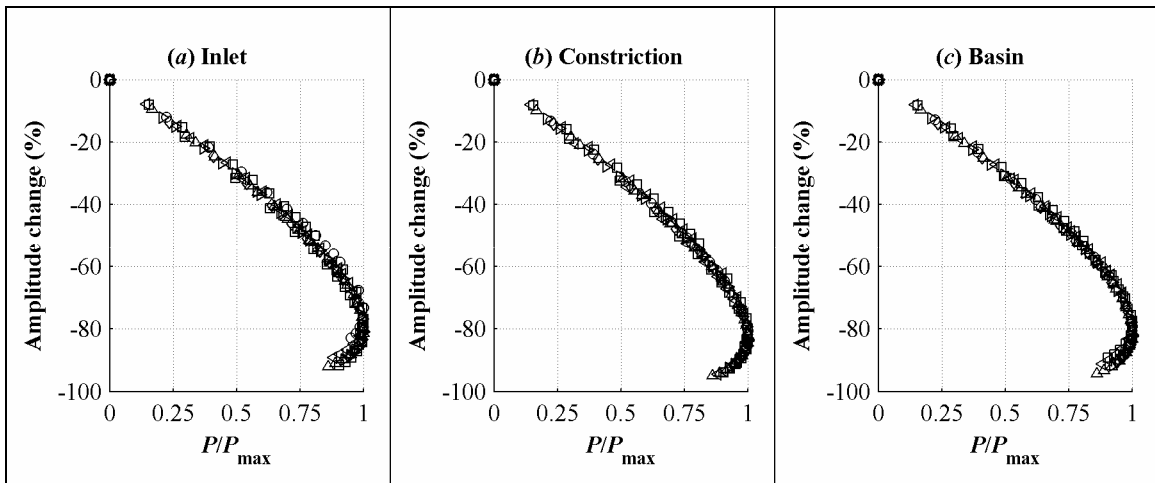


Figure 4.15 – Non-dimensional change in kinetic power density in single constriction networks. All series in Table 4.2 are displayed.

The change in tidal amplitude is only equivalent between cases in the terminal basin, as shown in Figure 4.16. The tidal range increase seaward of the constriction is geometry-specific.

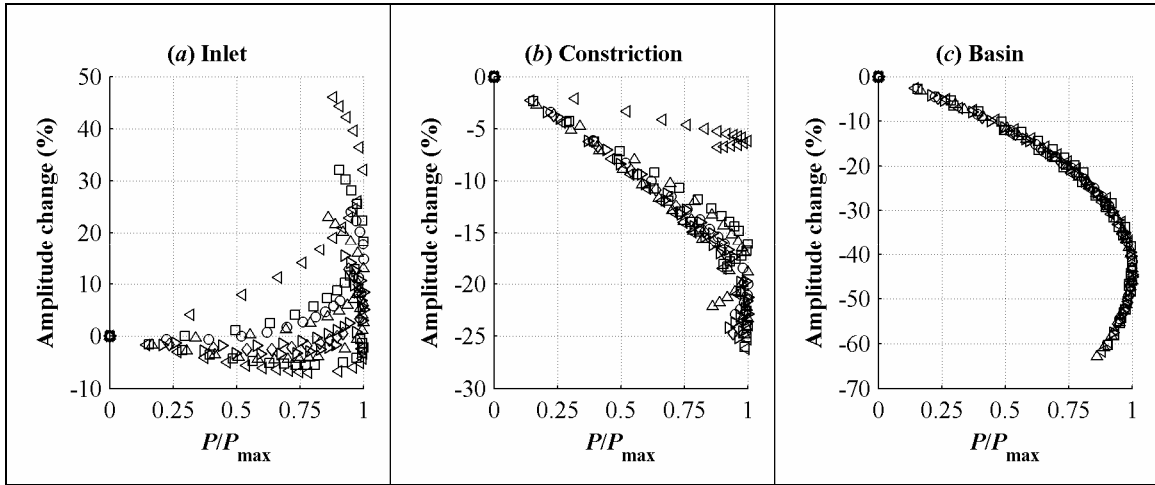


Figure 4.16 – Non-dimensional change in tidal amplitude in single constriction networks. All series in Table 4.2 are displayed.

Therefore, the response of quantities derived principally from velocity (transport, power density, and frictional power dissipation) may be readily compared between different geometries on the basis of P/P_{\max} .

4.2.3. Comparison with Analytical Results

The theory proposed by Garrett and Cummins [20] and then extended by Blanchfield et al. [14,34] and Karsten et al. [12] serves as a useful tool to verify the predictions made by the channel model. Conversely, model results may be used to test the general validity of the assumptions underpinning the theory.

As discussed in Chapter 3, the theoretical maximum possible dissipation due to turbines (P_{\max}) for a single constriction network is given by [14]

$$P_{\max} = \gamma \rho g \zeta_0 Q_0. \quad (4.36)$$

Using the relations developed in Chapter 2, P_{\max} is related to the theoretically extractable resource by the ratio of extraction to total dissipation. In (4.36), Q_0 is the maximum flow rate in the constricted channel without extraction and ζ_0 is the tidal amplitude seaward of the constricted channel without extraction. The last four terms in represent the work done by the tide to drive the volume flow rate through the constricted channel. γ is a function of two dimensionless parameters: β and λ_0^* . β describes the relation between the surface area of the basin and the wavelength of the tidal forcing. λ_0^* describes the natural frictional resistance of the constricted channel. Blanchfield et al. [14] describe a procedure for computing these constants based on

geometric properties of the system, while Karsten et al. [12] describe a procedure based solely on the properties of the tidal regime. Both proceed from the same set of dynamic equations discussed in Chapter 3. As noted by Karsten et al. [12], because of different approximations applied, these procedures yield slightly different results, but γ is not particularly sensitive to either β and λ_0^* .

Here, the approach recommend by Karsten et al. is used, in which:

$$\beta = \frac{R_0}{R_0 - \cos \phi_0}, \text{ and} \quad (4.37)$$

$$\lambda_0^* = \frac{\sin \phi}{(R_0 - \cos \phi_0)^2}. \quad (4.38)$$

R_0 is the amplitude ratio over the constricted channel and ϕ_0 is the relative phase lag over the same distance. γ is then given by:

$$\gamma = \frac{2^{1/2} \beta \lambda_1^*}{R_0 \left((\beta - 1)^2 + \sqrt{(\beta - 1)^4 + 4(\lambda_0^* + \lambda_1^*)^2} \right)^{3/2}}, \quad (4.39)$$

for the value of λ_1^* which maximizes the function. λ_1^* is a non-dimensional representation of drag due to in-stream turbines and is dynamically analogous to λ_0^* .

Table 4.3 presents a comparison between the theoretical and model predictions of P_{\max} for all geometries and tidal forcings tested. The computed values for γ fall into the range allowed by theory ($0.19 < \gamma < 0.26$) [34]. Agreement between the model and theoretical predictions is quite reasonable for most cases and indicates that the model is accurately reflecting the dynamics of kinetic power extraction.

Table 4.3 – Comparison between theoretical and model predictions for the maximum possible turbine dissipation in a single constriction network, using the procedure described in Karsten et al.

Case	Variation	β	λ_0^*	Γ	$\frac{P_{\max, \text{model}}}{P_{\max, \text{theory}}}$	$\frac{\zeta_{0, \max}}{\zeta_{0, \text{initial}}}$	Basin Phase Shift
S1	Base case	11	26	0.21	1.03	1.00	1.0°
S2	$L_3 = 60\text{km}$	16	30	0.22	0.93	0.94	0.5°
S3	$L_3 = 100\text{km}$	9	24	0.20	1.19	1.10	1.9°
S4	$b_2 = 1.5\text{km}$	8	25	0.20	1.13	1.07	0.9°
S5	$b_2 = 2.5\text{ km}$	14	27	0.22	0.97	0.97	1.1°
S6	$H_{123} = 30\text{m}$	8	41	0.19	1.40	1.26	4.5°
S7	$H_{123} = 70\text{m}$	16	25	0.22	0.91	0.93	0.4°
S8	$\zeta_{0, \text{external}} = 2.8\text{m}$	11	31	0.21	1.06	1.03	1.2°
S9	$\zeta_{0, \text{external}} = 2.0\text{m}$	11	22	0.21	1.00	0.99	0.9°
S10	$L_1 = 80\text{km}$	11	24	0.21	1.07	1.02	0.9°

The model response is in agreement with most of the assumptions made in the derivation of the theoretical response (see Chapter 3 for a discussion of these assumptions). However, the theoretical assumption that the tidal amplitude seaward of the constriction remains constant is not in agreement with model results. This has also been observed for two-dimensional modeling by Karsten et al. [12]. As seen in Table 4.3, the variation between theoretical and modeled P_{\max} is closely correlated with the relative change in amplitude outside the constriction ($\zeta_{0, \max} / \zeta_{0, \text{initial}}$). While the theory assumes that the constricted channel is directly connected to the ocean, the model includes an inlet region. As previously shown in Figure 4.4, the change in tidal amplitude is relatively minor at the open boundary, but increases in magnitude towards the constriction.

The assumption of co-tidal behavior in the basin is also not supported in all cases. For example, in case S6 the shallow depth slows the wave propagation speed and results in a moderate phase shift across the basin.

From this comparison, it is reasonable to conclude that the one-dimensional channel model accurately reflects the dynamics of power extraction. It is also reasonable to conclude that there are cases in which theory may lead to over and underpredictions of P_{\max} . A similar comparison using the procedure described by Blanchfield et al. is detailed in Appendix 6, but does not produce materially different results.

Maximum dissipation is unlikely to be achieved in practical situations for several reasons. First, the declining marginal extraction for each additional turbine near the maximum point creates a

strong economic disincentive. For most sites inventoried in North America [6], reducing the kinetic power density by more than 25-50% would lead to unfavorable project economics. Therefore, as inferred from Figure 4.15, economically-driven development would be restricted to no more than 50-75% of P_{\max} if a site may be reasonably approximated as a single constriction network. Second, the environmental impacts at P_{\max} are relatively high, with reductions to the tides and currents on the order of 40%. Finally, even for devices operating at the theoretical maximum efficiency, many rows of turbines are necessary to dissipate P_{\max} . For example, with the baseline geometry and tidal forcing, twenty-four rows of turbines with a downstream spacing of 200 m are required to dissipate P_{\max} . At most tidal energy sites identified to date in North America [6], the resource is localized over too small an area to support this many rows of turbines. Therefore, efficient device packing, which could minimize inter-turbine spacing, may be important for large-scale developments.

4.2.4. Influence of Tidal Regime

The influence of different tidal regimes on the response to extraction may be investigated by expanding the forcing to four harmonic constituents (M2, K1, S2, and O1). As discussed in Chapter 1, depending on the relative amplitudes of the constituents, the resulting tidal signal is classified by the form factor (F) as semidiurnal, mixed mainly semidiurnal, mixed mainly diurnal, or diurnal. In this section, the elevation time series shown in Figure 1.2 has been calibrated such that the power density in segment 2 is approximately equal for all four regimes (2.5 kW/m^2). The network geometry is as described in Table 4.1 and the baseline tidal regime for each case is quantified in Appendix 5. With increasing diurnal character, greater amplitude is required in order to achieve the same power density. All else being equal, tides with longer periods generate slower currents. The frequency of occurrence for speeds in each of these tidal regimes is shown in Figure 4.17. While all four regimes have the same time-averaged power density over the neap-spring cycle, with increasing diurnal character the mean and mode of the distribution move towards zero.

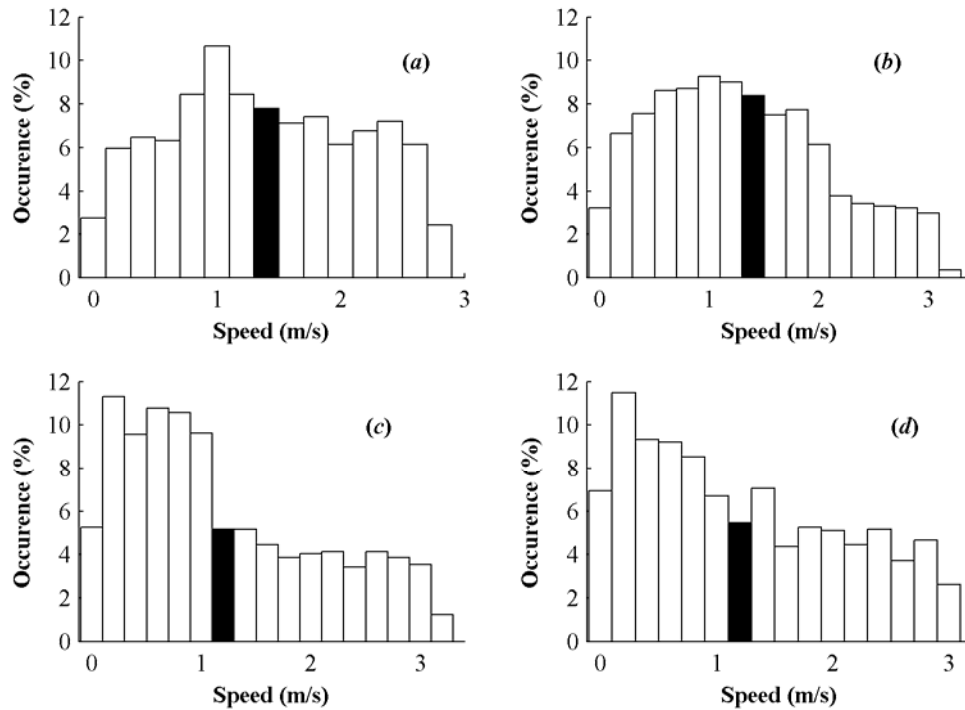


Figure 4.17 – Occurrence distribution of speeds for different tidal regimes. Black bar denotes mean speed. Speed is reported for the entrance to segment 2 (constricted). (a) semidiurnal ($F=0.1$), (b) mixed, mainly semidiurnal ($F=0.9$), (c) mixed, mainly diurnal ($F=2.3$), (d) diurnal ($F=4.7$).

Over the fortnightly neap-spring cycle, the difference in instantaneous power density between these regimes is particularly striking, as shown in Figure 4.18. As the diurnal character of the tide increases, the lulls between periods of high power density are extended. In a diurnal regime, devices with a cut-in speed will sit idle for longer periods of time and, therefore, have a lower capacity factor. For the representative tidal regimes considered here, a device with a cut-in speed of 0.8 m/s would operate ~75% of the time in a semidiurnal regime, but less than 60% of the time in a diurnal regime. This would negatively impact project economics because, while both sites may produce the same average power on an annual basis, the equipment for the diurnal site will need to be rated to produce power in more intense, intermittent bursts. This is also indicated by Figure 4.18, where the peak kinetic power density for the semidiurnal regime is lower than for the diurnal regime, even though both regimes have the same average kinetic power density. Because of this, and the infrequency of sites with large diurnal tides, most commercial interest is in sites with semidiurnal or mixed, mainly semidiurnal regimes [11].

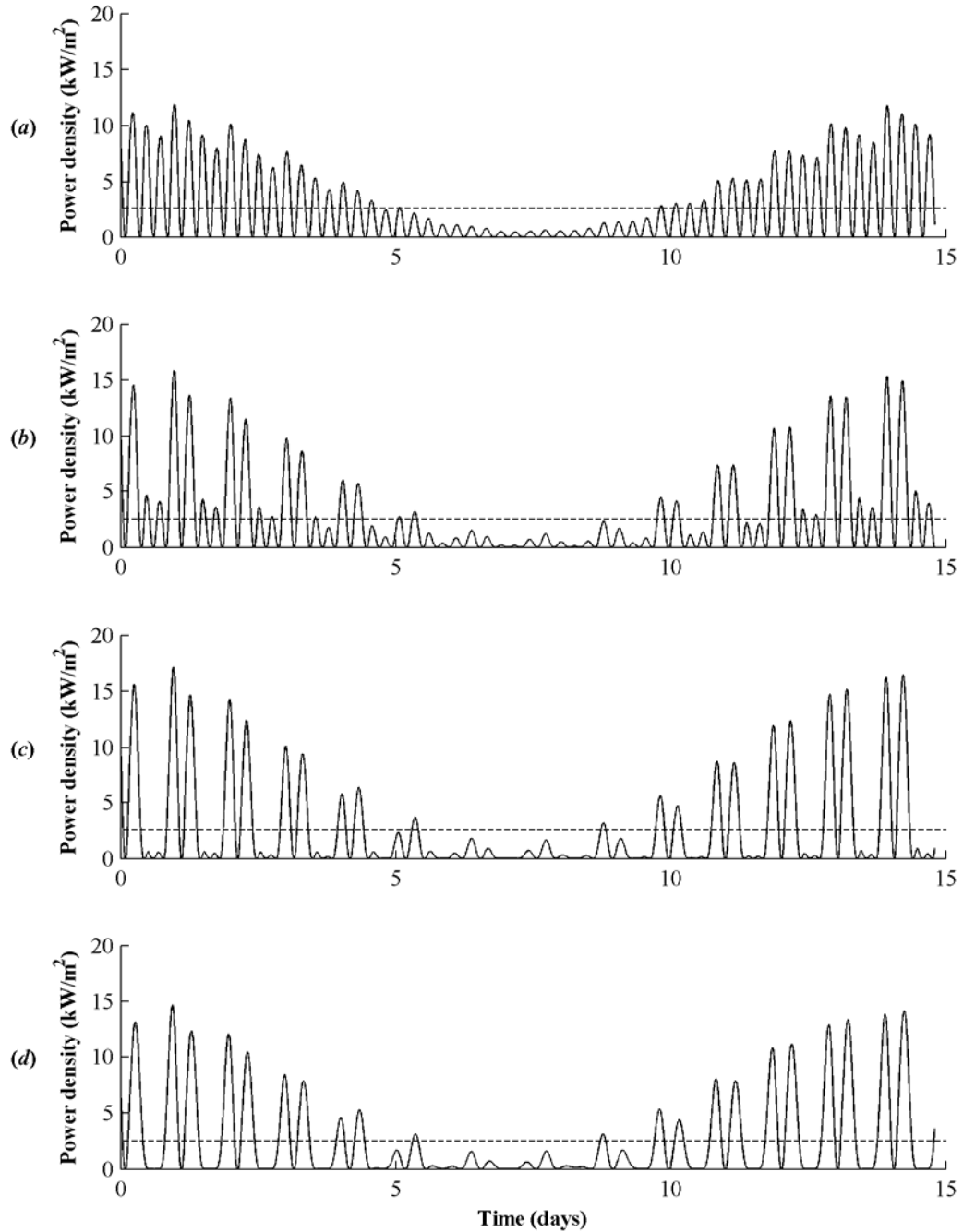


Figure 4.18 – Power density time series for four tidal regimes. The dashed line is the average over a 14.8 day neap-spring cycle (2.5 kW/m^2 for all cases). (a) semidiurnal ($F=0.1$), (b) mixed, mainly semidiurnal ($F=0.9$), (c) mixed, mainly diurnal ($F=2.3$), (d) diurnal ($F=4.7$).

In order to simplify the visualization of results, the far-field effects for all cases are quantified for a single, reference dissipation of 300 MW. This is representative of a very large array for which P/P_{\max} is appreciable and extraction effects are readily apparent. The response of each of the four tide constituents at the reference dissipation is shown in Figure 4.19. The relative change in the amplitude and phase of each constituent is relatively similar for each tidal regime and trends by segment are identical to those observed for a single-constituent forcing in the same network. However, the relative reductions in semidiurnal constituents (M2 and S2) are more than twice those of the diurnal constituents (K1 and O1). This implies that power is being primarily extracted at semidiurnal frequencies, which is consistent with semidiurnal frequencies producing the highest velocities.

The response of the currents shows the same trends, as presented in Figure 4.20.

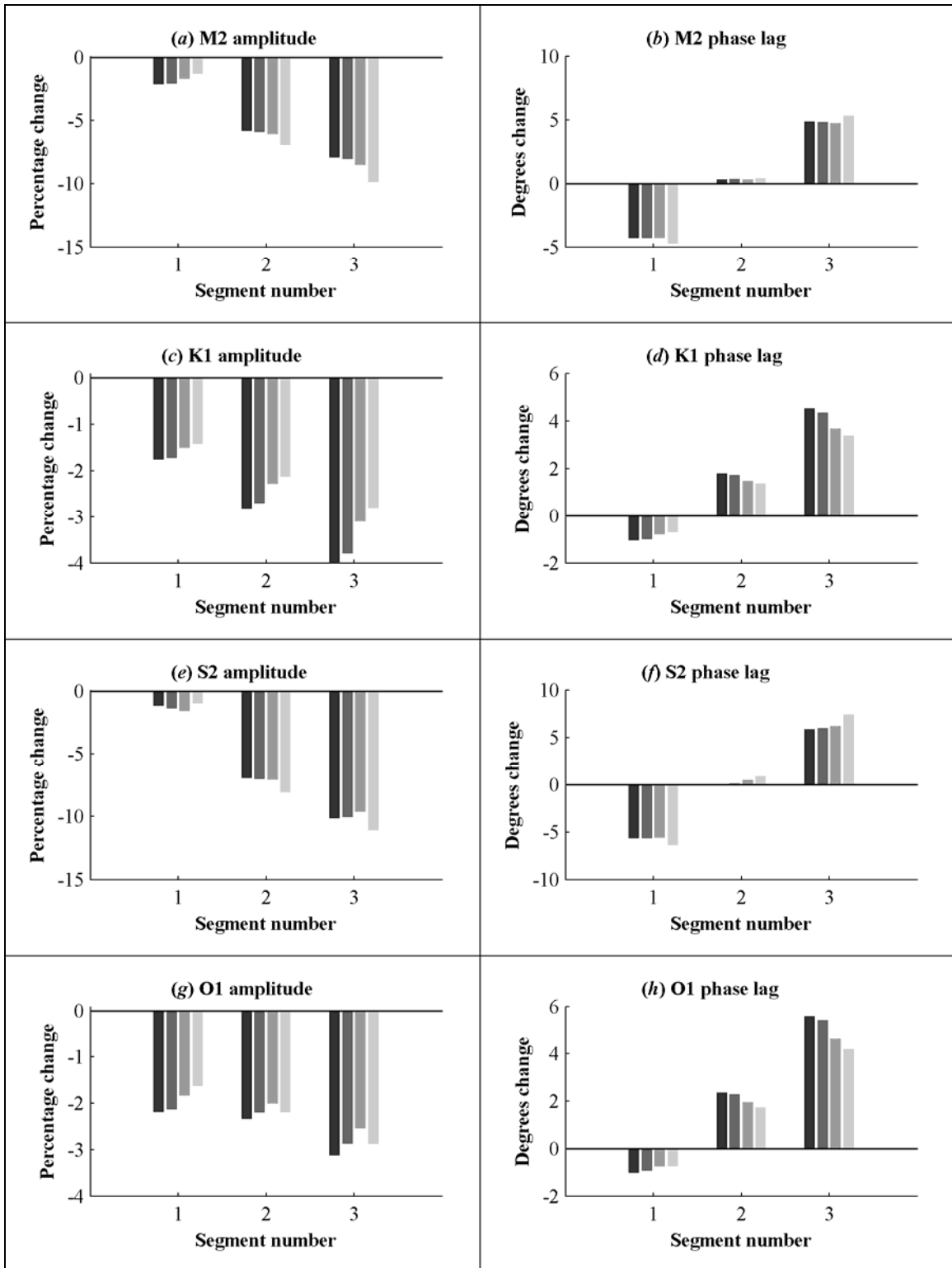


Figure 4.19 – Tide constituent response to 300MW turbine dissipation in a single constriction network for four tidal regimes. Regimes from darkest to lightest (left to right): semidiurnal, mixed mainly semidiurnal, mixed mainly diurnal, diurnal. For these regimes, 300 MW corresponds to $0.2 \leq P/P_{\max} \leq 0.4$.

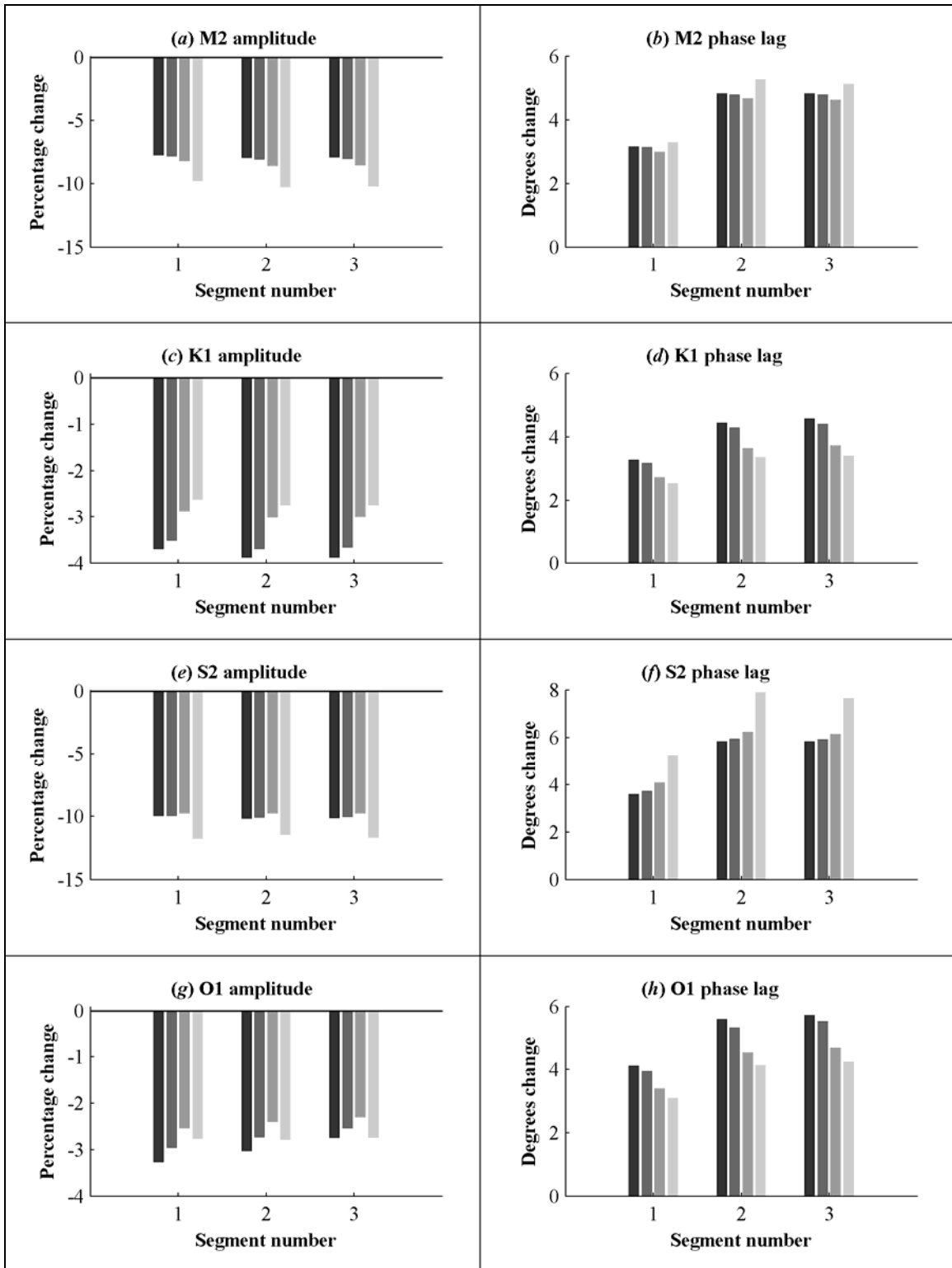


Figure 4.20 – Current constituent response to 300MW turbine dissipation in a single constriction network for four tidal regimes. Regimes from darkest to lightest (left to right): semidiurnal, mixed mainly semidiurnal, mixed mainly diurnal, diurnal.

Relative changes to total transport and kinetic power density are plotted against non-dimensional turbine dissipation (P/P_{\max}) in Figure 4.21. In both cases, the non-dimensional response is equivalent between tidal regimes.

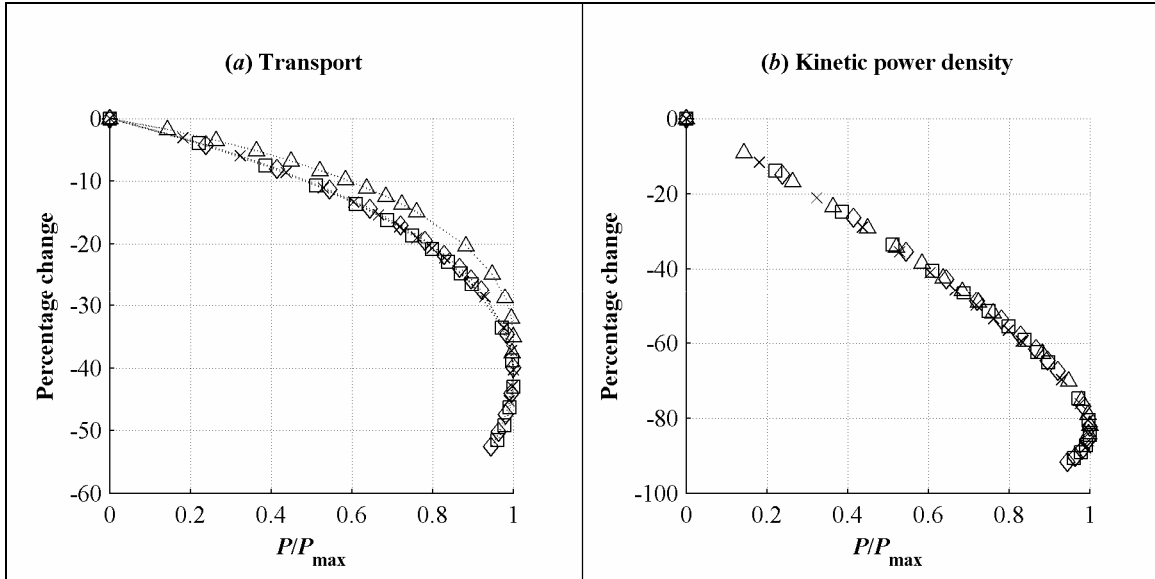


Figure 4.21 – Non-dimensional response to turbine dissipation in a single constriction network for four tidal regimes. \diamond semidiurnal, \square mixed mainly semidiurnal, \triangle mixed mainly diurnal, \times diurnal.

Garrett and Cummins [20] propose a correction factor to the analytical relation for maximum turbine dissipation (4.36) when the forcing includes multiple tidal constituents. For cases in which losses in the constricted channel are dominated by friction, this factor (R) is given by

$$R = 1 + \frac{9}{16} (r_1^2 + r_2^2 + \dots + r_n^2), \quad (4.40)$$

where r_n is the ratio of the amplitude of the n^{th} constituent to the amplitude of the dominant constituent (M2 for semidiurnal regimes, K1 for diurnal). $P_{\max, \text{theory}}$, as computed by (4.36) for the dominant constituent, is then multiplied by this factor to account for the effect of multiple constituents. However, this correction is intended for use only for a phase driven tide between two infinite bodies of water and the authors recommend caution when it is applied to other dynamic systems [54]. This concern appears justified since the comparison between the theoretical and model predictions for P_{\max} is relatively poor, as shown in Table 4.4.

Also, as shown in Table 4.4, all other factors being equal, the maximum dissipation increases with the diurnal character of the tide. This presents an economic trade-off, since while it may be

possible to extract more power from a diurnal regime, the cost of energy also increases with diurnal character due to lower capacity factors.

Table 4.4 – Comparison between theoretical and model predictions for maximum turbine dissipation under four tidal regimes (single constriction network).

Tidal regime	R	$\frac{P_{\max,\text{model}}}{P_{\max,\text{theory}}}$	$P_{\max,\text{model}}$ (MW)
Semidiurnal	1.15	1.19	800
Mixed, mainly semidiurnal	1.59	1.02	860
Mixed, mainly diurnal	1.15	1.13	1100
Diurnal	1.18	1.44	1400

4.2.5. Influence of Turbine Dynamics

Analysis up to this point has involved devices without rated or cut-in speeds. Such a device would extract power in proportion to the kinetic power incident over the rotor swept area for all possible water speeds (Regime II in Figure 1.3). Practical devices will not extract power until the currents have reached a minimum value ($u_{\text{cut-in}}$) and will extract constant power above a maximum speed (u_{rated}). Device inertia and internal friction determine $u_{\text{cut-in}}$. The rated speed is chosen to optimize a device for the lowest cost of energy. The optimized rated speed depends on the tidal regime for a particular site [7]. As discussed previously, the following assessment is representative of devices with variable pitch rotors.

The velocity profile in the constricted channel and the power dissipated by turbines with $u_{\text{cut-in}} = 0.7$ m/s and $u_{\text{rated}} = 1.75$ m/s is shown in Figure 4.22. The tidal forcing is by a single constituent (M2). The effect of both nonlinearities on power dissipated by turbines is quite clear. Because the turbine cross-sectional area is defined in terms of the blockage ratio, the rated power changes slightly in time with the channel cross-section. These nonlinearities also result in a non-sinusoidal velocity time series because the resistance to flow varies with the stage of the tide as the turbines move through their three operating regimes (Figure 1.3). As a consequence, harmonic analysis of the M2 current is misleading as P approaches P_{\max} . The period of the currents does, however, remain constant (~ 12.42 hours), so the averaging window for transport and kinetic power density is unchanged from the approach described in Section 4.1.5. The tidal signal maintains its sinusoidal character and comparisons of the M2 tidal response between different levels of dissipation appear valid (Figure 4.22a).

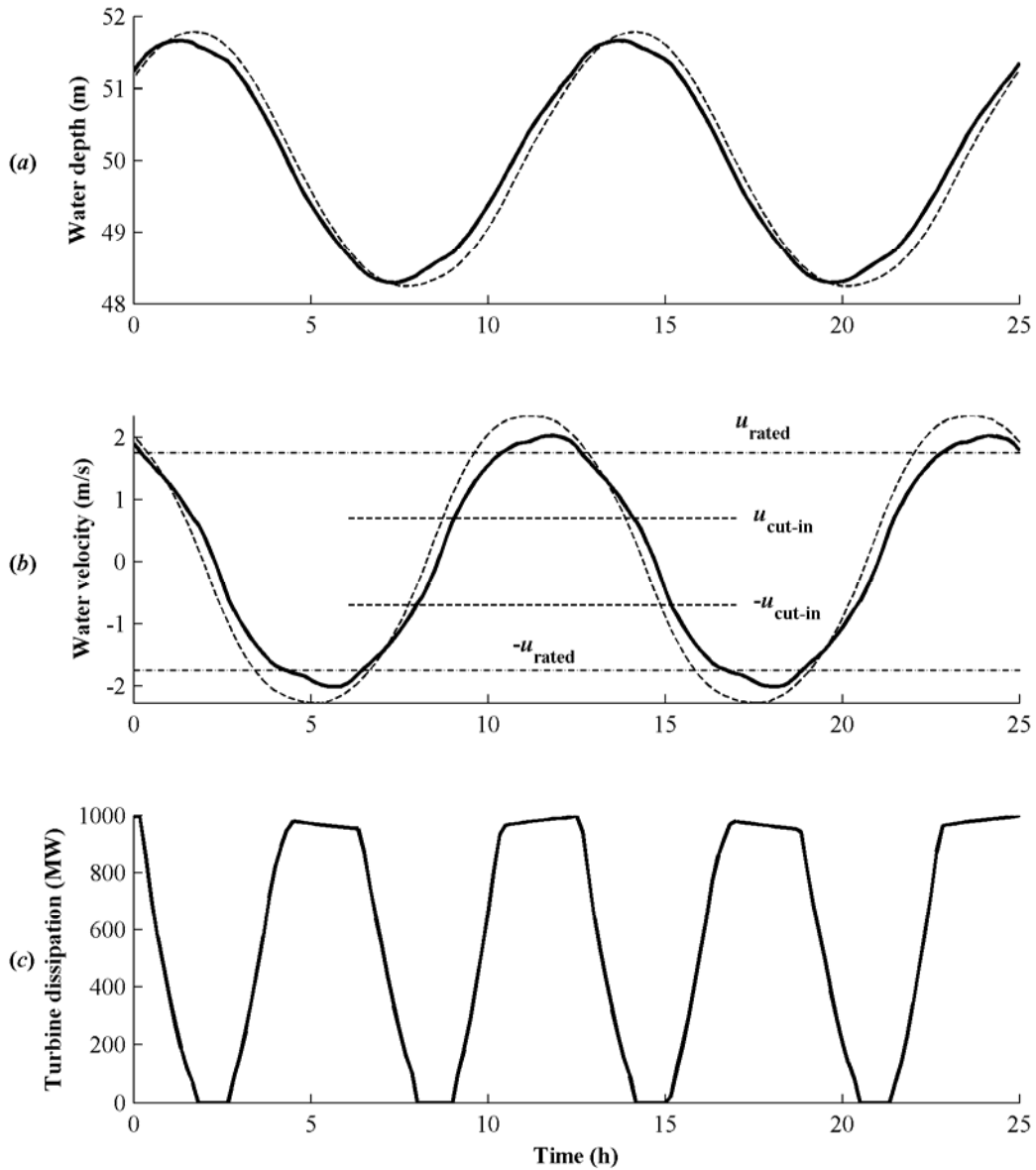


Figure 4.22 – Time series with power dissipation including turbine dynamics. Solid line: extraction by rows of turbines. Dashed line: no extraction. (a) water depth at constriction inlet, (b) water velocity at constriction inlet, (c) power dissipated by turbine transects.

As shown in Figure 4.23, up to $P/P_{\text{max}} = 0.6$, the inclusion of either rated or cut-in speed has very little influence on the relative changes to tides (a) or kinetic power density (b). These nonlinearities do alter the relative change in transport by $\sim 2\%$ (c). When either nonlinearity is included, less kinetic power is extracted by each row of turbines since both nonlinearities restrict

power extraction to a smaller range of velocities. The inclusion of the cut-in speed reduces far-field impacts. The cut-in speed allows low velocity flow to pass unimpeded through the array. Because transport varies directly with velocity, while kinetic power varies with its cube, not extracting power below the cut-in speed does not greatly reduce the kinetic power extracted over the tidal cycle, but does reduce the environmental footprint of the array. The inclusion of rated speed somewhat increases the impact of extraction on transport, which may be explained in a similar manner. The relative influence of either nonlinear effect depends on the frequency distribution of velocities relative to the rated and cut-in speeds. For the cases shown in Figure 4.23, the velocity exceeds the rated speed for over 40% of the tidal cycle ($P/P_{\max}=0.6$), but is below cut-in for only 25%. As a result, the effect of the rated speed is greater than that of the cut-in speed.

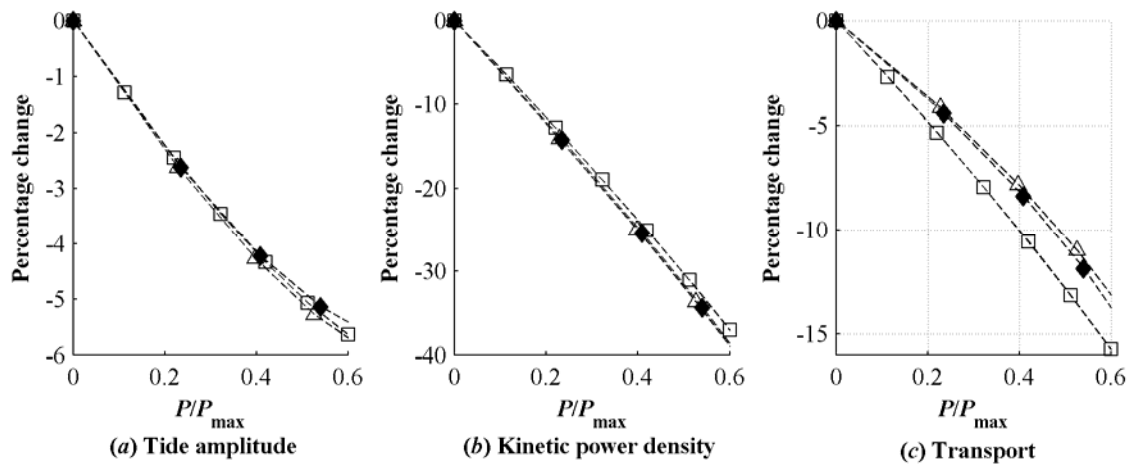


Figure 4.23 – Non-dimensional response to extraction up to $P/P_{\max} = 0.6$ including turbine dynamics. ◆ linear response, □ rated speed = 1.5 m/s, △ cut-in speed = 1.0 m/s. Response for all effects reported at inlet to constricted channel.

As extraction increases, the peak velocity decreases. This means that turbines spend less time in the rated regime with increasing levels of extraction (provided that the rated power being modeled is physically realistic). As a result, the influence of a rated speed declines as $P \rightarrow P_{\max}$. Therefore, P_{\max} is generally independent of rated speed, as shown in Figure 4.24. The cut-in speed does, however, continue to influence the effects of extraction up to P_{\max} and it is possible to dissipate slightly more power with a higher cut-in speed. However, since less power is extracted by each row of turbines as the cut-in speed increases, there is an economic disincentive for higher cut-in speeds.

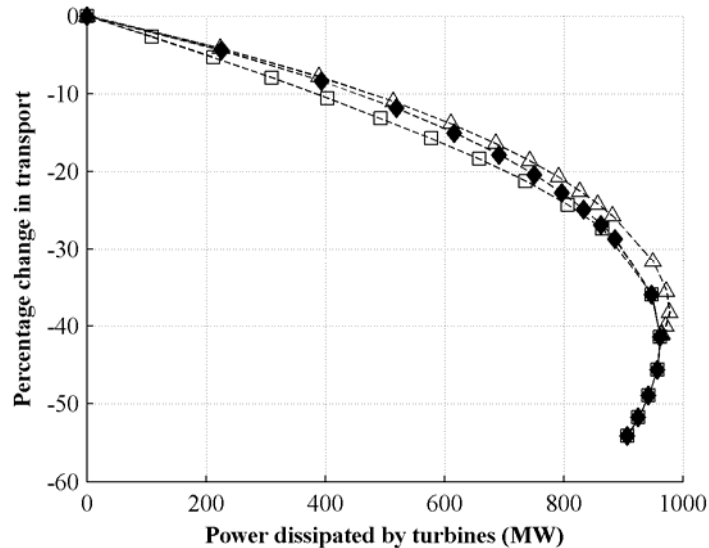


Figure 4.24 – Non-dimensional response to extraction including turbine dynamics. ◆ linear response, □ rated speed = 1.5 m/s, △ cut-in speed = 1.0 m/s.

For multiple tidal constituents, the behavior is similar and depends on the distribution of velocities relative to the rated and cut-in speeds. For example, the effect of a particular cut-in speed would be higher in a diurnal regime than a semi-diurnal regime of equal power density.

In general, the inclusion of device nonlinearity does not greatly alter the system response and will be neglected in subsequent modeling.

4.3. Summary

A one-dimensional channel model has been developed to study the far-field effects of kinetic power extraction. The model agrees well with the analytical theory proposed by Blanchfield et al. [14]. For a simple network consisting of a narrow channel connecting a large basin to the open ocean, kinetic power extraction is shown to reduce the tidal range, currents, transport, frictional dissipation, and kinetic power density. The reduction for a particular level of extraction depends on the geometry of the network and tidal forcing. Device dynamics also affect the response, but to a much lesser degree. The response is in proportion to the level of extraction. Low levels of extraction (e.g., $P/P_{\max} \rightarrow 0$), as would be the case for a pilot project, are unlikely to measurably alter tides or currents. As the number of turbines increases, there is a diminishing marginal benefit of extraction because of declining power density. That is to say, each additional turbine generates less power. As maximum dissipation is approached, the marginal increase in extraction for each additional turbine becomes uneconomically small. Since maximum dissipation is related to the maximum extractable resource by the ratio of extraction to dissipation for a particular array

(Chapter 2), this indicates that it is not practically possible to extract the maximum power from a potential in-stream site.

As a function of P/P_{\max} , the relative response of currents, as well as quantities principally derived from currents (e.g., kinetic power density), are equivalent for systems with different segment geometries. This is as predicted by theory. This equivalence extends to different tidal regimes and suggests that it may be possible to develop analytical predictions of P_{\max} under different regimes.

For a network consisting of a single constriction, the changes associated with kinetic power extraction may lead to a number of environmental impacts. The reduction in the tidal amplitude could alter shoreline ecosystems. For example, portions of mud flats could become either permanently submerged or exposed. Reduced currents could increase sediment deposition rates. Since frictional power dissipation serves as a proxy for mixing, a reduction in frictional dissipation could drive changes to dissolved oxygen, nutrients, and basic biological productivity. Again, while these effects are present at any level of extraction, as $P/P_{\max} \rightarrow 0$ the changes become undetectably small. However, to generate a practically useful amount of power generally requires $P/P_{\max} > 0.1$, at which point there will be measurable far-field effects associated with extraction. Of the effects quantified, it is not apparent by inspection which might have the greatest ecological impact. It is also not clear what relative change is required to have ecological significance. A determination of this will likely need to be made on a site-by-site basis.

5. Application of 1D Channel Model: Tidal Energy Extraction from Channel Networks

Chapter 4 investigated the influence of estuary geometry, tidal regime, and device dynamics on the system response with a single constriction connecting a basin to the sea. While this is a good prototype for a number of tidal energy sites (e.g., Massett Sound [14]), most sites involve a greater degree of complexity. In the United States, inventories have identified energetic currents in Cook Inlet and the southeast region of Alaska [55] (Figure 5.1), Puget Sound, Washington [56] (Figure 6.1), and the coast of Maine [57] (Figure 5.2). These are topographically complex networks, each with a number of possible sites and multiply-connected branches.

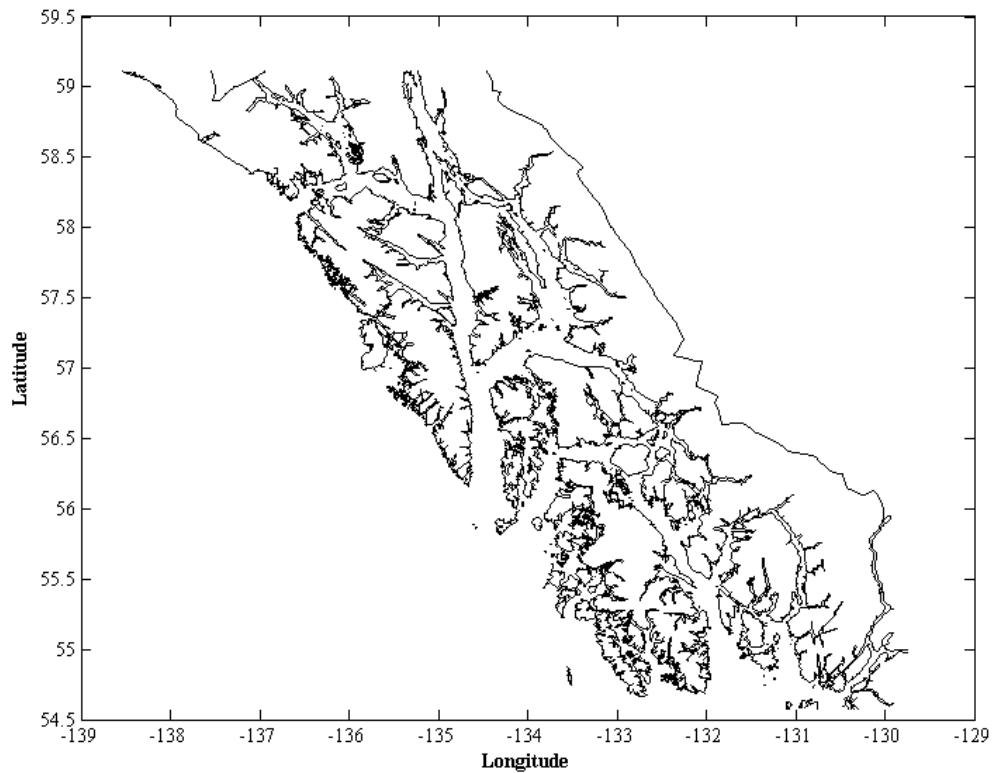


Figure 5.1 – Coastline for southeast region of Alaska [58].

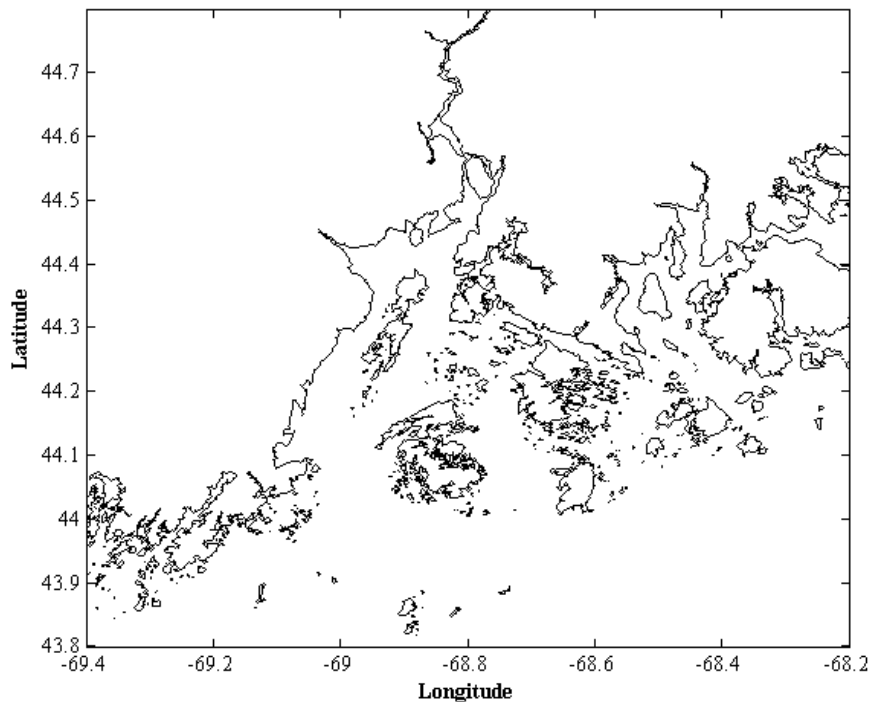


Figure 5.2 – Coastline for Penobscot Bay, coast of Maine [58].

In terms of resource assessment, it is desirable to calculate the theoretically extractable resource (related to maximum dissipation) for a site using only measurements of tidal regime, rather than modeling the response of the entire network to extraction. As shown in Chapter 4, this is possible to reasonable accuracy when the network consists of a single constriction using the analytical relations proposed by Blanchfield et al. [14,34] and Karsten et al. [12].

In this chapter, the 1D channel model is applied to idealized networks with three objectives:

- (1) To quantify the changes to the tidal regime due to in-stream energy extraction in terms of tides, currents, transport, power dissipation, and kinetic power density.
- (2) To determine if there are optimal distributions for turbines when there are multiple possible development sites in the same network.
- (3) To determine whether it is possible to determine the theoretically extractable resource from natural conditions.

Three prototypical networks are considered: a multiply-connected network for flow around an island, a network with two branches, and a network with serial constrictions. Schematics for these

channel networks and, as a point of reference, the single constriction network are presented in Figure 5.3. These networks consist of one or more channel segments connected by junctions that are either serial (1:1), divergent (1:2), or convergent (2:1). Energy may be extracted by in-stream turbines in constricted channel segments denoted by a resistive element. There are, therefore, three levels of variation considered here. The highest level is the topology of the network, which is shown schematically in Figure 5.3. The next level consists of networks with the same topology, but with different geometric properties for equivalent segments. The lowest level describes the extraction of kinetic power from different locations in a network with fixed topology and segment geometry.

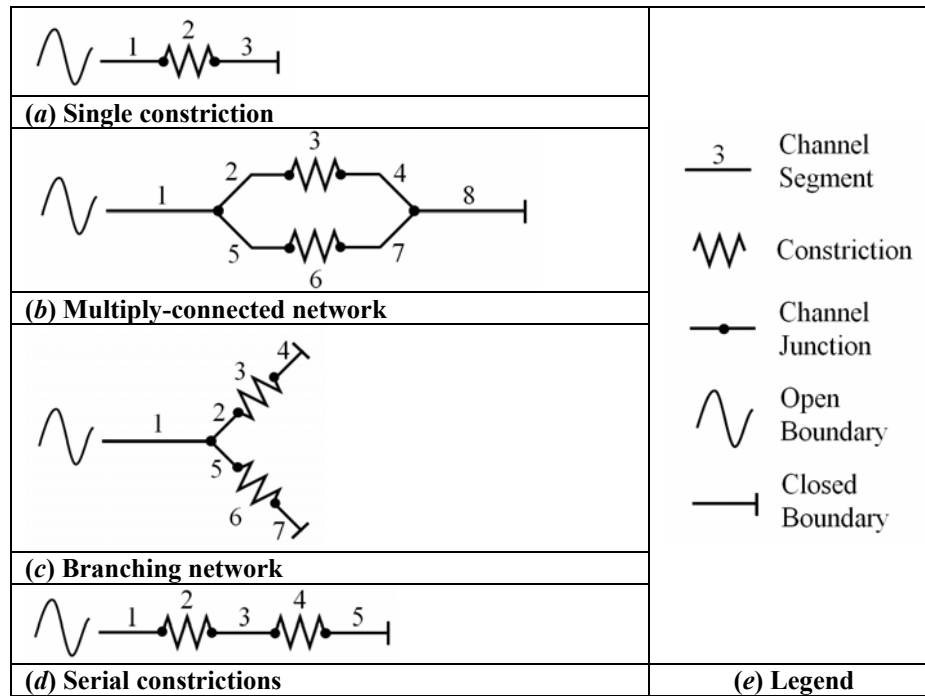


Figure 5.3 – Schematics of prototype channel networks. Segments are numbered as referenced in the text. Power may be extracted from segments which are denoted by a resistive element.

Since the focus of this investigation is on channel dynamics, the tidal forcing is limited to the M2 constituent and turbines are assumed to have no cut-in or rated speed. The methods for assessing far-field effects and calculating the power dissipated by turbines are as described for a single constriction network in Chapter 4. In order to simplify visualization of results in networks with up to eight segments, the far-field effects for all cases are quantified for a single, reference dissipation of 300 MW, which is representative of a very large array. For the networks modeled, 300 MW of dissipation corresponds to $0.3 \leq P/P_{\max} \leq 0.5$ and generally results in relative far-field changes on the order of 10-20% for tides and currents. As a point of comparison, the effects of

extraction on a single constriction network are shown in Figure 5.4. These results correspond to 300 MW of turbine power dissipation in Figure 4.5 (tides), Figure 4.8 (currents), Figure 4.11 (total power dissipated), and Figure 4.12 (kinetic power density). As discussed in Section 4.2.1, the change to total power dissipation in segment 2 includes both increased power dissipated by the turbine and decreased power dissipated by natural friction.

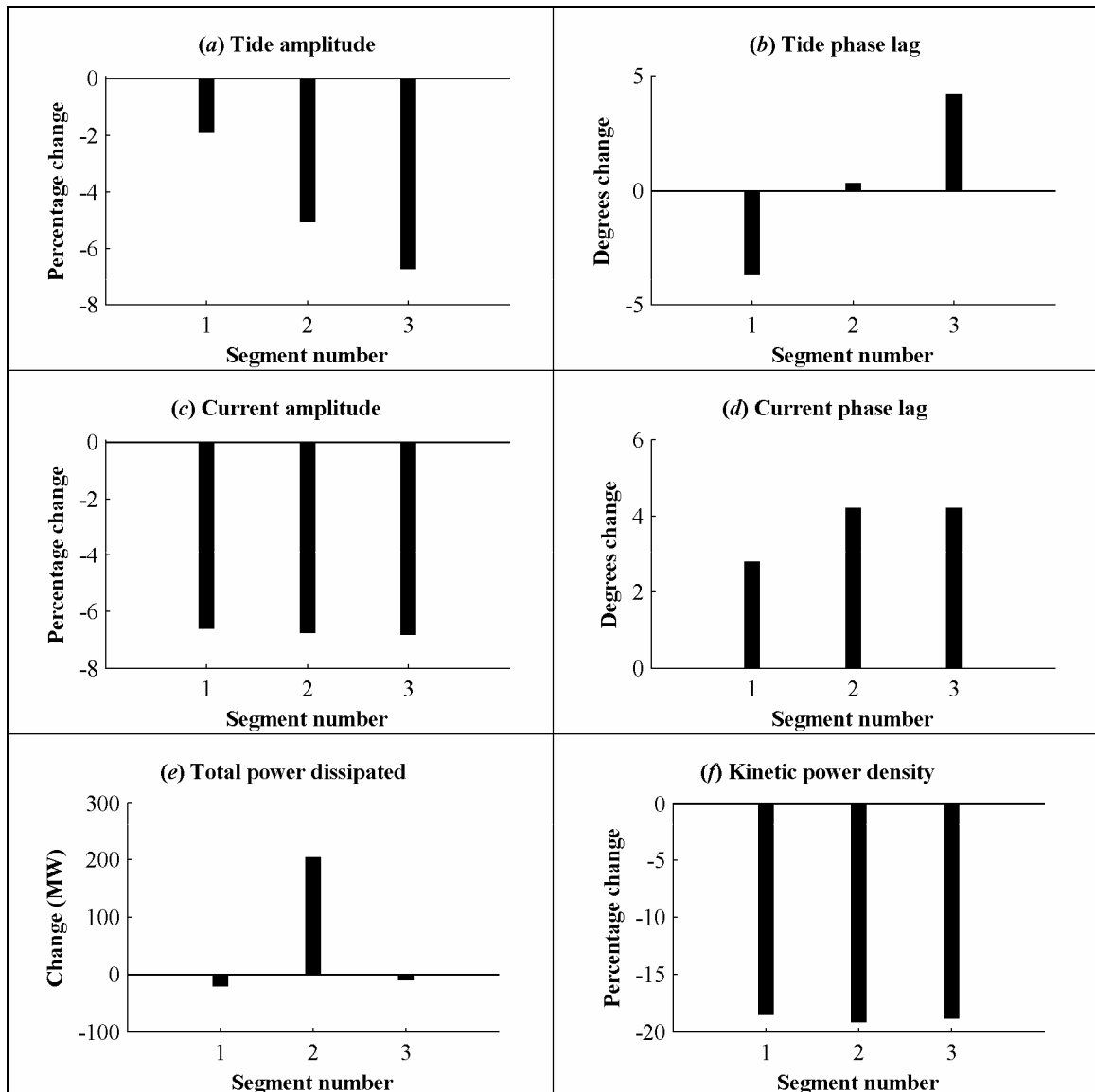


Figure 5.4 – Single constriction network response to 300MW turbine dissipation ($P/P_{\max} = 0.3$).

5.1. Multiply-Connected Networks

The prototype for a multiply-connected network is flow around an island, with each branch containing a constriction where power may be extracted (Figure 5.3*b*). Geometric properties for each channel segment are presented in Table 5.1, and the baseline tidal regime is listed in Appendix 5. The upper (segments 2-3-4) and lower (segments 5-6-7) branches are geometrically symmetric.

Table 5.1 – Baseline properties for multiply-connected network channel segments

Segment Description	1 Inlet	2	3 Upper Branch	4	5	6 Lower Branch	7	8 Basin
Length (L) (km)	40	40	5	40	40	5	40	80
Width (b) (km)	20	10	2	10	10	2	10	20
Depth (H) (m)	50	50	50	50	50	50	50	50
Manning roughness (n)	0.035	0.035	0.035	0.035	0.035	0.035	0.035	0.035
Forcing amplitude (m)	2.0							

The system's response to extraction is shown in Figure 5.5. Two distributions of turbines are considered – one in which all turbines are located only in segment 3 (upper branch) and one in which turbines are evenly distributed between the two branches. When power is extracted from only one branch, the flow adjusts to the path of least resistance and the velocity increases in the other branch. When extraction is evenly distributed between branches, the resistance to flow is the same in each branch and the system response is dynamically equivalent to that of a single constriction network. In both cases, the frictional resistance in the network increases, so less total flow enters the system (segment 1). Recall that the relative changes to currents and transport are nearly identical, as discussed in Section 4.2.1.

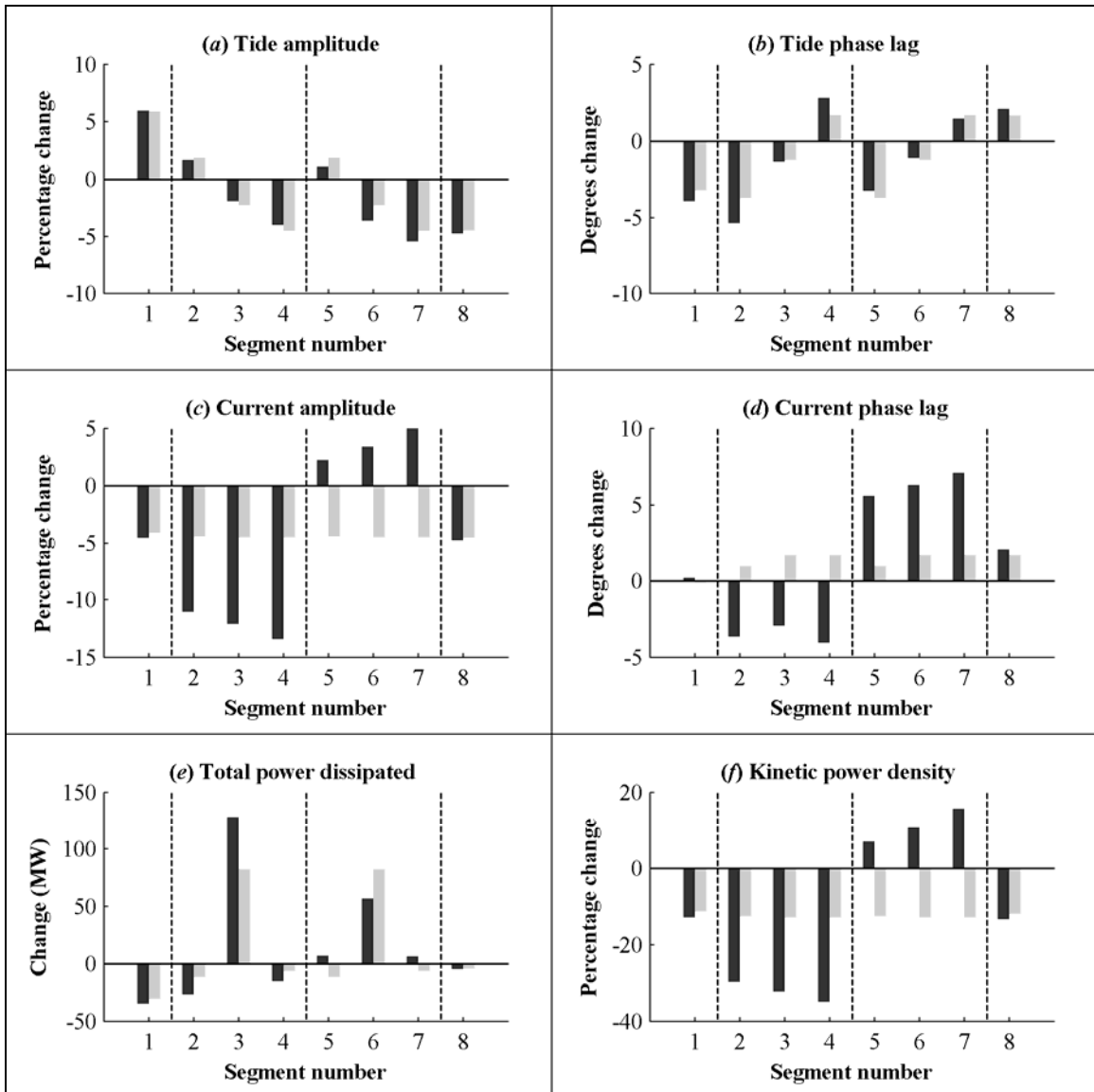


Figure 5.5 – Multiply-connected network response to 300MW turbine dissipation. Black bars denote a case in which power is extracted only from segment 3 ($P/P_{max} = 0.5$). Grey bars denote a case in which power extraction is evenly distributed between segments 3 and 6 ($P/P_{max} = 0.4$).

When power is extracted only in segment 3, the following changes to the tidal regime are observed (Figure 5.5, black bars):

- (1) Tides: Seaward of the constricted channels in both branches, the amplitude of the tide increases and the phase lag decreases. In both constricted channels, the amplitude and phase lag decrease. The amplitude decrease is more pronounced in the branch without extraction (segments 5-6-7). The amplitude augmentation in segment 1 (inlet) is on the same order as the amplitude decrease in the terminal basin.

- (2) Currents: Because turbine extraction in segment 3 (upper branch) increases resistance to flow in that branch, flow is redirected into the lower branch, with current amplitude increasing and phase lag decreasing. Currents are reduced in the branch with extraction and, to a lesser extent, in the inlet and terminal basin.
- (3) Total power dissipated: Because of flow redirection, the velocity increases in the lower branch, resulting in greater frictional power dissipation. In the inlet, upper branch, and terminal basin, frictional power dissipation decreases as a consequence of reduced velocity. However, in the constricted channel of the upper branch, the total power dissipation increases because the decline in frictional dissipation is eclipsed by the turbine dissipation.
- (4) Kinetic power density: Also because of flow redirection, the kinetic power density in the lower branch increases. Elsewhere in the system, the kinetic power density declines as a consequence of reduced velocity.

When extraction is distributed between the two branches, the change in each branch is identical and the dynamics are equivalent to a single constriction network.

Intuitively, one would expect a “penalty” of sorts as a consequence of flow redirection. This hypothesis is tested by comparing performance between evenly distributed extraction, in which there is no redirection, and extraction in only one branch. As shown in Figure 5.6, without flow redirection, the maximum dissipation (P_{\max}) is 20% higher. Further, as seen in Figure 5.5, for a given level of dissipation, velocity-related far-field effects are minimized when dissipation is evenly distributed. However, it may not be practical to evenly distribute dissipation between branches. First, existing navigational traffic or fish/marine mammal migration corridors may restrict the area available for in-stream development. Second, branches could be sufficiently asymmetric that currents could not economically support in-stream turbines in both locations. Fortunately, as previously observed by Couch and Bryden [60], it is still possible to extract considerable power when turbines are located only in one branch and the far-field effects are quite similar up to $P/P_{\max, \text{optimal}} \approx 1/2$, as shown in Figure 5.6.

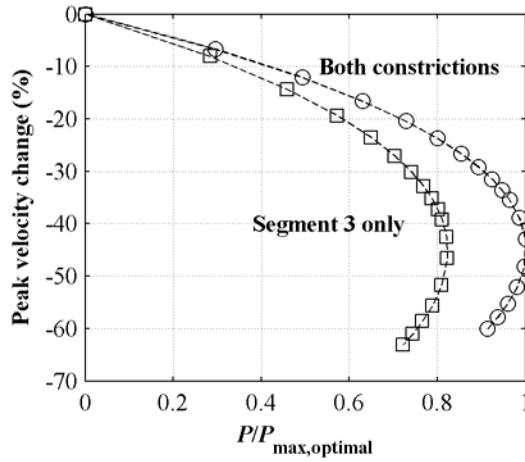


Figure 5.6 – Effect of redirection in multiply-connected networks. Change in current amplitude is measured in segment 3 (upper constriction). □ denotes extraction only from segment 3 (upper branch). ○ denotes equal extraction from segments 3 and 6 (both branches).

In modeling the Johnstone Strait, Sutherland et al. [13] have previously demonstrated that the theoretical prediction for maximum power (4.36) is not valid for multiply-connected networks. This is not surprising, since the dynamics underlying the theory do not allow for flow redirection. As for the single constriction network, a number of perturbations about the base geometry are investigated (Table 5.2) for this network topology. Non-dimensional extraction effects are equivalent only for the branch of the network with extraction (Figure 5.7a). In other segments, non-dimensional effects vary with segment geometry, as shown for the terminal basin in (b).

Table 5.2 – Multiply-connected network geometries

Case	Variation	Symbol (Figure 5.7)
M1	Base case	◇
M2	$L_8 = 60\text{km}$	△
M3	$L_8 = 100\text{km}$	□
M4	$b_{3,6} = 1.5\text{km}$	◁
M5	$b_{3,6} = 2.5\text{ km}$	▽
M6	$b_6 = 10\text{km}$	*
M7	$H_{\text{all}} = 30\text{m}$	▷
M8	$H_{\text{all}} = 70\text{m}$	o

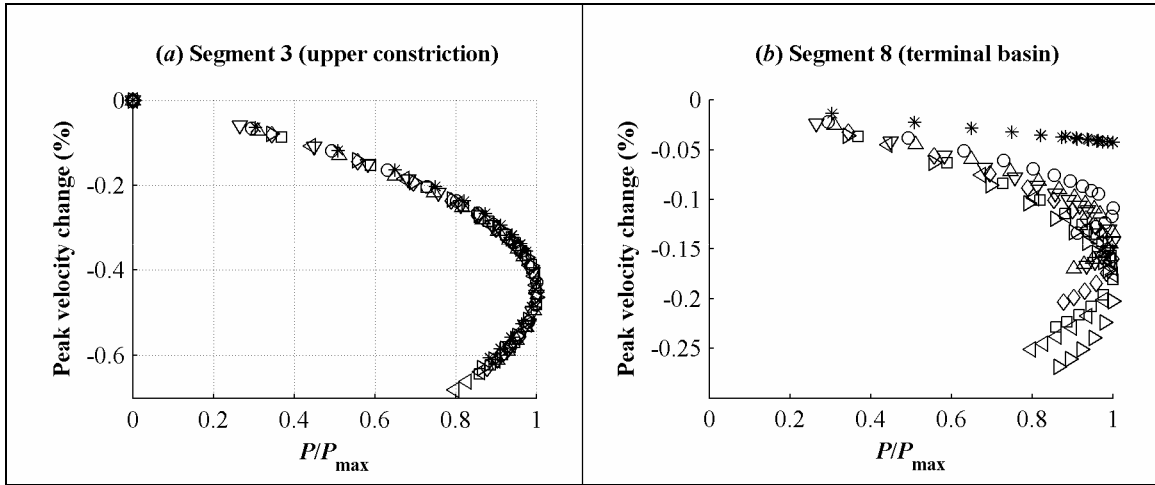


Figure 5.7 – Non-dimensional response to dissipation for multiply-connected networks. Panels show the response in different segments. Symbols relate to a particular geometry identified in Table 5.2. Extraction is only from segment 3 (upper constriction).

5.2. Branching Networks

In a branching network, the main flow bifurcates, but does not converge at a downstream location (Figure 5.3c). Geometric properties for each channel segment are presented in Table 5.3 and the baseline tidal regime is listed in Appendix 5. The upper branch (segments 2-3-4) and lower branch (segments 5-6-7) are symmetric for the baseline geometry.

Table 5.3 – Baseline properties for branching network channel segments

Segment Description	1 Inlet	2	3 Upper Branch	4	5	6 Lower Branch	7
Length (L) (km)	40	40	5	80	40	5	80
Width (b) (km)	20	10	1.5	10	10	1.5	10
Depth (H) (m)	50	50	50	50	50	50	50
Manning roughness (n)	0.035	0.035	0.035	0.035	0.035	0.035	0.035
Forcing amplitude (m)	2.0						

The response of the branching network to extraction is shown in Figure 5.8. As for the multiply-connected network, results are presented for the cases of turbines in only one branch and turbines evenly distributed between the two branches. Some redirection is observed, but it is less pronounced than in the multiply-connected network since each branch is not connected to a common terminal basin. For the case in which power is extracted only in segment 3, the following changes to the tidal regime are observed:

- (1) Tides: Landward of the upper constriction (segment 3), the amplitude of the tide decreases and the phase lag increases. Elsewhere in the network, the amplitude of tide increases and the phase lag decreases. The increase in amplitude and decrease in phase

lag in the branch without turbines (segments 5-6-7) is relatively small. This is consistent with the results of Karsten et al. [12] results for the Minas Passage is a dynamically similar network.

- (2) Currents: The increased resistance to flow decreases currents and increases the phase lag in the upper branch (segments 2, 3, and 4) and in the inlet to the system (segment 1). There is a minor augmentation of currents in the lower branch caused by the increased tidal range adjacent to the branching point.
- (3) Total power dissipated and kinetic power density: Changes to dissipated power and kinetic power density are directionally similar to changes in the current amplitude, which is as expected. For example, diversion of flow into the lower branch somewhat increases total power dissipation.

When extraction is evenly distributed between the two branches, the change in each branch is identical and the dynamics are equivalent to a single constriction network.

Figure 5.9 compares the effects of even and uneven turbine dissipation. As for the multiply-connected network, power dissipation is maximized when extraction is evenly distributed between the branches. Since redirection is less pronounced than in multiply-connected networks, the penalty associated with a non-optimized distribution is also less severe. The maximum dissipation is only 14% higher when redirection is eliminated and velocity-related far-field effects are comparable up to $P/P_{\max, \text{optimal}} \approx 3/4$.

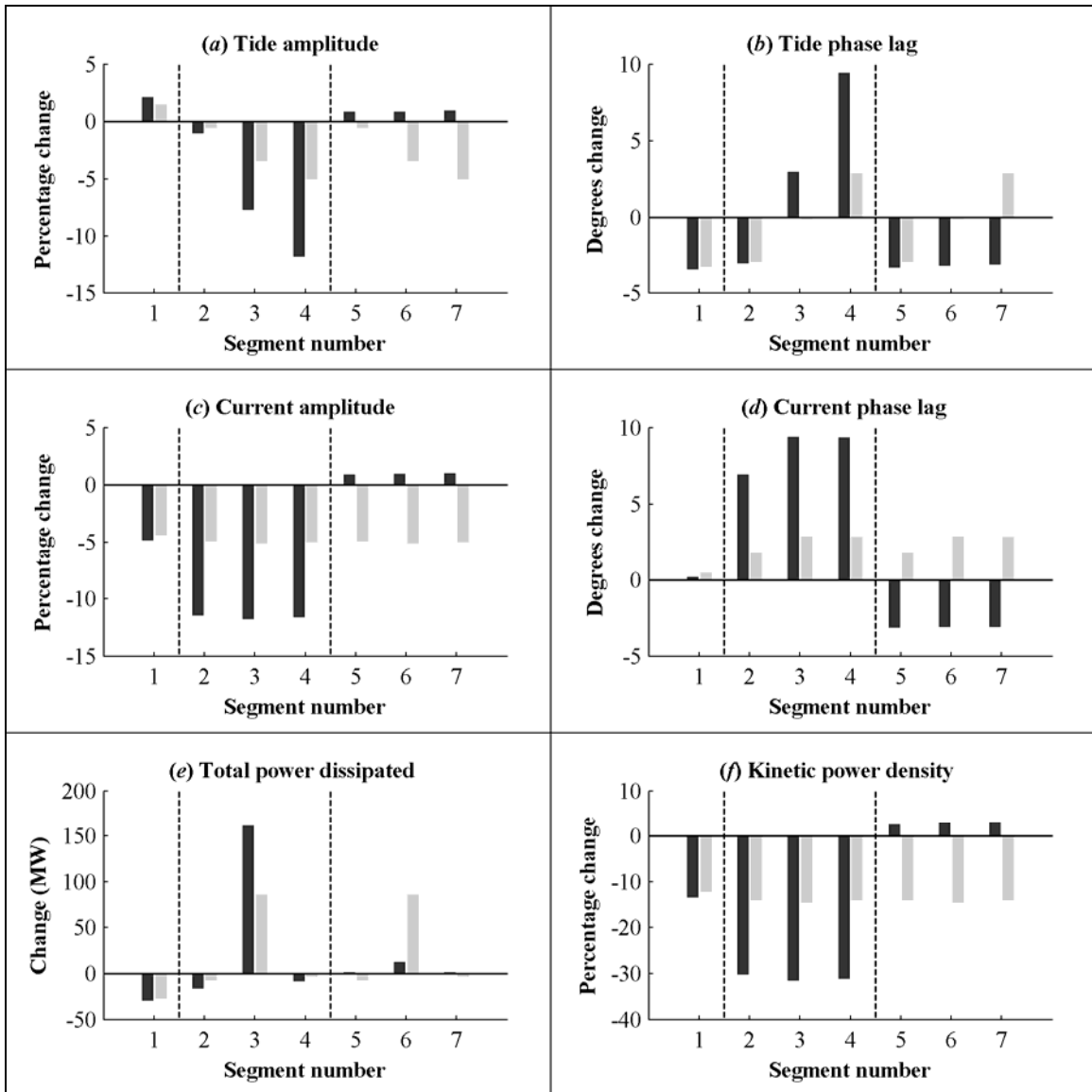


Figure 5.8 – Branching network response to 300MW turbine dissipation. Black bars denote a case in which power is extracted only from segment 3 ($P/P_{\max} = 0.5$). Grey bars denote a case in which power extraction is evenly distributed between segments 3 and 6 ($P/P_{\max} = 0.5$).

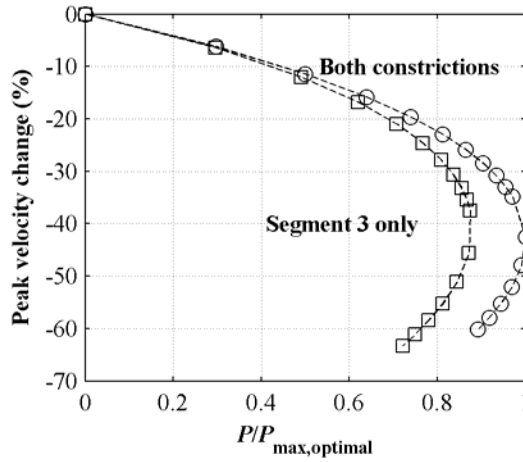


Figure 5.9 – Effect of redirection in branching networks. Change in current amplitude is measured in segment 4 (upper basin). □ denotes extraction only from segment 3 (upper branch). ○ denotes equal extraction from segments 3 and 6 (both branches).

In their investigations of extraction effects in the Minas Passage, Karsten et al. [12] have shown that the theoretically predicted maximum dissipation (4.36) somewhat overpredicts the modeled P_{\max} . This is ascribed to the reduction in tidal amplitude seaward of the constriction, which is not allowed by the theory. Model simulations for perturbations about the geometric base case show similar results, with the variation between modeled and theoretical predictions for P_{\max} closely correlated with the change in amplitude, as shown in Table 5.4. For the same reason, the theory also underpredicts P_{\max} when extraction is optimized between branches (case B1*), since a stronger restorative forcing is set up when there is no redirection.

Table 5.4 – Comparison between theoretical and model predictions for maximum possible turbine dissipation (branching network). Power is extracted only from segment 3 unless otherwise noted.

Case	Variation	Symbol (Figure 5.10)	γ	$\frac{P_{\max, \text{model}}}{P_{\max, \text{theory}}}$	$\frac{\zeta_{0, \max}}{\zeta_{0, \text{initial}}}$
B1	Base case	◇	0.20	0.99	0.97
B1*	Base case		0.20	1.13	1.06
B2	$L_4 = 60\text{km}$	△	0.21	0.95	0.95
B3	$L_4 = 100\text{km}$	□	0.20	1.07	1.02
B4	$b_3 = 1\text{km}$	◁	0.19	1.07	1.02
B5	$b_6 = 2\text{km}$	▽	0.21	0.95	0.95
B6	$b_6 = 10\text{km}$	*	0.20	1.03	0.99
B7	$H_{\text{all}} = 30\text{m}$	▷	0.19	1.16	1.10
B8	$H_{\text{all}} = 70\text{m}$	○	0.22	0.97	0.95

* power extracted evenly from segments 3 and 6

As shown in Figure 5.10, non-dimensional changes to currents are nearly equivalent in the branch with extraction (a), but not in the other branch (b) or system inlet.

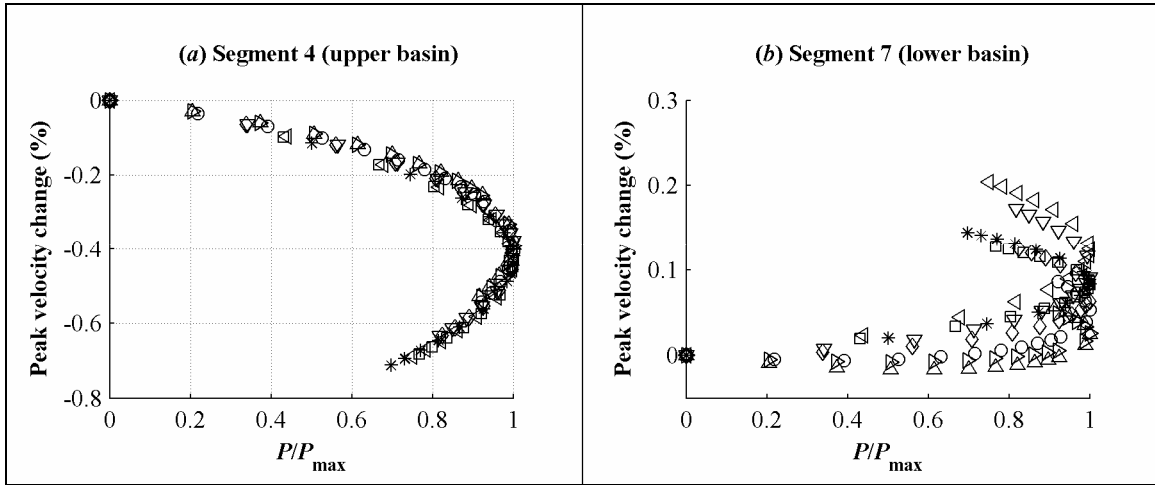


Figure 5.10 – Non-dimensional response to dissipation for branching networks. Panels show the response in different segments. Turbines extract power only from segment 3. Symbols relate to a particular geometry identified in Table 5.4.

5.3. Serial Constriction Networks

The final network considered consists of multiple constrictions in series. The prototype for this network (Figure 5.3*d*) has two constrictions, but these results extend to networks with additional serial constrictions. Geometric properties for each channel segment are presented in Table 5.5 and the baseline tidal regime is listed in Appendix 5.

Table 5.5 – Baseline properties for serial constriction network channel segments

Segment Description	1 Inlet	2 Seaward Constriction	3 Intermediate Basin	4 Landward Constriction	5 Terminal Basin
Length (L) (km)	40	5	60	5	80
Width (b) (km)	10	2.2	10	1.5	10
Depth (H) (m)	50	50	50	50	50
Manning roughness (n)	0.035	0.035	0.035	0.035	0.035
Forcing amplitude (m)	2.1				

Extraction effects are shown in Figure 5.11 for the case in which power is extracted from *either* the seaward constriction (black bars) or landward constriction (grey bars). When power extracted from both locations (not shown), the effect is an amalgam of the two extremes. This is considered in more detail in Chapter 6 for serial constrictions in Puget Sound, Washington. The response shown in Figure 5.11 is analogous to the response of a single constriction network in terms of the response landward and seaward of the segment with extraction. However, the effects of extracting power from segment 4 are more pronounced than for the same level of extraction in segment 2.

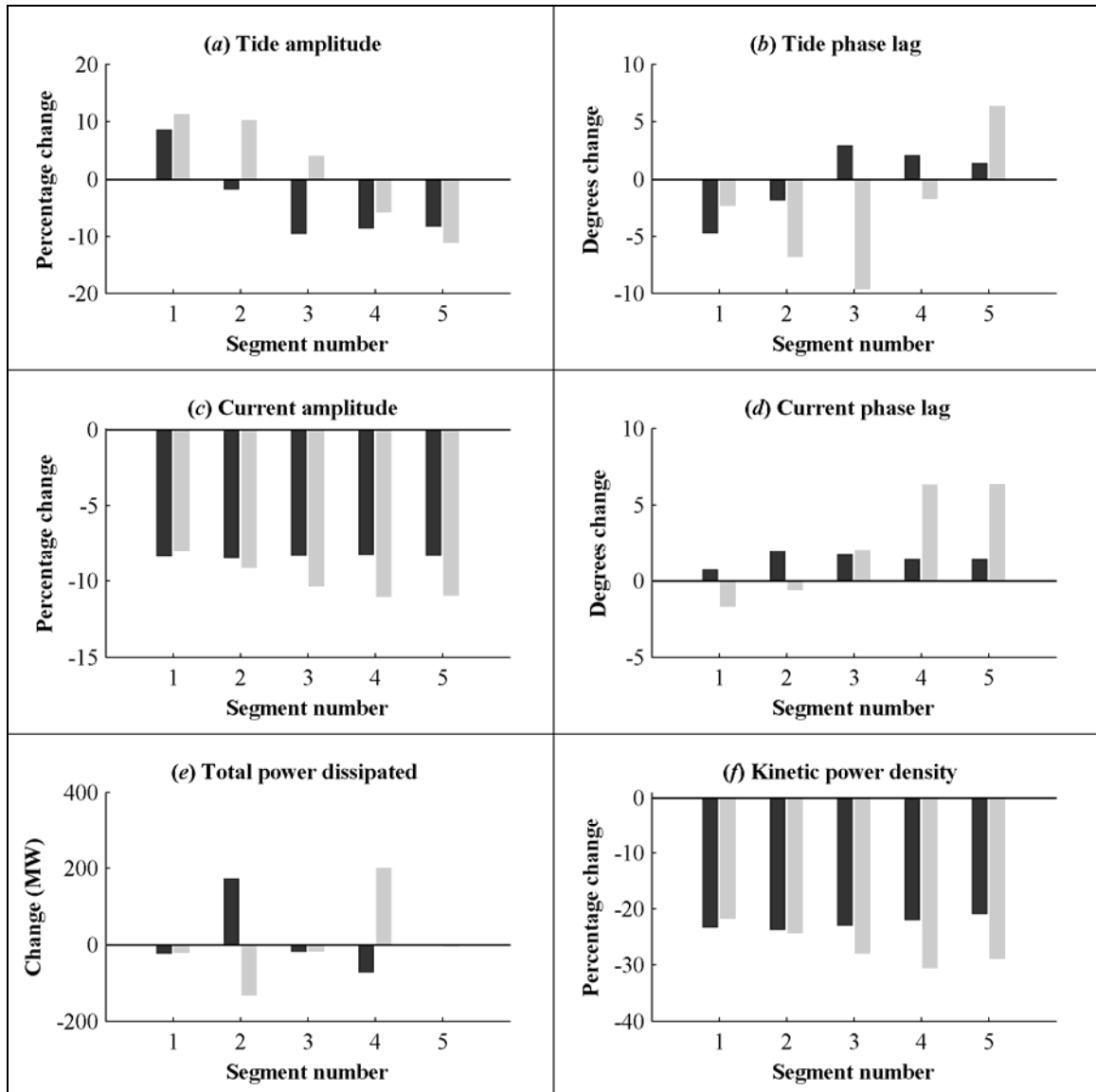


Figure 5.11 – Serial constriction network response to 300MW turbine dissipation. Black bars denote a case in which power is extracted only from segment 2 ($P/P_{\max} = 0.4$). Grey bars denote a case in which power is extracted only from segment 4 ($P/P_{\max} = 0.5$).

Intuitively, since there is no flow redirection, one might expect that theory (4.36) would accurately predict P_{\max} . However, as shown in Table 5.6, this is not the case and the theory underpredicts P_{\max} by at least 25%. In the table, γ^* is the value that γ in (4.36) would need to take on in order for $P_{\max, \text{theory}}$ to equal $P_{\max, \text{model}}$. For extraction in either constriction, the values of γ^* are higher than allowed by theory ($0.19 \leq \gamma \leq 0.26$ [34]). This is consistent with previous results, since the amplitude adjacent to the constriction increases as P approaches P_{\max} . This sets up a restorative forcing not allowed by the assumptions underlying the theory. The co-tidal assumption

is also inappropriate when power is extracted from the seaward constriction, because the “basin” (segments 3, 4, and 5) experiences a large phase shift.

When currents are driven by a phase difference between two arms of the open ocean there is no restorative mechanism and the theory accurately predicts P_{\max} . This is demonstrated in model results for serially connected passages in the Johnstone Strait by Sutherland et al. [13], which show good agreement with the theory proposed by Garrett and Cummins [20].

Table 5.6 – Comparison between theoretical and model predictions for maximum possible turbine dissipation (serial constriction network). For each geometric variation, extraction occurs either in segment 2 or segment 4. γ^* is an implied value from equation (4.36) for which $P_{\max,model}/P_{\max,theory}$ would be unity.

Case	Variation	Extraction Segment	Symbol (Figure 5.12)	γ^*	$\frac{P_{\max,model}}{P_{\max,theory}}$	$\frac{\zeta_{0,max}}{\zeta_{0,initial}}$	$P_{\max,model}$ (MW)
R1	Base case	2	◇	0.32	1.60	1.45	840
		4	◆	0.28	1.32	1.20	600
R2	$\zeta_{0,external} = 1.7\text{m}$	2	△	0.32	1.62	1.44	580
		4	▲	0.27	1.26	1.15	420
R3	$\zeta_{0,external} = 2.5\text{m}$	2	□	0.31	1.56	1.40	1150
		4	■	0.29	1.36	1.25	810
R4	$b_2 = 1.5\text{km}$	2	◁	0.31	1.58	1.39	760
		4	◀	0.32	1.50	1.32	530
R5	$b_2 = 2.9\text{km}$	2	▽	0.32	1.54	1.43	880
		4	▼	0.26	1.27	1.17	630

While the theory does not accurately predict P_{\max} , non-dimensional effects are equivalent in the terminal basin (segment 5), as shown in Figure 5.12a. The non-dimensional response is independent of segment geometry throughout the network if power is extracted from the seaward constriction. This is expected, since it is analogous to a single constriction network with a large phase shift in the terminal basin. However, when power is extracted from the landward constriction (segment 4), the non-dimensional response varies with segment geometry for both the intermediate basin (b) and inlet.

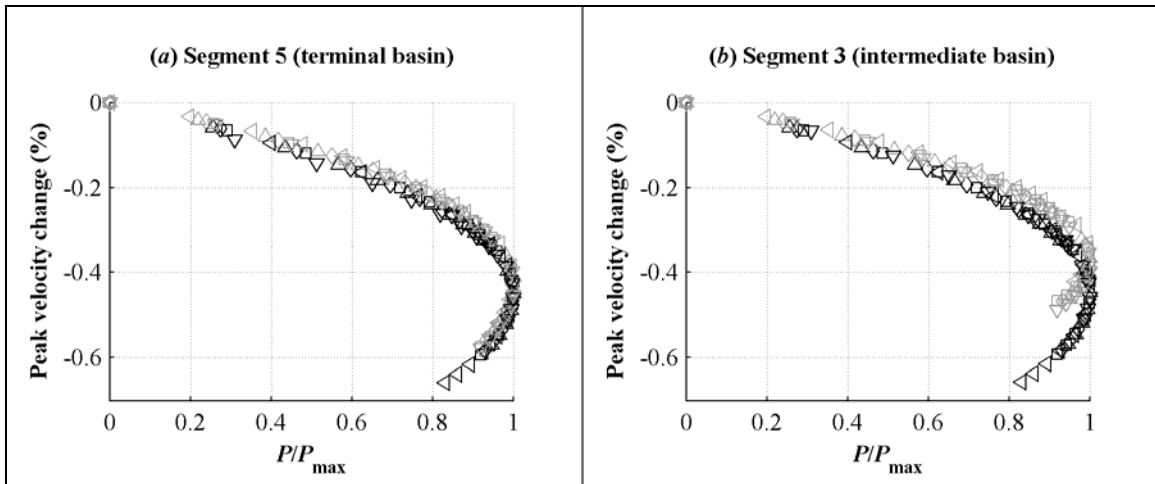


Figure 5.12 – Non-dimensional response to dissipation for serial constriction networks. Panels show the response in different segments. Symbols relate to a particular geometry identified in Table 5.6. Black markers denote extraction in segment 2 (seaward constriction). Grey markers denote extraction in segment 4 (landward constriction).

Finally, returning to a point raised earlier, Table 5.6 shows that, for all cases modeled, P_{\max} is highest when power is extracted from segment 2 (seaward constriction). One possible explanation in line with the existing theory is that because power is dissipated as the tide propagates into an estuary, there is less power available to do work at the landward constriction. This may present a trade-off between the cost of power and the amount of power generated since sites with higher power densities are predicted to generate power at lower cost [7]. For example, in case R5, the natural power density in segment 4 is twice as high as in segment 2. Therefore, each turbine in segment 4 will initially produce twice as much power as one in segment 2, with a corresponding difference in the cost of power. However, as shown by the relative differences in P_{\max} , nearly 40% more power could be generated if turbines were placed in segment 2.

5.4. Hybrid Networks

Intuitively, one would expect hybrid networks incorporating features of two or more prototypical networks to behave in a manner that is qualitatively described by a superposition of the prototypes. That supposition is tested here for a branching network, where one branch includes serial constrictions. A schematic of this network is shown in Figure 5.13 and geometric properties for each channel segment are presented in Table 5.7. The baseline tidal regime is listed in Appendix 5.

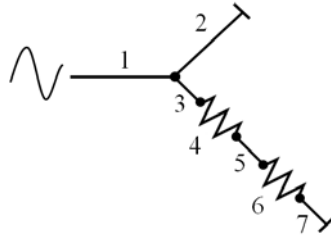


Figure 5.13 – Schematic of a hybrid branching-serial network. Symbol notation is as described in Figure 5.3e.

Table 5.7 – Baseline properties for hybrid network channel segments

Segment Description	1 Inlet	2 Upper Branch	3	4	5	6	7
Length (L) (km)	40	80	40	5	60	5	80
Width (b) (km)	20	10	10	2.2	10	1.5	10
Depth (H) (m)	50	50	50	50	50	50	50
Manning roughness (n)	0.035	0.035	0.035	0.035	0.035	0.035	0.035
Forcing amplitude (m)	1.5m						

The system's response to extraction from either segment 4 or segment 6 is shown in Figure 5.14. As hypothesized, the response is a qualitative amalgam of a branching network and serial constriction network. As for a serial constriction network, extracting the same amount of power from segment 6 (landward constriction) leads to larger far-field impacts than for power extraction from segment 4 (seaward constriction). As for a branching network, the tidal regime in the branch without extraction (segment 2) is augmented. Quantitatively, however, the augmentation to the tides and currents is much greater than for the branching prototype, even though P/P_{\max} is comparable between the two cases. This indicates that simple, prototype networks may be useful for qualitative, but not quantitative, prediction of the extraction response in more complicated networks.

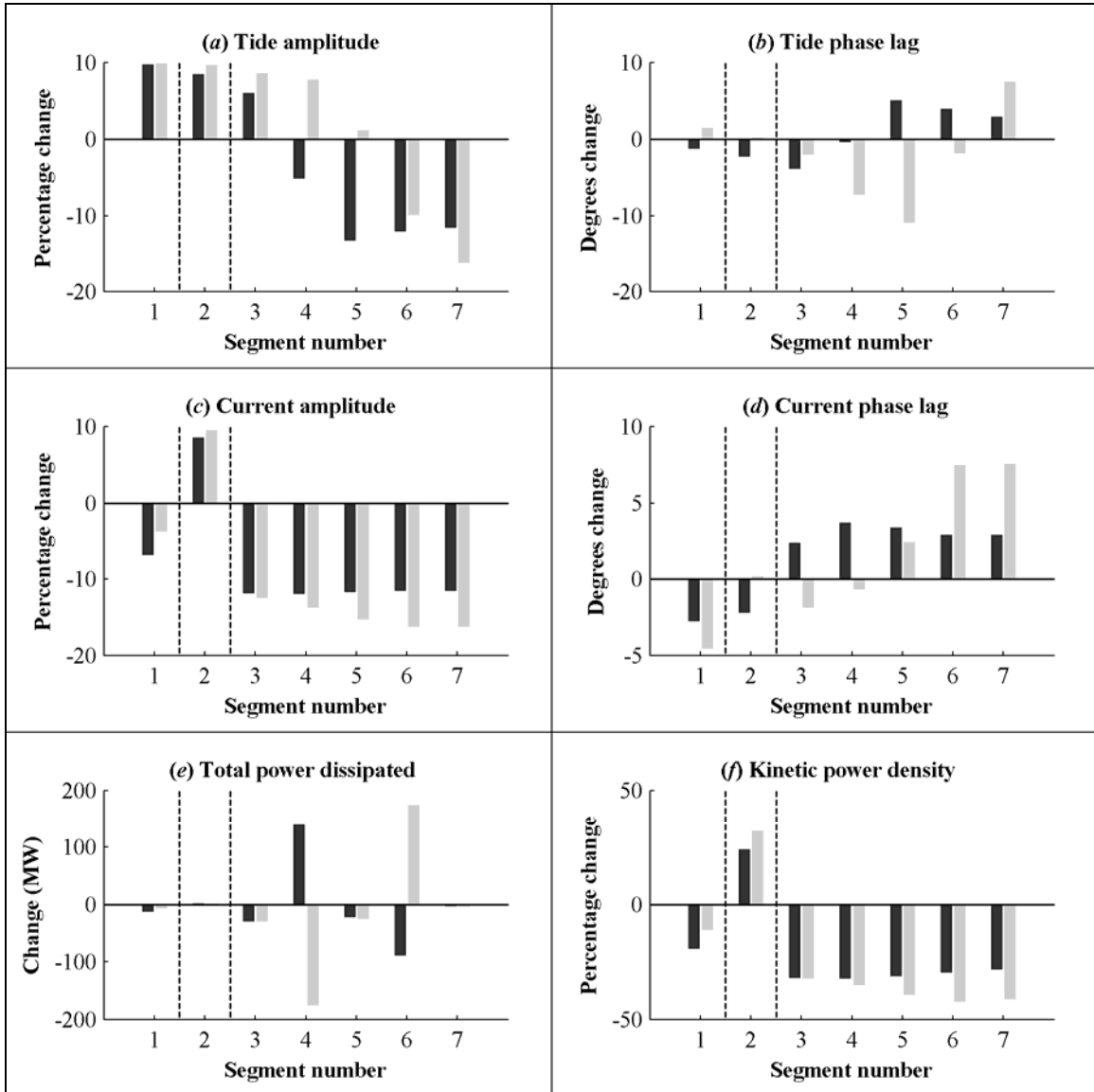


Figure 5.14 – Hybrid network response to 300MW turbine dissipation. Black bars denote a case in which power is extracted only in segment 4 ($P/P_{\max} = 0.5$). Grey bars denote a case in which power is extracted only in segment 6 ($P/P_{\max} = 0.7$).

5.5. Potential for Extrapolation

Figure 5.15 shows the segments where the non-dimensional response is independent of segment geometry for a particular topology (e.g., Figure 5.12a). In the figure, black lines indicate locations where non-dimensional effects are equal for that topology (independent of the geometric properties of the particular segments) and grey lines denote locations where non-dimensional effects depend on the geometry of each segment. The tidal response is very site-specific and not,

generally, a function of non-dimensional turbine dissipation (P/P_{max}) for the topologies presented here.

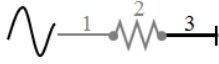
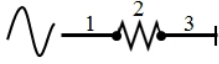
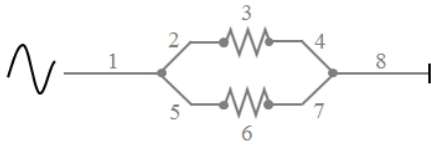
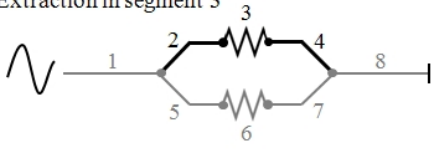
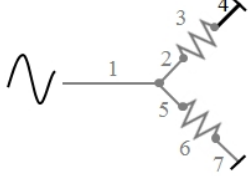
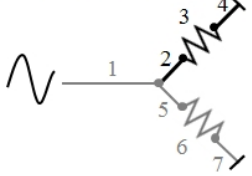
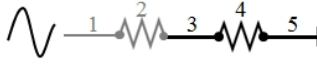
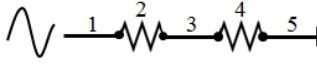
	Tides	Currents
Single Constriction		
Multiply-Connected Network		Extraction in segment 3 
Branching Network	Extraction in segment 3 	Extraction in segment 3 
Serial Network	Extraction in segment 2  <i>If extraction in 4, segment 5 only</i>	Extraction in segment 2  <i>If extraction in 4, segment 4 and 5 only</i>

Figure 5.15 – Segments of prototype channel networks with equivalent responses to extraction. Non-dimensional effects independent of segment geometry in black segments, but depend on segment geometry in grey segments.

A comparison of the non-dimensional response curves for the four prototype networks reveals that the relative changes to kinetic power density with respect to P/P_{max} is quite similar for all prototypes, as shown in Figure 5.16. This is also the case for transport. These similarities suggest that the response may also be similar in more complicated networks, which would allow extrapolation of P_{max} based on the system response to lower levels of power dissipation. This could reduce the computational expense associated with a trial-and-error approach to determining P_{max} .

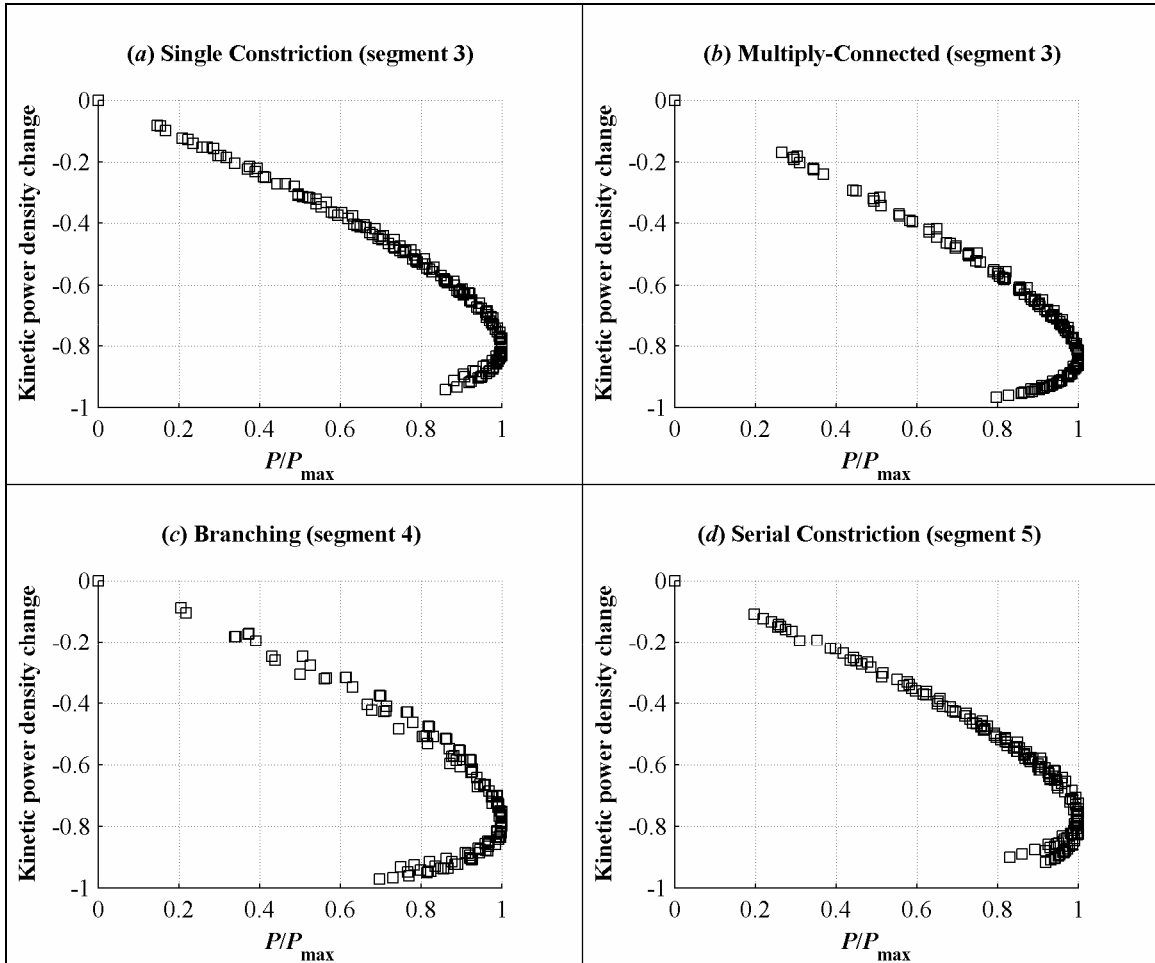


Figure 5.16 – Relative changes to kinetic power density with non-dimensional turbine dissipation (all networks). Each \square denotes the response of a particular geometry to a particular level of dissipation. Network type and location noted in panel captions.

The non-dimensional response curves for both transport (Q) and kinetic power density (K) are well-described by 4th order polynomials of the form

$$\frac{P}{P_{\max}} = A(\Delta v)^4 + B(\Delta v)^3 + C(\Delta v)^2 + D(\Delta v) + E, \quad (5.1)$$

where Δv is the relative change in either transport or kinetic power density. The leading coefficients for transport and kinetic power density are listed in Table 5.8 and Table 5.9, respectively. For the single constriction, branching, and serially connected networks, these coefficients are derived from the response in the terminal basin. For the multiply-connected network, coefficients are derived from the response in the constriction with extraction. The R^2 statistic for each fit is also given. Using (5.1), the value of P_{\max} may be extrapolated from the

relative change in either transport or kinetic power density for $P < P_{\max}$. Because these fits are approximations to the actual response, the coefficients for transport and kinetic power density may not be directly related.

Table 5.8 – Polynomial fit coefficients for non-dimensional response curves (transport basis).

Network	<i>A</i>	<i>B</i>	<i>C</i>	<i>D</i>	<i>E</i>	<i>R</i> ²
Single Constriction	-9.57	-16.7	-14.5	-6.21	0.00507	0.9955
Branching	-9.25	-18.1	-16.2	-6.64	0.0119	0.9908
Serial Constriction	-7.11	-12.9	-12.6	-5.89	0.00352	0.9912
Multiply-connected	-0.881	-3.78	-8.08	-5.17	0.000595	0.9992

Table 5.9 – Polynomial fit coefficients for non-dimensional response curves (kinetic power basis).

Network	<i>A</i>	<i>B</i>	<i>C</i>	<i>D</i>	<i>E</i>	<i>R</i> ²
Single Constriction	-2.76	-3.54	-2.02	-2.02	-0.00277	0.9985
Branching	-4.48	-6.90	-4.43	-2.68	-0.00299	0.9917
Serial Constriction	-2.09	-2.16	-1.26	-1.94	-0.00850	0.9968
Multiply-connected	-4.22	-6.35	-3.48	-2.13	-0.00286	0.9975

The hybrid network (Figure 5.13) provides a test case for this technique, since P_{\max} is already known. Figure 5.17 shows the relative error associated with extrapolating to P_{\max} on the basis of the relative change in transport or kinetic power density. Extrapolations using the polynomial fits for serial, branching, and single constriction networks are shown, as these prototypes most closely resemble the hybrid network. The accuracy of the extrapolation improves as the modeled $P \rightarrow P_{\max}$, which indicates that the approach is fundamentally sound. That is to say, P_{\max} for the hybrid network corresponds to a reduction in the kinetic power density on the order of 80%, as it does for other prototype networks. The accuracy of the method degrades for smaller P , which is not surprising given the scatter in the non-dimensional responses for the prototype networks underlying the polynomial fits.

The results for the hybrid case indicate that this approach may be useful, if cautiously applied. Extrapolation is only accurate to within 20% when $P > P_{\max}/3$. While P_{\max} is not known *a priori* (else there would be no need for this extrapolation), $P \approx P_{\max}/3$ generally corresponds to reductions in transport of more than 5% and reductions in kinetic power density of more than 15%. Changes in either quantity should be calculated in a terminal basin landward of the location where power is extracted. The preliminary application of the technique suggests that extrapolation on either basis (transport or kinetic power density) provides similar results. As such, extrapolation on the basis of transport is preferable, because that quantity may be readily derived from the tidal prism. The level of accuracy obtained by this method may be sufficient for

preliminary resource assessments and could be preferable to determining P_{\max} by trial-and-error modeling. Further refinement and testing of this approach may be warranted.

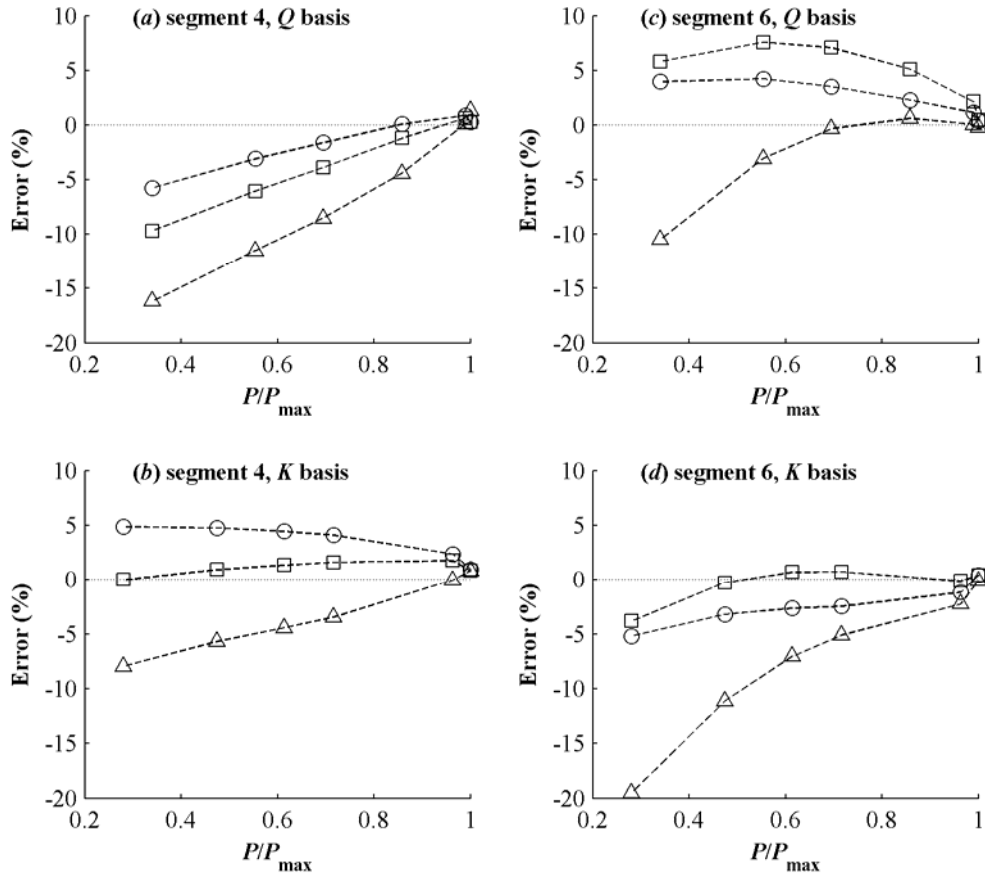


Figure 5.17 – Errors associated with extrapolation of P_{\max} from response at $P < P_{\max}$ for the hybrid network. Each point corresponds to an extrapolation to P_{\max} based on the relative change in either transport or kinetic power density. P/P_{\max} for this relative change is indicated on the abscissa, and is known *a priori* from trial-and-error modeling. The segment with power extraction is noted, as is the basis for the extrapolation, either transport (Q) or power density (K). Symbols denote extrapolation using the polynomial coefficients for a particular prototype network: \square single constriction, \circ serial constriction, \triangle branching.

5.6. Conclusions

The analysis in this chapter has quantified the response to extraction for several types of channel networks. Changes to the tides, currents, and dissipated power are observed when kinetic power is extracted in any channel. Depending on the type of network, the tidal regime may be either locally reduced or augmented. This is in contrast to a single constriction network, in which the tidal regime is generally reduced by extraction. When augmentation occurs, there may be direct

human impacts. Increased currents could enhance coastline erosion. An expansion of the tidal range would increase the surface area of mudflats and, during some stages of the tide, inundate areas that are currently dry. While the augmentation of currents may be either small in comparison to the reduction elsewhere in the system or on the same order as reductions, there are no cases tested in which the relative augmentation is much greater than the relative reduction. This could, however, be the case if one branch of a network were pushed towards resonance as a consequence of extraction at another branch.

In branching or multiply-connected networks, if power is only extracted from one branch in the network, flow will be redirected into the other branches. Optimally, extraction should be evenly distributed between the branches. For economic or environmental reasons, this may not be possible. The penalty for operating off-optimum is higher in multiply-connected networks than for branching networks. In either case, significant power extraction from a single branch is still possible. For serial constrictions, maximum power extraction corresponds to turbines operating only in the constricted channel closest to the open ocean. However, it is economically preferable to operate turbines in the constriction with the highest power density, so this also presents a trade-off.

A formula for calculating the maximum possible dissipation (P_{\max}) has been proposed by Garrett and Cummins [20] and extended by Blanchfield et al. [34] and Karsten et al. [12]. As shown in Figure 5.18, the differences between modeled and theoretical P_{\max} are nearly linear with the change in tidal amplitude seaward of the constriction where power is extracted. Karsten et al. [12] report similar results in their work modeling power extraction from the Bay of Fundy. Since neglecting this dynamic response may lead to a theoretical underprediction of P_{\max} by up to 60%, the assumption of constant amplitude seaward of the constricted channel might be revised in future theoretical development.

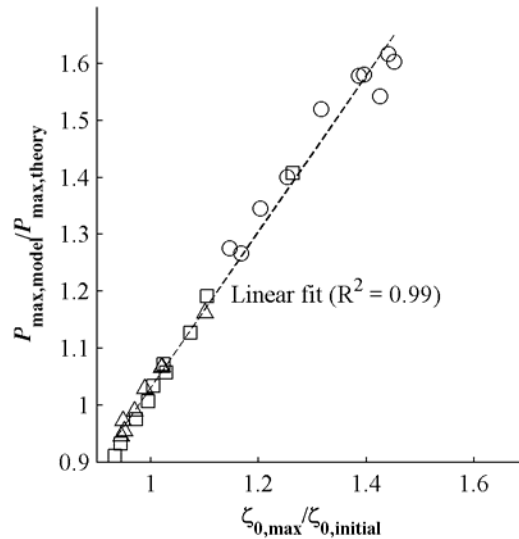


Figure 5.18 – Correlation of change in tidal elevation seaward of constriction with variation from theory. Symbols denote different geometries for each network prototype: \square single constriction, \circ serial constriction, \triangle branching.

Theory suggests that the non-dimensional current response to extraction should be equivalent between different geometries. As shown in Figure 5.15, this is accurate in portions of the prototype networks for currents (and, by extension, transport and kinetic power density). Taking advantage of similarities in the response between different networks, it may be possible to extrapolate the value of P_{\max} in more complicated networks based on the relative change in transport or kinetic power density for $P < P_{\max}$. As demonstrated for the hybrid network, extrapolation to P_{\max} is accurate to within 20% if the dissipated power used to make the extrapolation is greater than $1/3P_{\max}$. Since, P_{\max} is not known *a priori*, extrapolation should only be attempted when the relative change in transport is greater than 5% or the relative change in kinetic power density is greater than 15%. Extrapolation for smaller relative changes may greatly over or underpredict P_{\max} .

When systems are an amalgam of the prototypical networks, site-specific modeling is generally required to quantify the full-range of far-field impacts. However, the response to extraction may be qualitatively described as a combination of the responses for the underlying networks.

A general limitation to either theoretical prediction of the system response or extrapolation based on prototypical networks is the inability to broadly predict changes to the tides (Figure 5.15). In particular, neither approach is capable of predicting an increase in tidal range seaward of the point

of extraction. As mentioned above, this augmentation to the natural regime could have significant social consequences and should be quantified as part of resource assessment efforts.

In conclusion, while it is desirable to predict the extraction response of complicated networks from observations, this is only presently feasible under restrictive conditions (i.e. single constriction network with near-constant tidal amplitude seaward of constriction). Since extraction affects the resource at other locations in a network, it is not appropriate to add up P_{\max} for each site in isolation in order to estimate P_{\max} for the entire network, particularly for serial networks. Since there may be trade-offs associated with extraction at different sites in a network, regional resource assessment is actually a constrained optimization problem. Site-specific modeling of extraction effects is required for rigorous resource assessment.

6. Application of 1D Channel Model: Tidal Energy Extraction from Puget Sound

One low cost approach to assessing the resource potential for a region is the application of the 1D channel model, in which only the essential features of a network are retained. While this approach is not suitable for all potential tidal energy sites, if the flow is dominantly one-dimensional this method would be expected to yield reasonably acceptable results. Two-dimensional or three-dimensional models are also viable, but the computational cost may be high if there is not an existing model for the region to serve as a calibrated baseline. In this chapter, the 1D channel model is applied to Puget Sound, Washington, an estuary where development of the in-stream resource is proposed. The results discussed here have been submitted for publication in *Proc. IMechE. Part A: J. Power and Energy* [16].

6.1. Tidal Energy in Puget Sound

Previous studies [56] have identified Puget Sound, Washington, United States as a promising in-stream resource. Puget Sound (Figure 6.1) is a fjord estuary approximately 240 km in length along its major axis, and structurally consists of a series of deep basins separated by shallow and narrow sills. Two other basins (Hood Canal and Whidbey Basin) branch from the main axis. Over the sill in northern Admiralty Inlet (northern end of Puget Sound) and Tacoma Narrows (southern end of Puget Sound), tidal currents are quite strong and might economically support in-stream energy extraction [60, 61]. The majority of the tidal exchange between Puget Sound and the Strait of Juan de Fuca – Strait of Georgia system is across the Admiralty Inlet sill, excepting a small, but vigorous, exchange driven by phase differences through Deception Pass at the northern end of Whidbey Basin. The tidal forcing is nearly a standing wave with maximum current and range slightly less than 90° out of phase. The type of tide is mixed, mainly semi-diurnal with a strong diurnal inequality. An excellent description of the tides and currents of Puget Sound is given in Mofjeld and Larsen [62]. There are currently a number of tidal in-stream projects proposed for Puget Sound. The furthest along, in northern Admiralty Inlet, is approaching the pilot stage. This would involve a small array of devices to gain operational experience and begin to answer pressing near-field environmental questions [63].

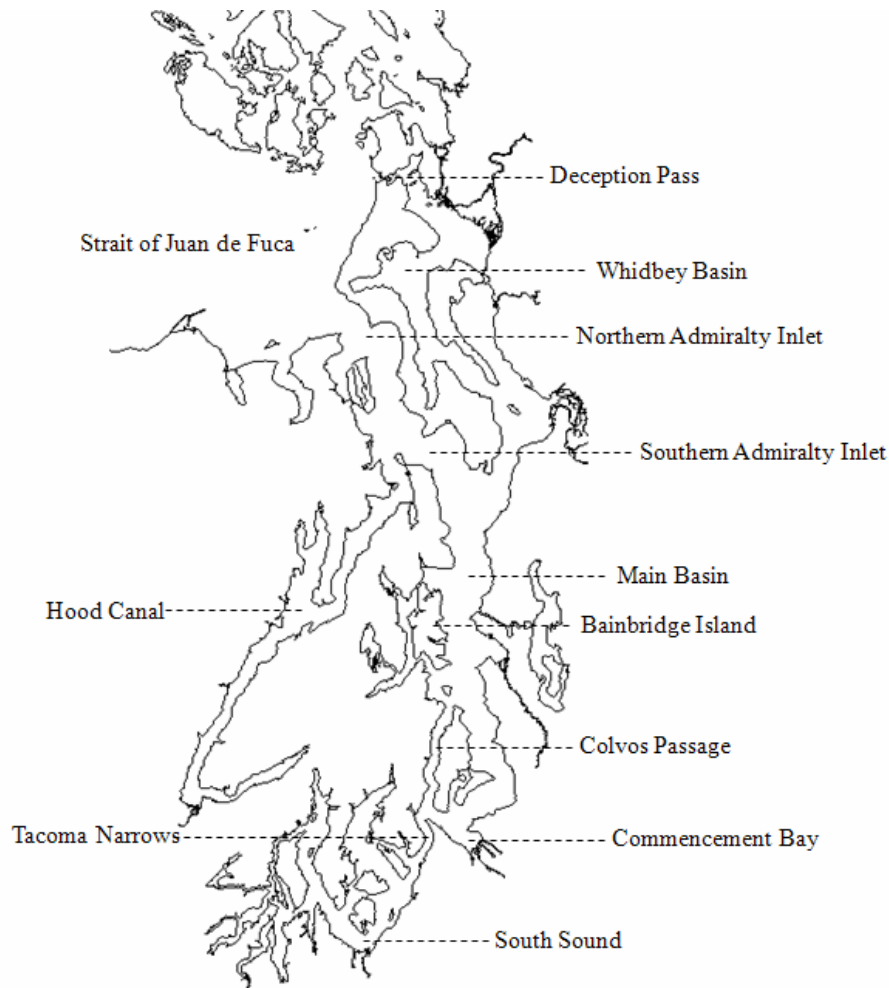


Figure 6.1 – Puget Sound coastline with major features labeled.

In recent years, there have also been growing environmental concerns related to hypoxia in Hood Canal [64] and the basins of the South Sound [65]. In order for tidal energy development to proceed in Puget Sound, any projects undertaken should not significantly exacerbate hypoxia, or other environmental stresses already present. While the modeling technique employed here cannot directly address these questions, it is a useful tool to establish a basic understanding of the far-field, barotropic effects of in-stream tidal energy extraction from Puget Sound. This is distinguished from possible baroclinic effects related to changes in temperature and salinity. To this end, the barotropic effects of array development in Admiralty Inlet and Tacoma Narrows are quantified using the 1D channel model. Section 6.2 describes the process of grid generation, Section 6.3 describes the procedure used to calibrate the model, and Section 6.4 describes the barotropic effects of energy extraction. This chapter concludes with a discussion of these effects in the context of proposed site development and the long-term potential for Puget Sound.

6.2. Grid Generation

For the purposes of this model, the topography of Puget Sound is described as a multiply-connected network of thirty-seven rectangular channels of constant cross-section, as shown in Figure 6.2. The model includes the major basins (Main Basin, Hood Canal, Whidbey Basin, and the South Sound) and the two major sills (Admiralty Inlet and Tacoma Narrows), but excludes Deception Pass and subsumes a number of islands (e.g., Bainbridge Island), channels (e.g., Colvos Passage), and embayments (e.g., Commencement Bay) into the network of uniform cross-section channels. The modeling approach requires that for each segment the length, width, mean water depth, and roughness coefficient be selected as representative of the actual channel. The prescription of geometric properties (depth, width, and length) for each segment is described here, while the prescription of the roughness coefficient is discussed in the context of model calibration (Section 6.3.2). Puget Sound is first broken down into thirty-seven segments representing key bathymetric features (Figure 6.2). Segment boundaries have been chosen to preserve the essential structure of Puget Sound without introducing unnecessary complication into what is already a highly idealized model. Within each segment, publicly available bathymetric data for Puget Sound [66] are interpolated onto a 250 m grid and used to calculate the average depth, total surface area, and an effective length for each segment. Since bathymetric data are referenced to mean lower low water (MLLW), segment depths are coarsely adjusted to mean sea level (MSL) using corrections developed for tsunami inundation modeling [67]. The effective width is computed by dividing the segment surface area by the effective length. The volume of each segment is the product of the mean depth and surface area. This method achieves reasonable agreement with previous calculations of the volumes of Puget Sound's major basins [62] (Table 6.1). Geometric properties for each segment are listed in the Appendix 7.

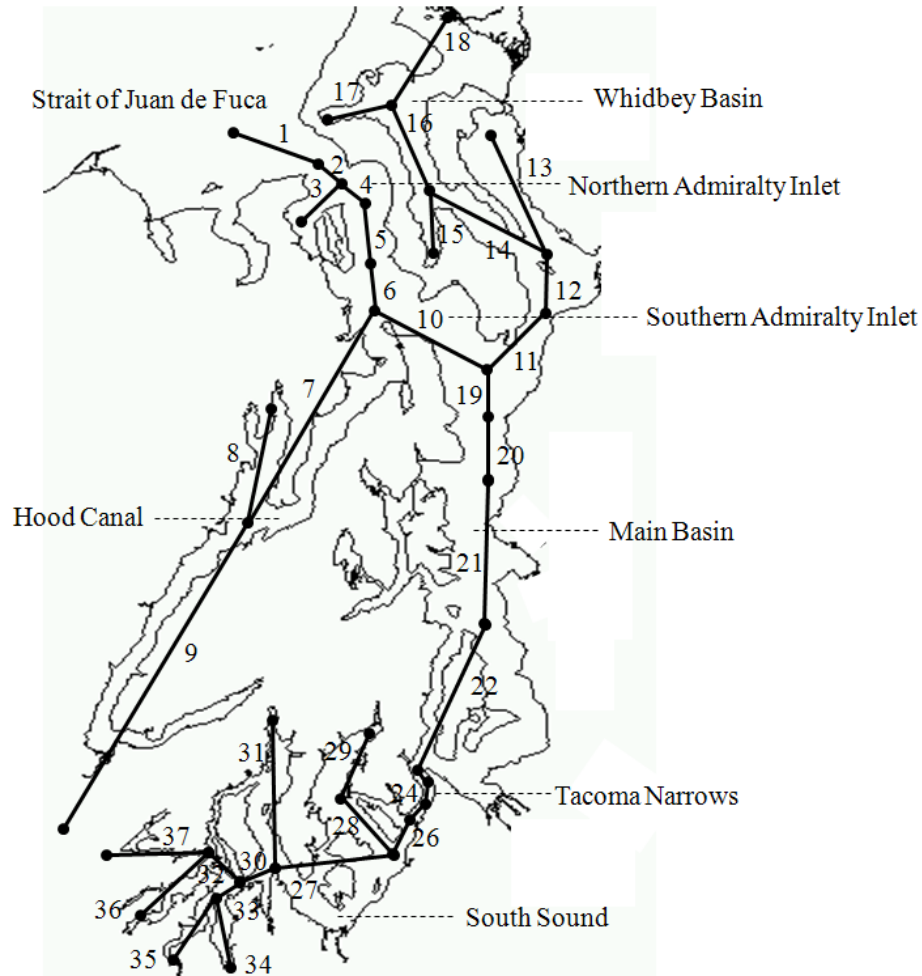


Figure 6.2 – Puget Sound channel network superimposed on Puget Sound coastline. Solid black lines denote channel segments (numbered) and black dots denote channel junctions or boundaries.

Table 6.1 – Volumes of major basins in Puget Sound

Basin Volume (km ³)	Model	Mofjeld and Larsen [62]	Difference
Admiralty Inlet	21.1	21.7	-3%
Main Basin	78.5	77.0	2%
South Sound	16.7	15.9	5%
Hood Canal	26.6	25.0	6%
Whidbey Basin	29.3	29.1	1%
Total	172.2	168.7	2%

The grid shown in Figure 6.2 is the product of several iterations. While it is possible to incorporate additional segments to further resolve other network features, this increases the effort required to calibrate and run the model. An example of an earlier grid which resolves the multiply connected nature of the South Sound and flow around Bainbridge Island is shown in Figure 6.3. This could be relevant for a study involving in-stream extraction from those areas (e.g., Agate

Passage and Rich Passage around Bainbridge Island), but this level of detail is not required to study extraction in Admiralty Inlet or Tacoma Narrows.

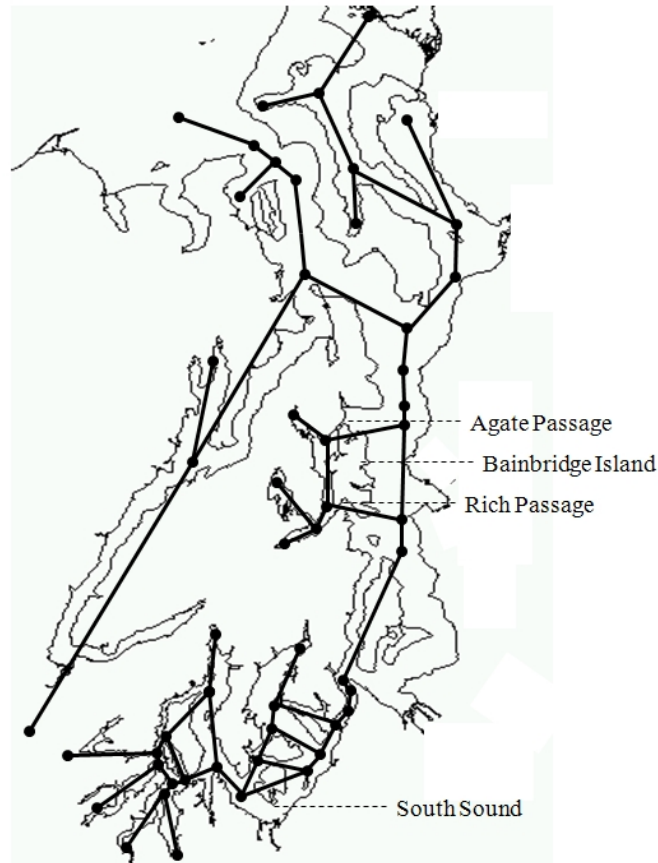


Figure 6.3 – Version of Puget Sound channel network resolving features of flow in South Sound and around Bainbridge Island.

6.3. Model Calibration

The model is calibrated against observed tidal amplitudes and phases compiled by Lavelle et al. [68]. Lavelle et al. investigates the structure of tides and currents of Puget Sound using a high-resolution 1D model consisting of several hundred channel segments. The present model is forced at the open boundary with the eastern end of the Strait of Juan de Fuca by six tidal constituents (M2, S2, N2, K1, O1, and P1). The external amplitude and phase for each constituent are chosen to minimize the least-squares error between observations and model values for the tidal regime. Model runs are 200 days in length, including a five day spin-up period. One advantage of 1D versus 3D models is computational efficiency. For example, on a dual-core workstation, 200 days of model time requires only 2.5 days of clock time. A 3D model of the Puget Sound currently

undergoing calibration on a parallel computing cluster with 120 nodes requires 6 days of clock time to simulate 35 days of model time. Model calibration consists of four comparisons:

1. Modeled tidal amplitude and phase of six forced constituents (M2, S2, N2, K1, O1, and P1) as analyzed by *t_tide* [50] against observations compiled by Lavelle et al. [68] for forty-three locations in Puget Sound. *t_tide* automatically determines the amplitude and phase of the tidal constituents using a least-squares fit.
2. Modeled M2 transport amplitude into the major basins of Puget Sound against modeled M2 transport amplitude reported in Lavelle et al.
3. Modeled frictional power dissipation in the major basins of Puget Sound against modeled frictional power dissipation reported in Lavelle et al.
4. Modeled kinetic power density in the constricted channels at Admiralty Inlet and Tacoma Narrows against recent observations.

In cases where there is a conflict between calibration metrics, the observational data for tidal amplitude and phase are given precedence. For example, if the agreement with frictional power dissipation may only be improved by worsening the agreement with tidal phase, then no changes are made.

6.3.1. Tidal Amplitude

Results showing the spatial agreement for amplitude calibration are presented in Figure 6.4 for the M2 and K1 tides (respectively, the dominant semidiurnal and diurnal tides). In general, tidal amplitudes are lowest in Admiralty Inlet and highest in the terminal basins of the South Sound. The model amplitude is, on average, within a few percent of observed amplitude.

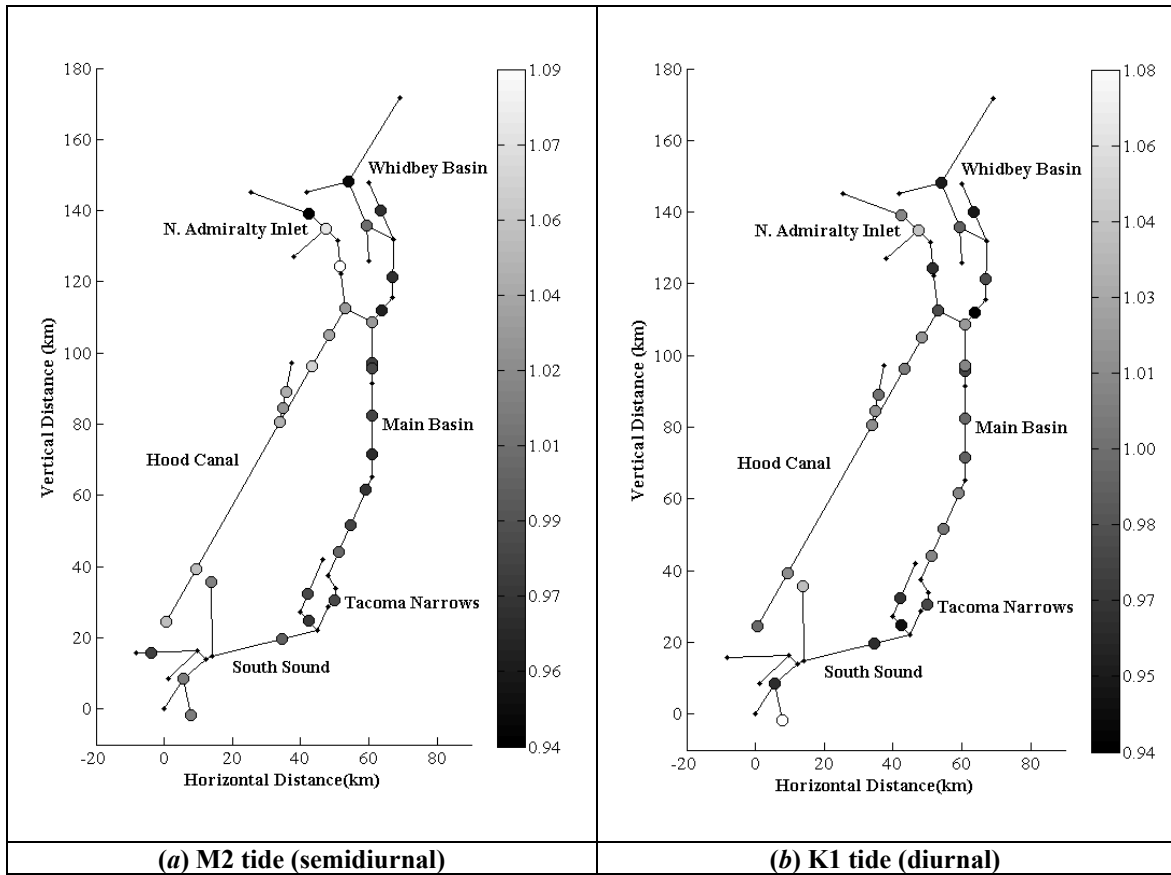


Figure 6.4 – Comparison of modeled to observed tidal amplitude. Each circle is the location of the comparison and shading corresponds to the ratio of modeled amplitude to observed amplitude. Smaller dots denote junctions between channel segments.

A more compact presentation of these results for all six tidal constituents is shown in Figure 6.5. The mean error between observed and modeled amplitude is within 5% for all constituents. The calibrated external forcing amplitudes are tabulated in Table 6.2.

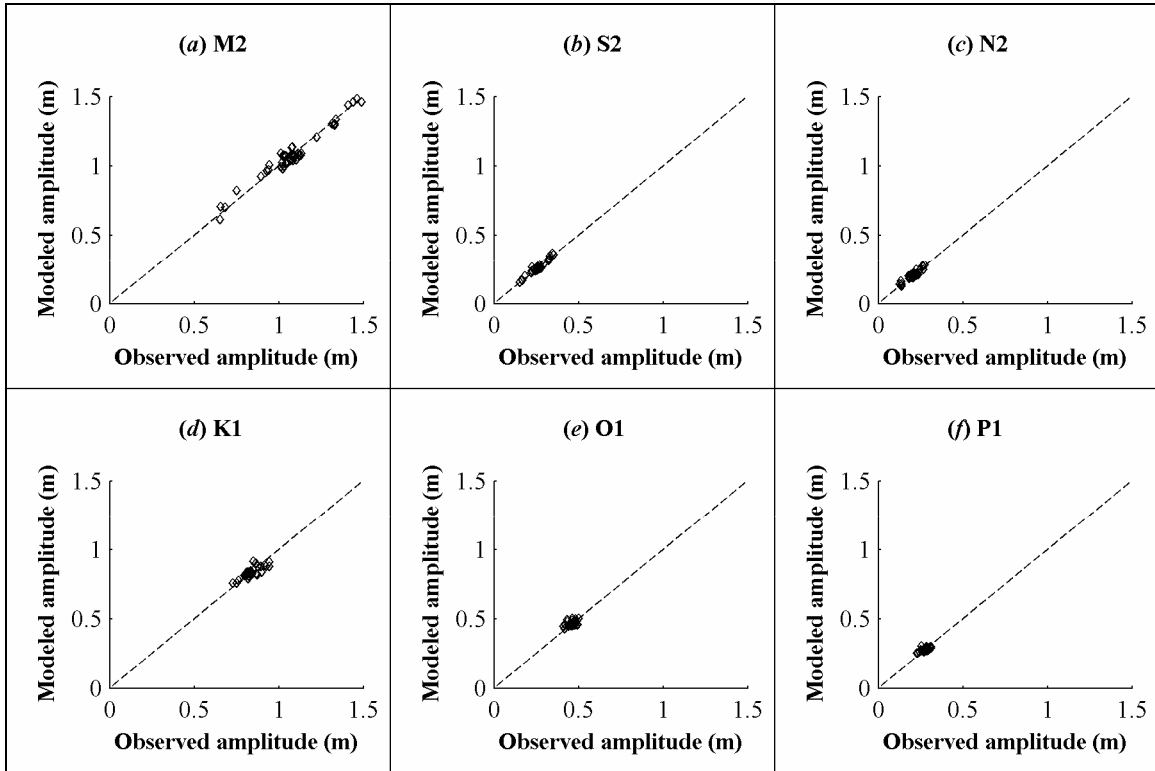


Figure 6.5 – Tidal amplitude calibration by constituent. Each point corresponds to a comparison at a particular point in the model domain. The dashed line represents a 1:1 agreement between modeled and observed amplitudes.

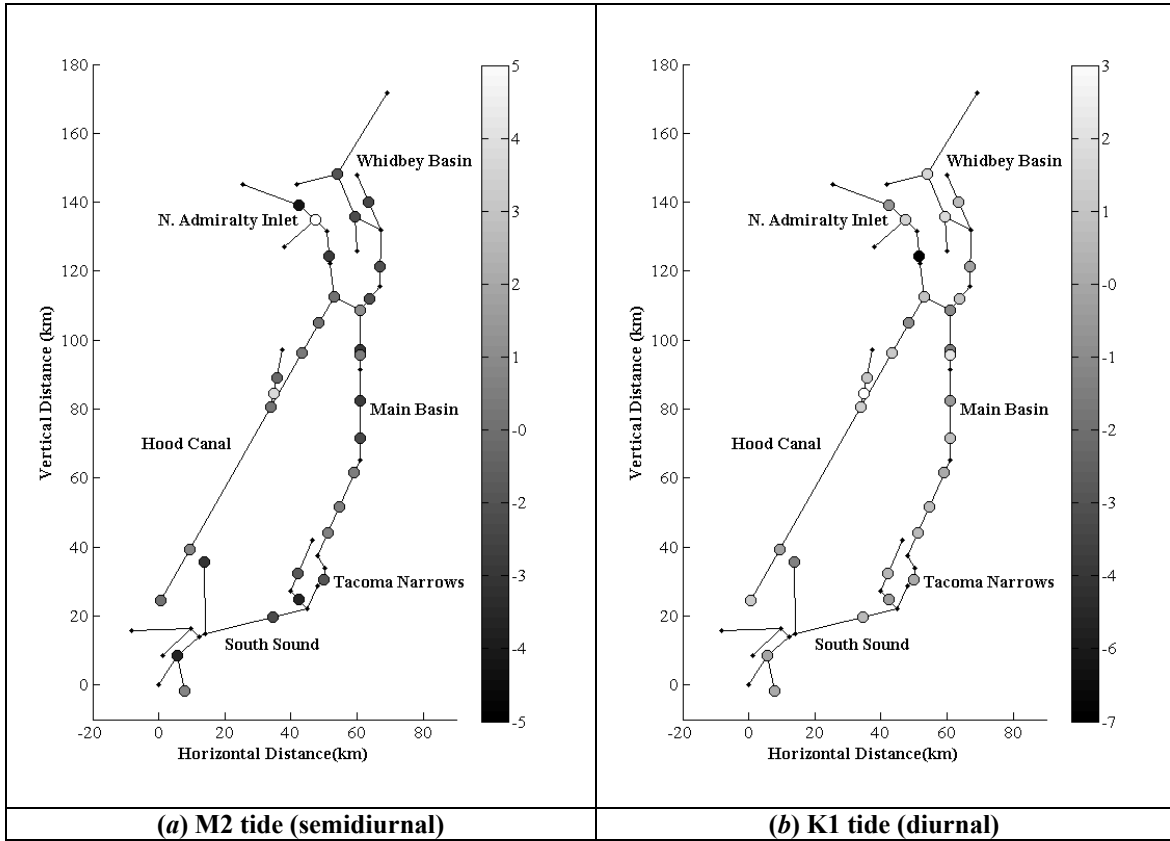
Table 6.2 – External tide boundary values

Constituent	Name	Amplitude (m)	Phase Lag (°)	Period (h)
Principal semidiurnal lunar	M2	1.421	21.25	12.42060
Diurnal declinational	K1	0.917	336.9	23.93447
Principal semidiurnal solar	S2	0.375	323.03	12.0
Lunar diurnal	O1	0.510	200.05	25.81934
Lunar elliptic semidiurnal	N2	0.283	127.0	12.65835
Solar diurnal	P1	0.309	136.8	24.06589

6.3.2. Tidal Phase Lag

Calibration of the tidal phase lag involves adjustment of both the externally specified phase lag and the frictional coefficient for each model segment, since the energy dissipated determines the change in phase lag [52]. The Manning roughness coefficient in each model segment is initialized to a value of $0.035 \text{ m/s}^{1/3}$, corresponding to a rough, natural channel [42]. In the sill regions, this baseline value gives good agreement with observations. However, the modeled phase lag within some segments would be nearly constant, which does not agree with observations. The problem is not unique to this particular effort and an analogous situation was encountered in the calibration of the Lavelle et al. model [68]. In that model, frictional dissipation is assumed to be linear with

velocity. A uniform bottom friction is able to accurately capture the phase lag propagation in the deeper basins but significantly under predicts the phase lag increase over the sills. In order to improve calibration, surface roughness is elevated in the sill regions. In the present model, the variation between modeled and observed phase lag indicates quadratic friction is not a good description for dissipation in the slower-moving regions of the model, just as linear friction is not a good description for dissipation over the sills. In strictly mechanical terms, the roughness coefficients can be increased to improve phase lag agreement. This adjustment is required only in deep basins or segments for which a number of small channels are aggregated into a single channel. In the first case, the increased roughness coefficient is an expression of dissipation due to gravitational circulation, which cannot be represented by a barotropic model. In the second case, the increased roughness is an expression of mixing losses at channel junctions and the lower velocities that result when multiple channels are combined into a single, wider channel. The spatial agreement between modeled and observed phase lag is shown for the M2 and K1 tides in Figure 6.6. Results from the phase lag calibration for all constituents are shown compactly in Figure 6.7. The final values for the roughness coefficient in each segment are given in the Appendix 7 and values for the calibrated external phase lag are listed along with the external amplitude in Table 6.2. The mean error between observed and modeled phase lag is 3 degrees, which is quite reasonable considering that the observations [68] indicate cross-channel variations in the phase lag by nearly 3 degrees.



(a) M2 tide (semidiurnal) **(b) K1 tide (diurnal)**
Figure 6.6 – Comparison of modeled to observed tidal phase lag. Each circle is the location of the comparison and shading corresponds to the difference between modeled amplitude and observed phase lag. Smaller dots denote junctions between channel segments.

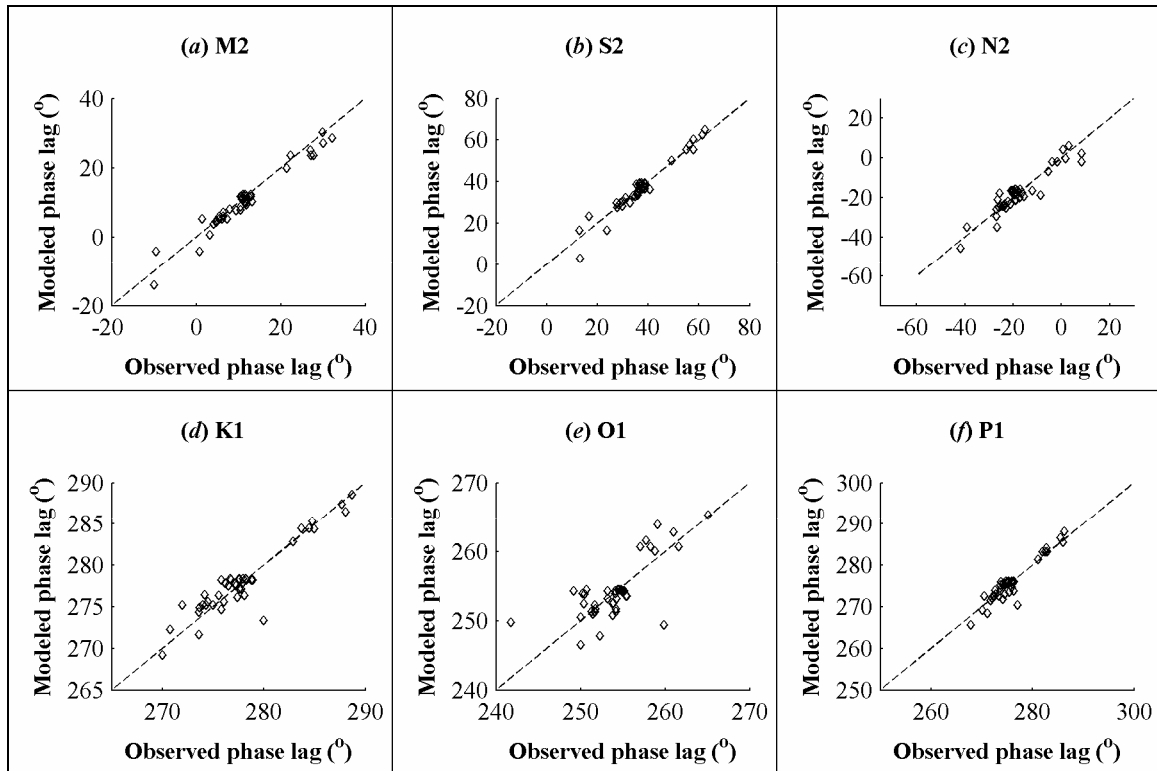


Figure 6.7 – Tidal phase lag calibration by constituent. Each point corresponds to a comparison at a particular point in the model domain. The dashed line represents a 1:1 agreement between modeled and observed phase lag.

6.3.3. Total Dissipated Power

Figure 6.8 shows a schematic for the total power dissipated in the major basins of Puget Sound and a comparison to model results presented in Lavelle et al. [68]. Most of the energy flux into Puget Sound is dissipated over the shallow sills separating the major basins. The total power dissipated over the entire Puget Sound system is comparable between the two models, though the present model dissipates more power in the Main Basin and Tacoma Narrows and less across the sill in northern Admiralty Inlet. While it would be possible to reduce the roughness coefficients in some basins to improve the agreement with power dissipation, this would degrade the phase lag calibration, which is against observations, rather than modeled data. This model also matches the observed phase lags in the Main Basin better than the Lavelle et al. model.

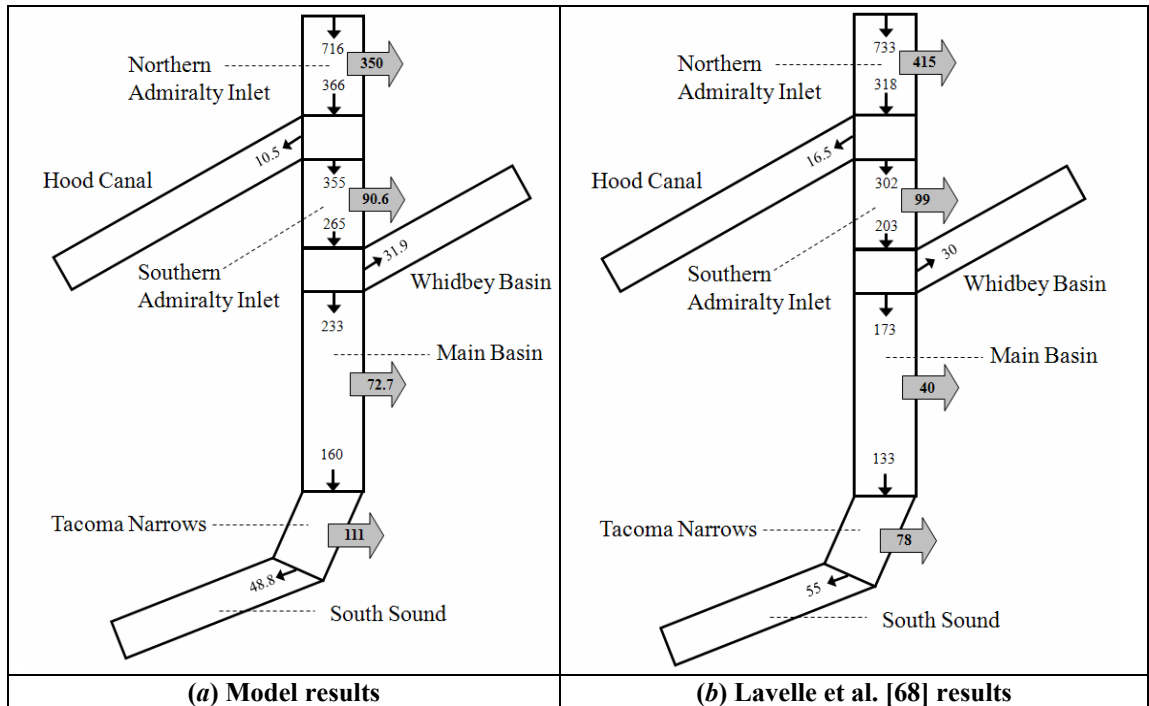


Figure 6.8 – Power dissipation in regions of Puget Sound (MW). Grey arrows indicate power dissipated in major basins or sill regions. Smaller arrows indicate energy flux (MW) between sections.

6.3.4. Tidal Transport

Tidal transport (the volume of water transported by tidal forcing) is a difficult calibration since errors are cumulative to the head of the system. That is to say, an under or over estimation of the transport in one model segment affects all transport calculations seaward of that point. A comparison of the transport for the M2 and K1 constituents between this model and the results presented in Lavelle et al. [68] is made in Table 6.3.

Table 6.3 – Comparison of modeled transport amplitudes to amplitude modeled by Lavelle et al. [68]

M2 Transport (m ³ /s)	M2 Transport Amplitude (m ³ /s)			K1 Transport Amplitude (m ³ /s)		
	Model	Lavelle et al.	Variation	Model	Lavelle et al.	Variation
N. Admiralty Inlet	3.8x10 ⁵	3.3x10 ⁵	16%	1.6x10 ⁵	1.3x10 ⁵	18%
S. Admiralty Inlet	2.8x10 ⁵	2.5x10 ⁵	10%	2.5x10 ⁴	1.9x10 ⁴	31%
Main Basin	1.9x10 ⁵	1.6x10 ⁵	16%	1.1x10 ⁵	9.9x10 ⁴	13%
South Sound	4.8x10 ⁴	3.5x10 ⁴	37%	3.0x10 ⁴	2.6x10 ⁴	15%
Hood Canal	6.1x10 ⁴	4.5x10 ⁴	34%	7.1x10 ⁴	6.0x10 ⁴	18%
Whidbey Basin	7.3x10 ⁴	6.4x10 ⁴	14%	3.1x10 ⁴	2.4x10 ⁴	28%

Agreement is worse than for the tides or power dissipation, with this model predicting substantially higher transport than the previous effort by Lavelle et al. This is somewhat surprising, since the total transport over a tidal cycle is roughly the product of tidal amplitude and

surface area of the domain, both of which agree quite well with observational data. Agreement is poorest in the South Sound and Hood Canal, but there are some mitigating considerations. There are few reported transport values in the South Sound and the comparison for that region is made in a channel where the flow bifurcates around an island. Since this bifurcation is subsumed into a single channel segment in this model, but explicitly modeled by Lavelle et al., one would expect the present effort to indicate a higher transport. For the Hood Canal, the transport is significantly greater than results presented by Lavelle et al. but dissipation is almost 50% lower. However, recent modeling of Hood Canal [69] indicates that the Lavelle et al. model overpredicts dissipation in Hood Canal, which would, in turn, cause an underprediction of transport. Finally, it is possible to account for the cumulative nature of transport errors by a simple back-calculation in which the transport errors present in the terminal basins are subtracted from the transport along the main axis of Puget Sound (N. and S. Admiralty Inlet and the Main Basin). If this is done, the transport in this model only varies from Lavelle et al. by at most 5%. This would indicate that this model is treating transport along the major axis in roughly the same manner as Lavelle et al. and that the variations are predominantly in the terminal basins.

6.3.5. Kinetic Power Density

While a point-wise velocity calibration is not generally possible due to significant cross-channel and vertical variability, the modeled kinetic power density over the sill regions is broadly comparable with recent observations. The model predicts a kinetic power density in Northern Admiralty Inlet of 0.8 kW/m^2 and an average kinetic power of 230MW on a cross-channel transect, which compares well with the recent ADCP measurements [70]. For Tacoma Narrows, the model values of 1.1 kW/m^2 and 65MW are somewhat lower than recent measurements, but there is significant cross-channel and along-channel variability in the central region of Tacoma Narrows [71]. These comparisons provide additional confidence that the model represents the in-stream kinetic resource at both potential development sites. Power densities in other model segments are less than 0.2 kW/m^2 , which is too low to be economically recoverable by in-stream turbines.

6.4. Extraction Effects in Puget Sound

Since one goal of this effort is to determine the far-field effects of various in-stream projects, the relations presented in Chapter 2 are used to relate extracted and dissipated power. The following assumptions are made:

- (1) Turbines operate in a linear manner, without a rated or cut-in speed.

- (2) The ratio of turbine swept area to channel cross-section (ε) is 1/3.
- (3) The streamtube velocity ratio (α) is 11/16. This is the ratio of the velocity at the end of the wake expansion region to the velocity upstream of the turbine.

The assumed value for the streamtube velocity ratio (α) corresponds to a free-stream efficiency ($\varepsilon = 0$) of 45%, which is reasonable for a commercial array. For the purposes of this analysis, it is assumed that the streamtube velocity ratio is constant with increasing blockage. Therefore, for $\varepsilon = 1/3$, the extraction efficiency increases to over 80%. The maximum Froude number in Admiralty Inlet or Tacoma Narrows is less than 0.15. Under these conditions, the performance metrics for the full solution (Section 2.2.4) and simplified solution (Section 2.2.5) vary by about 1% and the simplified solution, which is independent of Froude number, is sufficiently accurate. For turbines in this configuration, 82% of the total power dissipated by turbines is attributable to extraction, with the balance attributable to wake losses.

Since the maximum output of the array is relevant for assessing other engineering limits (e.g., interconnection capabilities), additional assumptions are made with respect to the capacity factor and balance of system efficiency. The capacity factor (ratio of average to rated extracted power) is assumed to be 30%, in line with commercial feasibility studies [61]. Based on modeling from Chapter 4, the influence of the rated and cut-in speed on extraction effects will be minimal. The balance of system efficiency is assumed to be 90%. The rated electrical capacity of an array ($P_{e,\text{rated}}$) dissipating power, $P_{\text{dissipated}}$, is given by

$$P_{e,\text{rated}} = \left(\frac{P_{\text{dissipated}}}{CF} \right) \left(\frac{P_{\text{extracted}}}{P_{\text{dissipated}}} \right) \eta_{\text{balance of system}} \quad (6.1)$$

The changes to the tidal regime with extraction are quantified in terms of:

- Amplitude and phase of the tides (water surface elevation) for the six forced constituents.
- Cumulative tidal transport (sum of the absolute value of transport passing through a cross-sectional area) over the model run time. Changes to the cumulative transport for each constituent are not quantified.
- Power dissipated in major sections of Puget Sound (time average)
- Kinetic power density in Admiralty Inlet and Tacoma Narrows (time average)

Baseline values in each region of Puget Sound are listed in Table 6.4.

Table 6.4 – Baseline tidal regime in Puget Sound

	M2 Tide (semidiurnal)		K1 Tide (diurnal)		Cumulative Transport ¹	Dissipated Power ²	Model Segment ³
	Amp	Phase	Amp	Phase			
Region	m	deg	m	deg	m ³	MW	
Strait of Juan de Fuca	0.62	-13.9	0.74	268.6	4.48×10^{12}	-	1
N. Admiralty Inlet	0.82	0.7	0.79	273.4	4.27×10^{12}	350	5
Hood Canal	1.10	5.7	0.84	275.5	2.63×10^{11}	10.5	9
S. Admiralty Inlet	0.95	5.6	0.81	275.3	3.41×10^{12}	90.6	10
Whidbey Basin	1.04	10.5	0.83	278.2	3.27×10^{11}	31.9	16
Main Basin	1.01	8.5	0.82	276.7	2.12×10^{12}	72.7	21
Tacoma Narrows	1.14	15.3	0.86	280.5	1.07×10^{12}	111	24
South Sound	1.43	28.0	0.90	287.2	2.63×10^{11}	48.8	30

¹Over simulation period as calculated by (4.30).

²Power dissipated between first and last segment in region (see Appendix 7 for regional boundaries).

³Model segment chosen as representative of a particular region.

6.4.1. Power Extraction in Admiralty Inlet

Modeling indicates that power extraction from Admiralty Inlet could reduce tides, transport, power dissipation, and kinetic power density throughout Puget Sound. However, it is very important to note that these effects are directly proportional to the magnitude of extraction. A very low level of extraction, as is the case for a pilot project extracting $O(5 \text{ MW})$, has very minimal far-field effects. The effects on the tide are presented in Figure 6.9. Only the M2 and K1 tides are shown, as they are representative of the semidiurnal and diurnal constituent responses. For the M2 tide, the amplitude decreases (*a*) and phase lag increases (*b*) uniformly over the interior of Puget Sound. The decrease in amplitude represents a contraction of the tidal range with attendant implications for near-shore and shoreline ecosystems. The situation is reversed in the Strait of Juan de Fuca with an increase in amplitude and decrease in phase lag. The change in phase lag is consistent with the physics of the problem. Because of the additional power dissipation by turbines, the phase lag will increase across the Admiralty sill. This is analogous to the effect of tuning bottom friction during model calibration. However, since the operation of turbines leads to generally lower velocities and, therefore, reduced frictional dissipation, the phase lag in the Strait of Juan de Fuca decreases. While the phase lag increases landward of extraction, this is a superposition of two effects: an increase in the reference phase lag over the Admiralty sill caused by turbine dissipation and a decrease in the phase lag change across subsequent basins caused by reduced velocity. As such, the phase lag change in the South Sound is smaller than the phase lag change in southern Admiralty Inlet or the Main Basin.

The system response is nearly linear, indicating that these cases are on the lower end of the theoretically extractable resource for Admiralty Inlet. The diurnal response (Figure 6.9c,d) is weaker than the semidiurnal, which is consistent with the results for the single constricted network evaluated in Chapter 4. The diurnal amplitude is reduced at all locations, which is qualitatively different from the semidiurnal response, but again analogous to the response in a single constriction network.

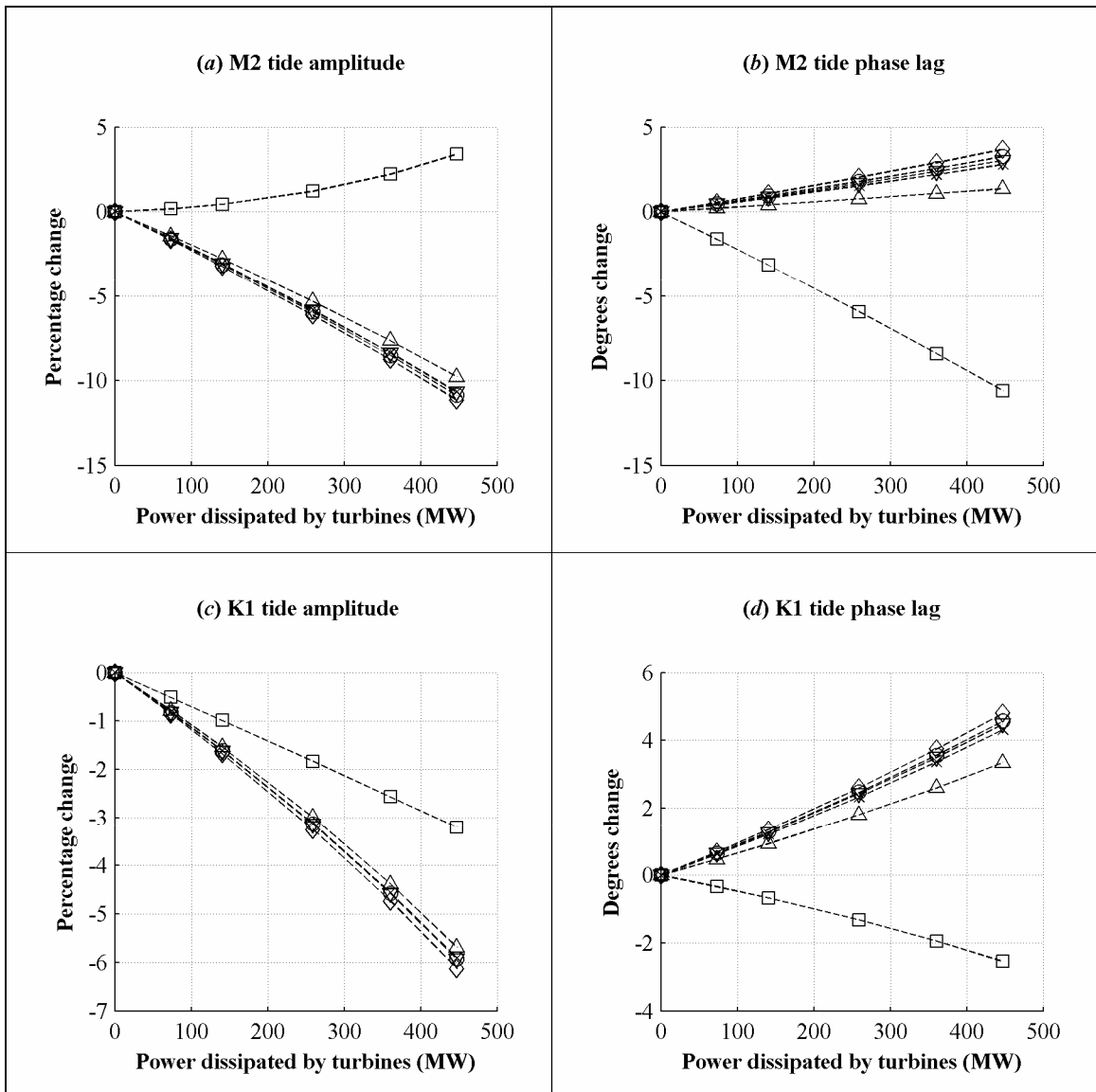


Figure 6.9 – Relative change to tides in Puget Sound due to power extraction in Admiralty Inlet. Symbols denote discrete number of turbine transects: 1,2,4,6, and 8 (□ S. Juan de Fuca, ◇ N. Admiralty Inlet, ○ Hood Canal, × Whidbey Basin, ▽ Main Basin, △ South Sound).

The same magnitude of relative change is seen with respect to tidal transport (Figure 6.10a), which decreases throughout the system. The relative changes are nearly indistinguishable between regions of Puget Sound. This is unsurprising since the model drives all flow into Puget Sound through Admiralty Inlet. The inclusion of the relatively small exchange through Deception Pass should not significantly alter these results. Conversely, high levels of extraction in Admiralty Inlet could alter the exchange through Deception Pass as a result of changed tidal amplitudes and phase at both ends of the channel.

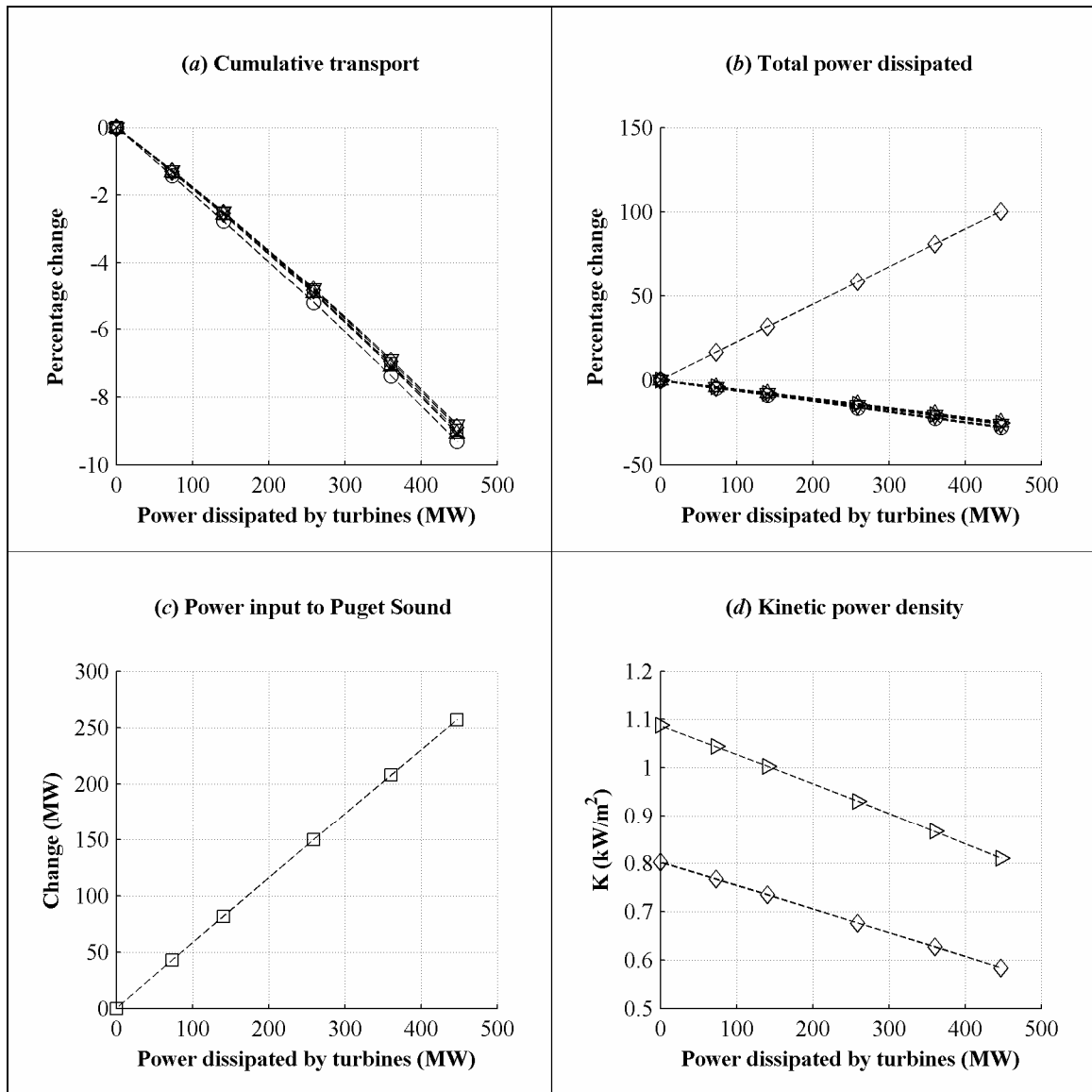


Figure 6.10 – Relative changes in Puget Sound due to power extraction in Admiralty Inlet. Symbols denote discrete number of turbine transects: 1,2,4,6, and 8 (\square S. Juan de Fuca, \diamond N. Admiralty Inlet, \circ Hood Canal, \times Whidbey Basin, ∇ Main Basin, \triangleright Tacoma Narrows, \triangle South Sound).

The effect on the power dissipated over the sills and in the basins of Puget Sound is quantitatively more pronounced than the response of the tides and transport (Figure 6.10*b*). In northern Admiralty Inlet, where additional power is dissipated by operation of turbines, the total power dissipated increases. However, as discussed previously, the power dissipated by friction declines everywhere in the system as a consequence of lower velocities. Though this model uses quadratic drag as a proxy for all power dissipation mechanisms, the reduction in frictional dissipation could be indicative of reduced mixing in the terminal basins, with implications for dissolved oxygen levels.

The additional power dissipated in Admiralty Inlet results in both reduced frictional dissipation throughout the system and an increased energy flux into Puget Sound (Figure 6.10*c*). For extraction in Admiralty Inlet, $\sim 1/2$ of the dissipation due to turbines is offset by decreased frictional dissipation and $\sim 1/2$ by an additional debit of power from the Strait of Juan de Fuca-Strait of Georgia system.

The decline in velocity translates to a decrease in the kinetic power density, as shown in Figure 6.10*d*. This effect is of particular relevance at the extraction site itself because kinetic power density is one of the key economic drivers for in-stream development [61]. Since the kinetic power density declines with extraction, there is a decreasing marginal benefit in terms of power generation for each additional turbine deployed at the site. The system-wide nature of these effects also means that extraction at Admiralty Inlet will reduce the resource in Tacoma Narrows. Therefore, the economic and power potential for these two sites is fundamentally linked.

6.4.2. Power Extraction in Tacoma Narrows

The system response to power extraction in Tacoma Narrows is more complicated with a relatively uniform response along the main axis of Puget Sound (Admiralty Inlet, Main Basin, South Sound), but relatively minor effects on the basins branching seaward of Tacoma Narrows (Hood Canal, Whidbey Basin).

For the M2 tide (Figure 6.11*a*), there is an amplitude reduction landward of extraction (South Sound) and amplitude increase in the seaward direction along the main axis, in Hood Canal, and in Whidbey Basin. In contrast, the change to the M2 phase lag (*b*) is much more uniform with nearly homogeneous decreases seaward of extraction and increases landward. The drivers for these trends are the same as those discussed for Admiralty Inlet. The diurnal response is qualitatively similar to the response to extraction in Admiralty Inlet with respect to both amplitude (*c*) and phase lag (*d*) seaward and landward of the extraction location.

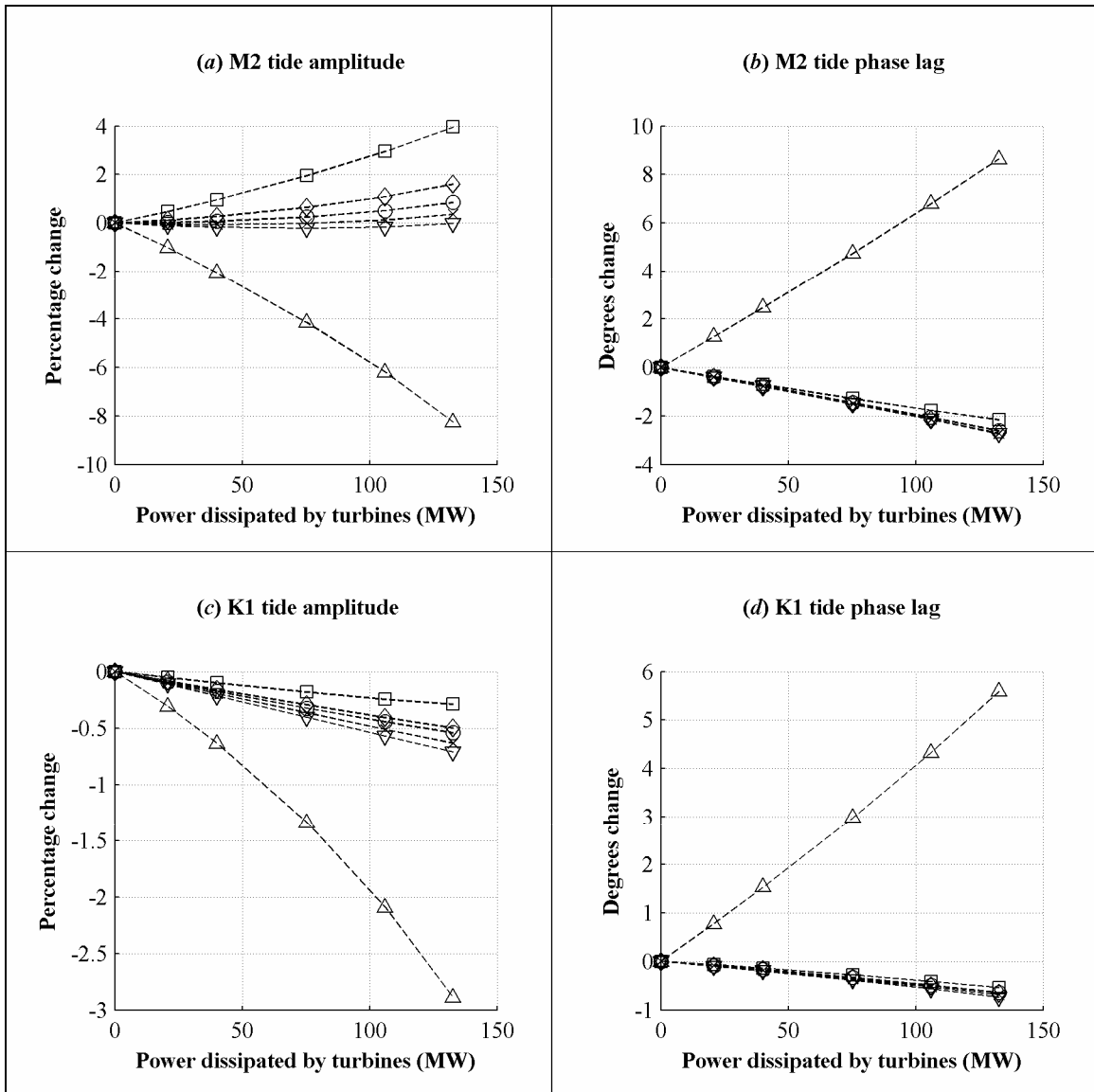


Figure 6.11 – Relative change to tides in Puget Sound due to power extraction in Tacoma Narrows. Symbols denote discrete number of turbine transects: 1,2,4,6, and 8 (□ S. Juan de Fuca, ◇ N. Admiralty Inlet, ○ Hood Canal, × Whidbey Basin, ▽ Main Basin, △ South Sound).

Changes to the cumulative transport (Figure 6.12a) show considerable spatial variability. Along the main axis of Puget Sound, the transport is reduced, but increases slightly in Whidbey Basin and Hood Canal. This indicates a minor flow redirection into these basins as a result of increased resistance to flow through Tacoma Narrows.

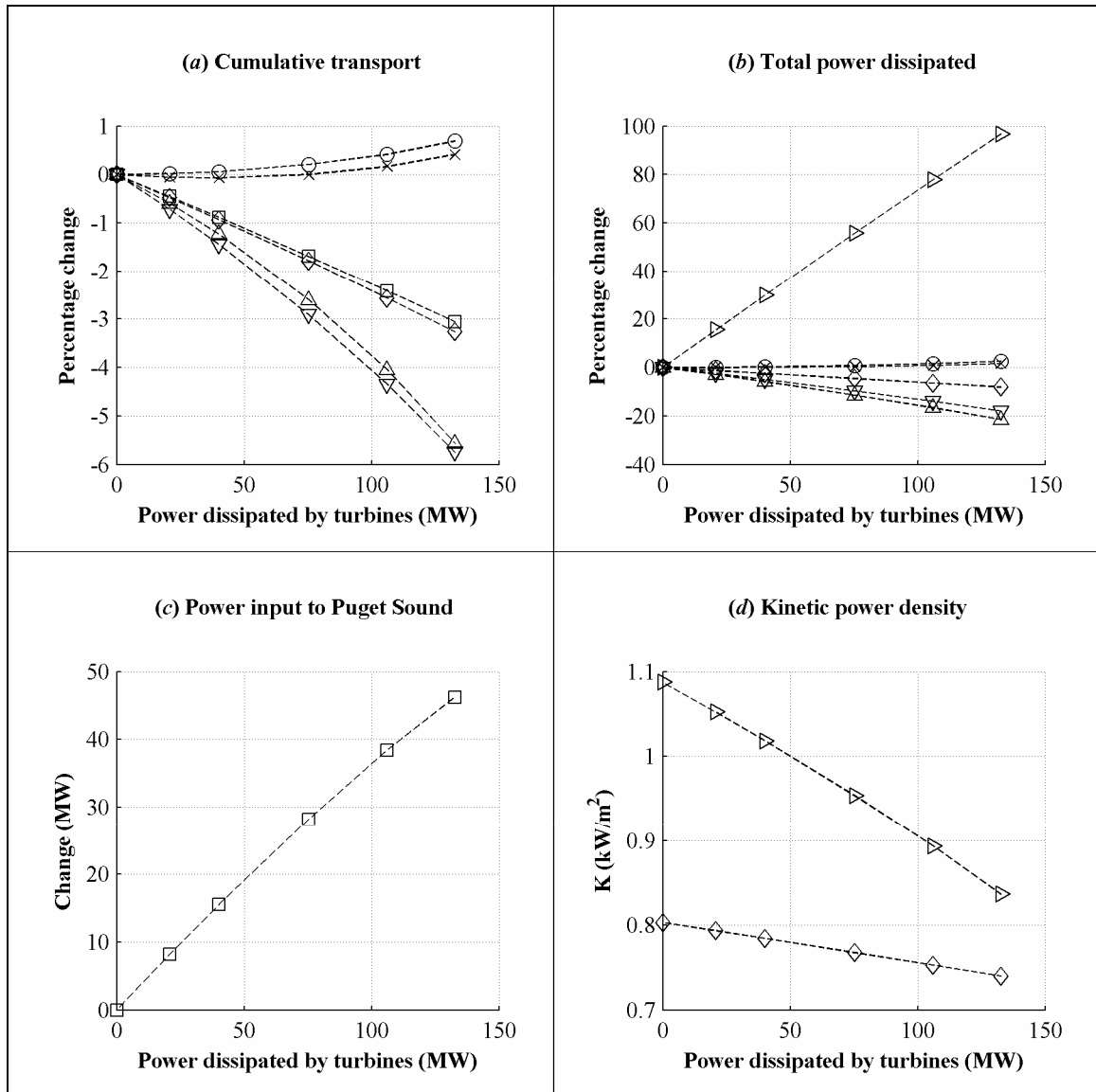


Figure 6.12 – Relative changes in Puget Sound due to power extraction in Tacoma Narrows. Symbols denote discrete number of turbine transects: 1,2,4,6, and 8 (\square S. Juan de Fuca, \diamond N. Admiralty Inlet, \circ Hood Canal, \times Whidbey Basin, ∇ Main Basin, \triangleright Tacoma Narrows, \triangle South Sound).

For total power dissipation (Figure 6.12*b*), the response along the main axis of Puget Sound is qualitatively similar to turbine operation in Admiralty Inlet, with declining power dissipation along the main axis, except in Tacoma Narrows. As is the case for transport, frictional dissipation increases very slightly in the basins branching seaward of Tacoma Narrows because of flow redirection.

The increased dissipation in Tacoma Narrows balanced by a decrease in frictional dissipation throughout Puget Sound and an increase in the power input to the system (Figure 6.12*c*). For

Tacoma Narrows, as for Admiralty Inlet, $\sim 1/2$ of dissipation by turbines is offset by increased energy flux at the head of the system.

Dissipation of power by in-stream turbines in Tacoma Narrows decreases the kinetic power density at that site and exerts a mutual influence on the power density at Admiralty Inlet (Figure 6.12*d*).

6.4.3. Implications for Project Development

So far, this analysis has considered only the cases of extraction in either Admiralty Inlet or Tacoma Narrows. Since development of in-stream energy at either site has system-wide effects, one would expect that simultaneous development would result in cumulative, system-wide effects that are an amalgam of the response to extraction at either site. As shown for the effect on transport in Figure 6.13, this is indeed true with joint extraction cases falling between the curves established for single-site development at each location.

As discussed in Chapter 2, only a portion of the power dissipated by an array of turbines is available for conversion to electrical power due to unavoidable losses associated with wake mixing. Using the assumptions listed at the beginning of this section, the system response can be recast in terms of the rated electrical capacity of an array (Figure 6.13 – top axis). Viewed in this manner, the development potential for Puget Sound is significant. An array with 650 MW rated electric capacity in Admiralty Inlet (200 MW average generation) would, for example, reduce the tidal transport in the South Sound by 5%. This is a measurable reduction, but this is also a significant level of power generation, on par with a large wind farm.

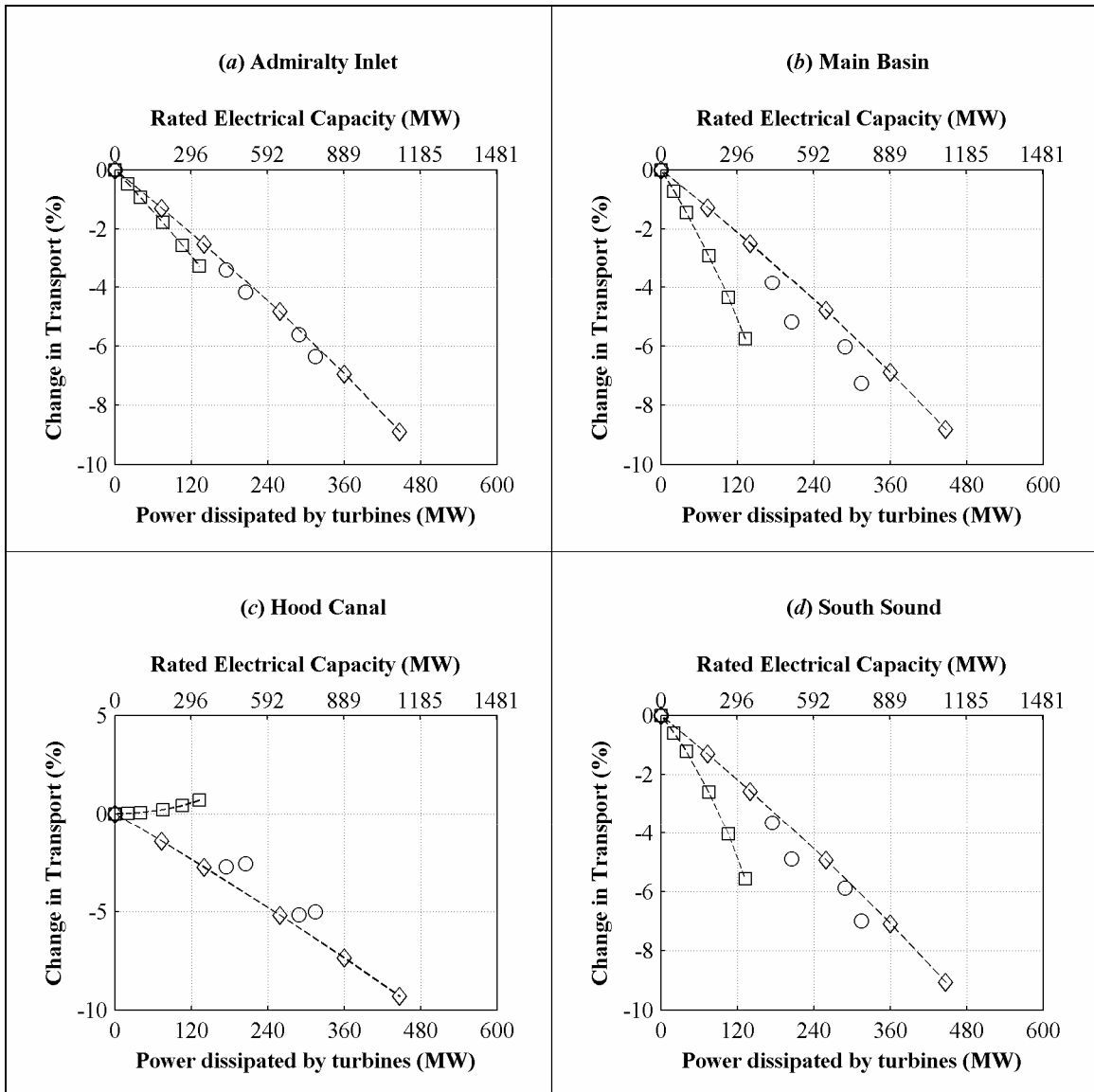


Figure 6.13 – Relative change to tidal transport in Puget Sound as a function of power dissipated by turbines in Tacoma Narrows and Admiralty Inlet. Symbols denote discrete number of turbine transects: 1,2,4,6, and 8. (\diamond extraction in N. Admiralty Inlet, \square extraction in Tacoma Narrows, \circ extraction in both N. Admiralty Inlet and Tacoma Narrows). Baseline values for each region are listed in Table 6.4.

These results also point to a complex trade-off in choosing where to develop tidal energy projects in Puget Sound. For any level of dissipation by in-stream turbines and, by extension, power generation, the *scale* of impact on the main axis of Puget Sound (South Sound, Main Basin, and Admiralty Inlet) is greater when development is concentrated in Tacoma Narrows. However, the *scope* of impact is larger when development is concentrated in Admiralty Inlet, with transport reductions both along the main axis and the branching basins (Hood Canal, Whidbey Basin). The

magnitude of the trade-offs to be considered and the potential for cumulative impacts indicate a need for regional coordination, rather than treating each site in isolation. Finally, in comparing the response to extraction for these two sites, it is clear that the maximum in-stream power potential in Admiralty Inlet is much greater than Tacoma Narrows. Due to the cumulative effects of site development, the potential for the entire Puget Sound is *not* the sum of each site's individual potential.

6.5. Comparison to Qualitative Predictions

Having now modeled extraction at two locations in Puget Sound, a qualitative comparison is made between the modeled behavior and the behavior which could be predicted by the prototypical networks discussed in Chapter 5.

For extraction in Admiralty Inlet, the prototypes suggest a general decrease in the tidal regime for Puget Sound since the entire region south of Admiralty Inlet is effectively a “basin”. The tidal range would, however, be expected to somewhat increase in the Strait of Juan de Fuca based on the behavior of serial and single constriction networks. This is exactly the response seen in the model (Figure 6.9, Figure 6.10). The serial constriction prototype also correctly predicts that the power potential for Admiralty Inlet should be higher than for Tacoma Narrows.

For extraction in Tacoma Narrows, the serial constriction prototype suggests reductions to transport, power dissipation, and kinetic power density along the main axis of Puget Sound. Also along the main axis, the tidal range should increase seaward of Tacoma Narrows and decrease landwards. Both Hood Canal and Whidbey Basin branch from the main axis seaward of Tacoma Narrows. Based on the branching network prototype, the tidal regime of these branches should be somewhat augmented, though not to the same extent that the tidal regime is reduced along the main axis. Again, this is exactly the behavior seen in the model (Figure 6.11, Figure 6.12) and builds confidence in the value of qualitative predictions for the behavior of more complicated systems using the results from prototypical networks.

Puget Sound is effectively a small branch in the Strait of Juan de Fuca – Strait of Georgia system. Assuming that branching will behave in a qualitatively similar manner to a prototypical network, development in either Admiralty Inlet or Tacoma Narrows should augment the tides in the Strait of Georgia and the Strait of Juan de Fuca. It is unclear, however, whether this augmentation will be small in comparison to the reduction in Puget Sound (as is the case for the branching prototype and the branching basins of Puget Sound) or on the same order as the reduction (as is the case for

the hybrid network). Since, approximately 75% of the water entering through the Strait of Juan de Fuca passes into the Strait of Georgia versus 25% into Puget Sound [62], it would be anticipated that the effect of extraction on the tides outside of Puget Sound would be limited. Additional modeling is required to address this point.

6.6. Effects of Possible Development on Puget Sound

This model may also be used to obtain a preliminary estimate for the effects of a proposed pilot project in Admiralty Inlet and a commercial array that is the subject a feasibility study for the same site.

The near-term goals for tidal energy development in Puget Sound are much more limited and call for the installation of a pilot demonstration facility consisting of no more than three devices with a rated capacity of at most 3 MW [63]. The goal of this a pilot project would be to gain operational experience with utility-scale devices and to begin answering some key near-field environmental questions. Using the same assumptions as for a commercial plant, the largest proposed pilot array would, on average, dissipate 1.2 MW of kinetic power. The far-field effects of extraction from an array this size would have an immeasurably small effect on the tidal regime of Puget Sound, as detailed in Table 6.5. Any detectable effects should be confined to near-field flow variations in the immediate vicinity of the devices.

Table 6.5 – Far-field effects of proposed Admiralty Inlet pilot project on regions of Puget Sound (1.2 MW average dissipation).

	Admiralty Inlet	Tacoma Narrows	Main Basin	Hood Canal	Whidbey Basin	South Sound
Tide						
M2 amplitude (mm)	-0.2	-0.3	-0.3	-0.3	-0.3	-0.3
K1 amplitude (mm)	-0.1	-0.1	-0.1	-0.1	-0.1	-0.1
Cumulative transport (%)	-0.02	-0.02	-0.02	-0.02	-0.02	-0.02
Dissipated power (MW)	+1.0	-0.07	-0.05	-0.008	-0.02	-0.03
Kinetic power density (kW/m²)	0.8	1.1	-	-	-	-

A recent study investigates the technical and economic feasibility of a commercial array of turbines in Admiralty Inlet which would extract, on average, 45 MW of kinetic power (135 MW rated electric capacity) [61]. This corresponds to 55 MW of average dissipation. For an installation of this size, the far-field impact would be small, but possibly measurable, as detailed in Table 6.6.

Table 6.6 – Far-field effects of possible Admiralty Inlet commercial project on regions of Puget Sound (55 MW average dissipation).

	Admiralty Inlet	Tacoma Narrows	Main Basin	Hood Canal	Whidbey Basin	South Sound
Tide						
M2 amplitude (cm)	-1.0	-1.3	-1.2	-1.3	-1.2	-1.5
K1 amplitude (cm)	-0.5	-0.5	-0.5	-0.5	-0.5	-0.5
Cumulative transport (%)	-1.0	-1.0	-1.0	-1.1	-1.0	-1.0
Dissipated power (MW)	+43	-3.3	-2.3	-0.4	-1.1	-1.4
Kinetic power density (kW/m²)	0.8	1.1	-	-	-	-

There are also engineering considerations which might preclude the construction of an array of this size. For example, the rated electrical capacity of 135 MW would possibly exceed the available interconnection capacity near the project site. Therefore, in addition to the ecological impacts of a commercial project, there may also be infrastructure barriers. An array of this size in Admiralty Inlet would not be expected to significantly reduce the kinetic power density at Tacoma Narrows and, therefore, have no impact on project economics at that site.

There is a large potential resource in Puget Sound but there are similarly far-reaching environmental questions which must be addressed. The average electrical demand for the city of Seattle is approximately 1200 MW on average. A large-scale development in either Admiralty Inlet or Tacoma Narrows could supply an appreciable fraction of this with limited changes to the barotropic tidal regime (e.g., 5% reduction in tidal range for 200MW average generation). A clear next step is to extend this assessment to the baroclinic regime to study the effects of extraction on stratified flows. Beyond this lies the more daunting task of quantifying the biological implications for changes to salinity, transport, and mixing due to in-stream energy extraction.

7. 3D Models for Far-field and Near-field Extraction Effects

As demonstrated in Chapter 6, a 1D model is an efficient tool for preliminary resource assessment of in-stream tidal energy sites. The model described in this dissertation could be refined in a number of ways. For example, the governing equations could be modified to allow for prismatic channels of variable width and depth. This would enable more accurate representations of estuarine bathymetry. Or, the model could be modified to solve the governing equations using an implicit, rather than explicit, numerical algorithm. This could allow for longer time steps and decreased simulation time. However, these are both incremental changes that would be unlikely to provide additional insight into the basic physics of kinetic power extraction. Depth-averaged 2D models are also suitable for exploring far-field extraction effects [12,13,15] and are able to faithfully reproduce the tides and currents in topographically complex estuaries (e.g., Johnstone Strait, British Columbia).

However, neither 1D nor 2D models are capable of fully investigating the effects of kinetic power extraction on the baroclinic tidal regime. Baroclinic effects drive a number of ecologically important processes, including the transport of oxygen-rich water from the open ocean to regions of low oxygen concentration within estuaries. In Hood Canal, Washington, for example, these renewals occur only a few times a year and may be disrupted by high levels of fresh-water run-off [72]. If these renewals were to be permanently disrupted by turbine operation, there could be significant consequences for hypoxic (low oxygen) or anoxic (no oxygen) conditions in the deeper basins of Puget Sound. A numerical model able to rigorously investigate baroclinic effects must be capable of simulating the tidal regime for a period of years at a reasonable computational cost. This effort also requires a suitable representation for turbines, or turbine arrays, in a 3D model. In a 2D model, as in a 1D model, the water column is vertically averaged and a representation of turbines as bottom drag [12,13,15] is consistent with the physics of kinetic power extraction. In three dimensions, the turbine diameter is of the same characteristic length as the water depth and representing the turbines as increased bottom drag would remove power from the wrong portion of the water column. Since baroclinic circulation is driven by well-defined vertical density gradients, the model for extraction must act on the flow in a vertically-accurate manner.

This extraction model would also be applicable to the study of array-scale redirection. This involves the diversion of high speed flow around arrays which are not evenly distributed on a

channel cross-section [19] and is analogous the flow redirection observed in multiply-connected networks in Chapter 5.

The length scales required to fully resolve viscous flow over a turbine blade are $O(10^{-3}$ m), while the surface area of complex estuaries is $O(10^9$ m²) and the Reynolds numbers in energetic tidal are $O(10^8)$. Therefore, models capable of resolving the forces acting on a turbine are not suitable for investigating turbine effects on an estuary-scale. A parameterization of a device, or an array of devices, is needed. Bottom drag is one such parameterization, but is not physically justified in three dimensions. A robust parameterization must:

- (1) *Dissipate the same amount of power as an actual array of turbines.* From an environmental standpoint, matching dissipation is more important than matching extraction since far-field effects depend on the power dissipated.
- (2) *Accurately represent the extent of near-field changes in the flow.* For example, the wake of a parameterized device or array should have a persistence similar to the actual device or array.
- (3) *Have low computational overhead.* The inclusion of turbines should not greatly increase the time required for an estuary-scale simulation of baroclinic effects or near-field flow changes.

This chapter begins with a review of techniques developed to simulate kinetic power extraction in three dimensions. Techniques are primarily evaluated on the basis of their potential application to the study of estuary-scale effects. This is followed by a brief discussion of the differences between various 3D oceanographic models. Finally, preliminary results are presented for the implementation of in-stream turbines in one particular oceanographic model, SUNTANS.

7.1. Approaches for Numerical Modeling of Kinetic Power Extraction

In Section 7.1.1, three-dimensional numerical models for tidal in-stream energy extraction are reviewed. In Section 7.1.2, analogues from wind energy are considered. This section concludes with a description of a parameterized turbine representation suitable for estuary-scale modeling.

7.1.1. Numerical Models of Tidal In-stream Energy Extraction

Antheaume et al. [74,75] implement a model for arrays of vertical axis turbines in FLUENT, a commercial CFD code, to predict power generation for an array. The FLUENT simulation incorporates blade element momentum theory to predict device performance, rather than

resolving the flow over the turbine rotor. Blade element momentum theory extends the actuator disc concept described in Chapter 2 to a series of concentric streamtubes over the turbine swept area. The FLUENT model for an individual device is validated against both a more detailed simulation of the same device using vortex theory and wind tunnel measurements of a vertical axis turbine. In the FLUENT simulation, the effects of the free surface and seabed are neglected, and the incoming flow is assumed to be uniform. These approximations are not appropriate for an estuary-scale modeling effort.

Bahaj et al. [10, 76-82] develop numerical simulations of horizontal axis turbines also using blade element momentum theory. The models proposed by Bahaj et al. are used to predict blade forces, the onset of cavitation, and device performance. Modeling is for a single device and is not yet extended to arrays. Models are validated against cavitation tunnel studies of small-scale turbines (e.g., 0.8 m diameter). Device wakes are also investigated using a laboratory flume. In the flume experiments, the wake is generated either by a scale model of a device or by a porous mesh parameterizing the device.

Sun et al. [83] use FLUENT to model the changes to the flow in a small-scale channel (1.5 m wide and 1 m deep) for partial obstruction by a porous mesh parameterizing a turbine. In future work, simulations will be validated against flume experiments [84] and then scaled up to full-size devices. The effect of the free surface is included in the simulation. The free surface implementation in FLUENT is computationally inefficient for this class of problems and has a high cost for a large domain. However, the parameterization of a horizontal axis turbine as elevated drag over is a low-cost parameterization for a device.

None of the models discussed here are directly applicable to estuary-scale flows. FLUENT, while a powerful tool, is ill-suited for regional oceanographic simulations. However, the approaches taken by these authors to validate device parameterization are instructive.

A general challenge in this effort is a lack of tidal turbine data for model validation. There have been fewer than a dozen full-scale device demonstrations worldwide and detailed observations of the flow field from these activities have not entered the public domain. Consequently, neither flume experiments nor numerical models have been rigorously validated against field measurements. In contrast, a number of wind turbine farms have been instrumented [e.g., 85] and these data have been used to validate numerical models and develop engineering rules for optimal wind turbine spacing.

7.1.2. Numerical Models of Wind Energy Extraction

The simulation of large wind turbine arrays in complex terrain is an active area of research. Excellent reviews of wind turbine wake aerodynamics may be found in Vermeer et al. [86] and Crespo et al. [87]. The industry standard approach for predicting array performance is to apply blade element momentum theory to a single device and then extend the results to an array using empirical rules to account for wake interaction and topography. Since there are no array-scale experimental data for tidal energy systems, an analogous approach is not possible in the short-term. Therefore, the methods of primary interest are the ones for which the effects of an array are modeled from the basic physics. In general, the flow field, aside from the influence of the devices, is readily described by conventional CFD codes. Array-scale parameterizations for wind turbines include:

- (1) *Increased surface drag*, as used in regional simulations for far-field effects of wind farms. This is the nearest analogue to the modeling of estuary-scale effects for tidal energy arrays. In this method, the effect of the array is parameterized as elevated surface roughness. As previously noted, representing in-stream turbines as bottom drag is not appropriate for 3D simulation. This method cannot accurately predict the performance of the parameterized devices to changing inflow conditions.
- (2) *Applying an actuator disc approximation for an individual device*, in which the forces acting on the rotor are distributed over its swept area. These forces may be either uniform or vary radially. Surficial forces act as a discontinuity in the direction of the flow. These forces are determined either by a coarse parameterization (e.g., uniform drag coefficient) or by a higher order sub-model (e.g., blade element momentum theory). If higher order sub-models are used to represent the device, it is possible to make reasonably accurate predictions of performance.
- (3) *Vortex theory models*, in which a turbine blade is described by lifting lines of bound vortices in the flow. Vortex models accurately reproduce the near wake structure and performance of an individual turbine. These are also the lowest-cost class of models capable of reproducing the coherent vortex structure which exists within a few diameters of the device. However, this class of methods is too computationally intensive to be applied to an array.
- (4) *Direct Navier-Stokes solution*, in which the viscous forces on the rotor are fully resolved. This method has a high computational cost and is not suitable for simulation

of more than a single turbine. However, it is the most accurate method for modeling device performance under a wide variety of operating states and inflow conditions and accurately reproduces the near wake structure.

Once the effect of the turbine on the flow has been prescribed by one of these methods for the near wake, the far wake and wake interactions with other devices, topography, and ambient turbulence may be investigated using a Navier-Stokes solution to the flow field. Higher order turbulence closures are required to reproduce anisotropy experimental observed in the wake [88], but a $k-\varepsilon$ closure is suitable for basic investigation.

The in-stream tidal simulations reviewed in the previous section are derivative of these approaches. Antheaume et al. [74,75] use an actuator cylinder (vertical axis equivalent of an actuator disc) with a blade element momentum sub-model. Sun et al. [83] use increased drag over part of the water column to parameterize power extraction, which is consistent with the underlying physics. Bahaj et al. [76-81] use blade element momentum theory to predict device performance.

As for tidal energy simulation, most work in this area of wind energy research is focused on device performance prediction, rather than modeling of arrays. A few recent papers are indicative of the status of array-scale modeling.

Eidsvik [89] demonstrates the use of nested atmospheric models with increasing resolution and complexity to characterize the wind resource in mountainous terrain. This progression allows the results of a large-scale atmospheric model for weather prediction to drive higher resolution models for wind resource mapping in topographically complex terrain. While no device performance predictions are made in this work, this method would be applicable to situations in which kinetic power extraction by wind turbines only influences the flow in the highest resolution model. However, for tidal energy simulations (where extraction has significant far-field effects), the highest resolution model would either be required to provide feedback to the lower resolution models (two-way nesting) or a parameterization of extraction would need to be included in the lower resolution models. Two-way nesting of oceanographic models has been proposed by Fringer et al. [90], but not yet implemented. One-way nesting may be more feasible in the short term, but would require a computationally intensive iterative approach to develop consistent device parameterizations at different grid resolutions.

Migoya et al. [91] consider the effect of terrain on wind farm performance using the UPMPARK code [92]. UPMPARK makes a number of approximations which reduce the governing equations to parabolic form and is suitable for simulating arrays of turbines. The operation of turbines is assumed to not affect the wind regime far upstream or downstream of the array. The model agrees well with observations of a wind farm in moderately complex terrain, but performs poorly in regions with rapidly changing topography. This study also uses FLUENT to model the wind resource in complex terrain, but the computational cost is deemed too high to directly model turbine performance or resolve wakes. It does not appear viable to adapt the UPMPARK code to tidal turbines. The code parameterizes the turbine rotor as a velocity discontinuity containing the device and wake. As a result, the pressure field is uniform in the axial direction through the domain. The implementation of energy extraction as a velocity, rather than force or pressure, discontinuity would appear to violate mass conservation and is not appropriate for tidal simulations.

Masson et al. [93] and Ammara et al. [94] investigate array performance using an actuator disc model for turbines. The flow field is modeled by a steady-state Navier-Stokes implementation. Devices are described by a non-uniform distribution of surficial forces over the rotor swept area. The surficial forces are applied along the interface between grid volumes and are modeled by blade element momentum theory. Results show good agreement with experimental data. This method is probably too computational intensive for estuary-scale simulations, but could provide a useful framework for determining the performance of an array of in-stream turbines on a limited domain. This is similar to the method used by Antheuame et al. [74,75] to study the performance of vertical axis tidal turbines.

7.1.3. Approach for Estuary-scale Modeling

For three-dimensional estuary-scale modeling of far-field effects, the only feasible approach discussed above is a variation on the method employed by Sun et al. [83], in which a device or several devices are parameterized as elevated drag in a region of the model. This provides a vertically-accurate representation of kinetic power dissipation by in-stream turbines. Of the three requirements laid out at the beginning of this chapter, this approach clearly satisfies the requirement of low computational cost. However, it is not clear, *a priori*, that this approach can accurately describe the near-field influence or dissipation of an actual device. Given the computationally feasible grid resolution, it is not possible to resolve an actuator disc in an estuary-scale simulation. However, an investigation of near-field effects for moderately sized

arrays should not require a model of an entire estuary, and an actuator disc parameterization may be appropriate in these cases.

7.2. 3D Oceanographic Models

A number of 3D oceanographic models are used in research and industry including: ROMS [95,96], SUNTANS [73], FVCOM [97], and SELFE/ELCIRC [98]. These models may be classified by the structure of the grid, treatment of pressure dynamics, and available turbulence closures. These codes are all parallelized and able to model baroclinic effects. A high-level summary of these models is given in Table 7.1.

Table 7.1 – Comparison of 3D oceanographic models

Code	Horizontal Grid	Vertical Grid	Dynamics	Turbulence Closure
ROMS	Structured	Terrain-following	Hydrostatic*	Generic Length Scale (GLS)
SUNTANS	Unstructured	Fixed coordinate	Non-hydrostatic	Mellor-Yamada 2.5
FVCOM	Unstructured	Terrain-following	Hydrostatic*	GLS
SELFE	Unstructured	Hybrid	Hydrostatic	GLS

*Non-hydrostatic version in development

As discussed in Chapter 2, theory suggests that the pressure field immediately upstream and downstream of the turbine may be non-hydrostatic. Since SUNTANS is written as a non-hydrostatic code, it is the logical choice to study this effect. It is also possible to run SUNTANS in a hydrostatic mode to directly investigate the effect of non-hydrostatic pressure on the turbine parameterization.

7.2.1. SUNTANS

SUNTANS, the Stanford Unstructured Non-hydrostatic Terrain-following Adaptive Navier-Stokes Simulator, is a three-dimensional, quasi non-hydrostatic oceanographic code developed at Stanford University [73]. The code solves the Navier-Stokes equations using a finite volume discretization on a grid which is unstructured horizontally, but structured vertically. Pressure is decomposed into a hydrostatic and non-hydrostatic component. Density depends on salinity, which allows for stratified flow. The turbulence closure is Mellor-Yamada 2.5. SUNTANS is implemented in C and uses an MPI parallelization with automatic load balancing [73]. The code remains under active development at Stanford University. Updates which have been developed and may be included in future releases of the main version are a new advection scheme for wetting and drying of tidal flats, immersed boundary conditions, and a generic length scale (GLS) turbulence closure. SUNTANS is used to accurately simulate internal waves in Monterey Bay [99] and the interaction of tides with complex bathymetry in the Snohomish River estuary [100].

The Navier-Stokes equations, as solved by SUNTANS, are

$$\nabla \cdot \mathbf{u} = 0, \quad (7.1)$$

$$\frac{\partial u}{\partial t} + \nabla \cdot (\mathbf{u}u) - fv + bw = -\frac{1}{\rho} \frac{\partial q}{\partial x} - g \frac{\partial \eta}{\partial x} + \nabla_H \cdot (\nu_H \nabla_H u) + \frac{\partial}{\partial z} \left(\nu_V \frac{\partial u}{\partial z} \right), \quad (7.2)$$

$$\frac{\partial v}{\partial t} + \nabla \cdot (\mathbf{u}v) + fu = -\frac{1}{\rho} \frac{\partial q}{\partial y} - g \frac{\partial \eta}{\partial y} + \nabla_H \cdot (\nu_H \nabla_H v) + \frac{\partial}{\partial z} \left(\nu_V \frac{\partial v}{\partial z} \right), \text{ and} \quad (7.3)$$

$$\frac{\partial w}{\partial t} + \nabla \cdot (\mathbf{u}w) - bu = -\frac{1}{\rho} \frac{\partial q}{\partial z} + \nabla_H \cdot (\nu_H \nabla_H w) + \frac{\partial}{\partial z} \left(\nu_V \frac{\partial w}{\partial z} \right). \quad (7.4)$$

In the above equations, u , v , and w are the Cartesian components of velocity, \mathbf{u} is the vector form of velocity, q is the non-hydrostatic component of pressure, η is the free surface elevation, f and b are the Coriolis terms, and ν_H and ν_V are the horizontal and vertical turbulent eddy viscosities. ∇_H is compact notation for the horizontal gradient operator,

$$\nabla_H = \frac{\partial}{\partial x} \hat{i} + \frac{\partial}{\partial y} \hat{j}. \quad (7.5)$$

In the formulation given above, the pressure term has been split into a hydrostatic (η) and non-hydrostatic (q) component. The solution is by a predictor-corrector algorithm, the full details of which are described in Fringer et al. [73].

The unstructured horizontal grid uses triangular elements, thus forming prismatic, triangular volumes. A Voronoi diagram of the SUNTANS grid is shown in Figure 7.1 [73]. Voronoi points lie at the center of the circumcircle passing through the vertices of each triangular element. Delauney edges connect the vertices of each element [73]. Voronoi lines connect adjacent Voronoi points and are orthogonal to the Delauney edges on an ideal grid consisting of equilateral triangles. Horizontal velocities are defined normal to the vertical midpoint of each cell face at the intersection of the Voronoi line and Delauney edge. Vertical velocity and non-hydrostatic pressure are defined at the Voronoi point at the intersection of vertical levels.

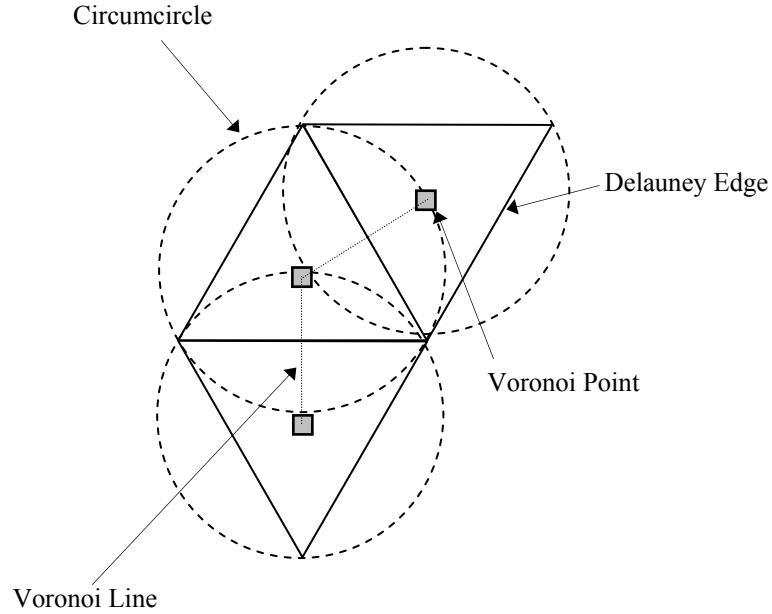


Figure 7.1 – Voronoi diagram of unstructured grid.

7.3. Implementation of Parameterized Turbines

7.3.1. Mechanics of Implementation

Turbines have been parameterized in SUNTANS as elevated drag obstructing a portion of the flow in a manner similar to the one used by Sun et al. [83]. The elevated drag corresponds to additional source terms in the momentum conservation equations, (7.1) and (7.2). For testing purposes, turbines are aligned perpendicular to the along-channel flow and the y -component source term is zero. As suggested by unpublished research on changes to flow around fish cages [101], the additional drag due may be included in the discretized equations as

$$D_{j,k} = -\beta \Delta t u_{j,k} |u_{j,k}|, \quad (7.6)$$

where $D_{j,k}$ is the drag acting at horizontal index j and vertical level k , $u_{j,k}$ is the velocity at the same location, Δt is the model time step, and β is a constant parameterizing the drag across the cell. Defining the relation between β and the power extracted by a real device represents the main challenge to this approach. The discretized drag term is functionally similar to the relation for bottom friction in a 1D model given by (4.4). This approach differs fundamentally from an actuator disc in three respects. First, the force representing the turbine acts over a finite cell volume, rather than as a spatial discontinuity. Second, the turbine exerts only a normal force on the flow, rather than both a force in the normal and tangential directions. Finally, the turbine is considerably undersampled at the coarse grid resolutions used here.

The feasibility of this device parameterization is demonstrated on a 2D (x - z) grid. This greatly reduces the complexity of the problem, but still allows for investigation of the role of hydrostatic pressure and vertical resolution. A comparison is also made between the performance of the parameterized turbine and the theoretical performance for a turbine with a comparable blockage ratio.

7.3.2. Numerical Domain

The numerical domain used to prototype this implementation of parameterized turbines is a 2D (x - z) channel 4 km in length, with a nominal depth of 40 m. In a 2D domain, the horizontal grid is one cell wide and composed of equilateral triangles with a cell center separation of 12 m. The vertical grid resolution (Δz) is 2.5 m. The domain is open on both ends, a no-slip condition is prescribed at the seabed, and a free-slip condition is prescribed for the channel walls and free surface. For the purposes of a steady-state test, the model is forced by a constant flow rate of 100 m²/s. This results in a depth-averaged velocity of 2.5 m/s. The bottom roughness (z_0) is selected such that the vertical velocity structure is approximately described by a 1/7th power law;

$$u(z) = u_{ref} \left(\frac{z}{z_{ref}} \right)^{1/7}. \quad (7.7)$$

Here u is the horizontal velocity as a function of depth, z is the depth, and the *ref* subscript denotes the reference depth. On a time-averaged basis, the vertical structure for tidal energy sites is well-characterized by a power law of this type [70]. Figure 7.2 compares the vertical structure of the horizontal velocity against one described by a 1/7th power law.

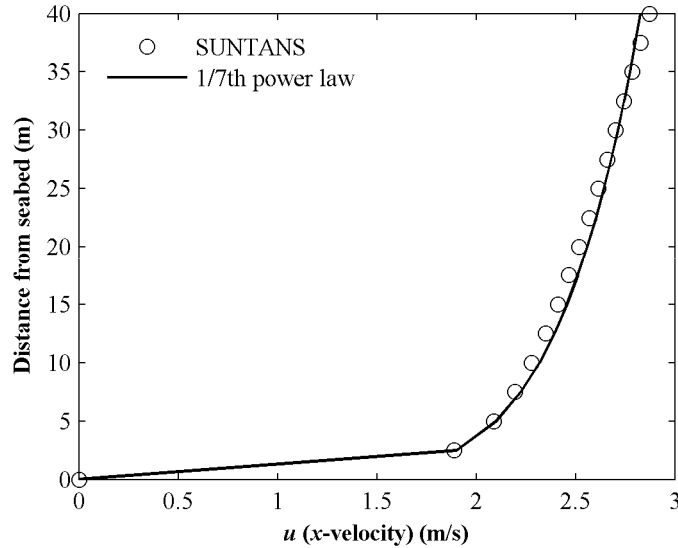


Figure 7.2 – Vertical structure of horizontal velocity (x-component) in the prototype domain without power extraction.

SUNTANS calculates a drag coefficient based on a rough wall law [102]

$$C_D = \left[\frac{1}{\kappa} \ln \left(\frac{1}{2} \frac{\Delta z}{z_0} \right) \right]^{-2}, \quad (7.8)$$

where κ is the von Karman constant ($\kappa = 0.4$) and Δz is the vertical grid spacing. A bottom roughness of 5×10^{-3} m corresponds to a drag coefficient of 5×10^{-3} , in-line with measurements for an estuarine sill [68].

For basic investigation, elevated drag ($\beta = 0.3$) is prescribed in one horizontal cell spanning four vertical levels, as shown in Figure 7.3. This corresponds to an array of devices 10m in height. The value of β used here is for illustrative purposes only and a preliminary description of the relation between β and device performance is made in Section 7.3.6. The flow structure is described in terms of two non-dimensional coordinates: x/D in the horizontal plane and z/D in the vertical plane, where D is the turbine diameter. For this 2D simulation, D is taken as the vertical dimension of the blockage (10 m) and the origin in both dimensions is at the vertical centerline of the turbine.

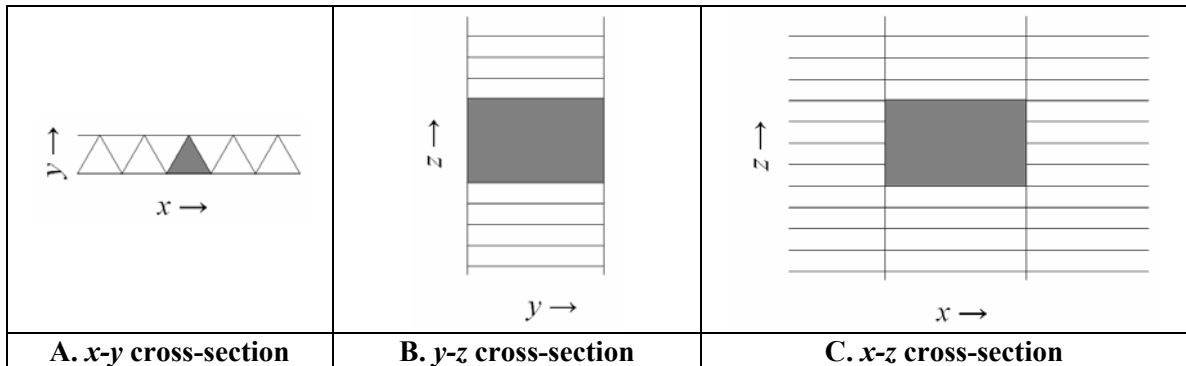


Figure 7.3 – Sample cross-sections of the prototype grid for turbine parameterization in SUNTANS. Lines denote cell edges. The shaded cells include the horizontal momentum source term parameterizing the turbine.

7.3.3. Near-field Extraction Effects

The effect of the parameterized turbine on the horizontal velocity field is shown in Figure 7.4a for a longitudinal x - z cross-section. The 2D velocity vector field for the same cross-section is shown in plot (b). Qualitatively, the behavior is similar to that described by the streamtube theory presented in Chapter 2. Upstream of the turbine, the horizontal velocity around the turbine axis begins to slow, while the free stream is accelerated around the blockage. This flow acceleration may have implications for scour around turbine foundations if the seabed substrate is a material other than bedrock (e.g., consolidated sediments). Downstream of the turbine there is a pronounced velocity deficit, which diminishes with increasing distance from the device. Across the turbine, vertical velocity (c) and non-hydrostatic pressure (d) are elevated from the free-stream values. Because the grid is two-dimensional, changes to the lateral (x - y) flow structure cannot be quantified.

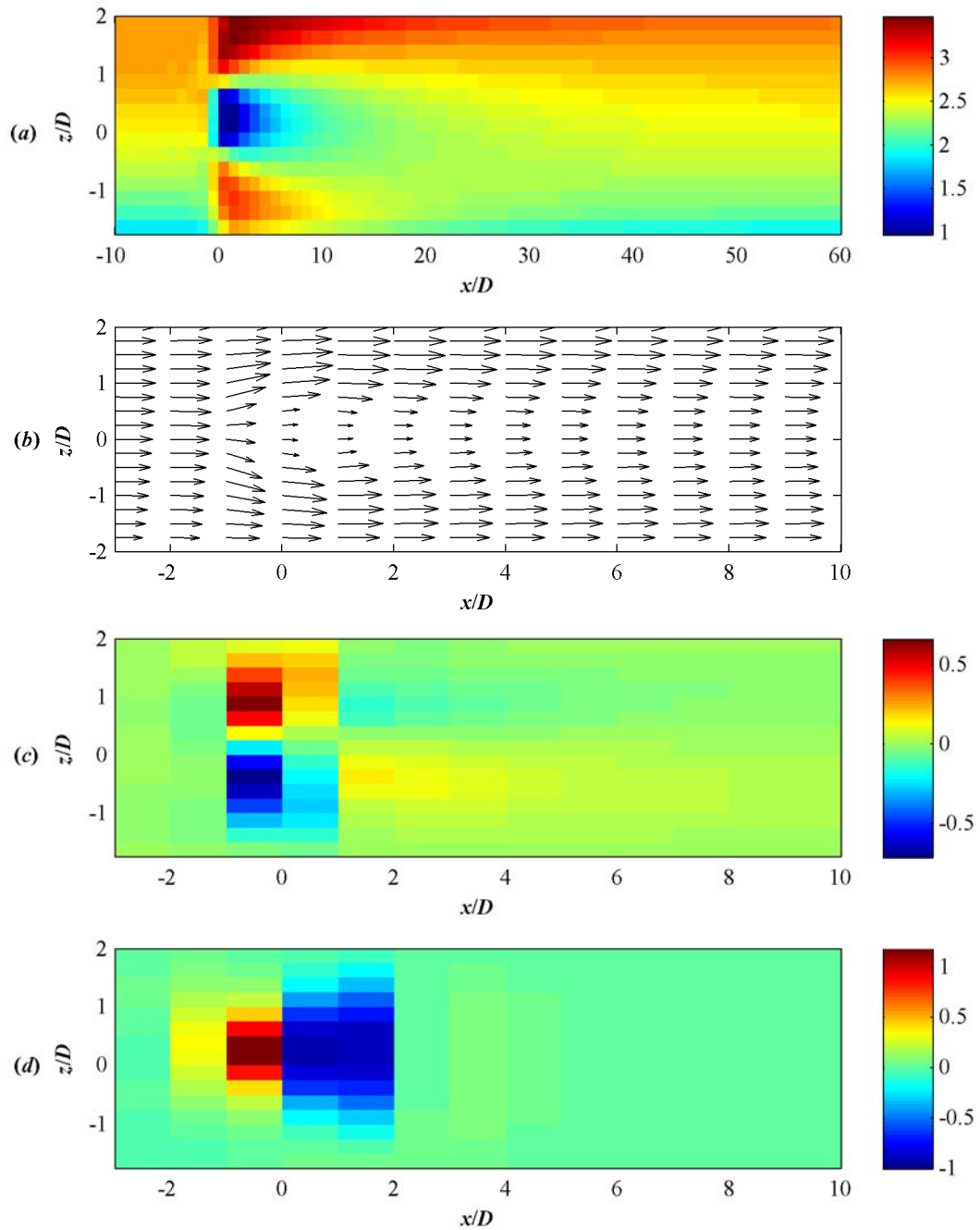


Figure 7.4 – Flow quantities on a non-dimensional x - z cross-section passing through a parameterized turbine ($D = 10\text{m}$, $\beta = 0.3$). (a) x -component of velocity (m/s), (b) x - z plane velocity vectors, (c) z -component of velocity (m/s), (d) non-hydrostatic pressure. The region containing the parameterized turbine is defined by $0 \leq x/D \leq 10$ and $-0.5 \leq z/D \leq 0.5$.

Figure 7.5 shows the non-dimensional velocity deficit downstream of the turbine. The non-dimensional velocity deficit for each vertical level is defined as

$$\frac{\Delta u}{u_0} = \frac{u - u_0}{u_0}, \quad (7.9)$$

where u_0 is the velocity upstream of the turbine. The velocity deficit declines to less than 10% within twenty turbine diameters.

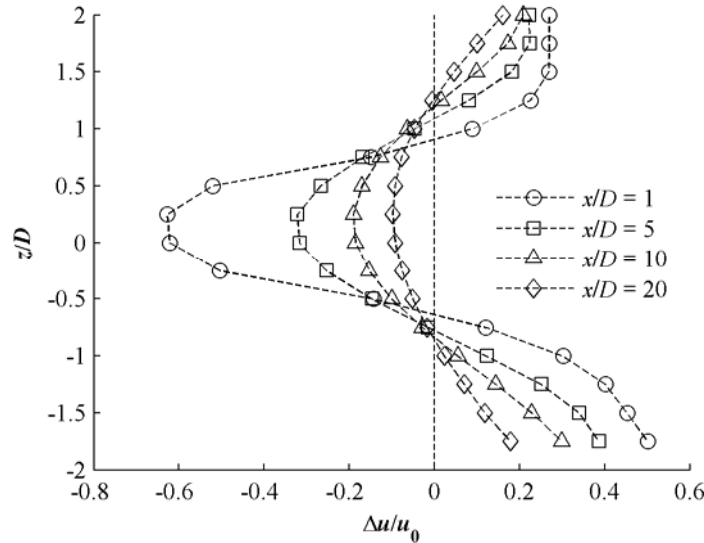


Figure 7.5 – Non-dimensional velocity deficit at four downstream positions ($D=10\text{m}$). Velocities are normalized by conditions $10D$ upstream of the turbine.

Bahaj et al. [76] report a similar decay (10% deficit at $20D$) in experiments with a porous disc simulating a turbine in a water channel. The decay reported in Sun et al. [83] is slightly faster ($\sim 13\%$ deficit at $10D$). However, the deficit decay in all three investigations is much slower than observed for a wind farm by Höglström et al. [85], who report a decay to $\sim 7\%$ within $10D$. This suggests that there may be a fundamental difference in wake persistence for marine energy systems.

Figure 7.6 highlights the exchange of potential and kinetic energy across the parameterized turbine. Results are consistent with the streamtube theory presented in Chapter 2, with the free surface dropping sharply over the turbine, and then rising as the wake mixes with the free stream. The profile is qualitatively similar to the ones reported in Sun et al. for a 3D simulation [83] and in flume experiments by Myers and Bahaj [82]. The free surface decrease is accompanied by a comparable increase in depth-averaged velocity, indicating an exchange of potential and kinetic energy as a consequence of energy extraction.

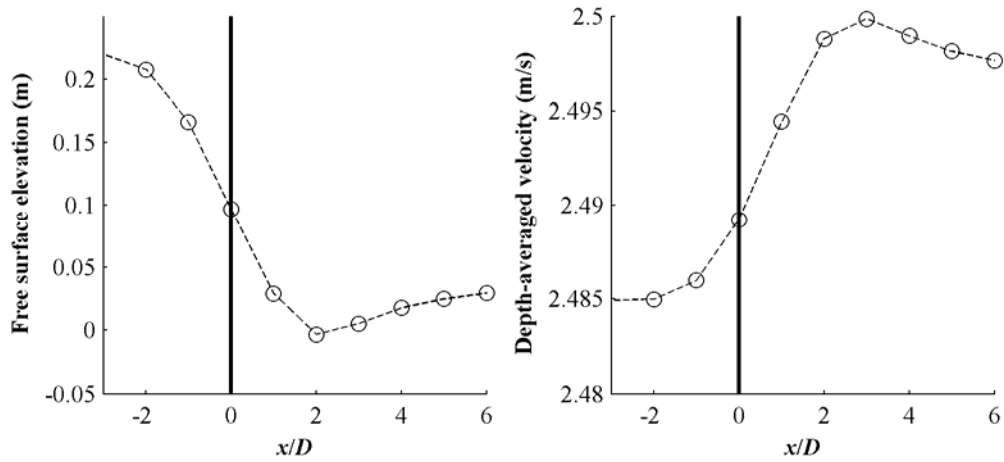


Figure 7.6 – Free surface and depth-averaged velocity change across the parameterized turbine. The solid black vertical line marks the location of the turbine.

7.3.4. Wake Mixing

As discussed by Vermeer et al. [86], there are two mechanisms by which the velocity deficit in the wake is replenished by the free stream. Primarily, shear between the low velocity wake and free stream gives rise to turbulent mixing. Of lesser, though still considerable importance, is the ambient shear in the mean flow. The relative contribution of each of these terms is investigated by adjusting the seabed condition to free-slip, which eliminates the ambient vertical shear. As shown in Figure 7.7, the velocity deficit decays faster with vertical shear. This indicates that both wake shear and ambient shear contribute to the re-energization of the wake in the turbine simulation. Since the profile depends on the diameter of the turbine and elevation above the seabed, Figure 7.7 is meant only as a representative example.

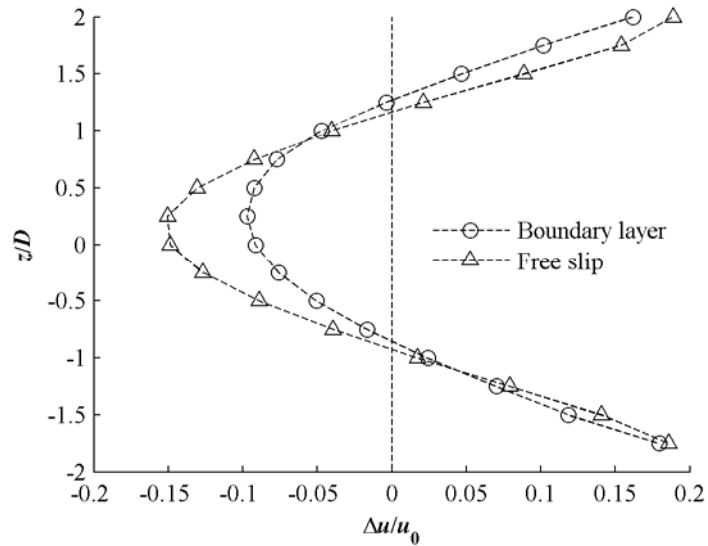


Figure 7.7 – Non-dimensional velocity deficit at $x/D = 20$ ($D=10\text{m}$), comparing the effect of vertical shear. Reported velocities are normalized by conditions $10D$ upstream of the turbine.

In Figure 7.8, the mixing rate is visualized in terms of the vertical eddy diffusivity. Note that far from the turbine (e.g., $x = 60D$), the turbulent diffusivity is still elevated compared to the background levels upstream of the turbine, regardless of the ambient shear. This indicates that complete mixing of the wake with the free stream requires a very long time scale.

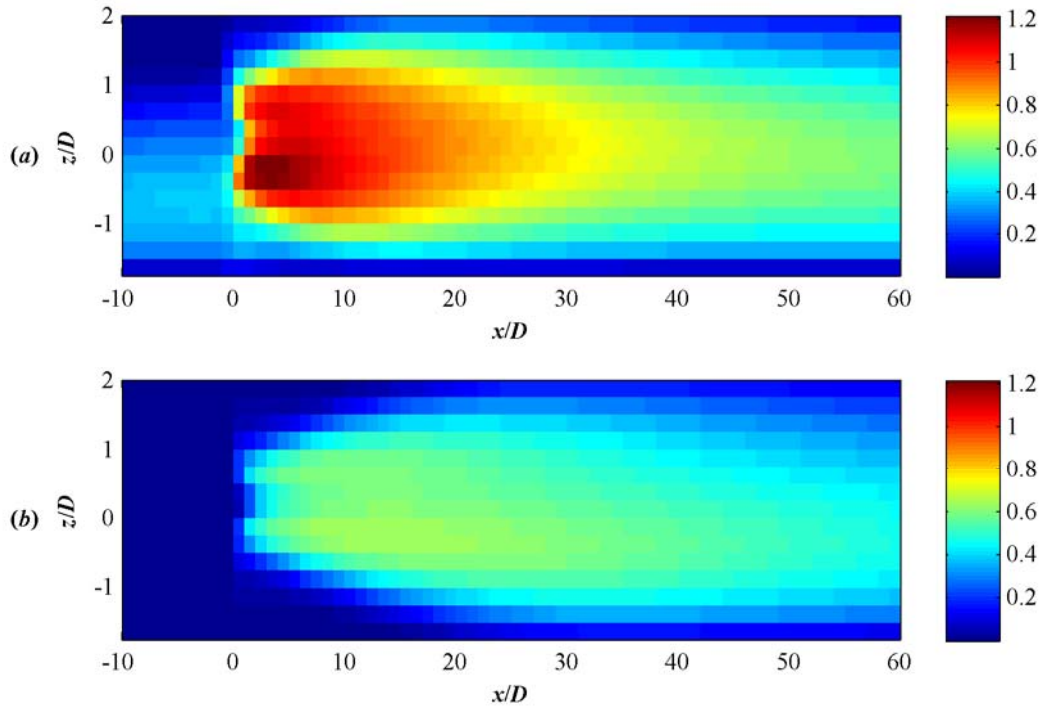


Figure 7.8 – Comparison of vertical eddy diffusivity (v_t) between a case with vertical shear (a) and without (b).

As shown in Figure 7.9, the mixing rate for the wake also depends on the vertical resolution of the grid. The cases shown are for a no-slip seabed and include the effect of vertical shear. In all cases, a measurable velocity deficit persists at $x = 60D$ downstream of the turbine, though the magnitude of the deficit is 50% greater for the coarser resolution. This may be somewhat problematic, because the baseline vertical resolution is relatively high for an estuary-scale simulation. If high vertical resolution is required to accurately model wake persistence (the second requirement for an appropriate model given at the start of this chapter), this would significantly increase the computational cost for a 3D estuary simulation.

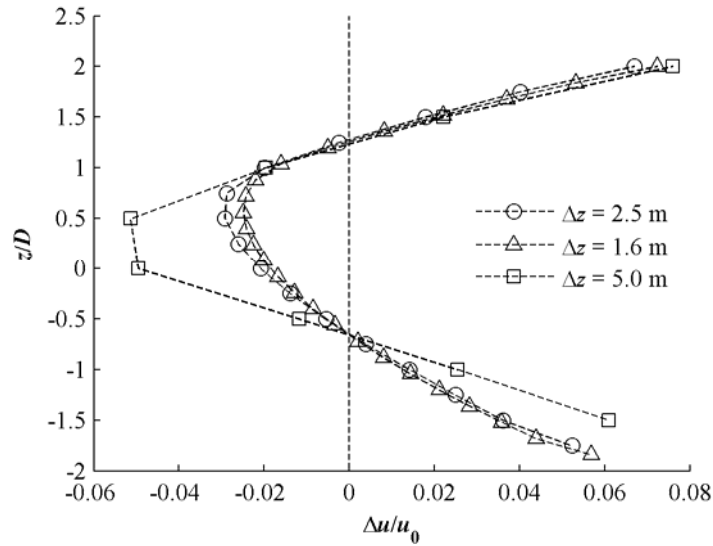


Figure 7.9 – Non-dimensional velocity deficit at $x/D = 60$ ($D=10$ m) for three different vertical resolutions (Δz). Reported velocities are normalized against conditions $10D$ upstream of the turbine.

7.3.5. Effect of Non-hydrostatic Pressure

As previously discussed, SUNTANS is well-suited to investigate the relative importance of non-hydrostatic pressure in a turbine simulation. The depth-averaged velocity and free surface elevation profiles shown previously in Figure 7.6 are repeated in Figure 7.10 along with a hydrostatic case. The two solutions are relatively similar, but the hydrostatic case shows numerical dispersion upstream of the turbine. While the hydrostatic case requires a slightly shorter time step for stable calculation, it has much lower computational cost and only half as much clock time at the non-hydrostatic case.

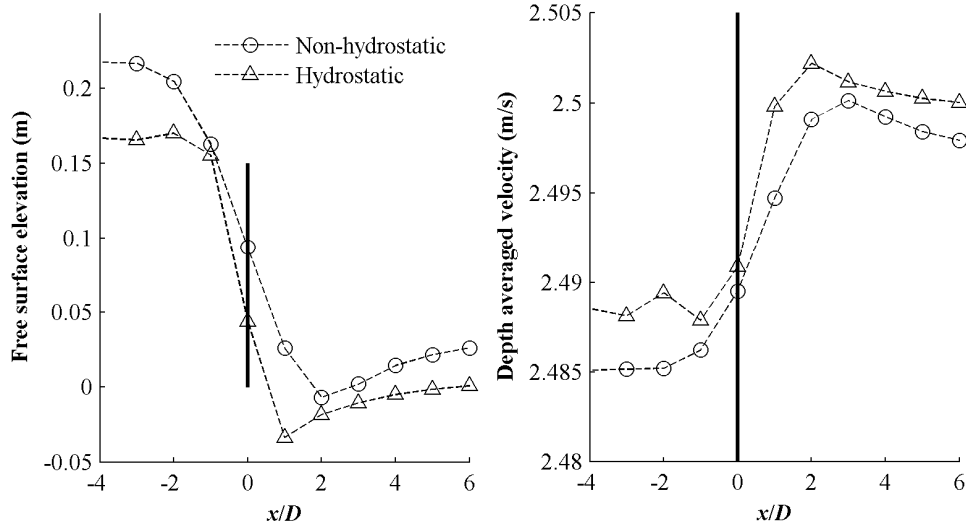


Figure 7.10 – Free surface and depth-averaged velocity change across the parameterized turbine with different pressure treatments. The solid black vertical line marks the location of the turbine.

7.3.6. Comparison with Theory

While the grid resolution used here is too low to directly calculate the extraction efficiency for the parameterized turbine, it is still feasible to calculate the dissipation coefficient (η_d). This is done in two ways: using the theoretical relation developed in Chapter 2, and a direct calculation from the model output. Since the theory assumes that frictional losses with the seabed are negligible in comparison to other losses (extraction loss and wake loss), the most relevant comparison is made when a free-slip condition is imposed at the seabed.

As derived in Chapter 2, the dissipation coefficient is given by (2.36);

$$\eta_d = \frac{1}{\varepsilon} \left(1 - \left(\frac{u_5}{u_0} \right)^2 + \frac{2}{Fr_0^2} \left(1 - \frac{u_0}{u_5} \right) \right). \quad (7.10)$$

The subscript notation used here is as shown in Figure 2.3, where u_0 is upstream up the turbine ($x_0 = -10D$) and u_5 is far downstream of the turbine ($x_5 = 200D$). However, a measurable velocity deficit persists at x_5 , as shown in Figure 7.11. This indicates that wake mixing is not complete and complicates the interpretation of results. At this point, it is not clear if the wake mixing in SUNTANS is unrealistically slow, though this is suspected. The blockage ratio (ε) is calculated as the ratio of the turbine diameter to the water depth at x_0 . For this simulation, $\varepsilon \approx 0.25$ (10 m

turbine in ~ 40 m of water). This calculation is sensitive to the value of u_5 , since u_0/u_5 is close to unity.

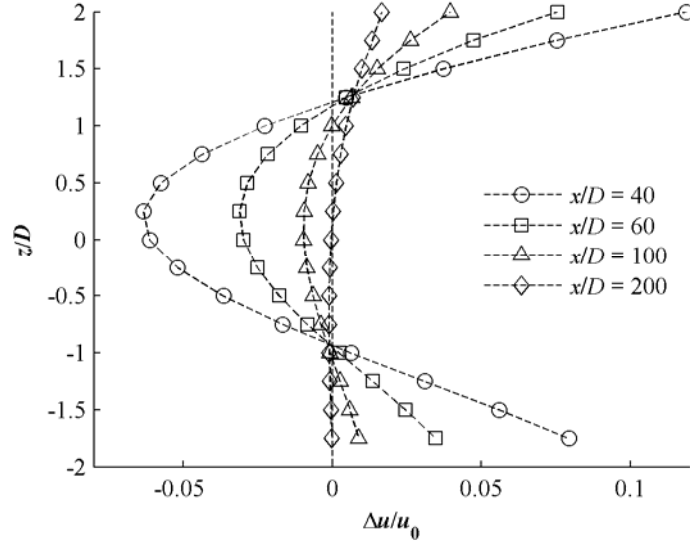


Figure 7.11 – Non-dimensional velocity deficit at four positions far downstream of parameterized turbine ($D=10$ m). Reported velocities are normalized against conditions $10D$ upstream of the turbine.

The velocity upstream of the turbine (u_0) is uniform. The velocity downstream of the turbine (u_5) is taken as the depth-averaged velocity,

$$u_5 = \frac{\sum_{k=1}^N u_k \Delta z_k^*}{\sum_{k=1}^N \Delta z_k^*} . \quad (7.11)$$

Here, the summation is over all vertical levels (N) and Δz_k^* is the thickness of the k^{th} vertical level and includes the contribution of the free surface $k=N$.

For two dimensional flow (x - z cross-section) the coefficient of dissipation (η_d) is calculated directly from model output as the ratio of the change in the total power between x_0 and x_5 to the reference power across the turbine;

$$\eta_d = \frac{\left[\sum_{k=1}^N u_k \Delta z_k^* \left(\frac{1}{2} u_k^2 + g \Delta z_k^* \right) \right]_{x=x_0} - \left[\sum_{k=1}^N u_k \Delta z_k^* \left(\frac{1}{2} u_k^2 + g \Delta z_k^* \right) \right]_{x=x_5}}{\frac{1}{2} \sum_{k=7}^{10} u_k^3 \Delta z_k^*} . \quad (7.12)$$

In the above equation, the summation indices for the reference power are over the vertical levels with non-zero drag factor (β). This is the discretized form of (2.35).

A comparison between the dissipation coefficient obtained from theory (7.9) and model (7.11) is given in Table 7.2. Dissipation coefficients are shown for a range of drag factors ($0.2 \leq \beta \leq 0.4$). For $\beta \geq 0.3$, agreement between the two approaches is reasonable. However, for smaller values of β , the two methods give rather different results, with theory predicting significantly higher dissipation coefficients.

Table 7.2 – Comparison between theoretical and model data calculations for dissipation coefficient (η_d). The Extraction coefficient is also given by theory ($Fr = 0.13$, $\varepsilon = 0.25$) for cases in which model and theory are in agreement for the dissipation coefficient.

Drag factor (β)	0.20	0.25	0.30	0.35	0.40
η_d from theory (7.9)	1.34	1.45	1.58	1.69	1.79
η_d from model (7.11)	0.76	1.05	1.34	1.64	1.96
$\eta_{d,model} / \eta_{d,theory}$	0.57	0.72	0.85	0.97	1.09
α from theory	-	-	0.44	0.41	0.39
η_e from theory	-	-	1.02	1.04	1.05

As shown in Figure 7.4a,b, the horizontal velocity profile around the parameterized turbine is relatively one-dimensional and the formulae to predict theoretical performance derived in Chapter 2 may be reasonably accurate. Therefore, when the dissipation coefficient is well-described by theory ($\beta \geq 0.3$), the extraction coefficient may also be calculated from theory, even if the grid does not resolve the velocity at the end of the wake expansion region (u_3). Because the dissipation coefficient (η_d) is a function of the upstream Froude number (Fr), blockage ratio (ε), and streamtube velocity ratio (α), it is possible to determine α if the other three quantities are known. With α specified for the parameterized turbine, the extraction coefficient (η_e) and ratio of extraction to dissipation may be readily determined using the relations presented in Chapter 2. The theoretically estimated values of η_e are, therefore, shown in Table 7.2 for cases in which the model and theory agree well for the dissipation coefficient.

7.4. Summary

A prototype for a parameterized device has been demonstrated in the SUNTANS oceanographic code. The parameterization is equivalent to a porous mesh blocking a portion of the flow. A number of properties of the parameterization are explored on a 2D (x - z) grid. Qualitatively, the flow field around the parameterized turbine is as predicted by other laboratory-scale experiments and modeling of in-stream turbines. If the pressure treatment is restricted to the hydrostatic regime, the numerical solution develops significant dispersion in the vicinity of the turbine, which

may contaminate the solution to an unacceptable degree. Results do depend significantly on vertical resolution.

A preliminary comparison is presented between the model and theory, with respect to the dissipation coefficient. The model agrees well with theory for higher values of the drag factor (β), but indicates that the model understates power dissipation for smaller values of β . This may be related to the long time scales for complete mixing in the model. Further work is required. This would involve:

- (1) *Extension to 3D simulation.* While the 2D simulation considered here provides considerable insight, a 3D simulation incorporating flow redirection in the lateral dimension would be more representative of an actual turbine.
- (2) *Experiments with higher and lower horizontal resolution grids.* The horizontal grid resolution discussed here (12 m) is too fine for an estuary-scale simulation, but also too coarse to fully characterize the wake. Turbine parameterization with different horizontal grid resolutions should be investigated.
- (3) *Investigation of the effect of turbulence closures other than Mellor Yamada 2.5 (MY2.5).* Most Navier-Stokes solvers for wind turbine arrays use a k - ϵ turbulence closure, which is higher order than MY2.5. An investigation of other closures could be attempted using a Generic Length Scale (GLS) turbulence implementation, which is adjustable to a number of popular closure schemes, including k - ϵ and MY2.5. A GLS implementation has been developed for SUNTANS, but has not yet been incorporated into the main release of the code.

These steps will build towards an understanding of how to appropriately parameterize turbines in terms of the drag factor, β . If successful, this type of modeling could serve as a robust tool for studying the near-field effects of arrays and the baroclinic effects of tidal in-stream energy extraction.

8. Conclusions and Future Work

Using the power in tidal streams to generate electricity is a promising concept. Numerical models have a unique role in the responsible development of this resource because regulators will not give consent for a turbine array if the effects of its operation are unknown. A range of models are available and the selection of an appropriate model depends on the question being addressed. Three-dimensional, non-hydrostatic models are well-suited to the study of near-field effects. However, one-dimensional or two-dimensional models are more appropriate for characterizing far-field effects, given their lower computational cost on large domains.

8.1. Long-term Potential for Tidal Energy

This dissertation suggests several preliminary conclusions with regard to the utilization of in-stream tidal resources.

Responsible development of the resource will be constrained by a number of limits, including far-field extraction effects. Modeling and theory both indicate that high levels of power extraction may result in changes to the tidal regime with respect to tides, currents, transport, and mixing. These have environmental, social, and economic consequences. Reductions to the tidal range have clear environmental ramifications, including modifications to near-shore ecology. Since kinetic power density varies with the cube of velocity, reductions in currents negatively impact project economics. As shown by numerical models of channel networks, kinetic power extraction may either locally augment or reduce tides. Increases to the tidal range could be particularly concerning, since this could inundate presently dry land. The magnitude of these effects depends primarily on the magnitude of extraction, but also on a number of site specific parameters. Using information about the natural tidal regime, it is possible to predict a limited subset of these effects without undertaking detailed modeling. However, modeling is presently the only viable method for predicting the full range of environmental, social, and economic effects of kinetic power extraction.

Generating electricity from tidal currents presents a number of trade-offs, generally between the impacts of extracting power and the cost the electricity. The most obvious of these is the reduction in marginal benefit for each additional turbine added to a site. While larger arrays may benefit from economies of scale and would generate more power, beyond a certain point the reductions in power density could increase the cost of energy. Another trade-off involves the type of tidal regime. While more power may be extracted from diurnal tidal regimes, the cost of

energy for such a project would be higher because of extended periods of low velocity. A third trade-off is seen for serial networks, where more power may be extracted from constricted channels closer to the open ocean. However, sites with a higher, more economically attractive, power density may be found further landward. Fourth, in multiply-connected networks, extraction in only one branch of the system will have the effect of diverting flow into other branches and reducing the theoretically extractable power. This may be prevented by extracting equal power from each branch. However, this may not be economic if the power density is only high in one branch. It is anticipated that a similar effect will occur when arrays of turbines are not evenly distributed across a channel. However, since currents are rarely uniform over a large area, the economic incentive is to install turbines only in the regions of strongest currents. Finally, actuator disc theory indicates that as array packing increases on a channel cross-section, the efficiency of individual turbines will be enhanced, and the cost of energy should decrease. However, this effect also increases wake losses and so, for the same far-field impacts, a less efficient (and more costly) array is able to generate more electric power.

In-stream tidal energy is worth pursuing, but is not a “silver bullet”. There is no single solution that satisfies both growing energy demand and a desire to generate electricity in a more sustainable manner. Site inventories completed to date for the United States indicate that in-stream tidal energy could be regionally important to Maine, the Pacific Northwest, and Alaska. This thesis indicates that the recoverable resource for Puget Sound, Washington might be on the order of 200 MW (average electric generation). Note that this is a preliminary estimate for which the ecosystem implications have not been explored. While the recoverable resource is small in comparison to wind energy, in-stream tidal energy is able to leverage technology developed by the wind industry (devices) and oil and gas industry (foundations). As a result, there may be less need for fundamental research on the mechanics of power extraction. Most of the research and policy questions center on the effects this technology may have on the natural environment. This is in contrast to wave energy, where there is significant interest in developing new and novel concepts to improve the efficiency of power extraction and reduce the environmental footprint for device moorings.

8.2. Future Work

Since in-stream tidal energy is a relatively new research area, there remain broad avenues of future work, some of which could be pursued from the basis of this dissertation.

8.2.1. Device Performance

While the theoretical performance of devices has been established, basic experimental investigation is required to resolve how device performance will change with increasing blockage ratios and at what point mixing between the device wake and free stream will invalidate a streamtube analysis. These questions might be addressed in a laboratory flume at reasonable scale. Additionally, streamtube theory is not able to predict device performance in flows of moderate to high Froude number. While the Froude number is low in most in-stream tidal applications, this is not the case in rivers or constructed channels.

Since effective empirical methods have been developed to predict power output from arrays of wind turbines, the inability to explicitly model large arrays has not been a hindrance to the development of wind energy. However, this modeling capability will be more important in the development of in-stream tidal energy. For wind farms, in order to prevent wakes from degrading performance, significant inter-turbine separation is typical (6-10 rotor diameters downstream, 1.5-3 rotor diameters cross-stream) [94]. This is effective, but relies on the general uniformity of the wind resource over a large geographic area. The benefits of denser array has been demonstrated numerically [94], but not yet in the field. In the case of highly energetic tidal streams, the kinetic resource is much more localized and limited than atmospheric winds, meaning that an optimized turbine packing will be essential. Therefore, there is a need to develop models capable of resolving flow on the scale of an individual turbine and extend these models to turbine arrays.

8.2.2. Extraction Effects

The far-field effects investigated as part of this dissertation and, indeed, in all other work to date, consider only barotropic effects; that is, changes which treat tidal streams as well-mixed. While this may be the case in sill regions because of to vigorous mixing, estuaries are often stratified as a consequence of the density difference between salt water and fresh water. The effects of in-stream extraction on this, the baroclinic tidal regime, are unknown at this time. Baroclinic effects drive a number of ecologically important processes, including the transport of oxygen-rich water from the open ocean to regions of low oxygen concentration within estuaries. Investigation of these effects will require well-calibrated, two or three-dimensional models capable of simulating estuarine circulation over a period of years in a computationally efficient manner. A framework for this type of investigation is presented in Chapter 7 for a three-dimensional model.

Near-field effects involving changes to the three-dimensional flow field in the vicinities of devices are also of interest. A better understanding of near-field effects is required to predict

changes to sediment deposition or scour around arrays, as well as accurately predict the power output from arrays that are not evenly distributed on a channel cross-section.

In order to determine environmentally acceptable levels of extraction, both barotropic and baroclinic far-field effects must be placed in the context of ecosystem changes. While it seems logical that reducing the tidal range by a fraction of a millimeter would be unlikely to have measurable consequences, but reductions on the order of a meter would have very significant consequences, there is little information available to evaluate the trade-off between environmental impact and the benefits of renewable power generation.

In addition to these topics, there are similarly broad investigations to be made in the areas of biological impact (e.g., aggregation and avoidance behavior for fish and marine mammals migrating near a large array). Targeted research is also required to understand how devices perform in turbulent flows, to improve the survivability of devices in the marine environment, and to develop low-cost foundation technology suitable for deep water sites.

In-stream tidal energy is a rich and complex field with many research questions awaiting answers.

References

1. **Anon.** Energy Information Administration, United States Department of Energy.
<<http://www.eia.doe.gov/>> Accessed 23 Jan. 2008.
2. **McKenna, J.** “Severn barrage cost hits £23bn.” *New Civil Engineer* 15 May 2008
<<http://www.nce.co.uk>> Accessed 23 Jan. 2008.
3. **Boone, J.** *Secrets of the tide: tide and tidal current analysis and applications, storm surges and sea level trends.* 2004. (Horwood Publications, Chichester, UK)
4. **Defant, A.** *Physical Oceanography, Volume II.* 1961. (Pergamon Press, New York)
5. **Hagerman, G.** and **Polagye, B.** Methodology for estimating tidal current energy resources and power production by tidal in-stream energy conversion (TISEC) devices. EPRI Technical Report *EPRI-TP-001 NA Rev 3*, 2006.
6. **Bedard, R., Previsic, M., Polagye, B., Hagerman, G., and Casavant, A.** North America tidal in-stream energy conversion technology feasibility study. EPRI Technical Report *EPRI TP-008 NA*. 2006.
7. **Polagye, B.** and **Previsic, M.** System level design, performance, cost and economic assessment – Tacoma Narrows Washington tidal in-stream power plant. EPRI Technical Report *EPRI-TP-006 WA*. 2006.
8. **Cada, G.** Potential environmental effects of marine and hydrokinetic energy technologies. 2008. Report to Congress, *Draft*.
9. **Anon.** Marine and Hydrokinetic Technology Database. Wind & Hydropower Technologies Program, United States Department of Energy.
<<http://www1.eere.energy.gov/windandhydro/hydrokinetic/default.aspx>> Accessed 23 Jan 2008.
10. **Batten, W., Bahaj, A., Molland, A., and Chaplin, J.** The prediction of the hydrodynamic performance of marine current turbines. *Renewable Energy*. 2008, **33**, 1085-1096.
11. **Hagerman, G.** Nova Scotia tidal in-stream energy conversion (TISEC): survey and characterization of potential project sites. EPRI Technical Report *EPRI-TP-003 NS Rev 2*. 2006.
12. **Karsten, R., McMillan, M., Lickley, M., and Haynes R.** Assessment of tidal current energy in the Minas Passage, Bay of Fundy. *Proc IMechE, Part A: J. Power Energy*. 2008, **222**(5), 493-507.

13. **Sutherland, G., Foreman, M., and Garrett C.** Tidal current energy assessment for Johnstone Strait, Vancouver Island. *Proc. IMechE Part A: J. Power and Energy*. 2007, **221**(2), 147-157.
14. **Blanchfield, J., Garrett, C., Rowe, A., and Wild, P.** Tidal stream power resource assessment for Massett Sound, Haida Gwaii. *Proc IMechE, Part A: J. Power Energy*. 2008, **222**(5), 485-492.
15. **Blunden, L. and Bahaj, A.,** Effects of tidal energy extraction at Portland Bill, southern UK predicted from a numerical model. *Proc. EWTEC 2007*, Porto, Portugal, 11-14 September, 2007.
16. **Polagye, B., Kawase, M., and Malte, P.** In-stream tidal energy potential of Puget Sound, Washington. Submitted to *Proc. IMechE Part A: J. Power and Energy*. 2009.
17. **Anon,** Black and Veatch Consulting, Ltd. "UK, Europe, and Global Tidal Energy Resource Assessment." Marine Energy Challenge Report No. 107799/D/2100/05/1.2004. London: Carbon Trust.
18. **Tarbotten, M. and Larson, M.** Canada ocean energy atlas (phase 1): potential tidal current energy resources, analysis background. Report to Canadian Hydraulics Centre. 2006. Ottawa, Ontario.
19. **Garrett, C. and Cummins, P.** Generating power from tidal currents. *J. Waterway, Port, Coastal, and Ocean Engineering*. 2004, **130**(3), 114-118.
20. **Garrett, C. and Cummins, P.** The power potential of tidal currents in channels. *Proc. R. Soc. Lond. A*. 2005, **461**, 2563-2572.
21. **Corten, G.** Heat generation by a wind turbine. *14th IEA Symposium on the Aerodynamics of Wind Turbines*. 2000. ECN Report: ECN-RX-01-001. 7 pp.
22. **Garrett, C. and Cummins, P.** The efficiency of a turbine in a tidal channel. *J. Fluid Mech.* 2007, **588**, 243-251.
23. **Eggleston, D. and Stoddard, F.** *Wind turbine engineering design*. 1987. (New York: Van Nostrand Reinhold.)
24. **Crespo, A., Hernández, J., and Frandsen, S.** Survey of modeling methods for wind turbine wakes and wind farm. *Wind Energy*. 1999, **2**, 1-24.
25. **Manwell, J., McGowan, J., and Rogers, A.** *Wind energy explained: theory, design, and application*. 2002. (New York: Wiley.)

26. **Bryden, I.** and **Couch, S.** How much energy can be extracted from moving water with a free surface: a question of importance in the field of tidal current energy? *Renewable Energy*. 2007, **32**(11), 1961-1966.
27. **Polagye, B., Malte, P., Kawase, M., and Durran, D.** Effect of large-scale kinetic power extraction on time-dependent estuaries. *Proc IMechE, Part A: J. Power and Energy*. 2008, **222**(5), 471-484.
28. **Evans, J.** and **Adamchak, J.** *Ocean engineering structures*. 1969. (Cambridge: MIT Press.)
29. **White, F.** *Fluid mechanics, 3rd ed.* 1994. (New York: McGraw-Hill.)
30. **Young, D., Munson, B., and Okiishi, T.** *A brief introduction to fluid mechanics*. 1997. (New York: John Wiley & Sons.)
31. **Frankel, P.** Personal communication. 2007. Marine Current Turbines, Bristol, UK.
32. **Roy, S., Pacala, S., and Walko, R.** Can large wind farms affect local meteorology? *J. Geo. Res.* 2004. doi:10.1029/2004/JD004763.
33. **Adams, M.** and **Keith, D.** A wind farm parameterization for WRF. *8th WRF Users Workshop*, June 2007, Boulder, CO.
34. **Blanchfield, J., Garrett, C., Wild, P., and Rowe, A.** The extractable power from a channel linking a bay to the open ocean. *Proc IMechE, Part A: J. Power Energy*. 2008, **222**(3), 289-297.
35. **Bryden, I.** and **Melville, G.**, Choosing and evaluating sites for tidal current development. *Proc. IMechE Part A: J. Power and Energy*. 2004, **218** (8), 567-577.
36. **Bryden, I.** and **Couch, J.**, ME1-marine energy extraction: tidal resource analysis. *Renewable Energy*. 2006, **31**, 133-139.
37. **Couch, S.** and **Bryden, I.**, The impact of energy extraction on tidal flow development. *Proc. 3rd IMarEST International Conference on Marine Renewable Energy*, 2004.
38. **Couch, S.** and **Bryden, I.**, Numerical modeling of energy extraction from tidal flows. *Proc. WREC 2005 Conference*, Aberdeen, Scotland, 22-27 May, 2005.
39. **Foreman, M., Sutherland, G., and Cummins, P.** M2 tidal dissipation around Vancouver Island: an inverse approach. *Cont. Shelf Res.* 2004, **24**, 2167-2185.

40. **Blunden, L.** and **Bahaj, A.** Initial evaluation of tidal stream energy resources at Portland Bill, UK. *Renewable Energy*. 2006, **31**, 121-132.
41. **Garcia-Navarro, P.** and **Saviron, J.** McCormack's method for the numerical simulation of one-dimensional discontinuous unsteady open channel flow. *J. Hydraulic Research*. 1992, **30**(1), 95-105.
42. **Wilcox, D.** *Basic fluid mechanics*, 2nd edition. 2000. (DCW Industries, La Cañada, California).
43. **Blayo, E.** and **Debreu, L.** Revisiting open boundary conditions from the point of view of characteristic variables. *Ocean Modeling*. 2005, **9**(3), 231-252.
44. **Chapman, D.**, Numerical treatment of cross-shelf open boundaries in a barotropic coastal ocean model. *J. Physical Oceanography*. 1985, **15**, 1060-1075.
45. **Arbic, B., Garrett, C., and Karsten, R.** The far-reaching back-effect of coastal tides upon open-ocean tides. *Eos Trans. AGU*, 2008. **89**(53), Fall Meet. Suppl. Abstract OS24B-01.
46. **Chaudhry, M.** *Applied Hydraulic Transients*. 1979. (Van Nostrand Reinhold: New York)
47. **Dronkers, J.** *Tidal computations in rivers and coastal waters*. 1964. (North-Holland Publishing: New York.)
48. **Aral, M., Zhang, Y., and Jin, S.** A computational method for wave propagation simulation in open channel networks. Technical Report from Georgia Institute of Technology, *MESEL-03-96*, 1996.
49. **Lai, C.** *Numerical modeling of unsteady open channel flow*, Advances in Hydrosience, V.T. Chow and B.C. Yen, eds. 1986. (Academic Press: New York.)
50. **Pawlowicz, R., Beardsley, B., and Lentz, S.** Classical tidal harmonic analysis including error estimates in MATLAB using T_TIDE. *Computers and Geosciences*. 2002, **28**, 929-937.
51. **Foreman, M., Walters, R., Henry, R., Keller, C., Dolling, A.** A tidal model for eastern Juan de Fuca Strait and the southern Strait of Georgia. *J. Geophysical Research*. 1995, **100**(C1), 721-740.
52. **Freeland, H. and Farmer, D.** Circulation and energetics of a deep, strongly stratified inlet. *Can. J. Fish. Aquat. Sci.* 1980, **37**(9), 1398-1410.

53. **Garret, C. and Cummins, P.** Limits to tidal current power. *Renewable Energy*. 2008, **33**, 2485-2490.
54. **Garret, C.** Personal communication. 2008. Professor, School of Earth and Ocean Sciences, University of Victoria, British Columbia.
55. **Anon.** Alaska Energy Authority, Renewable Energy Atlas of Alaska.
<<http://www.akenergyauthority.org/Reports and Presentations/EnergyAtlas2007.pdf>> Accessed 24 Jan 2008.
56. **Polagye, B., Bedard, R., and Previsic, M.** Tidal in-stream energy conversion (TISEC): survey and characterization of SnoPUD project sites in Puget Sound, EPRI Technical Report *EPRI-TP-003 WA*. 2007.
57. **Hagerman, G.** Maine tidal in-stream energy conversion (TISEC): survey and characterization of potential project sites. EPRI Technical Report *EPRI-TP-003 ME Rev 1*. 2006.
58. **Signell, R.** Coastline Extractor, National Geophysical Data Center (NGDC).
<<http://rimmer.ngdc.noaa.gov/>> Accessed 24 Jan 2008.
59. **Couch, S. and Bryden, G.** Numerical Modeling of Energy Extraction from Tidal Flows. Proceedings of *WREC 2005 Conference*. Aberdeen, Scotland May 2005.
60. **Polagye, B., Previsic, M., Hagerman, G., and Bedard, R.,** System level design, performance, cost and economic assessment – Tacoma Narrows Washington tidal in-stream power plant, EPRI Technical Report *EPRI-TP-006 WA*, 2006.
61. **Previsic, M., Bedard, R., and Polagye, B.** System Level Design, Performance, Cost and Economic Assessment – Admiralty Inlet Washington Tidal In-Stream Power Plant 2008 Update, EPRI Technical Report *EPRI-TP-006 SnoPUD Rev 1*. 2008.
62. **Mofjeld, H. and Larsen, L.** Tides and Tidal Currents of the Inland Waters of Western Washington. NOAA Technical Memorandum *ERL PMEL-56*. 1984.
63. **Collar, C.** Personal Communication, 2008. Senior Manager, Energy Resource Development, Snohomish Public Utility District.
64. **Newton, J., Bassin, C., Devol, A., Kawase, M., Ruef, W., Warner, M., Hannafious, D., and Rose, R.,** Hypoxia in Hood Canal: An overview of status and contributing factors. In

Proceedings of 2007 George Basin Puget Sound Research Conference. Vancouver, British Columbia, March 26-29, 2007.

65. **Edwards, K., Kawase, M., and Sarason, C.** Circulation in Carr Inlet, Puget Sound, During Spring 2003. *Estuaries and Coasts*, 2007, **32**(6), 945-958.
66. National Ocean Survey Hydrographic Survey Data.
<<http://www.ngdc.noaa.gov/mgg/bathymetry/hydro.html>> Accessed 24 Jan 2008.
67. **Mofjeld, H., Venturato, A., Titov, V., González, F., and Newman, J.** Tidal datum distributions in Puget Sound, Washington, based on a tidal model. NOAA Technical Memorandum *OAR PMEL-122*. 2002.
68. **Lavelle, J., Mofjeld, H., Lepriere-Doggett, E., Cannon, G., Pashinski, D., Cokelet, E., Lytle, L., and Gill, S.** A multiply-connected channel model of tides and tidal currents in Puget Sound, Washington and a comparison with updated observations. NOAA Technical Memorandum *ERL PMEL-84*. 1988.
69. **Kawase, M.**, Personal Communication, 2008. Associate professor. School of Oceanography, University of Washington, Seattle, WA.
70. **Leonov, D., Polagye, B., Thyng, K., Kawase, M., Malte, P., and Riley, J.**, Tidal Current Profile Modeling (Phase I), Technical Report to Snohomish PUD by the University of Washington, September, 2007.
71. **Hamner, B.** Tacoma Narrows Tidal Power Feasibility Study – Final Report. Report to Tacoma Power, Tacoma Public Utilities, City of Tacoma, Washington. 2007.
72. **Barnes, C. and Collias, E.** Some considerations of oxygen utilization rates in Puget Sound, *J. Marine Research*. 1958, **17**(1), 68-80.
73. **Fringer, O., Gerritsen, M., and Street, R.**, An unstructured-grid, finite-volume, non-hydrostatic, parallel coastal ocean simulator. *Ocean Modelling*. 2006, **14**, 139-173.
74. **Antheaume, S., Maître, T., and Achard, J.** Hydraulic Darrieus turbines efficiency for free fluid flow conditions versus power farm conditions. *Renewable Energy*. 2008, **33**, 2186-2198.
75. **Maître, T., Antheaume, S., Buvat, C., Corre, C., and Achard, J.**, An innovative modeling approach to optimize the design configurations of marine (river) cross-flow current energy converters' farm. *Proc. EWTEC 2007*, Porto, Portugal, 11-14 September, 2007.

76. **Bahaj, A., Myers, L., Thomson, M., and Jorge N.**, Characterising the wake of horizontal axis marine current turbines. *Proc. EWTEC 2007*, Porto, Portugal, 11-14 September, 2007.
77. **Molland, A., Bahaj, A., Chaplin, J., and Batten W.**, Measurements and predictions of forces, pressures, and cavitation on 2-D sections suitable for marine current turbines. *Proc. IMechE Part M: J. Engineering for the Maritime Environment*. 2004, **218** (2), 127-138.
78. **Batten W., Bahaj A., Molland, A., and Chaplin J.**, Hydrodynamics of marine current turbines. *Renewable Energy*. 2006, **31**, 249-256.
79. **Myers, L. and Bahaj, A.**, Power output performance characteristics of a horizontal axis marine current turbine. *Renewable Energy*. 2006, **31**, 197-208.
80. **Bahaj, A., Molland, A., Chpalin, J., and Batten, W.**, Power and thrust measurements of marine current turbines under various hydrodynamic flow conditions in a cavitation tunnel and a towing tank. *Renewable Energy*. 2007, **32**, 407-426.
81. **Bahaj, A., Batten, W., and McCann, G.**, Experimental verifications of numerical predictions for the hydrodynamic performance of horizontal axis marine current turbines. *Renewable Energy*. 2007, **32**, 2479-2490.
82. **Myers, L. and Bahaj, A.**, Wake studies of a 1/30th scale horizontal axis marine current turbine. *Ocean Engineering*. 2007, **34** (5-6), 758-762.
83. **Sun, X., Chick, J., and Bryden, I.**, Laboratory-scale simulation of energy extraction from tidal currents. *Renewable Energy*. 2008, **33**, 1267-1274.
84. **Sun, X., Bryden, I., Jeffrey, H., and Forehand, D.**, An experimental survey in the wake of a simulated tidal current turbine. *Proc. Inst. Marine Engineering, Science and Technology, Part A, Journal of marine engineering and technology*. 2008, **12**, 13-22.
85. **Högström, U., Asimakopoulos, D., Kambezidis, H., Helmis, C., and Smedman, A.**, A field study of the wake behind a 2 MW wind turbine. *Atmospheric Environment*. 1988, **22**(4), 803-820.
86. **Vermeer, L., Sørensen, J., and Crespo, A.**, Wind turbine wake aerodynamics. *Progress in Aerospace Sciences*. 2003, **39**, 467-510.
87. **Crespo, A., Hernandez J., and Frandsen, S.**, Survey of modeling methods for wind turbine wakes and wind farms. *Wind Energy*. 1999, **2**, 1-24.

88. **Gómez-Elvira, R., Crespo, A., Migoya, E., Manuel, F., and Hernández, J.**, Anisotropy of turbulence in wind turbine wakes. *J. Wind Engineering and Industrial Aerodynamics*. 2005, **93**, 797-814.
89. **Eidsvik, K.**, A system for wind power estimation in mountainous terrain. Prediction of Askervein Hill data. *Wind Energy*. 2005, **8**, 237-249.
90. **Fringer, O., McWilliams, J., and Street, R.**, A new hybrid model for coastal simulations. *Oceanography*. 2006, **19** (1), 64-77.
91. **Migoya, E., Crespo, A., García, J., Moreno, F., Manuel, F., Jiménez, Á., and Costa, A.**, Comparative study of the behavior of wind-turbines in a wind farm. *Energy*. 2007, **32**, 1871-1885.
92. **Crespo, A., Chacón, L., Hernández, J., Manuel, F., and Grau, J.C.**, UPMPARK: a parabolic 3D code to model wind farms. *Proc. European Wind Energy Conference 1994*, Thessalonica, Greece, 10-14 October, 1994, 454-459.
93. **Masson, C., Smaili, A., and Leclerc C.**, Aerodynamic analysis of HAWTs operating in unsteady conditions. *Wind Energy*, 2001, **4**, 1-22.
94. **Ammara, I., Leclerc, C., and Masson, C.**, A viscous three-dimensional differential/actuator-disk method for the aerodynamic analysis of wind farms. *J. Solar Energy Engineering*, 2002, **124**, 345-356.
95. **Shchepetkin, A. and McWilliams, J.** A method for computing horizontal pressure-gradient force in an oceanic model with a nonaligned vertical coordinate. *J. Geophys. Res.* 2003, **108**(C3), doi:10.1029/2001JC001047.
96. **Shchepetkin, A. and McWilliams, J.** The Regional Ocean Modeling System: A split-explicit, free-surface, topography following coordinates ocean model, *Ocean Modelling*. 2005, **9**, 347-404.
97. **Chen, C., Liu, C., and Beardsley, R.** An unstructured, finite-volume, three-dimensional, primitive equation ocean model: application to coastal ocean and estuaries. *Journal of Atmospheric and Oceanic Technology*. 2003, **20**, 159-186.
98. **Zhang, Y. and Baptista, A.** SELFE: A semi-implicit Eulerian-Lagrangian finite-element model for cross-scale ocean circulation. *Ocean Modelling*. 2008, **21**(3-4), 71-96.

99. **Jachec, S., Fringer, O., Gerritsen, M., and Street, R.**, Numerical simulation of internal tides and the resulting energetics within Monterey Bay and the surrounding area. *Geophysical Research Letters*. 2006, **33**, doi:10.1029/2006GL026314.
100. **Wang, B., Fringer, O., Giddings, S., and Fong, D.** High-resolution simulations of a macrotidal estuary using SUNTANS. *Ocean Modelling*. 2008, doi:10.1016/j.ocemod.2008.08.006.
101. **Fringer, O.** Personal communication. 2008. Assistant professor. Department of Civil Engineering, Stanford University, Palo Alto, CA.
102. **Fringer, O.** SUNTANS user guide. Environmental Fluid Mechanics Laboratory, Stanford University, Palo Alto, CA. 2007. <http://suntans.stanford.edu/documentation/user_guide.pdf>
103. **Banas, N. and Hickey, B.**, Mapping exchange and residence time in a model of Willapa Bay, Washington, a branching, macrotidal estuary. *J. Geophysical Research*. 2005, **110**, C11011, doi:10.1029/2005JC002950.
104. **Palma, E. and Matano, R.**, On the implementation of passive open boundary conditions for a general circulation model: The barotropic mode. *J. Geophysical Research*. 1998, **103** (C1), 1319-1341.
105. **Marsaleix, P., Auclair, F., and Estournel, C.**, Considerations on open boundary conditions for regional and coastal ocean models. *J. Atmospheric and Oceanic Technology*. 2006, **23**, 1604-1613.
106. **Carter, G. and Merrifield, M.**, Open boundary conditions for regional tidal simulations. *Ocean Modelling*. 2007, **18** (3-4), 194-209.
107. **Blumberg, A., and Kantha, L.**, Open boundary conditions for circulating models. *J. Hydraulic Engineering*. 1985, **11**, 237-255.
108. **Burges, S.** Lecture Notes, CEE 477 Open Channel Engineering. 2008. Department of Civil and Environmental Engineering, University of Washington, Seattle, WA.

Appendix 1: Boundary Conditions for 1D Models

The specification of open boundary conditions in oceanographic problems is an area of active research. Since tides may be described as a series of harmonic constituents, the most straightforward approach is to specify the tide as a function of time and then determine the currents at the boundaries using a characteristics-based method. This is an example of a clamped boundary condition, and, though quite common in oceanographic modeling, is demonstrably ill-posed [44]. Any waves propagating out from the interior of the domain will perfectly reflect off the clamped boundary. These spurious, numerical reflections will be eventually damped out by numerical diffusion and physical friction, but may contaminate the interior solution. Well-posed boundary conditions for oceanographic problems must satisfy three criteria:

- (1) *Radiative*: Allow waves propagating out from the interior of the domain to pass through the open boundary without reflection, as they do in the natural environment.
- (2) *Active*: Allow external information (such as the tides) to propagate into the domain.
- (3) *Stable*: Maintain the mean sea level over long simulation times, as well as maintain numerical stability.

The issue of open boundary conditions has been heavily discussed in the literature, predominantly for 2D and 3D simulations. Most papers discussing 1D models date from the 1950's-1970's and use clamped boundary conditions. Some modern 1D [48], 2D [12,13], and 3D models [103] continue to use clamped boundary conditions due to ease of implementation and available data, though they are known to be numerically reflective. Reviews of open boundary conditions relevant to ocean modeling are given by Chapman [44], Palma and Matano [104], Blayo and Debreu [43], Marsaleix et al. [105] and Carter and Merrifield [106]. Clearly, there is a sustained interest in this topic.

The most viable open boundaries for 1D simulation are a modified version of the Sommerfeld condition and a variation of the Flather condition, both of which radiate outgoing waves and admit incoming waves. Both are based on the inviscid form of the 1D shallow water equations. The requirement for the open boundary to admit incoming waves, while simultaneously transmitting outgoing waves, significantly restricts the available techniques to the sub-class of *active* open boundary conditions. For situations in which an internal response is being investigated in the absence of external forcing, *passive* open boundary conditions are suitable. Passive open boundary conditions need only absorb waves incident on the numerical boundary.

Numerical tests indicate that the Flather radiation condition proposed by Blayo and Debreu [43] satisfies the three requirements for an open boundary. The Flather radiation condition across an open boundary is expressed as

$$u \pm \sqrt{\frac{g}{h}}\eta = u_{ext} \pm \sqrt{\frac{g}{h}}\eta_{ext}, \quad (\text{A1.1})$$

where η is the free surface elevation and the *ext* subscript denotes conditions external to the boundary. The signs are negative for the left boundary and positive for the right. The Flather conditions is derived from the Sommerfeld radiation condition for free surface elevation and a phase speed equal to the shallow water phase speed

$$\frac{\partial \eta}{\partial t} + \sqrt{gh} \frac{\partial \eta}{\partial x} = 0, \text{ and} \quad (\text{A1.2})$$

a linearized form of the 1D continuity equation

$$\frac{\partial \eta}{\partial t} + h \frac{\partial \bar{u}}{\partial x} = 0. \quad (\text{A1.3})$$

Here \bar{u} is the linearized velocity. Subtraction of (A1.3) from (A1.2) yields

$$\frac{\partial}{\partial x} \left(\bar{u} + \sqrt{\frac{g}{h}}\eta \right) = 0, \quad (\text{A1.4})$$

which may be integrated to obtain (A1.1).

For the purposes of the 1D model described in this dissertation, the external velocity (u_{ext}) in (A1.1) has been assumed to be zero. In the formulation proposed by Blayo and Debreu, the Flather condition is applied to incoming waves and extrapolation of the characteristic speed is used for outgoing waves to specify both depth (h) and velocity (u) on the boundary.

The original form of the Sommerfeld radiation condition

$$\frac{\partial \phi}{\partial t} + c \frac{\partial \phi}{\partial x} = 0, \quad (\text{A1.5})$$

where c is the phase speed and Φ is the quantity being radiated (e.g., u), does not allow for information to propagate into the numerical domain. Therefore, Blumberg and Kantha [107] propose a modified form to “nudge” the solution back to a reference value at the boundary

$$\frac{\partial \phi}{\partial t} + c \frac{\partial \phi}{\partial x} = \frac{\phi - \phi_{ref}}{T_f}, \quad (\text{A1.6})$$

where T_f is a relaxation time and Φ_{ref} is the long-term reference value of the quantity being radiated. However, there is no rigorous method to select the relaxation time. A long relaxation time reduces to the Sommerfeld condition, while a very short one reduces to a clamped boundary. As such, this method is sometimes referred to as a partially-clamped boundary condition. Since the Flather condition does not require the specification of any empirical constants, it is superior for 1D modeling of extraction effects.

A barotropic relaxation experiment demonstrating the ability of an open boundary to radiate outgoing waves is presented below. The test domain consists of a 1D grid ($\Delta x = 100\text{m}$) which is 30 km long and 60 m deep. The left boundary is open, the right boundary is a solid wall. Figure A1.1 shows the free surface elevation at four different times when the open boundary is clamped and radiative. At time $t=0$ a sinusoidal “bump” of elevation 0.5 m is released at the center of the domain (*a*). This wave diffuses across the domain (*b*), generating some spurious oscillation due to the sharp gradient. In plot (*c*), the wave reaches the two boundaries. At the closed boundary, the wave is reflected back into the domain with amplitude equal to the incident wave (*d*, right boundary). At the open boundary, the clamped boundary condition inverts the wave and spuriously reflects it back into the interior, while the radiative condition transmits the wave with minimum reflection (*d*, left boundary).

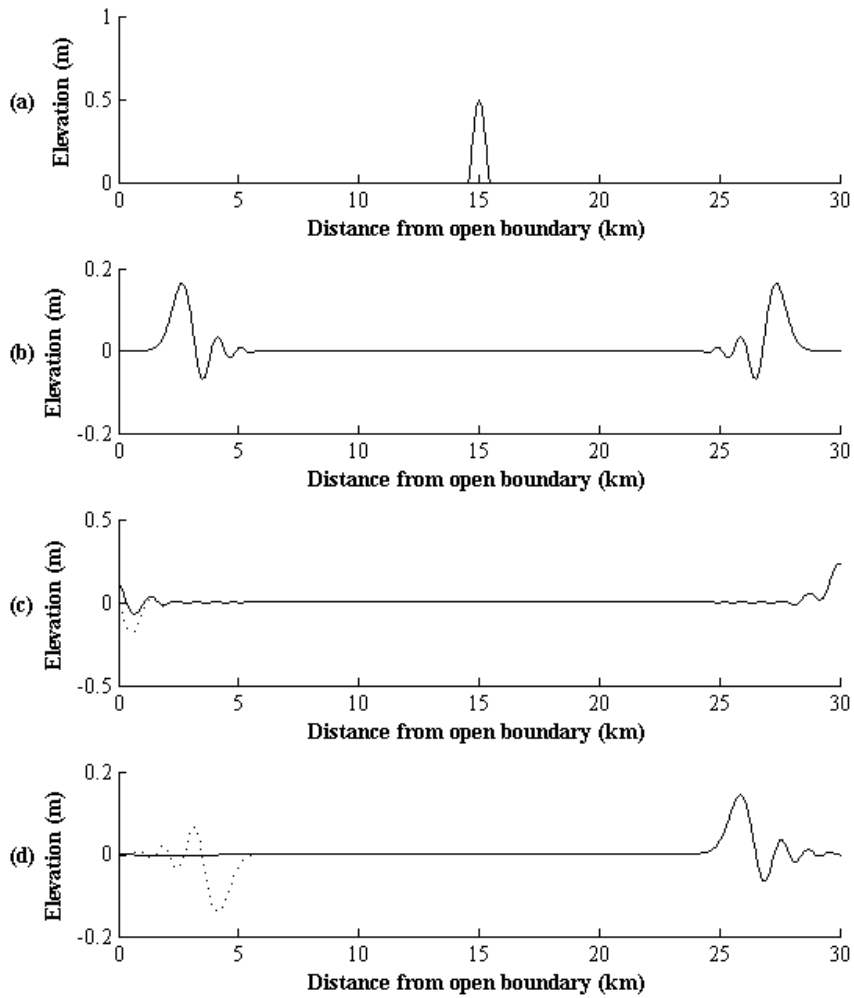


Figure A1.1 – Barotropic relaxation experiment. Solid line: Radiative open boundary proposed by Blayo and Debreu [43] (external elevation and velocity set to zero). Dashed line: clamped open boundary (elevation set to zero, velocity determined by method of characteristics).

Appendix 2: Method of Characteristics

As presented in Chapter 4, the positive and negative characteristic equations are, respectively

$$u + 2(gh)^{1/2} = C_p, \text{ and} \quad (\text{A2.1})$$

$$u - 2(gh)^{1/2} = C_n. \quad (\text{A2.2})$$

Note that since the shallow water phase speed is $(gh)^{0.5}$, the characteristics correspond to a pair of inviscid Riemann-invariants. Details are provided here for the negative characteristic constant (C_n). The derivation of the positive characteristic constant (C_p) is analogous. The discussion here is adapted primarily from Lai [49], but also includes some details presented in Chaudhry [46].

A stencil describing the path of the negative characteristic is shown in Figure A2.1. The horizontal axis is the spatial dimension (as labeled by grid points) and vertical axis is the time dimension. Interior points ($x > 0$) are solved for using the MacCormack algorithm in advance of this step. The substantial derivative with respect to the Riemann-invariant for a characteristic wave traveling at this velocity is

$$\frac{D_-}{Dt}(u - 2c) = -gS_f, \quad (\text{A2.3})$$

where c is the shallow water phase speed and S_f is the friction slope, as defined in the discussion of the shallow water equations in Chapter 4. Note that the effect of friction is to change what is an invariant quantity for inviscid flow. In discrete time Δt , a wave moving with characteristic speed $u-c$ moves from point R (Figure A2.1) to P .

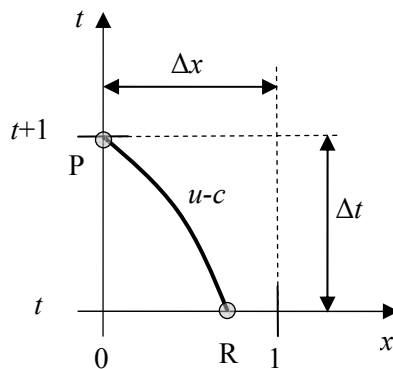


Figure A2.1 – Negative characteristic stencil (1D grid)

Integration along the Riemann quasi-invariant between points P and R yields

$$u_P - 2(gh_P)^{1/2} = u_R - 2(gh_R)^{1/2} - g\Delta t \int_R^P S_f = C_n. \quad (\text{A2.4})$$

However, since R is not generally coincident with a point on the numerical grid, x_R and the properties of the flow at that point (u_R, h_R) , must be interpolated to calculate C_n . A first-order approximation uses only information available at R . Second-order approximations use information from both P and R and are, as a result, iterative.

For the first order approximation, the characteristic wave speed from P to R is assumed to be invariant, and defined by conditions at R . Therefore, the distance traveled is given by

$$x_P - x_R = \int_R^P (u - c)_R dt = (u - c)_R \Delta t. \quad (\text{A2.5})$$

Note that $x_P = 0$. A similar approximation is applied to the frictional term in (A2.4). Linear interpolation of known properties at 0 and 1 to point R yields

$$\frac{x_P - x_R}{x_0 - x_1} = \frac{x_0 - x_R}{-\Delta x} = \frac{u_0 - u_R}{u_0 - u_1} = \frac{h_0 - h_R}{h_0 - h_1} = \frac{c_0 - c_R}{c_0 - c_1} = -(u_R - c_R) \frac{\Delta t}{\Delta x}. \quad (\text{A2.6})$$

Lai [49] solves this set of equations to write c_R , h_R , and u_R explicitly as

$$c_R = \frac{c_0 + \frac{\Delta t}{\Delta x} (c_0 u_1 - c_1 u_0)}{1 + \frac{\Delta t}{\Delta x} ((u_1 - c_1) - (u_0 - c_0))}, \quad (\text{A2.7})$$

$$u_R = \frac{u_0 + \frac{\Delta t}{\Delta x} (u_1 - u_0) c_R}{1 + \frac{\Delta t}{\Delta x} (u_1 - u_0)}, \text{ and} \quad (\text{A2.8})$$

$$h_R = h_0 - (h_1 - h_0) \frac{\Delta t}{\Delta x} (u_R - c_R). \quad (\text{A2.9})$$

For a second-order approximation, the only difference is that (A2.5) uses a trapezoidal approximation

$$x_P - x_R = \int_R^P (u - c) dt = \frac{1}{2} [(u - c)_R + (u - c)_P] \Delta t . \quad (\text{A2.10})$$

Once x_R has been calculated from the second-order approximation, the same linear interpolation scheme is applied. The trapezoidal approximation is also applied to the frictional term in (A2.4). The process iterates until the change in x_R between successive steps satisfies a defined tolerance.

For the positive characteristic constant

$$\frac{D_+}{Dt} (u + 2c) = -gS_f, \text{ and} \quad (\text{A2.11})$$

$$u_P + 2(gh_P)^{1/2} = u_L + 2(gh_L)^{1/2} - g\Delta t \int_L^P S_f = C_P, \quad (\text{A2.12})$$

where L is an intermediate point between the last grid point (N) and grid point $N-1$. The determination of the location of and properties at L proceeds in an analogous manner to that for R .

Appendix 3: Implementation Details for 1D Channel Model

A brief overview of the program structure for the 1D channel model is given in this appendix. The code is well-documented and is available from the author of this dissertation upon request.

Program input and output are via ASCII text files. Input files specify the grid properties, boundary conditions, tidal forcing, and representation of turbines. The output files are velocity and water depth at points specified by the input file.

The input file has the form:

```
[Case Name]
Sections, [number of segments, base 0]
Boundaries, [number of boundaries, base 0]
Constituents, [number of tidal constituents, base 0]
#SECTION#, [section number]
length, [length (m)]
b, [starting width, ending width (m)]
n, [Manning roughness coefficient]
H, [mean water depth (m)]
z, [reference elevation (m)]
dx, [grid spacing (m)]
xskip, [interval for output]
turbine_flag, [0=no turbines, 1=turbines]
```

The last grid point for each segment is always output, regardless of the *xskip* specification. The *#SECTION#* block repeats for each channel segment, as defined in the file header. Next, boundary conditions are specified. The format for open and closed boundaries, as well as interior junctions, are described below.

```
#BOUNDARY#, [boundary number]
type, open
section, [segment number], FIRST for first index or LAST for last index

type, closed
section, [segment number], FIRST or LAST

type, serial
section, [seaward segment number], LAST, [flood loss coefficient], [ebb loss coefficient]
section, [landward segment number], FIRST, [flood loss coefficient], [ebb loss coefficient]

type, diverge
section, [main channel segment number], LAST
section, [branch 1 segment number], FIRST
section, [branch 2 segment number], FIRST

type, converge
section, [main channel segment number], FIRST
section, [branch 1 segment number], LAST
```


section, [branch 2 segment number], LAST

The tidal forcing is described by the following block:

```
#FORCING#, [channel segment being forced], FIRST or LAST
[constituent name], [constituent amplitude (m)], [constituent period (h)], [constituent phase (degrees)]
```

The time parameters for the simulation are then specified. While the code will reduce the time step automatically to satisfy the Courant stability criteria (and report this in an error file), a variable time step complicates harmonic analysis.

```
#TIME#
step size, [step size (s)]
output step, [number of steps to take between reported outputs]
start time (s), [start time for simulation (s)]
end time (s), [end time for simulation (s)]
```

Following this, the number of turbine transects must be specified for each segment in the `#SECTION#` blocks for which `turbine_flag` is non-zero. The program is written to simulate a range of extraction scenarios as a batch for a particular geometry and tidal forcing. For example, in a system with a single constricted channel:

```
#EXTRACTION#, [reference number (e.g., 1)]
section, [channel segment with extraction]
min transects, [minimum number of transects to simulate – integer, greater than zero]
max transects, [maximum number of transects to simulate]
step transects, [steps between successive simulations]
sectionID, [alphabetic identifier for constriction in file output (e.g., A)]
```

Finally, the parameters for the turbine are specified.

```
#TURBINE SPEC#, [designation for turbine (e.g., Linear)]
cut-in speed, [cut-in speed (m/s)]
rated speed, [rated speed (m/s)]
eta, [dissipation coefficient for each row of turbines]
blockage, [blockage ratio for each row of turbines]
```

It is not required that segments or boundaries be input in successive order (e.g segment 2 may be specified after segment 4), but a logical layout is suggested to avoid confusion.

The program code is written in Visual Basic, using the Microsoft .NET specification and is compiled to an executable program. Program flow is broken down into a series of modules, each containing several subroutines. Key subroutines are described here in pseudo-code to give a flavor for program execution.

ChannelModel.vb: Main (module: subroutine)

This is a wrapper function which sets up each simulation case and calls the main solver routine.

Read in program variables from specified input file

Loop over all specified transects

 Sub-segment model segments with transects

 Initialize one-dimensional grid

 Initialize physical variables

 Run simulation with specified grid and transect (*SolveCase*)

End transect loop

ChannelModel.vb: SolveCase

This is the main solver routine and executes the solution to the governing equations.

Loop over simulation time

 Loop over all channel segments

 Loop over all grid nodes in each segment

 Update grid nodes for predictor step

 End grid node loop

 End channel segment loop

 Loop over all boundaries (both external and internal at junctions)

 Update boundary conditions for predictor step (*UpdateBoundary*)

 End boundary loop

 Loop over all channel segments

 Loop over all grid nodes in each segment

 Update grid nodes for corrector step

 End grid node loop

 End channel segment loop

 Loop over all boundaries (both external and internal at junctions)

 Update boundary conditions for corrector step (*UpdateBoundary*)

 End boundary loop

 Compute all physical variables at time = $t+1$ using results of predictor and corrector

 Check that the Courant stability condition is satisfied

 Reverse direction of predictor-corrector sweep

 Write physical variables to disk

End time loop

BoundaryConditions.vb: UpdateBoundary

This routine calls the update algorithm appropriate for the particular boundary type. For example, an open boundary at the start of a segment (left) or serial boundary at the end of a segment (right). Open and closed boundaries are handled by routines within this module. Internal junctions are handled by routines in the *Junctions.vb* module.

Junctions.vb: SerialJunction

The pseudo code for updating a serial junction is provided here. Divergent and convergent junctions follow similar routines.

```
Determine positive and negative characteristic constants using first order approximation
Loop while differences between successive iterations exceed specified tolerance
    Perform Newton-Rhapson iteration to solve four governing equations
    Update characteristic constants based on second order approximation
End iteration loop
```

Program output consists of a pair of flat text files with depth and velocity. An error file is generated if the Courant stability limit is exceeded or either the characteristic constant iteration or Newton-Rhapson iteration for junctions does not converge within a specified number of iterations. For the channel networks analyzed, 90% of the simulation time is associated with updates to interior nodes using the MacCormack predictor-corrector algorithm. Other operations, which constitute most of the written code, consume only 10% of the effort.

A post-processing utility converts output files into a MATLAB-readable format. This subsamples the depth and velocity files at specified gauge locations for further analysis. All calculations of harmonic constants and power extraction are carried out via a set of MATLAB routines. As with the source code, the post-processing utility and MATLAB routines are available upon request.

Appendix 4: Derivation of Dissipation Factor

In order to satisfy conservation of energy, the total upstream (subscript 1) potential and kinetic power must equal the total downstream (subscript 2) potential and kinetic power, plus power dissipated by turbines (extraction and wake losses)

$$P_{K,1} + P_{P,1} = P_{K,2} + P_{P,2} + P_t. \quad (\text{A4.1})$$

Here K denotes kinetic power, P denotes potential power, and the t subscript denotes power dissipated by turbines.

Equation (4.20): Turbine below Rated Speed

Assuming a flood tide ($u > 0$) then the power dissipated by a row of turbines is given by

$$P_t = \frac{1}{2} \rho u_1^3 A_t \eta_d, \quad (\text{A4.2})$$

where A_t is the turbine swept area and η_d is the coefficient of dissipation.

The balance between the flux of kinetic and potential energy is

$$g\rho(uh^2b)_1 + \frac{1}{2}\rho(u^3hb)_1 = g\rho(uh^2b)_2 + \frac{1}{2}\rho(u^3hb)_2 + \frac{1}{2}\rho u_1^3 A_t \eta_d, \quad (\text{A4.3})$$

where b is the width of the channel. Mass conservation requires

$$\rho(uhb)_1 = \rho(uhb)_2. \quad (\text{A4.4})$$

Defining the ratio of channel cross-sectional area to turbine swept area as ε and substituting (A4.4) allows (A4.3) to be simplified to

$$\frac{u_1^2}{2g}(1 - \eta_d \varepsilon) + h_1 = \frac{u_2^2}{2g} + h_2. \quad (\text{A4.5})$$

For the case of a flood tide, the dissipation coefficient is expressed in terms of u_2 , leading to a similar result.

Equation (4.24): Turbine above Rated Speed

Again considering the case of a flood tide take the case of a flood tide and assuming that the turbine drag decreases above rated speed (u_r), the amount of power dissipated is

$$P_t = \frac{1}{2} \rho u_r^3 A_t \eta_d. \quad (\text{A4.6})$$

Conservation of energy is then

$$g\rho(uh^2b)_1 + \frac{1}{2}\rho(u^3hb)_1 = g\rho(uh^2b)_2 + \frac{1}{2}\rho(u^3hb)_2 + \frac{1}{2}\rho u_r^3 A_i \eta_d. \quad (\text{A4.7})$$

Using the same conventions as before, this simplifies to

$$gh_1 + \frac{1}{2}u_1^2 = gh_2 + \frac{1}{2}u_2^2 + \frac{1}{2}\frac{u_r^3}{u_1}\varepsilon\eta_d. \quad (\text{A4.8})$$

Grouping similar terms, (A4.8) may be expressed as

$$\frac{u_1^2}{2g}\left(1 - \left(\frac{u_r}{u_1}\right)^3\right)\varepsilon\eta + h_1 = \frac{u_2^2}{2g} + h_2. \quad (\text{A4.9})$$

Appendix 5: Baseline Tidal Regimes for Prototype Channel Networks

Table A5.1 – Baseline tidal regime for single constriction network channel segments (single constituent forcing)

	1	2	3
M2 Tide			
Amplitude (m)	1.68	1.87	2.15
Phase Lag (°)	65	74	81
M2 Current			
Amplitude (m/s)	0.56	2.41	0.25
Phase Lag (°)	-11	-9	-8
M2 Transport			
Amplitude (m ³ /s)	2.90x10 ⁴	2.41x10 ⁴	1.24x10 ⁴
Phase Lag (°)	-11	-9	-8
Dissipated power (MW)	115	508	46
Kinetic power density (kW/m ²)	0.04	3.0	0.003

Table A5.2 – Baseline tidal regime for single-constriction network channel segments (semidiurnal regime)

	1	2	3
M2 Tide			
Amplitude (m)	1.4	1.5	1.8
Phase Lag (°)	46	55	62
K1 Tide			
Amplitude (m)	0.18	0.18	0.19
Phase Lag (°)	8	12	17
S2 Tide			
Amplitude (m)	0.67	0.74	0.86
Phase Lag (°)	40	52	61
O1 Tide			
Amplitude (m)	0.091	0.090	0.099
Phase Lag (°)	42	47	53
M2 Current			
Amplitude (m/s)	0.47	1.97	0.20
Phase Lag (°)	-30	-28	-27
K1 Current			
Amplitude (m/s)	0.028	0.11	0.011
Phase Lag (°)	285	287	287
S2 Current			
Amplitude (m/s)	0.24	1.00	0.10
Phase Lag (°)	328	331	332
O1 Current			
Amplitude (m/s)	0.013	0.052	0.0052
Phase Lag (°)	320	323	323
Mean Transport (m ³ /s)	1.63x10 ⁵	1.37x10 ⁵	7.06x10 ⁴
Dissipated power (MW)	94	434	32
Kinetic power density (kW/m ²)	0.04	2.5	0.003

Table A5.3 – Baseline tidal regime for single-constriction network channel segments (mixed, mainly semidiurnal)

	1	2	3
M2 Tide			
Amplitude (m)	1.3	1.4	1.6
Phase Lag (°)	46	55	62
K1 Tide			
Amplitude (m)	1.1	1.1	1.2
Phase Lag (°)	8	12	17
S2 Tide			
Amplitude (m)	0.60	0.67	0.78
Phase Lag (°)	40	51	61
O1 Tide			
Amplitude (m)	0.55	0.54	0.59
Phase Lag (°)	42	47	52
M2 Current			
Amplitude (m/s)	0.43	1.81	0.19
Phase Lag (°)	-30	-28	-28
K1 Current			
Amplitude (m/s)	0.17	0.67	0.067
Phase Lag (°)	284	286	287
S2 Current			
Amplitude (m/s)	0.21	0.89	0.09
Phase Lag (°)	328	331	332
O1 Current			
Amplitude (m/s)	0.077	0.31	0.031
Phase Lag (°)	320	322	322
Mean Transport (m ³ /s)	1.57x10 ⁵	1.31x10 ⁵	6.77x10 ⁴
Dissipated power (MW)	87	425	17
Kinetic power density (kW/m ²)	0.04	2.5	0.003

Table A5.4 – Baseline tidal regime for single-constriction network channel segments (mixed, mainly diurnal)

	1	2	3
M2 Tide			
Amplitude (m)	1.0	1.1	1.2
Phase Lag (°)	45	55	62
K1 Tide			
Amplitude (m)	2.1	2.1	2.2
Phase Lag (°)	8	12	16
S2 Tide			
Amplitude (m)	0.47	0.54	0.60
Phase Lag (°)	39	51	61
O1 Tide			
Amplitude (m)	1.05	1.05	1.13
Phase Lag (°)	42	46	51
M2 Current			
Amplitude (m/s)	0.33	1.36	0.14
Phase Lag (°)	-31	-28	-28
K1 Current			
Amplitude (m/s)	0.32	1.29	0.13
Phase Lag (°)	284	285	286
S2 Current			
Amplitude (m/s)	0.16	0.68	0.07
Phase Lag (°)	329	332	332
O1 Current			
Amplitude (m/s)	0.15	0.60	0.060
Phase Lag (°)	319	321	321
Mean Transport (m ³ /s)	1.48x10 ⁵	1.22x10 ⁵	6.25x10 ⁴
Dissipated power (MW)	88	438	7
Kinetic power density (kW/m ²)	0.04	2.5	0.003

Table A5.5 – Baseline tidal regime for single-constriction network channel segments (diurnal)

	1	2	3
M2 Tide			
Amplitude (m)	0.64	0.72	0.78
Phase Lag (°)	44	54	62
K1 Tide			
Amplitude (m)	2.7	2.8	2.9
Phase Lag (°)	8	11	15
S2 Tide			
Amplitude (m)	0.30	0.35	0.37
Phase Lag (°)	36	49	62
O1 Tide			
Amplitude (m)	1.4	1.4	1.5
Phase Lag (°)	42	46	50
M2 Current			
Amplitude (m/s)	0.20	0.82	0.084
Phase Lag (°)	-31	-28	-28
K1 Current			
Amplitude (m/s)	0.42	1.70	0.17
Phase Lag (°)	283	285	285
S2 Current			
Amplitude (m/s)	0.095	0.40	0.040
Phase Lag (°)	332	336	336
O1 Current			
Amplitude (m/s)	0.19	0.78	0.078
Phase Lag (°)	318	320	320
Mean Transport (m ³ /s)	1.53x10 ⁵	1.24x10 ⁵	6.25x10 ⁴
Dissipated power (MW)	89	428	7
Kinetic power density (kW/m ²)	0.04	2.5	0.003

Table A5.6 – Baseline tidal regime for multiply-connected network channel segments

	1	2	3	4	5	6	7	8
M2 Tide								
Amplitude (m)	0.73	0.96	1.10	1.28	0.96	1.10	1.28	1.54
Phase Lag (°)	65	82	100	113	82	100	113	114
M2 Current								
Amplitude (m/s)	0.62	0.54	2.45	0.42	0.54	2.45	0.42	0.18
Phase Lag (°)	16	21	24	24	21	24	24	24
Dissipated power (MW)	275	92	537	42	92	537	42	24
Kinetic power density (kW/m ²)	0.05	0.03	3.2	0.02	0.03	3.2	0.02	0.001

Table A5.7 – Baseline tidal regime for branching network channel segments

	1	2	3	4	5	6	7
M2 Tide							
Amplitude (m)	1.06	1.32	1.46	1.70	1.32	1.46	1.70
Phase Lag (°)	71	78	91	101	78	91	101
M2 Current							
Amplitude (m/s)	0.58	0.45	2.53	0.20	0.45	2.53	0.20
Phase Lag (°)	2	7	11	11	7	11	11
Dissipated power (MW)	226	56	445	20	56	445	20
Kinetic power density (kW/m ²)	0.04	0.02	3.5	0.002	0.02	3.5	0.002

Table A5.8 – Baseline tidal regime for serial constriction network channel segments

	1	2	3	4	5
M2 Tide					
Amplitude (m)	0.93	0.95	1.11	1.31	1.53
Phase Lag (°)	55	76	96	108	117
M2 Current					
Amplitude (m/s)	0.56	2.4	0.44	2.3	0.18
Phase Lag (°)	15	20	23	27	27
Dissipated power (MW)	102	548	75	327	11
Kinetic power density (kW/m ²)	0.04	2.9	0.02	2.5	0.001

Table A5.9 – Baseline tidal regime for hybrid network channel segments

	1	2	3	4	5	6	7
M2 Tide							
Amplitude (m)	0.75	0.90	0.88	0.91	1.1	1.3	1.5
Phase Lag (°)	57	63	73	94	113	126	135
M2 Current							
Amplitude (m/s)	0.38	0.10	0.54	2.3	0.43	2.2	0.17
Phase Lag (°)	11	-27	33	37	40	45	45
Dissipated power (MW)	65	5	94	501	69	300	6
Kinetic power density (kW/m ²)	0.01	0.0003	0.04	2.7	0.02	2.3	0.001

Appendix 6: Alternative Calculation for Maximum Dissipation

In Chapter 4, the theoretical determination of the maximum possible dissipation for a single constriction network is detailed for the procedure given in Karsten et al. [12]. This approach computes the non-dimensional parameters which describe the system response to power extraction (β and λ_0^*) from the natural amplitude ratio and phase lag across the constriction. An alternative approach is given in Blanchfield et al. [14] in which these parameters are determined by the geometric properties of the constriction and basin. Note that this is somewhat less flexible than the method presented in Karsten et al. since the concept of a “basin” is ill-defined for serial constriction networks. β is a term describing the geometry of the terminal basin and constriction given by

$$\beta = \frac{g}{cA\omega^2}, \quad (\text{A6.1})$$

where A is the surface area of the basin, ω is the frequency of the dominant tidal constituent (M2 in this case), and c is a channel geometry term. c is given by

$$c = \int_0^L E^{-1} dx, \quad (\text{A6.2})$$

where E is the channel cross-sectional area and L is the channel length. For a rectangular channel of constant cross-section, (A6.2) reduces to

$$c = \frac{L}{Hb}, \quad (\text{A6.3})$$

where h is the time-mean water depth and b is the channel width. λ_0^* , the non-dimensional loss parameter, which for a rectangular channel is given as

$$\lambda_0^* = \frac{ga}{(c\omega)^2} \left(\int_0^L \frac{C_D}{HE^2} dx + \frac{1}{2E_e^2} \right) = \frac{ga}{(c\omega bH)^2} \left(C_D \frac{L}{H} + \frac{1}{2} \right), \quad (\text{A6.4})$$

where E_e is the exit cross-sectional area and C_D is the coefficient of drag for the channel. The first term relates to losses due to friction and the second to contraction and expansion losses. The drag coefficient is related to the Manning roughness coefficient (n) by [108]

$$C_D = \frac{2gn^2}{R_h^{1/3}}. \quad (\text{A6.5})$$

Once β and λ_0^* have been determined, an approximate value for γ is obtained visually from a chart in Karsten et al. [12]. γ varies over a relatively small range and is not particularly sensitive to β and λ_0^* so this method should not introduce unacceptable errors into the calculation. Once γ has been determined, $P_{\max, \text{theory}}$ may be calculated via (4.36). Table 4.3 is reproduced here using the alternative procedure. While the values of λ_0^* are somewhat different (likely because of differences in the way exit losses are modeled versus approximated in the theory) γ is largely unchanged and the comparison between model and theory is not materially different than those obtained using the method proposed by Karsten et al. [12].

Table A6.1 – Comparison between theoretical and model predictions for maximum possible turbine dissipation (single constriction network) using procedure described in Blanchfield et al.

Case	Variation	β	λ_0^*	γ	$\frac{P_{\max, \text{model}}}{P_{\max, \text{theory}}}$
S1	Base case	12	42	0.21	1.09
S2	$L_3 = 60\text{km}$	17	48	0.22	1.01
S3	$L_3 = 100\text{km}$	10	36	0.21	1.21
S4	$b_2 = 1.5\text{km}$	9	40	0.21	1.14
S5	$b_2 = 2.5\text{ km}$	16	43	0.22	1.05
S6	$H_{123} = 30\text{m}$	7	51	0.20	1.37
S7	$H_{123} = 70\text{m}$	17	38	0.22	1.00
S8	$\zeta_{0, \text{external}} = 2.8\text{m}$	12	49	0.21	1.10
S9	$\zeta_{0, \text{external}} = 2.0\text{m}$	12	36	0.21	1.07
S10	$L_1 = 80\text{km}$	12	41	0.21	1.13

Appendix 7: Segment Properties for Puget Sound Model

Table A4.1 – Channel segment properties. Channel segment numbers are shown in Figure 6.2.

Name	Puget Sound Region	Length km	Width Km	Depth m	n $s/m^{1/3}$
1 Strait of Juan de Fuca		18	15.2	62.0	0.035
2 Admiralty Inlet North	N. Admiralty Inlet	6.6	5.7	52.0	0.035
3 Port Townsend	N. Admiralty Inlet	12.2	4.4	15.7	0.035
4 Admiralty Bay	N. Admiralty Inlet	4.9	9.0	53.7	0.035
5 Admiralty Inlet South	N. Admiralty Inlet	9.4	6.4	78.3	0.035
6 Hood Canal Junction	N. Admiralty Inlet	9.5	10.8	53.5	0.035
7 Hood Canal North	Hood Canal	37.3	3.9	47.1	0.035
8 Dabob Bay	Hood Canal	17.0	4.2	82.9	0.090
9 Hood Canal South	Hood Canal	65.2	2.9	72.9	0.090
10 Useless Bay	S. Admiralty Inlet	8.8	8.8	74.3	0.090
11 Possession Sound	Whidbey Basin	9.3	3.5	128	0.200
12 Gedney Island	Whidbey Basin	16.1	6.9	79.3	0.200
13 Port Susan	Whidbey Basin	17.6	4.5	58.8	0.035
14 Saratoga Passage South	Whidbey Basin	8.8	6.2	82.9	0.150
15 Holmes Harbor	Whidbey Basin	10.1	2.6	34.3	0.035
16 Saratoga Passage North	Whidbey Basin	13.5	4.7	61.3	0.150
17 Penn Cove	Whidbey Basin	12.4	4.5	20.3	0.035
18 Skagit Bay	Whidbey Basin	28.1	3.4	12.9	0.050
19 Triple Junction	Main Basin	11.4	11.5	123	0.150
20 Main Basin North	Main Basin	5.8	7.6	124	0.150
21 Main Basin Central	Main Basin	26.3	13.6	85.1	0.150
22 Main Basin South	Main Basin	30.5	8.6	101	0.150
23 Tacoma Narrows North	Tacoma Narrows	4.1	2.0	43.3	0.035
24 Tacoma Narrows Central	Tacoma Narrows	3.4	1.7	35.6	0.035
25 Tacoma Narrows South	Tacoma Narrows	2.7	2.2	30.2	0.035
26 Fox Island	South Sound	7.3	4.7	55.1	0.055
27 Nisqually Reach	South Sound	31.4	4.0	49.2	0.075
28 Carr Inlet South	South Sound	7.1	4.3	74.0	0.035
29 Carr Inlet North	South Sound	16.1	4.5	34.2	0.035
30 Dana Passage	South Sound	2.2	1.7	20.2	0.035
31 Case Inlet	South Sound	20.7	4.1	24.5	0.035
32 Squaxin Island	South Sound	3.3	1.8	9.1	0.035
33 Cooper Point	South Sound	8.6	2.4	16.6	0.035
34 Budd Inlet	South Sound	10.4	2.2	6.6	0.035
35 Eld Inlet	South Sound	10.2	1.7	7.2	0.035
36 Totten Inlet	South Sound	11.5	2.0	8.6	0.035
37 Hammersley Inlet	South Sound	17.9	1.0	6.3	0.035

VITA**Biography**

Brian Polagye was born in Morristown, NJ. Over the years, he has lived in New Jersey, Massachusetts, Washington DC, London, and Brussels, but is happy to call Seattle home. He graduated from Princeton University in 2000 with a degree in Mechanical and Aerospace Engineering. For the next two years, he was employed as a strategy consultant with Dean & Company, a small firm based in Washington, DC and had the opportunity to work with clients throughout Europe. In 2005 he received a Master of Science in Mechanical Engineering from the University of Washington. His thesis focused on the economics of converting waste biomass to biofuels. In 2009 he earned a Doctor of Philosophy in Mechanical Engineering at the University of Washington. His dissertation focused on the environmental effects of energy extraction by in-stream tidal turbines.

Journal Publications

- **Polagye, B., Malte, P., Kawase, M., and Durran, D.** Effect of large-scale kinetic power extraction on time-dependent estuaries. *Proc. Inst. MechE, Part A: J. Power and Energy*. **222**(5), 2008.
- **Polagye, B., Malte, P., and Hodgson, K.** An economic analysis of bio-energy options using thinnings from overstocked forests. *Biomass and Bio-energy*, **31**(2-3), 2007.